HAL
open science

Modeling of single cell and network phenomena of the nervous system : ion dynamics during epileptic oscillations and inverse stochastic resonance

Anatoly Buchin

To cite this version:

Anatoly Buchin. Modeling of single cell and network phenomena of the nervous system : ion dynamics during epileptic oscillations and inverse stochastic resonance. Psychology. Ecole normale supérieure - ENS PARIS, 2015. English. NNT : 2015ENSU0041 . tel-01774505

HAL Id: tel-01774505

https://theses.hal.science/tel-01774505v1

Submitted on 23 Apr 2018

HAL is a multi-disciplinary open access archive for the deposit and dissemination of scientific research documents, whether they are published or not. The documents may come from teaching and research institutions in France or abroad, or from public or private research centers.

L'archive ouverte pluridisciplinaire **HAL**, est destinée au dépôt et à la diffusion de documents scientifiques de niveau recherche, publiés ou non, émanant des établissements d'enseignement et de recherche français ou étrangers, des laboratoires publics ou privés.

Thèse de Doctorat

En vue de l'obtention du grade de

DOCTEUR
DE L'ÉCOLE NORMALE SUPÉRIEURE

École doctorale

Cerveau Cognition Comportement

Discipline ou spécialité :

Neurosciences and Sciences Cognitives

Présentée et soutenue par :

Anatoly Buchin

le 30/11/2015

Titre

Modeling of single cell and network phenomena of the nervous system: ion dynamics during epileptic oscillations and inverse stochastic resonance

---

Unité de recherche Laboratoire des Neurosciences Cognitives

Thèse dirigée par Dr. Boris Gutkin

Dr. Anton Chizhov

Membres du jury

Dr. Maxim Bazhenov (rapp.)

Dr. Volker Steuber (rapp.)

Dr. Richard Miles (exam.)

Dr. Gilles Huberfeld (exam.)

Dr. Boris Gutkin (direct.)

Dr. Anton Chizhov (co-direct.)

Numéro identifiant de la Thèse :

Science, my lad, is made up of mistakes, but they are mistakes which it is useful to make, because they lead little by little to the truth.

Jules Verne

Essentially, all models are wrong, but some are useful.

George Edward Pelham Box

ABSTRACT

In this thesis we used dynamical systems methods and numerical simulations to study the mechanisms of epileptic oscillations associated with ion concentration changes and cerebellar Purkinje cell bimodal behavior. The general issue in this work is the interplay between single neuron intrinsic properties and synaptic input structure controlling the neuronal excitability.

In the first part of this thesis we focused on the role of the cellular intrinsic properties, their control over the cellular excitability and their response to the synaptic inputs. Specifically we asked the question how the cellular changes in inhibitory synaptic function might lead to the pathological neural activity. We developed a model of seizure initiation in temporal lobe epilepsy. Specifically we focused on the role of KCC2 cotransporter that is responsible for maintaining the baseline extracellular potassium and intracellular chloride levels in neurons. Recent experimental data has shown that this cotransporter is absent in the significant group of pyramidal cells in epileptic patients suggesting its epileptogenic role. We found that addition of the critical amount of KCC2-deficient pyramidal cells to the realistic subiculum network can switch the neural activity from normal to epileptic oscillations qualitatively reproducing the activity recorded in human epileptogenic brain slices.

In the second part of this thesis we studied how synaptic noise might control the Purkinje cell excitability. We investigated the effect of spike inhibition caused by noise current injection, so-called inverse stochastic resonance (ISR). This effect has been previously found in single neuron models while we provided its first experimental evidence. We found that Purkinje cells in brain slices could be efficiently inhibited by current noise injections. This effect is well reproduced by the phenomenological model fitted for different cells. Using methods of information theory we showed that ISR supports an efficient information transmission of single Purkinje cells suggesting its role for cerebellar computations.

Keywords: dynamical systems, temporal lobe epilepsy, KCC2 cotransporter, extracellular potassium, intracellular chloride, GABA reversal, cerebellum, Purkinje cells, bimodality, inverse stochastic resonance.

RÉSUMÉ

Dans cette thèse nous avons utilisé des méthodes de systèmes dynamiques et des simulations numériques pour étudier les mécanismes d'oscillations d'épilepsie associés à des concentrations d'ions dynamiques et au comportement bimodal des cellules Purkinje du cervelet. Le propos général de ce travail est l'interaction entre les propriétés intrinsèques des neurones simple et la structure d'entrée synaptique contrôlant l'excitabilité neuronale.

Dans la première partie de la thèse nous avons développé un modèle de transition de crise épileptique dans le lobe temporal du cerveau. Plus précisément nous nous sommes concentrés sur le rôle du cotransporteur KCC2, qui est responsable de la maintenance du potassium extracellulaire et du chlorure intracellulaire dans les neurones. Des données expérimentales récentes ont montré que cette molécule est absente dans un groupe significatif de cellules pyramidales dans le tissue neuronal de patients épileptiques suggérant son rôle épileptogène. Nous avons trouvé que l'addition d'une quantité critique de cellules pyramidale KCC2 déficient au réseau de subiculum, avec une connectivité réaliste, peut provoquer la génération d'oscillations pathologiques, similaire aux oscillations enregistrées dans des tranches de cerveau épileptogène humaines.

Dans la seconde partie de la thèse, nous avons étudié le rôle du bruit synaptique dans les cellules de Purkinje. Nous avons étudié l'effet de l'inhibition de la génération du potentiel d'action provoquée par injection de courant de bruit, un phénomène connu comme résonance stochastique inverse (RSI). Cet effet a déjà été trouvé dans des modèles neuronaux, et nous avons fournis sa première validation expérimentale. Nous avons trouvé que les cellules de Purkinje dans des tranches de cerveau peuvent être efficacement inhibées par des injections de bruit de courant. Cet effet est bien reproduit par le modèle phénoménologique adapté pour différentes cellules. En utilisant des méthodes de la théorie de l'information, nous avons montré que RSI prend en charge une transmission efficace de l'information des cellules de Purkinje simples suggérant son rôle pour les calculs du cervelet.

Mots-clés: systèmes dynamiques, épilepsie du lobe temporal, KCC2 cotransporteur, potassium extracellulaire, chlorure intracellulaire, inversion de GABA, résonance inverse stochastique, le cervelet, les cellules de Purkinje, bimodalité, bruit synaptique.

CONTENTS

ABSTRACT 3

RÉSUMÉ 4

CONTENTS 5-6

GENERAL INTRODUCTION 7-8

CHAPTER I
ION DYNAMICS DURING EPILEPTIC OSCILLATIONS 9-24
I.1 Introduction 9-10
I.2 Intracellular chloride 10-13
I.3 Extracellular potassium 13-15
I.4 Potassium and sodium 15-17
I.5 Potassium, sodium and chloride 18-19
I.6 Conclusions 20-21
I.7 References 22-24

CHAPTER II
THE ROLE OF K/Cl HOMEOSTASIS IN HUMAN SUBICULUM EPILEPSY 25-82
II.1 Introduction 25-26
II.2 Article 27-56
II.2.1 Abstract 27
II.2.2 Introduction 28-29
II.2.3 Material and Methods 30-34
II.2.4 Results 35-52
II.2.4.1 Absence of KCC2 leads to a depolarizing GABA reversal potential 35-37
II.2.4.2 Single cell consequences of KCC2(-) pathology 37-39
II.2.4.3 Gamma oscillations in KCC2(+) subiculum circuit 39-41
II.2.4.4 KCC2(-) pathology in the subiculum circuit 41-44
II.2.4.5 Analysis of the epileptic oscillations 44-47
II.2.4.6 KCC2(-) pathology in the subiculum circuit with endogenous potassium 47-50
II.2.4.7 Elimination of the KCC2(-) pathology prevents seizure 50-52
II.2.5 Discussion 53-56
II.3 Detailed model description 57-78
II.3.1 Seizure pharmacology 57-58
II.3.2 Pyramidal cell and interneuron model 59-64
II.3.3 Subiculum connectivity structure 65-67
II.3.4 Kation chloride cotransporter model 68-69
II.3.5 Potassium diffusion model 70-72
II.3.6 Local field potential model 73-76
II.3.7 Seizure detection algorithm 77-78
II.4 Future directions 77-70
II.5 References 83-89

CHAPTER III
NOISE-INDUCED PHENOMENA IN SINGLE NEURONS 90-101
III.1 Introduction 90-91
III.2 Neural noise sources 91-93
III.3 Stochastic resonance 93-95
III.4 Inverse stochastic resonance 96-97
III.5 Conclusions 98
III.6 References 99-101

CHAPTER IV
INVERSE STOCHASTIC RESONANCE 102-168
IV.1 Introduction 102
IV.2 Article 2 103-148
IV.2.1 Abstract 103
IV.2.2 Author summary 104
IV.2.3 Introduction 107-106
IV.2.4 Material and methods 107-113
IV.2.5 Results 114-134
IV.2.5.1 Purkinje cells exhibit inverse stochastic resonance (ISR) 134-116
IV.2.5.2 ISR parameters are related to Purkinje cell bistability 116-118
IV.2.5.3 An aEIF model describes Purkinje cell firing 118-121
IV.2.5.4 The aEIF model reproduces Purkinje cell bistability and ISR 121-124
IV.2.5.5 Bifurcation analysis of the aEIF model 124-126
IV.2.5.6 Functional role of ISR 126-130
IV.2.5.7 ISR optimizes information transfer 130-134
IV.2.6 Discussion 135-141
IV.2.7 Supplementary materials 142-148
IV.3 Detailed model description 149-161
IV.3.1 Adaptive exponential integrate-and-fire model 149-156
IV.3.2 Mutual information algorithm 157-159
IV.3.3 Synaptic noise estimation for Purkinje cell 160-161
IV.4 Future directions 162-163
IV.5 References 164-167

GENERAL CONCLUSIONS 168-170
References 171-172

ACNOWLEDGEMENTS 173-174

GENERAL INTORODUCTION

The brain is probably the most complex mechanism we know in nature. It posses complex dynamics and organization both on different spatial and temporal scales. There is a hierarchy of structural organization of the nervous system each with characteristic spatial scale: central nervous system ($1\,m$), subcortical structures ($10\,cm$), sensory maps ($1\,cm$), networks ($1\,mm$), neurons ($100\,\mu m$), synapses ($1\,\mu m$) and molecules ($1\,\mathring{A}$ - $100\,nm$). One could build similar hierarchy with the temporal scale ranging from milliseconds (spike generation) till days and years (long-term plasticity changes). Given such a high degree of complexity it is necessary to reduce the brain mechanisms to meaningful and understandable concepts on different levels of description. To achieve this long-term goal theoretical and computational neuroscience aim to uncover the basic principles of the nervous system function and organization. Similar to theoretical physics it uses mathematical models to investigate the basic mechanisms by generalizing and providing explanations for the experimental results. Although theoretical physics has hundreds years of modern scientific history, computational neuroscience is relatively new field matured only in the end of XX century. The theory of dynamical systems that was applied in the present work is one of the key conceptual frameworks in computational neuroscience aiming to explain the fundamental mechanisms of brain dynamics.

In first part this thesis we apply the dynamical system approach towards the mechanism of brain pathological oscillations observed in epilepsy. We aim to investigate the mechanisms of ion concentration changes associated with extracellular potassium and intracellular chloride and their role for seizure initiation. First we review the modern concepts of ion concentration dynamics associated with seizures in **CHAPTER I**. In this review we discuss known mechanisms of slow ion concentration changes of sodium, potassium and chloride associated with epileptic seizures. Then we investigate recently found pathway related to intracellular chloride regulation in pyramidal cells of human subiculum in **CHAPTER II**. We build the single neuron and neural network model to study epileptic oscillations and compare the results with *in vitro* slice data.

In the second part of this thesis we use dynamical systems to study the bimodal behavior of cerebellar Purkinje cells. Specifically we describe the role of synaptic noise provided by the neural network. First we make a short overview of neuronal noise and discuss the classical models of neural noise sources and its effects on single neurons behavior in **CHAPTER III**. Since this theme is very broad we restrict our description to stochastic and inverse stochastic resonance in single cells. In **CHAPTER IV** we investigate experimentally and theoretically using a phenomenological model the role of synaptic noise for Purkinje cells and suggest its role for cerebellum function.

In the final part **GENERAL CONCLUSIONS** we turn to the contribution of these two projects in a broad context. In particular we discuss the role of single

neuron nonlinear properties for normal and pathological brain dynamics and missing links in biophysical neural models.

CHAPTER I
ION DYNAMICS DURING EPILEPTIC OSCILLATIONS

I.1 Introduction

This chapter is a review of existing computational models of ion dynamics during seizure oscillations and certain related experiments. We mostly concentrate on ion concentration changes associated with seizure dynamics. We describe known models of intracellular chloride regulation, the interplay between potassium and sodium and unified models describing potassium, sodium and chloride. In conclusion section we point to the missing mechanisms of the existing models and propose the necessary corrections.

Mechanisms of seizure dynamics can be studied on different levels of brain organization from single cell up to the whole brain level. Many of these mechanisms are very hard to study experimentally since it requires simultaneous measurements of brain activity on various spatial and temporal scales. Therefore theoretical approaches provide significant insights into the mechanisms of epileptic brain dynamics, that could suggest new hypothesis for further experimental validation, as reviewed in (Lytton 2009).

Epilepsy is characterized by complex reorganization of neural circuits on different scales. These levels include cell death, axon sprouting, alterations in synaptic plasticity and intrinsic properties of neurons and glia. As a consequence it is very hard to find the key pathological pathways. Therefore detailed biophysical models are useful tools to investigate the particular mechanisms of epilepsy in neural circuits.

Biophysical models of single neurons mostly rely on conductance-based description of the neuronal membrane, initially proposed for squid axon in 1952 (Hodgkin and Huxley 1952). Hodgkin and Huxley have shown that there are minimally two currents – sodium and potassium needed to generate voltage oscillations during action potential generation and propagation. Later studies identified numerous additional intrinsic currents incorporated into the membrane that could substantially change single neuron behavior (Izhikevich 2007). This approach is extended for multi-compartmental models describing soma, axon and dendritic tree and taking into account spatiotemporal integration of synaptic input (Koch and Segev 1998).

To study the pathological changes associated with seizure generation using biophysical approach the behavior of the system is analyzed when the parameters of interest are varied to mimic the pathological conditions. On the other hand variations of the biophysical parameters could be studied to determine the desired behavior of the system. A combination of these theoretical

approaches helps to properly investigate pathological behavior and form testable predictions for new experiments.

Currents passing through ion channels depend on the ion concentrations inside and outside of neurons and corresponding electrochemical gradients. In the models using conductance-based description of a neuron the ion concentrations are usually considered constant due to various homeostatic mechanisms such as sodium-potassium pumps, glial buffering and diffusion in the extracellular space. Nonetheless in the pathological conditions like epilepsy and spreading depression the ion concentrations in the extracellular space and inside neurons are substantially altered. This leads to changes in reversal potential thus affecting the neural excitability. In this review we show how ion concentration changes could favor and potentially trigger seizure activity in various epilepsy models.

I.2 Intracellular chloride

Changes in intracellular chloride concentrations have the direct influence on the value of GABA reversal potential controlling the efficiency of inhibition (Kandel et al. 2000). In the early development GABA reversal potential is mostly excitatory due to high intracellular chloride levels due to significant NKCC1 expression. Later during development in the adult brain GABA becomes hyperpolarizing due to NKCC1 down-regulation and KCC2 up-regulation (Khalilov et al. 1999).

During the course of neural activity when the firing-rate is low the change of intracellular chloride concentration could be potentially neglected because of action of KCC2 cotransporter (Payne et al. 2003). Yet in case of intensive GABAergic inhibition the intracellular chloride could substantially accumulate in neurons (Kaila and Voipio 1987, Taira et al. 1997). This mechanism provides short-time decrease of inhibition at the synapses, a property known as ionic plasticity (Jedlička and Backus 2006, Raimondo et al. 2012). In this way the intracellular chloride concentration is an important factor shaping the neural activity that plays especially important role for epileptic brain dynamics characterized by the high firing rates.

The impairment of intracellular chloride homeostasis due to the KCC2 absence and/or NKCC1 overexpression has been found in epileptogenic human tissue from subiculum (Huberfeld et al. 2007) and cortical peritumoral tissue (Pallud et al. 2014). Local changes of intracellular chloride concentration could significantly affect the inhibition efficiency of different synapses thus contributing to the excitation-inhibition balance (Jedlička and Backus 2006).

In the single neuron model proposed by (Jedlicka et al. 2011) the authors have studied the consequences of GABAergic stimulation in the anatomically

realistic model of interneuron from (Gulyas et al. 1999). They have built the detailed conductance-based model of the inhibitory cell with passive conductances and inhibitory GABA synapses. In this model the radial and longitudinal intracellular chloride diffusion was taken into account in the whole neuron. They found that prolonged activation of the dendritic GABA synapses leads to the substantial increase of intracellular chloride concentration so that GABA reversal potential becomes excitatory, Fig.I-1A. This property is especially strong for the distal synapses compared to the proximal ones. In a more detailed pyramidal cell model taking into account the electrodiffusion and hydrocarbonate changes (Doyon et al. 2011) have found similar results indirectly confirmed by chloride imaging experiments in cultures.

In the other work Marchetti and colleagues (Marchetti et al. 2005) have studied oscillations in the developing chick spinal chord. Using simple mean-field model they showed that combination of slow intracellular chloride accumulation and synaptic depression could explain the periodic network oscillations, Fig.I-1B. In a theoretical study of a spatially connected networks (Rinzel et al. 1998) have found that changes in the GABA reversal potential could trigger propagating activity waves, which could be potentially related to the giant depolarizing potentials during development (Leinekugel et al. 1998). In the further works Jeong and Gutkin (Jeong and Gutkin 2007) proposed that changes in GABA reversal potential could provoke synchronous in-phase and anti-phase solutions in the large neural networks with slow synapses. Taken together these results indicate that changes in GABA reversal potential could substantially affect the single neuron and network dynamics in different parts of the nervous system.

Using slice experiments of hippocampal formation it has been observed that strong tetanic stimulation leading to seizure-like discharges promotes intracellular chloride accumulation measured by chloride imaging, Fig.I-1C, D (Isomura et al. 2003). In the later works of this group (Fujiwara-Tsukamoto et al. 2007) they found that GABA reversal potential becomes depolarizing during seizure-like events caused by tetanic stimulation due to chloride accumulation. They explained the increase of extracellular potassium and intracellular chloride concentration by strong activation of interneurons and pyramidal cells during extracellular stimulation.

Changes of GABA reversal potential due to intracellular chloride accumulation has been known for a long time (Kaila and Voipio 1987) in the experimental neuroscience. Yet in the theoretical works the role of intracellular chloride accumulation received relatively little amount of attention (Jedlička and Backus 2006). The single neuron models confirmed that on the single neuron level strong GABAergic stimulation leads to the substantial increase of intracellular chloride thus reducing the amount of inhibition. While neural

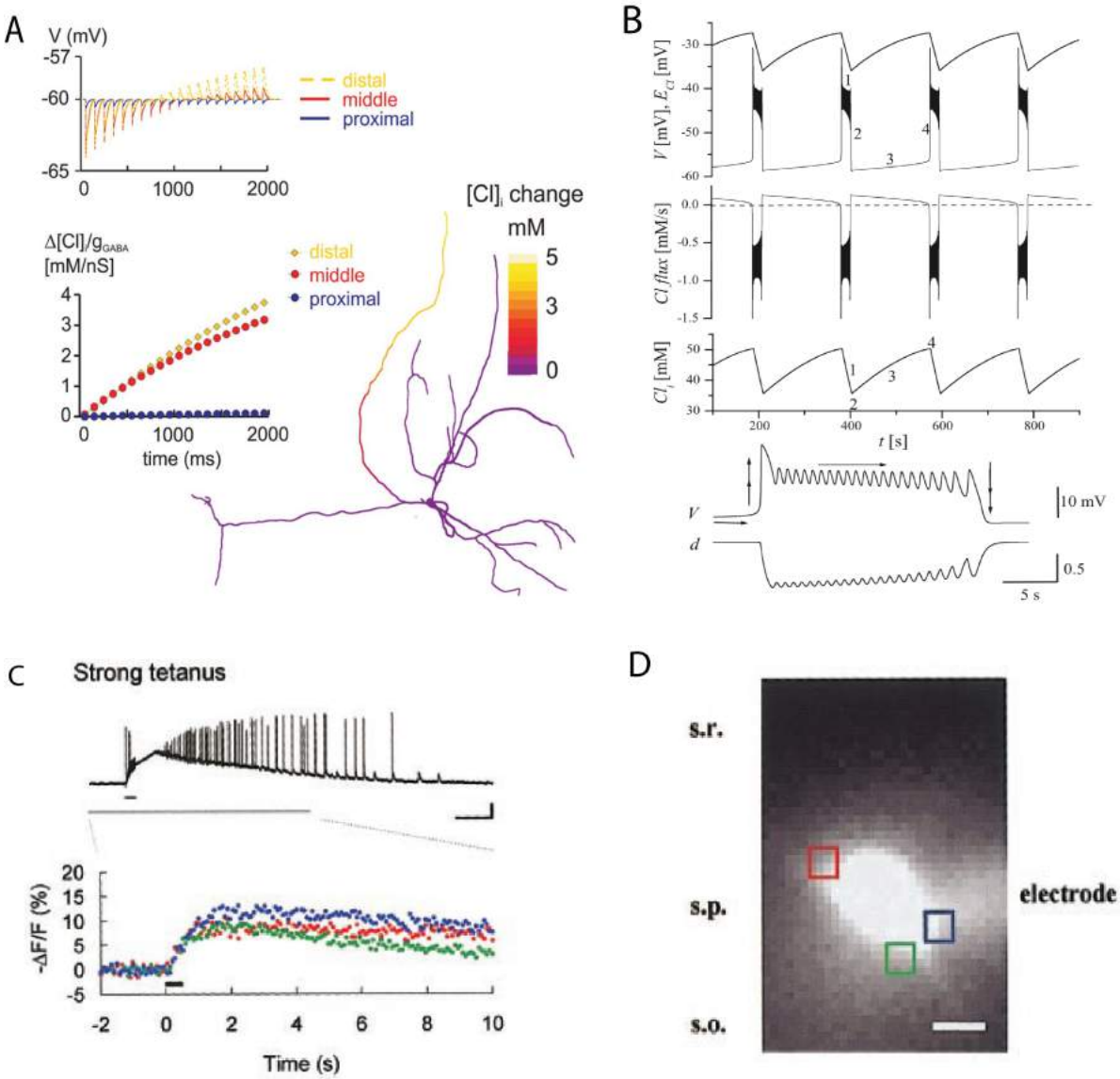

Figure I-1. Intracellular chloride accumulation in neural models and experiments
A – voltage changes on the distal, middle and proximal dendrites during GABAergic stimulation, 10 Hz 20 pulses and 13 GABA synapses. On the bottom are present the corresponding chloride changes. Spatial plot of the intracellular chloride accumulation after tetanic stimulation using 10 Hz activation of 13 GABA synapses of the distal dendrite. Color code corresponds to the intracellular chloride change. Adapted from (Jedlicka et al. 2011). B – periodic bursting activity generated in the population model describing depression and chloride accumulation. Top trace – voltage changes, middle trace – intracellular chloride concentration and flux changes, bottom – zoom in voltage and depression variable. Adapted from (Marchetti et al. 2005). C – response of the pyramidal cell in the hippocampal slice to the strong tetanic stimulation and corresponding changes in chloride luminescence measured by MEQ. Colors correspond to the probe location in D. Scale bars are 2s and 20 mV. D – one timeframe of chloride imaging with probe location; s. r. – stratum radiatum, s. p. – stratum piramidale, s.o. – stratum oriens. Scale bar is $10\mu m$. Panels C and D are adapted from (Isomura et al. 2003).

network models suggested that increasing GABA reversal potential promotes oscillations and synchrony. Thereby the dynamics of intracellular chloride and consequent GABA reversal potential changes is an important excitability mechanism for normal and pathological oscillations in the nervous system.

I.3 Extracellular potassium

Historically one of the first conductance-based models incorporating the dynamic ion concentrations in the context of seizure and spreading depression is the model of Kager and colleagues (Kager et al. 2000). In this work they constructed the pyramidal cell model consisting of multiple compartments with 5 ionic currents, sodium-potassium pump and glial uptake on each compartment. They based their approach on the CA3 pyramidal cell model from (Traub et al. 1994), yet included mechanisms of dynamic ion concentrations for sodium and potassium, Fig.I-2A. The authors showed that impaired glial uptake and strong synaptic stimulation leads to periodic spiking, Fig.I-2B associated with clonic epileptoform discharges. In this model they found the regimes associated with spreading depression, when neurons move to the depolarization block due to high potassium concentrations.

Based on this approach Bazhenov and colleagues (Bazhenov et al. 2004) used reduced model from (Mainen and Sejnowski 1996) to describe the ion dynamics including intracellular calcium, extracellular potassium with glial uptake and extracellular diffusion (Kager et al. 2000). This model reproduced periodic spiking and bursting activity caused by increased potassium concentration, Fig.I-2C. Compared to the previous studies (Kager et al. 2000) their model was able to show periods of bursting and spiking activity in response to current stimulation due to internal calcium dynamics and intrinsic currents in pyramidal cells. They generalized this model of potassium dynamics using the sparsely connected neural network consisting of interneurons and pyramidal cells. This network demonstrated an ability to maintain spike-and-wave oscillations in response to the current stimulation and subsequent extracellular potassium increase, Fig.I-2D. They also found that characteristic paroxysmal oscillations could be triggered by blockade of glial buffer and/or sodium-potassium pumps.

In further works of this group they have systematically analyzed the pyramidal cell dynamics as a function of intracellular calcium concentration (Fröhlich and Bazhenov 2006). They found characteristic transitions between bursting and tonic spiking regimes in terms of bifurcation structure of the model. In particular they studied the regime of bistability for extracellular potassium parameter between 5 and 5.4 mM allowing the pyramidal cell to demonstrate the transitions between slow bursting and tonic spiking. They proposed that this bistability cold explain the continuous transitions between

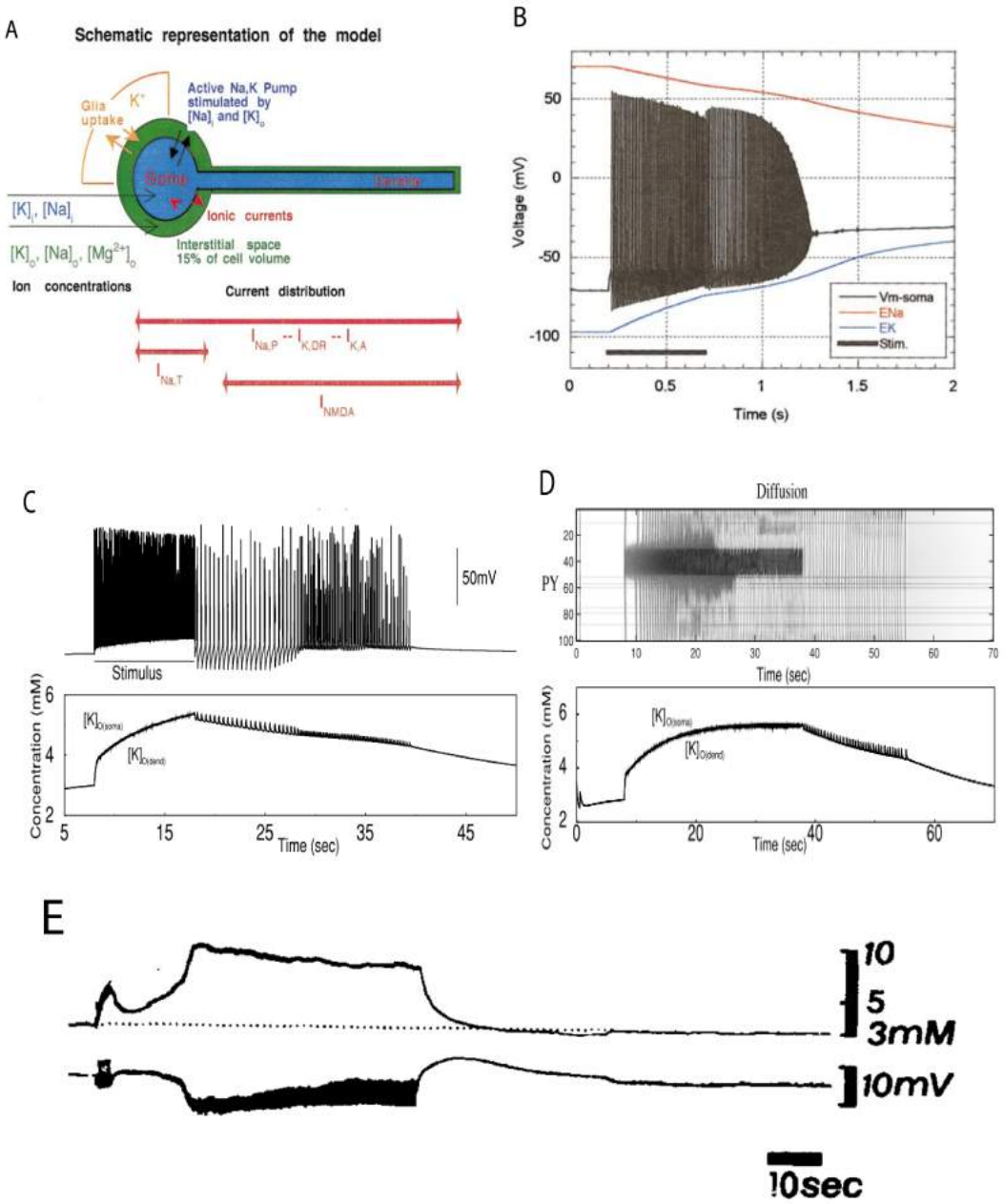

Figure I-2. Extracellular potassium dynamics in neuron models and experiment
A – Scheme of pyramidal cell model with the main components. B – simulated seizure-like discharge followed by spreading depression in response to injected current, 0.2 nA during 500 ms. Panels A and B are adapted from (Kager et al. 2000). C – response of the pyramidal cell model with dynamic extracellular potassium concentration to the current stimulation during 5 seconds with the subsequent periodic bursting and spiking activity. D – simulation of the network of pyramidal cells and interneurons when cells 35-45 received current stimulation during 10th second. Panesl C and D are adapted from (Bazhenov et al. 2004). E – simultaneous measures of extracellular potassium (top) and extracellular field potential (bottom) during tonic-clonic seizure evoked by electrical stimulation in the pericruciate cortex. Adapted from (Sypert and Ward 1974).

tonic and clonic phase of spike-and-wave discharges observed *in vivo* (Fröhlich et al. 2008).

In the later works they have tested the coexistence of healthy and pathological activity states in these networks (Fröhlich et al. 2010). They systematically studied the role of perturbations such as duration and stimulation strength leading to the transition from the normal to pathological state. They concluded that synaptic depression, potassium regulation mechanisms, intrinsic neuron currents and increase of intracellular chloride could substantially contribute to seizure dynamics.

To illustrate changes of extracellular potassium during seizure activity we present the simultaneous measures of extracellular potassium and field potential from (Sypert and Ward 1974), Fig.I-2E. In this work the recurrent seizure-like events were evoked by tetanic stimulation in cat neocortex. One could see that negative deflection of the extracellular field is strongly correlated with the extracellular potassium accumulation during seizure activity. There is also qualitative match between the time traces of extracellular potassium concentration in single neuron and network models and experimental data, Fig.I-2C, D, E.

Systematic impairment of extracellular potassium regulation has been known as a significant factor contributing to brain pathology for a very long time (Grafstein 1956, Fisher et al. 1975). Nonetheless only relatively recent advances in neural modeling using anatomically detailed (Kager et al. 2000) or reduced (Bazhenov et al. 2004) biophysical models allowed to study the detailed mechanisms of excitability associated with ion concentration changes. These models provide the insights into the role of extracellular potassium for brain pathologies like epilepsy and spreading depression and allow characterizing the limits of normal brain physiology.

I.4 Potassium and sodium

In the theoretical works Ullah and colleagues (Ullah et al. 2009, Barreto and Cressman 2011) have studied the interplay between intracellular sodium and extracellular potassium in single neuron and network models. The single neuron model takes into account the dynamics of sodium, potassium and chloride ions as well as slow potassium currents. The concentrations were computed using equations describing sodium-potassium pump, astrocyte potassium uptake and diffusion to the bath and extracellular space.

In the single neuron proposed in (Ullah et al. 2009) they found regimes of periodic spiking and resting activity, Fig.I-3A. Under balance conditions between sodium and potassium concentrations, the single neuron is capable to generate long periods of tonic spiking and resting state activity with the timescale similar to

the transitions between ictal discharges. In this system the extracellular potassium plays the role of positive feedback because it increases the reversal potential of potassium currents thus increasing the excitability, while intracellular sodium plays the role of a negative feedback since its accumulation decreases the value of sodium reversal potential needed for action potential generation. In this slow oscillatory regime the model is able to demonstrate the depolarization block during these oscillations, Fig.I-3A, B, resembling the single neuron behavior during seizures (Ziburkus et al. 2006).

In the companion work they constructed the neural network model (Barreto and Cressman, 2011) consisting of 100 pyramidal cells interneurons connected with Gaussian synaptic footprint with circular architecture, Fig.I-3C. They demonstrated that when the glial potassium uptake is impaired, the activity induced by current perturbations leads to periodic seizure-like activity characterized by single neuron depolarization block, Fig.I-3D. The overall dynamics of this network is similar to the single neuron case characterized by periods of tonic spiking and resting state, Fig.I-2A.

In the experimental work Karus and colleagues (Karus et al. 2015) have shown that intracellular sodium concentration is strongly correlated with seizure activity, Fig.I-3E. They used sodium imaging to show that this concentration significantly accumulates during short and long-lasting seizure episodes in pyramidal cells and astrocytes. One could see the correlation between the field potential and sodium concentration on the single neuron level during large and small epileptic event, Fig.I-3D. They also found that sodium accumulates very synchronously in the pyramidal cell population during seizures suggesting that it could be responsible for seizure termination as predicted in (Krishnan and Bazhenov, 2011). One could compare the time trace of sodium accumulation measured experimentally with the one predicted by the model and find a qualitative agreement, Fig.I-3A, D, E.

Addition of intracellular sodium to the extracellular potassium model on single neuron and network level revealed new oscillatory regimes associated with seizures. Using simulations it has been found that intracellular sodium and extracellular potassium are potential mechanisms responsible for autonomous transitions between interictal and ictal states. These results suggest the crucial role of these ions for generation of slow epileptic oscillations in neural networks.

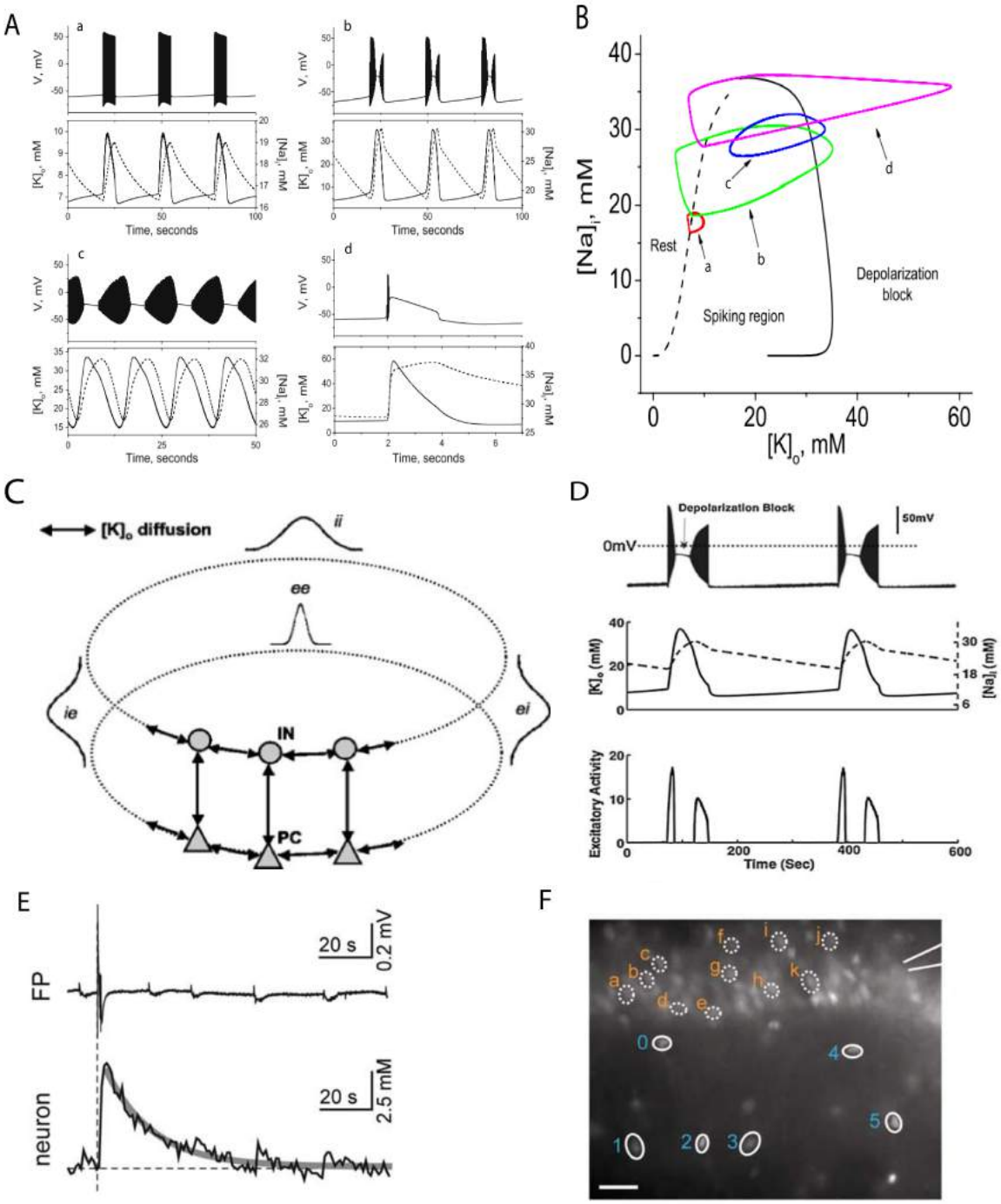

Figure I-3. Dynamics of intracellular sodium and extracellular potassium in models and experiment

A –single neuron patterns and ion concentration changes in single neuron model. B – state diagram of the single neuron model from A with corresponding ion concentration changes. Panels A and B are adapted from (Ullah et al. 2009). C – Structure of the network model with dynamic sodium and potassium concentrations. D – patterns of spontaneous activity of single neurons in the network. Panels C and D are adapted from (Barreto and Cressman 2011). E – field potential (FP) and single neuron sodium concentration change (calculated from the fluorescent signal) during the long epileptoform discharge. F – location of the pyramidal cells and astrocytes in the slice. Letters correspond to neurons, numbers to astrocytes. Panels E and F are adapted from (Karus et al. 2015).

I.5 Potassium, sodium and chloride

In the later works the group of Maxim Bazhenov included intracellular sodium accumulation into the model of spike-and-wave discharges (Krishnan and Bazhenov 2011). Similar to the previous studies this model included dynamic concentrations of potassium, chloride and sodium and the model of KCC2 cotransporter coupled with intracellular chloride concentration. They found that including mechanisms of intracellular sodium accumulation stops generation of the periodic spike-and-wave discharges after long period of oscillations, Fig.I-4A. They have found that increased intracellular sodium caused by intensive spiking during seizures could also explain the hyperpolarized post-ictal depression state in pyramidal cells. Intracellular chloride accumulation in this model increased seizure duration. Using methods of bifurcation theory they found that generation of seizures and their termination depends on the complex interplay of between sodium, potassium and chloride ions, Fig.I-4B.

In the work of (Wei et al. 2014) they showed that seizures and spreading depression could be described as two extreme cases of extracellular potassium dysregulation. They extended the modified Hodgkin-Huxley model using the conservation law for sodium, potassium and chloride ions and addition of O_2-dependence for the sodium-potassium pump and glia, Fig.I-3C. Similar to the works of (Ullah et al. 2009), Fig.I-3B they found a repertoire of dynamical states corresponding to seizure-like dynamics and spreading depression. In particular they found that spreading depression or seizures could be achieved either by manipulations of extracellular potassium or by reduction of oxygen, Fig.I-4D. In this work they proposed that seizures or spreading depression is the consequence of the conservation law for ions and metabolic processes related to oxygen rather than specific property of a neuron model.

Based on presented computational models of seizure dynamics we conclude that epileptic seizures involve the dynamic interplay of sodium, potassium and chloride ions as well as metabolic processes. Due to the conservation law all these ions should be considered together in one model to explain the complex seizure dynamics. Yet comparing these results with the previous work (Barreto and Cressman 2011) with only extracellular potassium and intracellular sodium one could see that using simplified approximations of constant intracellular potassium and extracellular sodium, Fig.I-3A, provides substantially similar dynamics to Fig.I-4D.

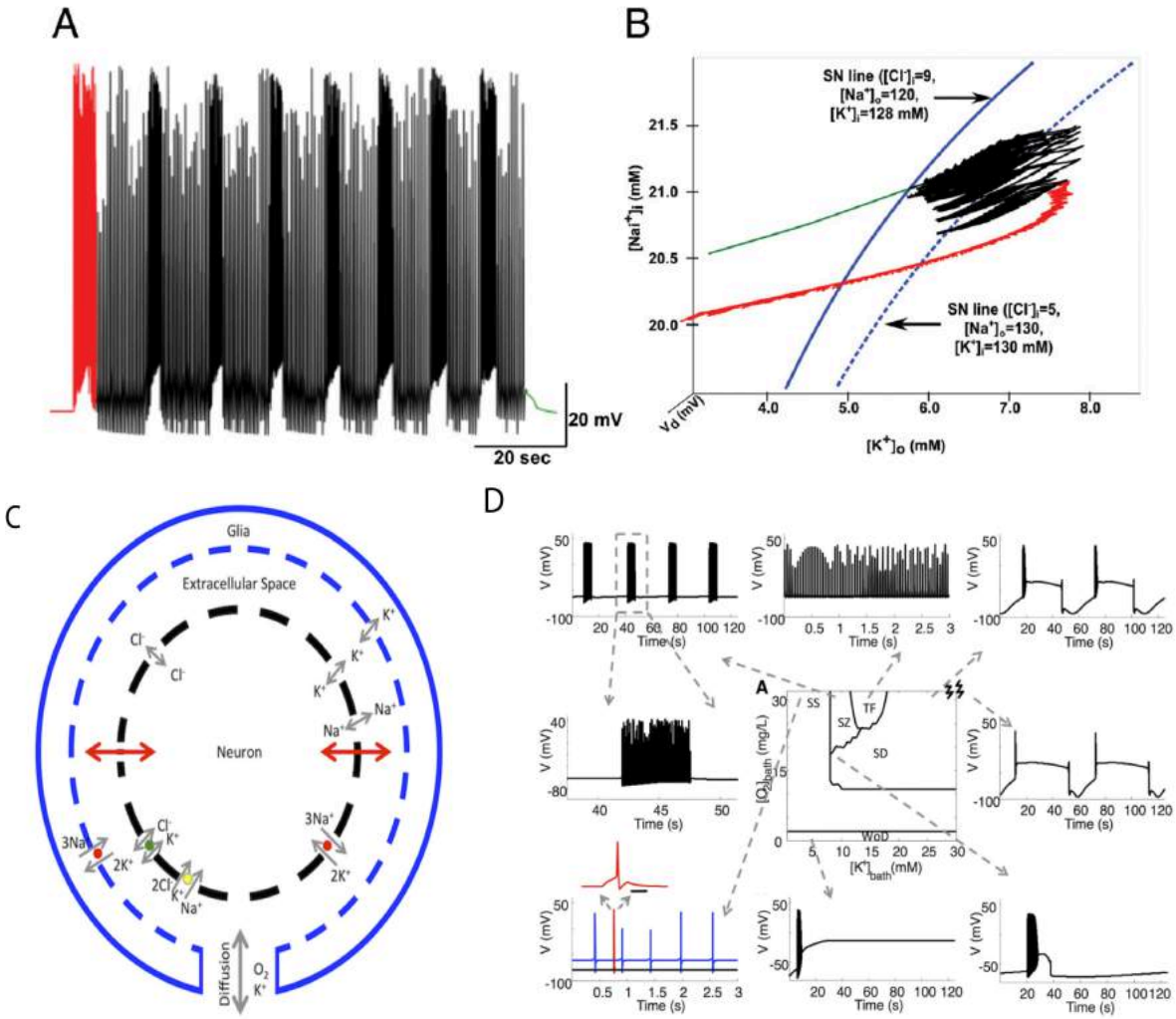

Figure I-4. Ion dynamics of potassium, sodium and chloride in single neuron and neural network models

A – membrane voltage trace of a pyramidal neuron from a small network of 10 PY and 2 IN, red is the period of current stimulation, black corresponds to oscillations during seizures, green is the end of seizure. B – trajectory of the single neuron in the network on the state diagram for extracellular potassium and intracellular sodium, the color code is the same as on A. Panels A and B are adapted from (Krishnan and Bazhenov 2011). C – pyramidal cell model scheme with ions pumps and cotransporters. D – repertoire of the model dynamic behavior depending on the extracellular potassium concentrations and the amount of oxygen in the extracellular solution, SS – single spikes, TF – tonic firing, SZ – seizure, SD – spreading depression. Panels C and D are adapted from (Wei et al. 2014).

I.6 Conclusions

In this review we described existing mechanisms of slow ion dynamics associated with seizure activity in single neuron and neural network models and qualitatively compared them with the available experimental data. The model of (Jedlicka et al. 2011) and (Doyon et al. 2011) shows that accumulation of intracellular chloride caused by GABAergic stimulation substantially modulates the amount of inhibition due to GABA reversal potential changes. On the network level changes in corresponding GABA reversal potential could provoke rhythm generation and synchrony in developing nervous system (Marchetti et al. 2005). The works of (Ullah et al. 2009) and (Barreto and Cressman 2011) showed that the interplay between sodium and potassium ions provides the mechanism for slow oscillations potentially associated with ictal discharges. The model of (Wei et al. 2014) predicts that mechanisms of seizure dynamics and spreading depression are not specific for a particular neuron model, yet mostly depend on the mechanisms of ion regulation, suggesting that seizure oscillations associated with ion concentrations is a general phenomena in the nervous system.

Qualitative comparison of presented models with the available experimental data showed that concentration of intracellular chloride (Isomura et al. 2003), extracellular potassium (Sypert and Ward 1974) and intracellular sodium (Karus et al. 2015) is strongly correlated with seizure activity. Considered computational models showed their qualitative agreement with the available data, yet none of them was completely verified. All considered models of epileptic oscillations assumed that ion concentration changes are causally related to seizure generation. While available data does not allow separating whether ion concentration changes are the reason or the consequence of epileptic oscillations. We believe that taking into account these theoretical considerations would help to propose novel experiments to precisely clarify the role of ion concentration changes during seizures.

Nonetheless in the aforementioned models one important link between extracellular potassium and intracellular chloride is not properly described. In the model of (Krishnan and Bazhenov 2011) changes of GABA reversal potential are not affected by GABAergic input and subsequent chloride accumulation. The GABAergic current in the model is calculated in the following way:

$$I_{GABA} = g_{syn}[O](V - V_{GABA})$$
$$V_{GABA} = -80mV$$

The intracellular chloride accumulates in this model only due to chloride leak currents, while GABA reversal potential remains unchanged (Bazhenov et al. 2004). This property does not allow it to take into account the decrease of inhibition in the pyramidal cells caused by intensive GABAergic input (Kaila and Voipio 1987, Jedlicka et al. 2011).

The link between potassium and chloride in this model is described using the phenomenological equation for chloride extrusion with potassium-dependent extrusion constant (Payne, 1997):

$$\frac{dCl^-_{IN}}{dt} = -\frac{k_{Cl}}{F} I_{Cl} + \frac{Cl^{\infty}_{IN} - Cl^-_{IN}}{\tau_{Cl}}$$

$$\tau_{Cl} = 100 + \frac{\tau^{\infty}_{Cl}}{1 + \exp(\{Cl^{\infty}_{IN} - K^+_{OUT}\} / \tau_{Kocl})}$$

It could properly describe the extrusion rate $1/\tau_{Cl}$ (Payne et al. 2003), yet the baseline of chloride concentration Cl^{∞}_{IN} is fixed regardless of the extracellular potassium. This property does not allow this model to take into account the baseline chloride concentration as a function KCC2 expression and extracellular potassium. Therefore it could not be used to explain the experimental observation of depolarizing GABA reversal potential associated with the increased intracellular chloride level due to KCC2 pathology (Huberfeld et al. 2007).

To take into account this missing link between the extracellular potassium and intracellular chloride we added the biophysical model of KCC2 from (Doyon et al. 2011) to the existing extracellular potassium model (Bazhenov et al. 2004):

$$\frac{dCl^-_{IN}}{dt} = -\frac{k_{Cl}}{F} I_{Cl} + I_{KCC2}$$

$$I_{KCC2} = \frac{I_{\max}(V_K - V_{Cl})}{(V_K - V_{Cl}) + V_{1/2}}$$

This KCC2 model is substantially similar to the Michaelis-Menten description of chloride extrusion (Staley and Proctor 1999). It allows directly link the concentration of intracellular chloride with extracellular potassium. It also explains both the baseline chloride concentration and chloride extrusion rate. In the next section we describe this novel chloride-potassium pathway and apply it to explain the epileptic oscillations recorded in human subiculum slices.

I.7 References

Barreto E, Cressman JR (2011) Ion concentration dynamics as a mechanism for neuronal bursting. J Biol Phys 37:361–373.

Bazhenov M, Timofeev I, Steriade M, Sejnowski TJ (2004) Potassium model for slow (2-3 Hz) in vivo neocortical paroxysmal oscillations. J Neurophysiol 92:1116–1132.

Doyon N, Prescott S a, Castonguay A, Godin AG, Kröger H, De Koninck Y (2011) Efficacy of synaptic inhibition depends on multiple, dynamically interacting mechanisms implicated in chloride homeostasis. PLoS Comput Biol 7:e1002149.

Fisher, R. S., Pedley, T. A., & Prince, D. A. (1976). Kinetics of potassium movement in normal cortex. *Brain research*, *101*(2), 223-237.

Fröhlich F, Bazhenov M (2006) Coexistence of tonic firing and bursting in cortical neurons. Phys Rev E - Stat Nonlinear, Soft Matter Phys 74:1–7.

Fröhlich F, Bazhenov M, Iragui-Madoz V, Sejnowski TJ (2008) Potassium dynamics in the epileptic cortex: new insights on an old topic. Neuroscientist 14:422–433.

Fröhlich F, Sejnowski TJ, Bazhenov M (2010) Network bistability mediates spontaneous transitions between normal and pathological brain states. J Neurosci 30:10734–10743.

Fujiwara-Tsukamoto Y, Isomura Y, Imanishi M, Fukai T, Takada M (2007) Distinct types of ionic modulation of GABA actions in pyramidal cells and interneurons during electrical induction of hippocampal seizure-like network activity. Eur J Neurosci.

Grafstein B (1956) Mechanism of Spreading Spreading Depression. J Neurophysiol 19:154–171.

Gulyás, A. I., Megías, M., Emri, Z., & Freund, T. F. (1999). Total number and ratio of excitatory and inhibitory synapses converging onto single interneurons of different types in the CA1 area of the rat hippocampus. The Journal of neuroscience, 19(22), 10082-10097.

Hodgkin, A. L., & Huxley, A. F. (1952). A quantitative description of membrane current and its application to conduction and excitation in nerve. The Journal of physiology, 117(4), 500-544.

Huberfeld G, Wittner L, Clemenceau S, Baulac M, Kaila K, Miles R, Rivera C (2007) Perturbed chloride homeostasis and GABAergic signaling in human temporal lobe epilepsy. J Neurosci 27:9866–9873.

Isomura Y, Sugimoto M, Fujiwara-Tsukamoto Y, Yamamoto-Muraki S, Yamada J, Fukuda a (2003) Synaptically activated Cl- accumulation responsible for depolarizing GABAergic responses in mature hippocampal neurons. J Neurophysiol 90:2752–2756.

Izhikevich, E. M. (2007). Dynamical systems in neuroscience. MIT press.

Jedlička P, Backus KH (2006) Inhibitory transmission, activity-dependent ionic changes and neuronal network oscillations. Physiol Res 55:139–149.

Jedlicka P, Deller T, Gutkin BS, Backus KH (2011) Activity-dependent intracellular chloride accumulation and diffusion controls GABA(A) receptor-mediated synaptic transmission. Hippocampus 21:885–898.

Jeong HY, Gutkin B (2007) Synchrony of Neuronal Oscillations Controlled by GABAergic Reversal Potentials. 729:706–729.

Kager H, Wadman WJ, Somjen GG (2000) Simulated seizures and spreading depression in a neuron model incorporating interstitial space and ion concentrations. J Neurophysiol 84:495–512.

Kaila K, Voipio J (1987) Postsynaptic fall in intracellular pH induced by GABA-activated bicarbonate conductance. Nature 330:163–165.

Kaila, K., & Voipio, J. (1987). Postsynaptic fall in intracellular pH induced by GABA-activated bicarbonate conductance.

Kandel, E. R., Schwartz, J. H., & Jessell, T. M. (Eds.). (2000). Principles of neural science (Vol. 4, pp. 1227-1246). New York: McGraw-Hill.

Karus C, Mondragão M a., Ziemens D, Rose CR (2015) Astrocytes restrict discharge duration and neuronal sodium loads during recurrent network activity.

Khalilov I, Dzhala V, Ben-ari Y, Khazipov R (1999) Dual Role of GABA in the Neonatal Rat. 09:310–319.

Khalilov, I., Dzhala, V., Ben-Ari, Y., & Khazipov, R. (1999). Dual role of GABA in the neonatal rat hippocampus. Developmental neuroscience, 21(3-5), 310-319.

Koch, C., & Segev, I. (1998). Methods in neuronal modeling: from ions to networks. MIT press.

Krishnan GP, Bazhenov M (2011) Ionic dynamics mediate spontaneous termination of seizures and postictal depression state. J Neurosci 31:8870–8882.

Leinekugel X, Khalilov I, Ben-ari Y, Khazipov R (1998) Giant Depolarizing Potentials : the Septal Pole of the Hippocampus Paces the Activity of the Developing Intact Septohippocampal Complex In Vitro. 18:6349–6357.

Lytton, W. W. (2008). Computer modelling of epilepsy. *Nature Reviews Neuroscience*, *9*(8), 626-637.

Mainen, Z. F., & Sejnowski, T. J. (1996). Influence of dendritic structure on firing pattern in model neocortical neurons. Nature, 382(6589), 363-366.

Marchetti C, Tabak J, Chub N, O'Donovan MJ, Rinzel J (2005) Modeling spontaneous activity in the developing spinal cord using activity-dependent variations of intracellular chloride. J Neurosci 25:3601–3612.

Marchetti, C., Tabak, J., Chub, N., O'Donovan, M. J., & Rinzel, J. (2005). Modeling spontaneous activity in the developing spinal cord using activity-dependent variations of intracellular chloride. The Journal of neuroscience,25(14), 3601-3612.

Pallud J, Le Van Quyen M, Bielle F, Pellegrino C, Varlet P, Labussiere M, Cresto N, Dieme M-J, Baulac M, Duyckaerts C, Kourdougli N, Chazal G, Devaux B, Rivera C, Miles R, Capelle L, Huberfeld G (2014) Cortical GABAergic excitation contributes to epileptic activities around human glioma. Sci Transl Med 6:244ra89.

Payne J a (1997) Functional characterization of the neuronal-specific K-Cl cotransporter: implications for [K+]o regulation. Am J Physiol 273:C1516–C1525.

Payne J a, Rivera C, Voipio J, Kaila K (2003) Cation-chloride cotransporters in neuronal communication, development and trauma. Trends Neurosci 26:199–206.

Raimondo J V., Markram H, Akerman CJ (2012) Short-term ionic plasticity at GABAergic synapses. Front Synaptic Neurosci 4:1–9.

Rinzel J, Terman D, Wang X, Ermentrout B (1998) Propagating Activity Patterns in Large-Scale Inhibitory Neuronal Networks. 279.

Rinzel, J., Terman, D., Wang, X. J., & Ermentrout, B. (1998). Propagating activity patterns in large-scale inhibitory neuronal networks. Science, 279(5355), 1351-1355.

Sypert GW, Ward a a (1974) Changes in extracellular potassium activity during neocortical propagated seizures. Exp Neurol 45:19–41.

Taira T, Lamsa K, Kaila K (1997) Posttetanic excitation mediated by GABA(A) receptors in rat CA1 pyramidal neurons. J Neurophysiol 77:2213–2218.

Traub RD, Jefferys JG, Miles R, Whittington M a, Tóth K (1994) A branching dendritic model of a rodent CA3 pyramidal neurone. J Physiol 481.

Ullah G, Cressman JR, Barreto E, Schiff SJ (2009) The influence of sodium and potassium dynamics on excitability, seizures, and the stability of persistent states. II. Network and glial dynamics. J Comput Neurosci 26:171–183.

Wei Y, Ullah G, Schiff SJ (2014) Unification of Neuronal Spikes, Seizures, and Spreading Depression. J Neurosci 01:1–27.

Ziburkus J, Cressman JR, Barreto E, Schiff SJ (2006) Interneuron and pyramidal cell interplay during in vitro seizure-like events. J Neurophysiol 95:3948–3954.

CHAPTER II
THE ROLE OF K/CI HOMEOSTASIS IN HUMAN SUBICULUM EPILEPSY

II.2 Introduction

This chapter consists of a manuscript submitted to the Journal of Neuroscience. In the **II.3 Detailed model description** section we provide the additional description of models being used in this study. In the **II.4 Future directions** section we review the current problems in the present study and discuss ways to solve them. The manuscript is written mostly by myself, yet my supervisors, Boris Gutkin and Anton Chizhov as well as collaborators Richard Miles and Gilles Huberfeld added substantial corrections.

The aim of this work is to investigate the role of interneuron inhibition on the pyramidal neurons and chloride homeostasis changes for generation of epileptic discharges in temporal lobe epilepsy. We followed the conventional «bottom-up» approach where we described the system using known biophysical mechanisms related to seizure dynamics. Our model was restricted to specifically investigate the role of intracellular chloride in pyramidal cells and extracellular potassium since it has been found that these pathways are associated with the absence of KCC2 cotransporter found in human epileptogenic tissue (Huberfeld et al. 2007). In particular we are concentrated on the link between extracellular potassium and intracellular chloride, since it has been left open in the recent seizure models (Krishnan and Bazhenov 2011).

We are aware that our model does not fully capture all biophysical mechanisms related to seizure dynamics such as changes in pH, extracellular volume, oxygen concentration and metabolic activity. These factors undoubtedly contribute to seizure dynamics, yet addition of all pathways at once does not allow determining the specific role and significance of each mechanism. Therefore various pathways should be studied separately in different models to determine their relevance.

We found that absence of KCC2 leads to higher excitability of pyramidal cells due to increased resting membrane potential and depolarizing GABA reversal potential. These excitability changes lead to higher susceptibility of pathological pyramidal cells to generate bursting activity. To study the consequences of GABA reversal potential changes we turned to the network model representing the local subiculum circuit. Addition of the critical amount of pathological pyramidal cells provoked the development of epileptic oscillations similar to the recordings from epileptogenic human subiculum. We found that epileptic oscillations are robust to synaptic parameter changes and coexist with the normal activity in the network. Thereby we characterized the pathological

pathway associated with the intracellular chloride that leads to epileptic oscillations in human subiculum.

II.2 Article 1
Reduced efficacy of the KCC2 cotransporter promotes epileptic oscillations in a subiculum network model

Anatoly Buchin[1, 2], Anton Chizhov[3, 4], Gilles Huberfeld[5, 6], Richard Miles[7] and Boris Gutkin[1, 8]

[1] *École normale supérieure, Laboratoire des Neurosciences Cognitives, Group for Neural Theory (France, Paris)*
[2] *Peter the Great St. Petersburg Polytechnic University (Russia, St. Petersburg)*
[3] *Ioffe Institute, Computational Physics Laboratory (Russia, St. Petersburg)*
[4] *Sechenov Institute of Evolutionary Physiology and Biochemistry of the Russian Academy of Sciences (Russia, Saint-Petersburg)*
[5] *Université Pierre et Marie Curie, Pitie-Salpetriere Hospital, Neurophysiology Department (France, Paris)*
[6] *Epilepsie de l'Enfant et Plasticité Cérébrale, INSERM U1129 (France, Paris)*
[7] *Institut du Cerveau et de la Moelle Epinière, Cortex et Epilepsie Group (France, Paris)*
[8] *NRU Higher School of Economics, Center for Cognition and Decision Making (Russia, Moscow)*

II.2.1 Abstract

The potassium-chloride cotransporter KCC2 is absent or non-functional in a minority of the subicular pyramidal cells in the hippocampal tissue from patients with pharmacoresistant temporal lobe epilepsies. KCC2 assists in regulating the basal intra-neuronal chloride and extracellular potassium levels. The dynamic changes in the internal chloride concentrations resulting from the repeated activation of GABAergic synapses may switch GABA neurotransmission from inhibition to excitation in the pyramidal cells. Such changes could initiate periodic bursting in pyramidal cells and contribute to the onset of an ictal epileptic event. We developed a biophysical model of a subicular pyramidal cell that incorporates the effects of the cotransporter KCC2 on chloride and potassium homeostasis. Using a neural network model, we found that decreasing KCC2 activity in a critical number of pyramidal cells led to seizure-like field oscillations that are linked to increased external potassium and intracellular chloride concentrations. This behavior, which is similar to that recorded from the human subiculum, suggests that reduced KCC2 cotransporter activity alone may generate ictal discharges.

II.2.2 Introduction

Epilepsy is a common, chronic neurological disorder characterized by recurring seizures (Ullah and Schiff 2009, Beghi et al. 2005). In many epileptic syndromes, treatment with anti-epileptic drugs becomes ineffective over time (Beghi et al. 2005). In particular, it has been suggested that defects in chloride homeostasis may contribute to the epileptic activities generated in tissue derived from patients with temporal lobe epilepsies associated with hippocampal sclerosis (Huberfeld et al. 2007) and in the tissue surrounding cortical tumors (Pallud et al. 2014). Changes in the expression of potassium-chloride transport proteins may be involved. It was found that the absence of KCC2 shifts the reversal potential of the GABAergic synaptic events from hyperpolarizing to depolarizing in human subicular pyramidal cells (Huberfeld et al. 2007). Of the proteins controlling chloride homeostasis, the KCC2 cotransporter maintains basal chloride levels using the ionic gradients created by the sodium-potassium pump to extrude intracellular chloride and potassium ions to the extracellular space (Payne et al. 2003). In addition to these basal effects, experimental (Kaila and Voipio 1987) and theoretical studies (Jedlicka et al. 2011), (Doyon et al. 2011) showed that intense GABAergic stimulation leads to progressive chloride accumulation and therefore shifts the reversal potential in a similar manner. Thus, intensive activation of GABA synapses combined with impaired KCC2 cotransporter expression or function may produce seizures.

Extracellular potassium levels, which affect neuronal excitability, could also contribute to seizure generation (Fröhlich et al. 2008). It has been known for many years that potassium ions accumulate in the extracellular space during seizures (Fertziger 1970) and spreading depression (Grafstein 1956, Kraio and Nicholson 1978). It has been suggested that intense neuronal firing could increase the extracellular potassium concentrations and create a positive feedback that may promote seizure generation. Recent computational models that incorporate this feedback with realistic extracellular potassium levels and with its control predicted periodic seizure-like firing patterns generated by single neurons (Barreto et al, 2009, Hübel and Dahlem 2014, Wei et al. 2014) and by recurrent neural networks (Bazhenov et al. 2004, Ullah et al. 2009, Krishnan and Bazhenov 2011).

Homeostasis and the dynamic changes in the chloride and potassium ion concentrations during the transition to seizure are not completely understood. The model described by Krishnan and Bazhenov (Krishnan and Bazhenov, 2011) suggested that the KCC2 extrusion rate could affect the seizure duration. A phenomenological model was used to describe the KCC2 activity in pyramidal cells; however, this model did not describe the baseline chloride concentration as a function of the KCC2 expression level. We propose that KCC2 treatments may be improved by using a detailed model that describes how KCC2 controls the basal intracellular chloride levels as a function of the external potassium levels (Payne 1997, Doyon et al. 2011) and how the cotransporter responds to the

dynamic changes in the chloride levels resulting from GABAergic synaptic stimulation (Fujiwara-Tsukamoto et al. 2007, Fujiwara-Tsukamoto et al. 2010, Isomura et al. 2003). This model may allow us to resolve the question of whether the presence of KCC2 has a pro-epileptic effect due to an increase in the extracellular potassium levels (Viitanen et al. 2010, Hamidi and Avoli 2015) and/or whether its absence is epileptogenic due to intracellular chloride accumulation and a depolarizing GABA reversal potential (Cohen et al. 2002, Huberfeld et al. 2007).

Therefore, we constructed an accurate two-compartment model of single pyramidal cells and interneurons of the subiculum, with special attention given to the effects of KCC2 on potassium and chloride homeostasis. Such neurons were incorporated into a neuronal network with realistic values for synaptic connectivity and an explicit treatment of ion exchange between the intra-neuronal and extracellular space. Neuronal voltages were used to derive the values for the local field potential (LFP) generated by the network during normal and epileptic activity. We found that the incorporation of KCC2-deficient cells into this network reproduced the ictal-like extracellular field potentials recorded in epileptogenic slices from the human subiculum. Thus, our results help to resolve the KCC2 controversy and provide a testable hypothesis for further experimental studies of intracellular chloride regulation in pyramidal cells.

II.2.3 Materials and Methods

Epileptic tissue: Temporal lobe tissue blocks containing the hippocampus, subiculum and part of the entorhinal cortex were obtained from 45 people with pharmacoresistant mesial temporal lobe epilepsies associated with hippocampal sclerosis (age 18–52 years, seizures for 3–35 years) undergoing resection of the amygdala, the hippocampus, and the anterior parahippocampal gyrus, as well as occasionally the temporal lobe and the anterior basal and lateral neocortex. All of the individuals gave their written informed consent and the study was approved by the Comité Consultatif.

Tissue preparation: The post-surgical tissue was transported in a cold, oxygenated solution containing 248 mM d-sucrose, 26 mM NaHCO3, 1 mM KCl, 1 mM CaCl2, 10 mM MgCl2 and 10 mM d-glucose, equilibrated with 5% CO2 in 95% O_2. The hippocampal-subicular-entorhinal cortical slices or isolated subicular slices (400 µm thick) were cut with a vibratome (HM650 V, Microm). They were maintained at 37 °C, and equilibrated with 5% CO2 in 95% O_2 in an interface chamber perfused with a solution containing 124 mM NaCl, 26 mM NaHCO3, 4 mM KCl, 2 mM MgCl2, 2 mM CaCl2 and 10 mM d-glucose. NBQX and d,l-AP5 were used to block glutamatergic signaling, and bicuculline or picrotoxin was used to block the GABA-A receptors. Ictal-like activity was induced by increasing the external K^+ concentration to 8 mM and reducing the Mg^{2+} concentration to 0.25 mM.

Recordings: Up to four tungsten electrodes etched to a tip diameter of ~5 µm were used for the extracellular recordings. The signals were amplified 1,000-fold and filtered to pass frequencies of 0.1 Hz to 10 kHz (AM systems, 1700). The intracellular recordings were made with glass microelectrodes containing 2 M potassium acetate and beveled to a resistance of 50–100 MΩ. The signals were amplified with an Axoclamp 2B amplifier in current-clamp mode. The intracellular and extracellular signals were digitized at 10 kHz with a 12–bit, 16-channel A-D converter (Digidata 1200A, Axon Instruments), and monitored and saved to a PC with Axoscope (Axon Instruments).

Data analysis: The recordings were analyzed with Clampfit 10 software from Spikoscope and programs written in Matlab 2015a.

Simulations: Single neuron and neural network simulations were performed in Matlab 2015a using the direct Euler method of integration, with a time step of 0.05 ms. We ensured that smaller time steps provided substantially similar results. The bifurcation analysis was performed in XPPAUT 7.0 and the AUTO package. In all simulations, we systematically varied the initial conditions to ensure the stability of the numerical results.

Neuron intrinsic properties: Single neuron activity was modeled using the conductances derived from previous studies (Mainen and Sejnowski 1996,

Krishnan and Bazhenov 2011). The intrinsic currents were selected to represent the major currents that contribute to the intrinsic dynamics of the pyramidal cells of subiculum (Jung et al. 2001, Staff et al. 2000). Similar to previous studies, we used the model of a regular spiking neuron for the pyramidal cells and a fast spiking neuron for the interneurons (Mainen and Sejnowski 1996, Bazhenov et al. 2004).

The following equations describe the evolution of voltage over time for these two compartments:

$$C_m dV_d / dt = -I_d^{Int} - g_c^d (V_d - V_s) - I_d^{leak} - I_d^{pump}$$
$$g_c^S (V_d - V_s) = -I_s^{Int} - I_s^{leak} - I_s^{pump}$$

where V_d is the voltage of the dendritic compartment, I_d^{leak} includes the sodium, potassium, and chloride leak currents (PY: $g_K = 0.044$, $g_{Na} = 0.02$, $g_{Cl} = 0.01$ mS/cm^2 ; IN: $g_K = 0.035$, $g_{Na} = 0.02$, $g_{Cl} = 0.01$ mS/cm^2), I_s^{leak} includes the sodium and potassium leak currents (PY: $g_{Na} = 0.019$, $g_K = 0.042$ mS/cm^2 ; IN: $g_{Na} = 0.019$, $g_K = 0.042$ mS/cm^2), and I_d^{Int} and I_s^{Int} are the sums of the intrinsic currents for the axosomatic and dendritic compartments, respectively. I_d^{pump} and I_s^{pump} are the sums of the Na^+ and K^+ ion currents ($I_{Na}^{pump}, I_K^{pump}$) via the Na^+-K^+ exchange pump for each compartment. The axosomatic and dendritic compartments were coupled by an axial current (PY: $g_C = 1.65$ μS ; IN: $g_C = 0.5$ μS). The axosomatic currents were assumed to be strong enough to instantaneously change the somatic membrane voltage such that the axosomatic compartment has no capacitance current. The current through the sodium-potassium pump was determined by the intracellular sodium (Na_{IN}^+) and extracellular sodium (Na_{OUT}^+) concentrations and is given by the following equations (Kager et al. 2000):

$$A = 1/(1 + K_{o\alpha} / K_{OUT}^+)^2 / (1 + Na_{i\alpha} / Na_{IN}^+)^3$$
$$I_{Na}^{pump} = 3 I_{\max} A \quad I_K^{pump} = -2 I_{\max} A$$

where $K_{o\alpha} = 3.5$ mM , $Na_{i\alpha} = 20$ mM , $Na_{IN}^+ = 20$, and $I_{\max} = 25$ mA/cm^2 .

The set of intrinsic currents of the dendritic compartment consisted of the $I_d^{Int} = I_{HVA} + I_{KCa} + I_{Km} + I_{Nap} + I_{Na}^d + I_{Ca} + I_d^{pump} + I_d^c + I_d^{leak}$ currents for the pyramidal cells and the $I_d^{Int} = I_d^{pump} + I_d^c + I_d^{leak}$ currents for the interneurons. The intrinsic currents for the somatic compartment are described as $I_d^{Int} = I_d^{pump} + I_d^c + I_d^{leak}$ for the pyramidal cells and interneurons, where I_s^{Int} consists of the voltage-gated sodium (PY and IN: $G_{Na} = 3450$ mS/cm^2) and delayed-rectifier potassium ($G_{Kv} = 200$ mS/cm^2) currents. The dendritic compartment had a high-threshold calcium current (I_{HVA}), a calcium-activated potassium current (I_{KCa}), a calcium current (I_{Ca}), a slowly

activating potassium current (I_{Km}), voltage-gated and persistent-sodium currents (I_{Na} and I_{Nap}, respectively) (Jung et al. 2001), and leak conductances (PY: $G_K = 0.044$, $g_{Na} = 0.02$, $g_{Cl} = 0.01$ mS/cm^2; IN: $G_K = 0.035$, $G_{Na} = 0.02$, $G_{Cl} = 0.035$ mS/cm^2). The full expressions for these current approximations were previously described (Mainen and Sejnowski, 1996, Krishnan and Bazhenov 2011).

Ion concentration dynamics: The model included the Ca^{2+}_{IN}, K^+_{OUT} and Cl^-_{IN} variable ion concentrations, leak currents, intrinsic currents, pump-mediated currents, extracellular diffusions, and glial activities, which determined the concentration of each ion. The reversal potentials for potassium and chloride were determined from the internal and external ion concentrations using the Nernst equation. The concentrations were calculated based on the active currents, sodium-potassium exchange pump, KCC2 cotransporter (Doyon et al. 2011), ion flow between the pyramidal cells and through the extracellular compartment (Wei et al., 2014). The evolution of K^+_{OUT} was modeled similar to (Krishnan and Bazhenov 2011), while the extracellular diffusion is modeled using a two-dimensional network. The intracellular potassium was set at K^+_{IN}=150 mM.

$$dK^+_{OUT}/dt = (k_K/Fd)(\Sigma I_K^{\text{int}} + I_K^{pump} - I_{KCC2}) + G$$
$$+\sum_{i=1}^{4} D_{ij}/\Delta x^2 (K^+_{OUT} - K^{+(i)}_{OUT}) + d_{bath}/\Delta l (K^+_{OUT} - K_{bath})$$
$$G = k_{ON}/k_{1N}(B_{\max} - B) - k_{OFF} K^+_{OUT} B$$
$$dB/dt = k_{ON}(B_{\max} - B) - k_{OFF} K^+_{OUT} B,$$

where the conversion factor *k*=10 10^3 cm^3, F=96489 C/mol, and the ratio between the cell volume and extracellular compartment d=0.15. D_{ij} is the element of diffusion matrix **D,** and $D_{ij} = 4\times10^{-6}$ cm^2/s for neighboring neurons (cat neocortex data (Fisher et al. 1976)) and $D_{ij} = 0$ otherwise. Each pyramidal cell has 4 neighboring cells, $\Delta x = 50$ μm was the mean distance between subicular pyramidal cell somata (Huberfeld et al. 2007), $d_{bath} = 4\times10^{-7}$ Hz is the coefficient for diffusion from the bath (Barreto and Cressman 2011, Florence et al. 2009) and $\Delta l = 200$ μm is the depth of the neurons in the slice. The external K^+_{OUT} concentration was assumed to be uniform in the network and to equilibrate very rapidly (Bazhenov et al., 2004). Glial K^+_{OUT} uptake was modeled by free buffer (with total capacity $B_{\max} = 500$ mM) with a concentration B, which bound and unbound from K^+_{OUT} with first-order kinetics, and the rates k_{ON} and k_{OFF} were given by $k_{ON} = 0.008$ and $k_{OFF} = k_{ON}/(1+\exp(-(K^+_{OUT} - K^+_{oth})/1.15))$, (Kager et al. 2007, Volman et al. 2007). K^+_{OUT} produced by the interneurons was assumed to

be negligible compared to the K^+_{OUT} produced by the pyramidal cells. In contrast, the K^+_{OUT} concentrations extruded by the pyramidal cells affected other neurons. For some simulations, extracellular diffusion from the bath solution to the network was set to zero to mimic the *in vivo*-like conditions.

The extracellular chloride concentration is assumed to be constant: $Cl^-_{OUT} = 130mM$. The intracellular chloride Cl^-_{IN} concentration was calculated from the following equations:

$$dCl_{IN} / dt = (k_{Cl} / F)(I_D^{Cl} + I_{GABA} + I_{KCC2})$$
$$I_{KCC2} = I_{KCC2}(V_K - V_{Cl}) / ((V_K - V_{Cl}) + V_{1/2}),$$

where I_D^{Cl} is the chloride leak current on the dendrite, $I_{KCC2} = 2\mu A / cm^2$ is the maximal current through the KCC2 cotransporter, V_K and V_{Cl} are the reversal potentials of potassium and chloride, and $V_{1/2} = 40\ mV$ is the voltage difference when the chloride current reaches its maximal value (Doyon et al. 2011). $I_{GABA} = \sum_i g^i_{GABA} s^i_{GABA}(V - V_{GABA})$ is the sum of the GABAergic currents received by the neuron. The KCC2 equation describes the current from the potassium and chloride ions via the cotransporter. This current could flow in both directions, depending on the sign of $(V_K - V_{Cl})$.

The intracellular calcium dynamics was modeled using the following equation:

$$dCa^{2+}_{IN} / dt = -(5.18 \times 10^{-5}) / D_{Ca} I_{HVA} + (2.4 \times 10^{-4} - Ca^{2+}_{IN}) / \tau_{Ca},$$

where $\tau_{Ca} = 800\ ms$ and $D_{Ca} = 0.85\ cm^2 mM / \mu A$.

The reversal potentials for each current were calculated according to the Nernst equations and continuously updated based on the internal and external ion concentrations:

$$V_K = \frac{RT}{F}\ln(\frac{K^+_{OUT}}{K^+_{IN}}),\ V_{Cl} = \frac{RT}{F}\ln(\frac{Cl^-_{IN}}{Cl^-_{OUT}}) \text{ and } V_{GABA} = \frac{RT}{F}\ln(\frac{Cl^-_{IN} + 4HCO^-_{3IN}}{Cl^-_{OUT} + 4HCO^-_{3OUT}}),$$

where $HCO^-_{3IN} = 16\ mM$ and $HCO^-_{3OUT} = 26\ mM$ (Doyon et al., 2011).

Network and synaptic model: We used 841 pyramidal cells and 225 interneurons to model the local subiculum network. The number of neurons was chosen to match the ratio of 80% excitatory and 20% inhibitory cells in the hippocampus. Increasing the overall size of the network had a minimal effect on

the network dynamics. The synaptic connectivity between these cells was random and based on estimates from the mouse subiculum (Peng et al. 2014): $P_{PY-PY} = 0.05$, $P_{IN-PY} = 0.65$, $P_{PY-IN} = 0.3$, $P_{IN-IN} = 0.4$. The peak conductances at the simulated synapses were randomly distributed with the following means PY-PY: 1.5 nS/cm^2 for AMPA and 0.02 nS/cm^2 for NMDA; PY-IN: 1 nS/cm^2 for AMPA; IN-PY: 0.7 nS/cm^2 for GABA; and IN-IN: 0.5 nS/cm^2 for GABA. The variances of the distributions of synaptic conductance were equal to 10% of the mean. The synaptic parameters were systematically varied to ensure the stability of the network activity. Both pyramidal cells and interneurons received a supplementary noisy excitatory synaptic input (AMPA) in order to provide spontaneous firing. Additional AMPA synaptic currents were modeled by an Ornstein-Uhlenbeck process (Renart et al. 2007): $\tau_{AMPA}\frac{dI_{AMPA}}{dt} = -I_{AMPA} + \sigma_{E/I}\eta(t)$, where $\tau_{AMPA} = 5.4\ ms$, $\sigma_E = 0.50\ \mu A/cm^2$ and $\sigma_I = 0.60\ \mu A/cm^2$. The time course of the currents at the AMPA, NMDA and GABA conductance-based synapses followed first-order kinetics, similar to those used in (Brunel et al., 2001).

LFP model: We computed a local field potential (LFP) corresponding to the activity generated by the neurons of the simulated network similar to (Chizhov and Rodrigues 2014). Pyramidal cells were assumed to provide the largest component for the LFP signal (Buzsáki et al. 2012). Each pyramidal cell generated a dipole $\varphi = -k[g_c^S(V_d^i - V_s^i)]$, similar to (Demont-Guignard et al. 2012, Wendling et al. 2012), where $k = 0.02$ is the proportionality coefficient for the pyramidal cell layer. A global LFP signal was computed as a superposition by assuming that all pyramidal cells contribute equally: $LFP = \sum_i \varphi_i$.

Seizure detection algorithm: The seizure-like events generated by the model were detected with an algorithm, which estimated the total power spectrum over a time window of 5 seconds. Events exceeding a manually set amplitude threshold were classified as seizures.

II.2.4 Results

II.2.4.1 Absence of KCC2 leads to a depolarizing GABA reversal potential

Fig.II-1A shows a pyramidal cell, including the intrinsic and synaptic conductances on the somatic and dendritic compartments. The active currents responsible for spike generation include the calcium currents that contribute to burst firing in the subicular pyramidal cells (Jung et al. 2001, Stanford et al. 2012). In this cell model, the random synaptic currents mediated by AMPA and NMDA receptors initiate firing. Each action potential induces an increase in the extracellular potassium concentrations in the model. Fig.II-1B shows the major ion pathways associated with extracellular potassium and intracellular chloride concentrations. Because K^{+}_{OUT} affects the reversal potential of all potassium currents (see the Materials and Methods), the increase of this parameter changes the excitability of the neuron model. At the same time, the sodium-potassium pump, glial buffer and diffusion to the neighboring cells restore the potassium concentration to the physiological level of ~4 mM. Despite the complex ion homeostasis mechanisms, the model reached a stable equilibrium at physiological ion concentrations.

In turn, GABA synapse activation results in an increase in the intracellular chloride concentrations in the dendrite compartment of the model, Fig.II-1B. The intracellular chloride concentration Cl^{-}_{IN} is then equilibrated by the KCC2 cotransporter, which extrudes chloride and potassium ions into the extracellular space. Thus, the increase in the intracellular chloride concentrations leads to higher V_{GABA} values, thus decreasing the efficacy of inhibition.

The baseline intracellular chloride level depends on the KCC2 activity in the model. In KCC2(+) cells, the baseline chloride concentration became fixed at 3.46 mM, which corresponds to the GABA reversal potential of $V_{GABA} = -78mV$. The resulting resting membrane potential became equilibrated at -70 mV. In the KCC2(-) cells, the intracellular chloride concentration increased to 11.3 mM, which corresponds to $V_{GABA} = -56mV$. In this case, the resting membrane potential became stable at -65 mV. Therefore, the absence of KCC2 leads to a depolarizing GABA reversal potential and an increased resting membrane potential due to the chloride leak currents (Krishnan and Bazhenov, 2011).

To study the role of intracellular chloride in the inhibitory input, the pyramidal cell model was stimulated by a GABA conductance similar to the experiment from (Cohen et al. 2002), Fig.II-1C. In this experiment, the membrane potential of a neuron was fixed in voltage clamp mode, while the

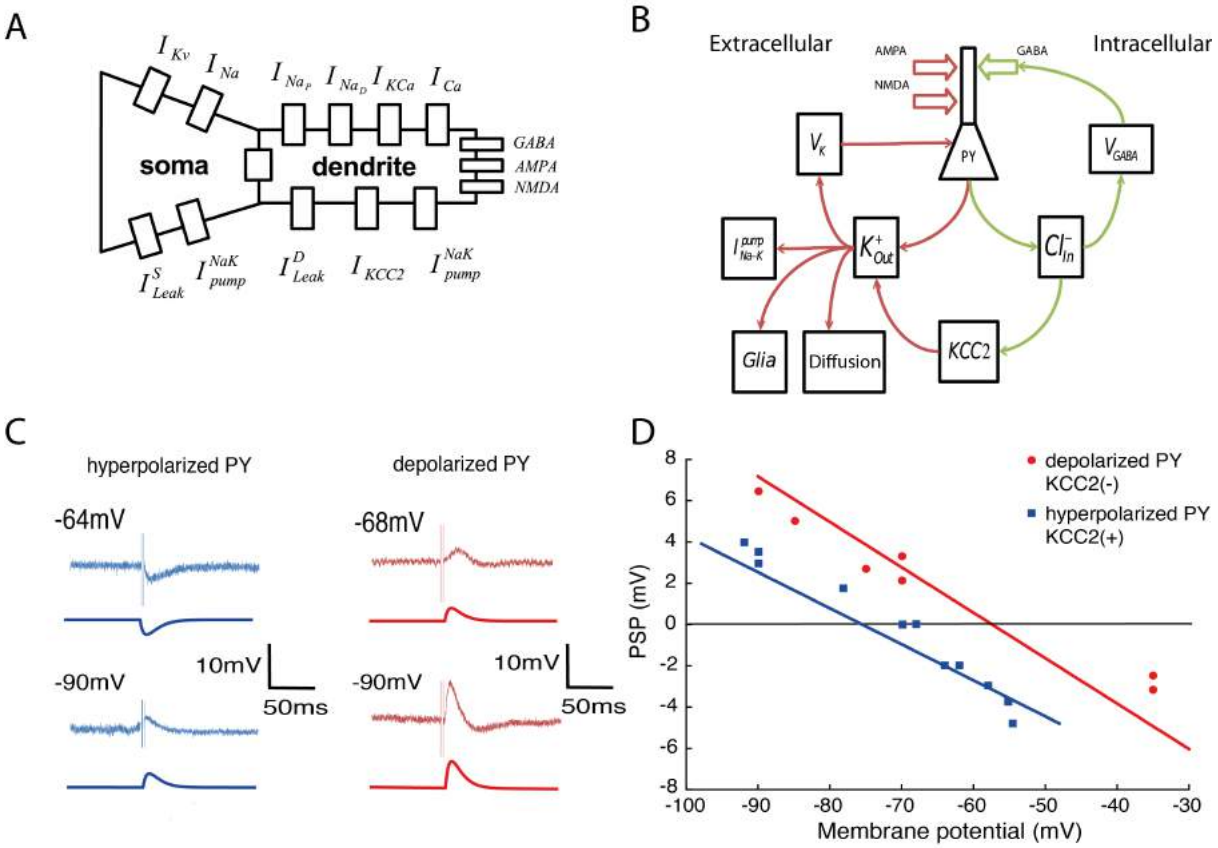

Figure II-1. Absence of KCC2 leads to a depolarizing GABA reversal potential
A - Scheme of the PY model with intrinsic currents; B - ion pathways in the single cell model; and C - experimental and model voltage traces during GABAergic stimulation. D - amplitude of the post-synaptic potential (PSP) during stimulation in the experiment (red and blue dots) and model (red and blue lines). The experimental traces in panels C and D are taken from (Cohen et al. 2002).

excitatory synaptic transmission was blocked by NBQX and APV. Then, extracellular stimulation was applied to stimulate the GABAergic neurons. In our model, the GABAergic synaptic current caused by extracellular synaptic stimulation was calculated using the second order synaptic kinetics from (Chizhov 2002).

To illustrate the dependence of the GABA currents on the presence of KCC2, we plotted the amplitude of the postsynaptic potential (PSP) as a function of a fixed membrane potential, Fig.II-1D. The characteristic experimental and model voltage traces are presented in Fig.II-1C. During GABAergic stimulation, the KCC2(+) pyramidal cell is hyperpolarized, while the KCC2(-) cells is depolarized. The blue and red lines are the predictions of the model based on the PSP amplitude measured in different cells. Thus, the absence of the KCC2 cotransporter in the model could explain the approximately 22 mV difference in the GABA reversal potential of the hyperpolarized and depolarized pyramidal cells.

II.2.4.2 Single cell consequences of KCC2(-) pathology

We studied the response of a model neuron to periodic synaptic stimulation to investigate the effects of KCC2(-) pathology at the single neuron level. Our aim was to mimic the reported responses from animal (Fujiwara-Tsukamoto et al., 2007), (Fujiwara-Tsukamoto et al. 2010) or epileptic human hippocampal slices (Huberfeld et al. 2011a) maintained in conditions where seizure-like events were evoked by extracellular stimulation.

Fig.II-2A, B present the voltage traces of the KCC2(-) and KCC2(+) cells when both of the cells were both periodically stimulated by 5 seconds of simultaneous AMPA, GABA and NMDA conductances with a 5 Hz frequency. Synaptic stimulation of these cells provoked sustained bursting activity after the application of the stimulus. The bursting activity of the KCC2(+) cell, Fig.II-2A, is much shorter than that of the KCC2(-) cell, Fig.II-2B. Both voltage traces contain a slow depolarization component after stimulation that is caused by extracellular potassium accumulation. This slow depolarization constitutes the main excitatory effect of extracellular potassium after stimulation.

The model neuron generated spikes after synaptic stimulation due to the increased ion concentrations. To explain this behavior, we plotted concentrations computed from the bifurcation analysis on the state diagram. Fig.II-2C shows how the intracellular chloride Cl^-_{IN} and extracellular potassium K^+_{OUT} concentrations affect the single neurons' behaviors. The black line corresponds to the border dividing the spiking/bursting and resting solutions in the model and is calculated as saddle-node bifurcation of a two-parameter diagram. The neuron in this region is continuously spiking or bursting. Thus,

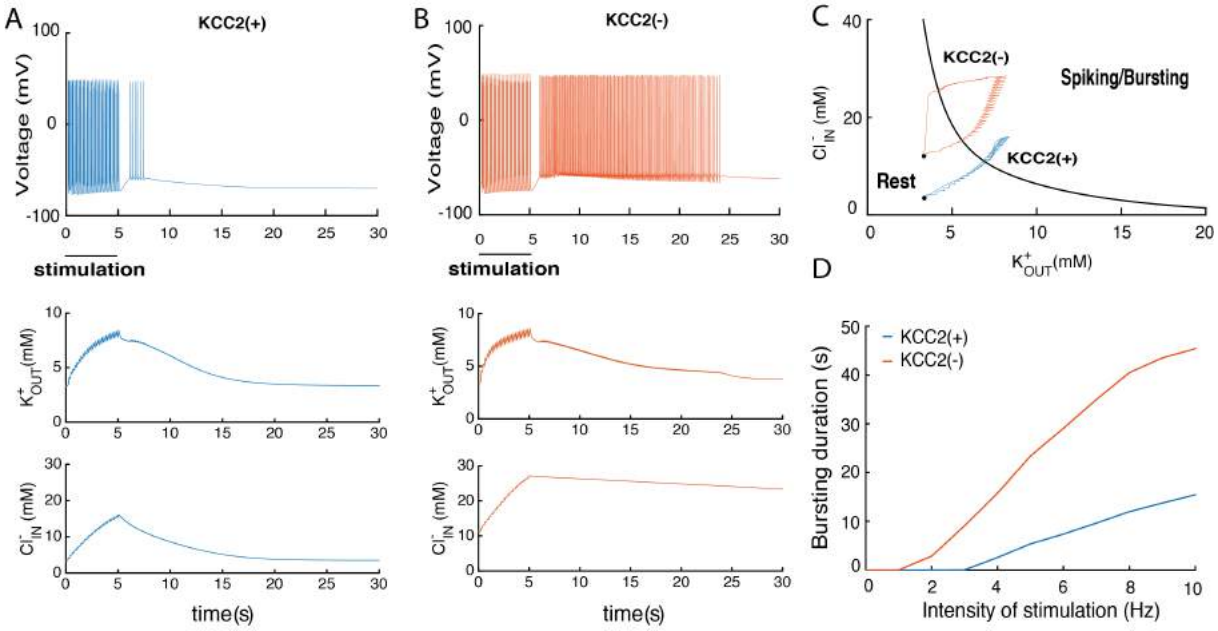

Figure II-2. Single cell consequences of the KCC2(-) pathology
A, B - voltage trajectories of the KCC2(-) and KCC2(+) PY models after stimulation with periodic AMPA, GABA and NMDA synaptic input for 5 seconds. The bottom panels show the changes in the concentrations of the corresponding ion. C - state diagram of the model, and the changes in the concentrations of the corresponding ion. The red and blue trajectories correspond to the KCC2(-) and KCC2(+) cells, respectively. D - Bursting duration caused by the increased ion concentrations after synaptic stimulation.

the high concentrations of K^+_{OUT} and Cl^-_{IN} moved the neurons to the spiking/bursting activity regime. The number of spikes during the burst varied according to the K^+_{OUT} concentration (Fröhlich and Bazhenov 2006b). Therefore, the last bursts contained only one spike, Fig.II-2A, B. The baseline chloride concentration Cl^-_{IN} affects the reversal potential of the chloride leak currents, providing additional depolarization for the KCC2(-) cells. Thus the absence of KCC2 cotransporter made a neuron more excitable by moving it closer to the spiking/bursting area on the state diagram, Fig.II-2C.

During synaptic stimulation, K^+_{OUT} and Cl^-_{IN} were increased due to spiking and GABAergic stimulation. When the ion concentrations became high enough, the cell moved to the spiking/bursting regime of activity, Fig.II-2C. In the KCC2(+) cell, the ion equilibrium is lower than the KCC2(-) cell due to the decreased intracellular chloride level. Therefore, the same synaptic stimulation moved the KCC2(-) cell further into the pathological spiking/bursting region compared to KCC2(+) cell. This provoked a longer period of bursting activity in these neurons due to the increased chloride ion concentrations. After self-sustained spiking and bursting, the activity in both cases returned to baseline Fig.II-2C black dots.

We evaluated the effect of the KCC2(-) pathology on the various intensities of the synaptic input. Stimulation of single KCC2(-) neuron moved the cell to the pathological regime for a lower stimulation frequency compared to the KCC2(+) neuron. We also found that the duration of the spiking and bursting in the KCC2(-) cell is much longer compared to that in the KCC2(+) cell. In this way, the presence of the KCC2(-) pathology increases the susceptibility of the pyramidal cell to generate bursting activity for various stimulation frequencies due to the increased intracellular chloride concentration Cl^-_{IN}.

II.2.4.3 Gamma oscillations in KCC2(+) subiculum circuit

To study the role of the KCC2 cotransporter in network oscillations, we constructed the subiculum circuit network consisting of interneurons (IN) and pyramidal cells (PY), see the Materials and Methods. The neurons were sparsely connected by conductance-based synapses to represent the local subiculum connectivity (Peng et al. 2014). All neurons in the network possessed the same dynamic K^+_{OUT} ion concentration, which affects both the PYs and INs, as well as the dynamic chloride concentration Cl^-_{IN} in the pyramidal cells.

In the presence of external excitation provided by 8 mM potassium and 0.5 mM magnesium in the bath solution (Huberfeld et al. 2011c), the

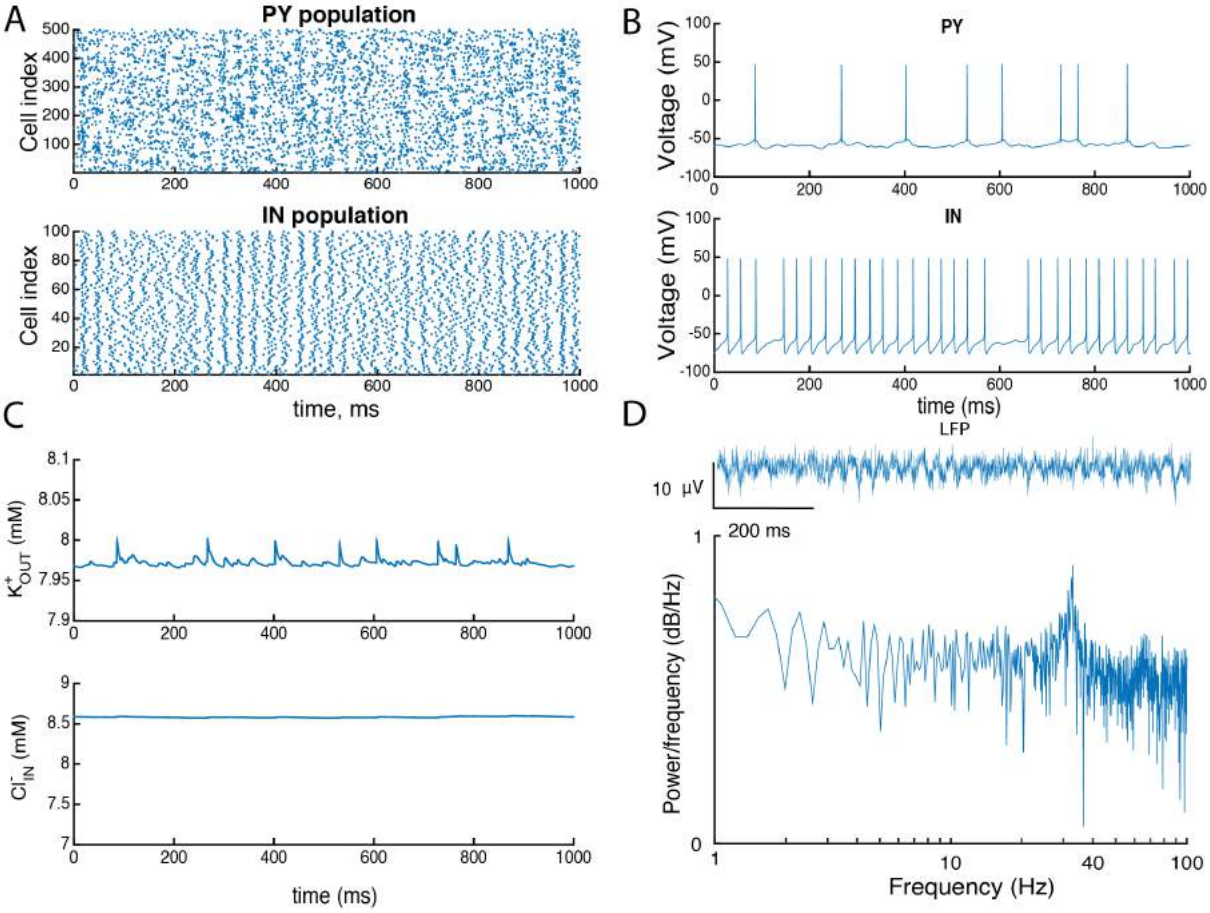

Figure II-3. Ion concentrations during gamma oscillations in the PY-IN network
A - raster plot of the pyramidal cell (PY) and interneuron (IN) population (only part of the network is shown); B - voltage traces from a representative PY and IN cells; C - K^+_{OUT} and Cl^-_{IN} concentrations during network activity; and D – the local field potential (LFP) computed from the network and power spectrum of the signal.

network model organized into the oscillatory regime, Fig.II-3A. It generated stable gamma oscillations with a main frequency of approximately 36 Hz. The frequency band of these oscillations is similar to that generated in hippocampal slices recorded in subiculum (Jackson et al. 2011, Stanford et al. 2014).

To illustrate the single neuron behavior during these oscillations, we plotted the characteristic recordings from the PY and IN populations, Fig.II-3B.
We found that the pyramidal cells in the network generated activity with a 9 Hz frequency, while the interneurons generated spikes with a frequency of approximately 36 Hz. This high firing rate of single cells results from the increased potassium concentration that provides substantial excitation for both populations. With smaller bath potassium concentrations, for example 4 mM, the network activity stops in both populations without additional external input.

Pyramidal cell and interneuron spiking during gamma oscillations led to an increase in the extracellular potassium and intracellular chloride concentrations. After 1-2 minutes of network activity equilibration, the concentrations of K^{+}_{OUT} and Cl^{-}_{IN} became stationary near the baseline of 7.96 mM for K^{+}_{OUT} and 8.6 mM for Cl^{-}_{IN} , Fig.II-3C. During spiking, there are local increases in the K^{+}_{OUT} concentration, yet the concentration quickly equilibrates after each spike is generated. The ion concentrations increased slightly during the course of the oscillatory cycle, but their concentrations did not increase much higher than the baseline levels. Thus, the oscillations provided by the PY-IN network led to quasistationary ion concentrations, such that the network activity stayed in the physiological regime.

Synchronous pyramidal cell firing during the gamma oscillations led to oscillations of the LFP computed for the PY population (see the Materials and Methods, Fig.II-3D). One could see that the single pyramidal cells did not generate spikes during each phase of the oscillation, but the entire population was engaged in the network oscillatory cycle Fig.II-3C. However, the inhibitory cells fired with one spike in almost every cycle of the network oscillation. This pyramidal neuron-interneuron interplay during oscillations is a classical example of the PING mechanism (Whittington et al. 2000). The frequency of these oscillations demonstrated a strong peak at 36 Hz, corresponding to the major frequency of PY population firing, Fig.II-3D.

II.2.4.4 KCC2(-) pathology in the subiculum circuit

We implemented a PY-IN network with different numbers of KCC2-deficeint cells to study the role of KCC2(-) pyramidal cells in seizure initiation. All neurons received an excitation from the external potassium present in the bath solution.potassiumwas increased to 8 mM to recreate the experimental conditions in slice experiments, see Materials and Methods. The concentration

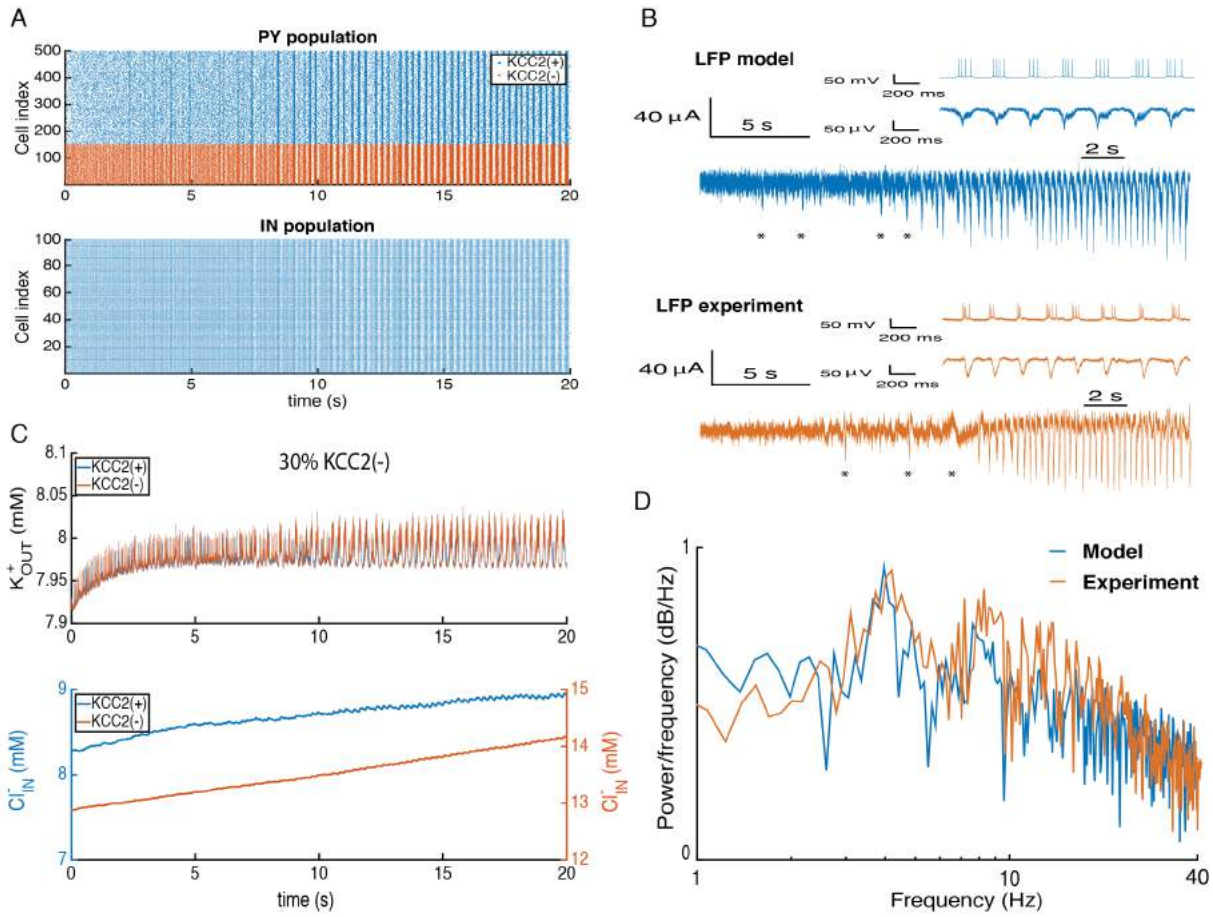

Figure II-4. KCC2(-) pathology in the subiculum circuit
A - raster plot of the pyramidal cell (PY) and interneuron (IN) populations during seizure initiation. B - extracellular potassium K^+_{OUT} and intracellular chloride Cl^-_{IN} accumulation during seizure initiation; C - LFP computed from the network and experimental LFP recordings; and D - power spectrum of the LFP model and the experimental recordings.

of extracellular potassium in the network was defined both by the network activity and bath solution. The KCC2(-) pyramidal cells were randomly located in the network space. We performed additional simulations to ensure that the KCC2(-) cell clusters did not provide substantially different results (data not shown). The initial conditions were set at the baseline ion concentrations for the KCC2(-) and KCC2(+) cells, which were calculated from the single neuron model, Fig.II-2C.

In the simulated network, we found that a 30% addition of KCC2(-) PY cells provoked synchronous population bursting similar to epileptic activity, Fig.II-4A. The increased intracellular chloride levels in the KCC2(-) cells led to the substantial activation of the interneuron population and the corresponding GABAergic synapses on the pyramidal cells. This occurred because the KCC2(-) cells possess the depolarizing GABA reversal potential. Therefore, these cells did not receive inhibition, leading to the generation of stronger spikes compared to the KCC2(+) cells.

As a consequence, the population of IN received substantial excitation from these cells, which activated the GABAergic synapses on the pyramidal cells. This activation provoked an increase in the intracellular chloride concentration Cl^-_{IN} in the pyramidal cells and a simultaneous increase in the K^+_{OUT} concentration due to increased pyramidal cell firing, Fig.II-4C. We found that the increase in the extracellular potassium concentration during the transition was relatively minor due to rapid diffusion to the bath solution containing 8 mM K^+_{OUT}. However, there was a significant accumulation of intracellular chloride in both the KCC2(-) and KCC2(+) pyramidal cells, leading to the substantial depolarization of the GABA reversal potential. This positive feedback loop between the K^+_{OUT} and Cl^-_{IN} concentrations and neuronal firing led to a further increase in excitation and synchrony. We should mention that although there were relatively small changes in the intracellular chloride concentrations in PY cells, Fig.II-4C, even a 1 mM increase led to an approximately 2-3 mV change in the GABA reversal potential. These changes substantially decreased the inhibition in the network, resulting in an excitation-inhibition imbalance. As a result these changes provoked the development of pathological oscillations characterized by synchronous bursting in both the PY and IN populations.

Then, we compared the LFP signal generated by the network with the field potential recordings from human subicular tissue during ictal discharge initiation, Fig.II-4B. The model LFP is able to capture the general dynamics of seizure initiation. Similar to the experimental trace at the beginning of the recording, there is strong noisy component of neural activity that gradually transforms into periodic population bursting, Fig.II-4A. In the model LFP, these are fast oscillations before seizure onset and result from strong pyramidal cell firing. After generating these fast oscillations, the network transformed into a 4 Hz oscillatory bursting regime, Fig.II-4A. This frequency characterizes the pyramidal cell bursting coupled with the LFP deviations in both the model and experiment, see

the insets in Fig.II-4B. Before the generation of periodic seizure oscillations, the network also generated several non-periodic synchronous population bursts resembling the pre-ictal discharges (Huberfeld et al. 2011), Fig.II-4B marked by asterisk in the experimental and model traces. These irregular discharges took place when the network approached the epileptic attractor, i.e., periodic bursting. These discharges were initiated by the recurrent AMPA synapses and terminated by the Ca^{2+}-dependent potassium currents. We determined the following sequence of events by analyzing our simulations in detail. The random noise input firing in a critical subset of neurons to initiate a cascade of firing from the recurrent excitatory synapses. This firing increases the Ca^{2+}-dependent potassium currents (spike-dependent) and thus decreases the excitability of each individual neuron involved in the population burst, eventually preventing them from firing in response to the terminating inputs and therefore terminating the burst. We predict that one could see the characteristic after-hyperpolarization and the corresponding increase in the extracellular potassium levels after each burst. Because the population bursts are randomly initiated, we suggest that the irregular character of these discharges could be partially explained by the synaptic noise present in the pyramidal cells and interneurons (Jirsa et al. 2014).

We analyzed the normalized power spectrum of the experimental and model LFP to compare the seizure dynamics between the model and experiment during epileptic oscillations, Fig.II-4D. In both cases, there is strong peak at 4 Hz corresponding to the main seizure frequency. The following peaks are the harmonics of this frequency. The LFP spectrum of the model is able to capture the main frequency peak and 1/f behavior of the signal (Buzsáki et al. 2012). We did not compare the frequencies beyond 40 Hz because these oscillations are not prominent during seizures. Although the detailed shape of the LFP signal and the single neuron voltage trace were not perfectly captured by our model, Fig.II-4C insets, the dynamics of the LFP signal and power spectrum during the seizure oscillations were reasonably matched, Fig.II-4D.

These results show that accumulation of K^{+}_{OUT} and Cl^{-}_{IN} in the subicular PY-IN network caused by the KCC2(-) pathology in pyramidal cells can lead to the development of seizure activity that is similar to the experimental recordings from epileptogenic slices of the human subiculum.

II.2.4.5 Analysis of the epileptic oscillations

We performed simulations for various values of the model parameters to analyze the stability of the epileptic oscillations in the network. We incorporated 30% KCC2(-) pyramidal cells into the PY-IN network and analyzed the emerging behavior of the system. To characterize the network excitability, we applied a seizure detection algorithm to the LFP generated by the network to capture the moment of seizure initiation.

An important characteristic of the pathological oscillations is the frequency of population bursts. We should mention that this value might significantly change during the course of seizure. Therefore, we only included the initial oscillation frequency once seizure has started. This frequency corresponds to the peak on the power spectrum during the epileptic oscillations, Fig.II-4D. The analysis showed that the frequency decreases with the number of KCC2(-) cells, Fig.II-5A. The bursting became longer as the duration of the population burst decreased, resulting in an increased inter-burst interval. It should not be misinterpreted as a decrease in the seizure activity because the population bursts became more prominent due to a longer duration.

We found that the network with extracellular potassium in the bath is tolerant of up 25% pathological KCC2(-) cells in the PY population, Fig.II-5A. A smaller number of these cells generate various oscillations within the gamma band, Fig.II-3. The seizure activity was not generated when there were fewer than this number cells, meaning that the time until seizure transition is formally infinite, dashed line in Fig.II-5A. However, epileptic oscillations were produced in the network when there was a critical number of KCC2(-) cells. We have found that the larger the proportion of KCC2(-) cells, the faster the transition. When there are more than 40% KCC2(-) cells in the network, the network switched to the pathological regime in less than 5 seconds, Fig.II-5A.

We examined the stability of the initiation of seizure-like activity with a supra-threshold proportion of KCC2(-) cells at varying mean strengths of the synaptic conductances. Similar to the other biophysical models, our network has a very large number of parameters that determine its dynamic behavior, which makes it impossible to study all parameter combinations. For this reason, we restricted our analysis to the synaptic conductances as the most important determinants of seizure dynamics.

To calculate the parameter regions that corresponded to the seizure oscillations, we analyzed the behavior of the network population with different synaptic conductance value combinations, similar to (Marder and Taylor 2011). To alter the synaptic connection strength, the mean of the synaptic parameter distribution was altered and expressed as a percentage of the initial mean (see Materials and Methods and Fig.II-5). We found that there is a large parameter region that corresponds to the resting state and epileptic oscillations with 30% KCC2(-) cells in the network, Fig.II-5B. An analysis of the network dynamics showed that two regions corresponded to the normal and seizure dynamics: in the black region, the network generated various

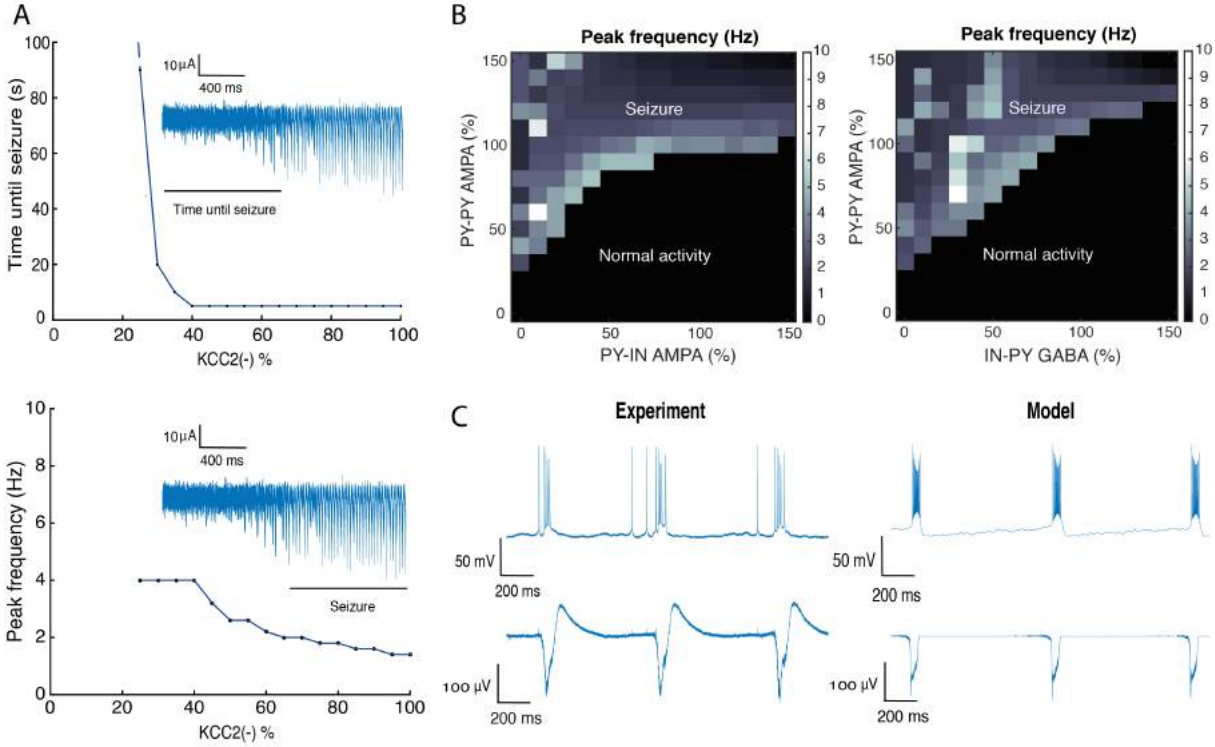

Figure II-5. Analysis of the epileptic oscillations

A - time until seizure initiation and the peak frequency of the network LFP as a function of the number of KCC2(-) cells in the network, insets – the characteristic LFP trace. B – LFP peak frequency as a function of the AMPA and GABA conductances in the network. C – population bursts generated after inhibition was blocked by BIC in the experimental recordings and the model. The synaptic conductance varied from 0 to 150%: PY-PY 0 – 2.25 nS/cm^2; PY-IN 0 – 1.5 nS/cm^2; IN-PY 0 – 1.05 nS/cm^2.

oscillations of different frequencies, and, in the white region, the network generated epileptic oscillations with frequencies between 1 and 10 Hz, depending on the parameters. The seizure initiation threshold depended on the strength of the recurrent excitation between the AMPA PY-PY pyramidal cells. In general, stronger recurrent excitation increased the seizure region, Fig.II-5B. In contrast, increasing the mean synaptic excitation strength of the AMPA PY-IN inhibitory cells reduced the tendency to produce ictal-like discharges. Similarly, increasing the mean inhibitory synapse (GABA IN-PY) strength reduced the space corresponding to the epileptic activity, Fig.II-5B. In the absence of any KCC2(-) PY cells, the network's ability to generate seizures was dramatically reduced (data not shown).

Evidently, the parametric analysis requiring the change of the synaptic connectivity in the network cannot be produced in the experimental conditions, thus making it impossible to compare the results from the model with the experimental data. However, for more consistency between the model and the experiment, we compared the model with the slice recordings when inhibition was blocked by BIC after seizure activity was established in the slice, Fig.II-5C, left panel. In this case, the network organized into periodic population bursts with a frequency within 1 Hz, similar to previous studies (Traub et al. 1987, de la Prida et al. 2006, Huberfeld et al. 2011). In this regime, the field potential recordings are completely phase locked with the pyramidal cell activity. We found that our network model is able to replicate this activity when inhibition is blocked, Fig.II-5C, right. In the network, these bursts were generated from the interplay between the recurrent excitation in the PY population and the cell's intrinsic currents I_{Ca}^{K} I_{Ca} (Traub et al. 1987, Jung et al. 2001), which are controlled by the Ca^{2+} dynamics. Even if the shape of the LFP differs from the experimental data to some extent, the frequency of the events is well replicated.

Therefore, we found that the epileptogenic effect of the KCC2(-) cells is robust and present in a wide range of synaptic conductances. As expected, the amount of synaptic inhibition provided by the population of IN could significantly reduce the ability of the network to generate seizures, while the recurrent excitation increases the ability of the network to generate seizure activity.

II.2.4.6 KCC2(-) pathology in the subiculum circuit with endogenous potassium

In the previous sections, we studied the role of the KCC2(-) pyramidal cells in epileptic oscillations in the presence of extracellular potassium in the bath solution and the potassium provided by the network activity. It allowed us to separate the contribution of K_{OUT}^{+} and Cl_{IN}^{-} to the seizure initiation mechanism. On the other hand, in the *in vivo*-like conditions, the extracellular

potassium concentrations primarily depend on the network activity, glial buffering and extracellular diffusion (Bazhenov et al. 2004). To recreate this scenario in our computational model, we performed simulations in the absence of extracellular potassium in the bath. To provide a similar level of depolarization as in the network with the bath solution, Fig.II-4, we adjusted the current input to the PY and IN populations to generate self-sustained activity within the physiological firing rate.

In the network with endogenous extracellular potassium concentrations, the addition of 40% KCC2(-) cells generated epileptic oscillations, Fig.II-6A. Similar to the network with extracellular potassium in the bath, Fig.II-4, the intensive firing of pathological cells leads to the gradual synchronization of the neurons in the network, provoking population bursting activity similar to the ictal discharge.

The mechanism of ictal activity in this network is described below. Increased firing of the pyramidal cells and interneurons induced a progressive increase in the K^{+}_{OUT} and Cl^{-}_{IN} concentrations in the network, Fig.II-6C. These changes induced an excitation-inhibition imbalance in the network, leading to the development of synchronous bursting activity after 12 seconds of simulation. After this transition, the extracellular potassium K^{+}_{OUT} concentrations rapidly increased due to the strong synchronous firing of the PY population. This created a positive feedback loop between spiking and the ion concentrations, leading to a further increase in excitability and synchronization. At the same time, the intracellular chloride concentration Cl^{-}_{IN} was also elevated due to increased interneuron firing, which increased the GABA reversal potential in the PY population.

The synchronous neuronal activity generated large LFP deviations, Fig.II-6B, similar to the extracellular potassium conditions, Fig.II-4B. The power spectrum of the network LFP of the signal shows a clear peak at approximately 8 Hz, which corresponds to the inter-burst interval (see the inset). There are more peaks in the LFP generated by the network during seizure compared to the extracellular potassium conditions, Fig.II-4B; however, the power spectrum possesses the same general shape.

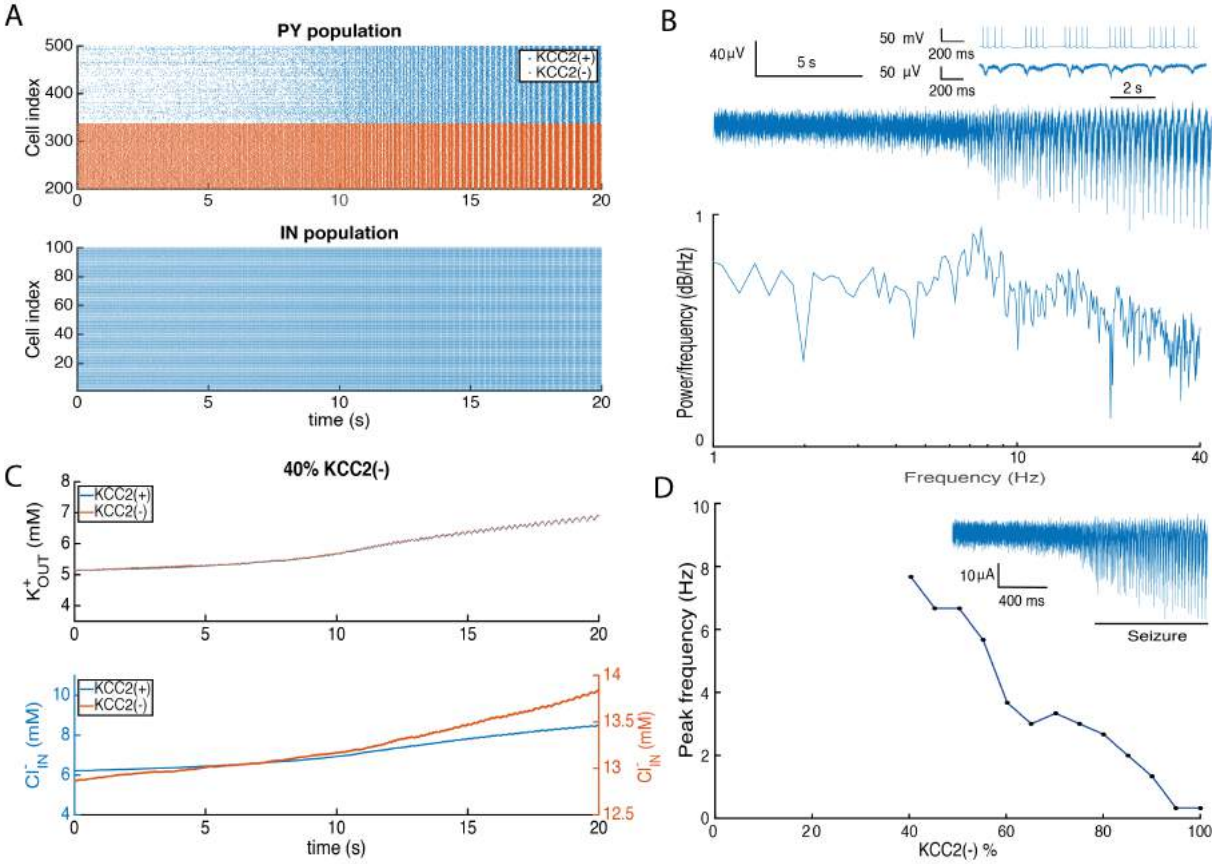

Figure II-6. Addition of KCC2(-) cells to the network with endogenous ion concentrations leads to the development of pathological oscillations

A - raster plot of the pyramidal cell (PY) and interneuron (IN) populations during seizure initiation. B - LFP trace computed from the network and the corresponding power spectrum, inset – the characteristic pyramidal cell activity during seizure. C - changes in the extracellular potassium K^{+}_{OUT} and intracellular chloride Cl^{-}_{IN} concentrations during seizure initiation. D - seizure frequency as a function of the amount of KCC2(-) cells in the network, inset – the characteristic LFP recording.

Similar to the network with the extracellular potassium in the bath, we found that a critical number of pathological KCC2(-) pyramidal cells are necessary for seizure initiation, Fig.II-6D. Pathological oscillations develop when there are more than 40% of these cells in the network. When there is smaller number of these cells, the network is able to tolerate the KCC2(-) pathology. Similar to the extracellular potassium condition, Fig.II-5A, the frequency of these oscillations decreases with the number of pathological cells in the network. When there are more than 90% KCC2(-) cells in the network, the oscillation frequency became very low, approximately 0.4 Hz. In this regime, long population bursts are generated with this frequency.

Thus, using the PY-IN cell network with endogenous potassium concentrations, we showed that decreasing the activity of the KCC2 cotransporter in the critical number of pyramidal cells leads to the development of seizure-like oscillations due to the accumulation of extracellular potassium and intracellular chloride. The removal of potassium from the extracellular compartment preserved the effect of synchronization, but shifted the oscillation frequency to a higher rate, which required a larger number of KCC2(-) cells to initiate seizures.

II.2.4.7 Dynamic elimination of the KCC2(-) pathology prevents seizure

In this section, we study the mechanisms of restoring chloride homeostasis in the network with endogenous potassium concentrations. We are interested in the effects produced by the recovery of the normal KCC2 function in the KCC2(-) pyramidal cells. The network was initialized with the same initial conditions as in Fig.II-6 at the end of the simulation to generate epileptic oscillations. After 5 seconds of seizure activity, the KCC2 function was restored in all KCC2(-) cells, causing a gradual decrease of synchrony in the PY and IN populations, Fig.II-7A. We found that after 45 seconds of KCC2 restoration, the network activity was transformed into the stable asynchronous firing regime, which corresponds to normal activity, Fig.II-7B.

The recovered KCC2 function in the pathological pyramidal cells returned the extracellular potassium K^{+}_{OUT} and intracellular chloride Cl^{-}_{IN} concentrations to the physiological values of 4.1 mM and 4 mM, respectively, Fig.II-7C. The mechanism of this transition is described below. After recovery of the KCC2 function, the intracellular chloride concentration started to decrease. This, in turn, reduced the excitatory drive to the IN population, leading to a further decrease in the intracellular chloride concentrations in the KCC2(+) and KCC2(-) pyramidal cells. These changes gradually reestablished the excitation-inhibition balance in the network and decreased the amount of synchrony between neurons. Consequently, the decreased pyramidal cell

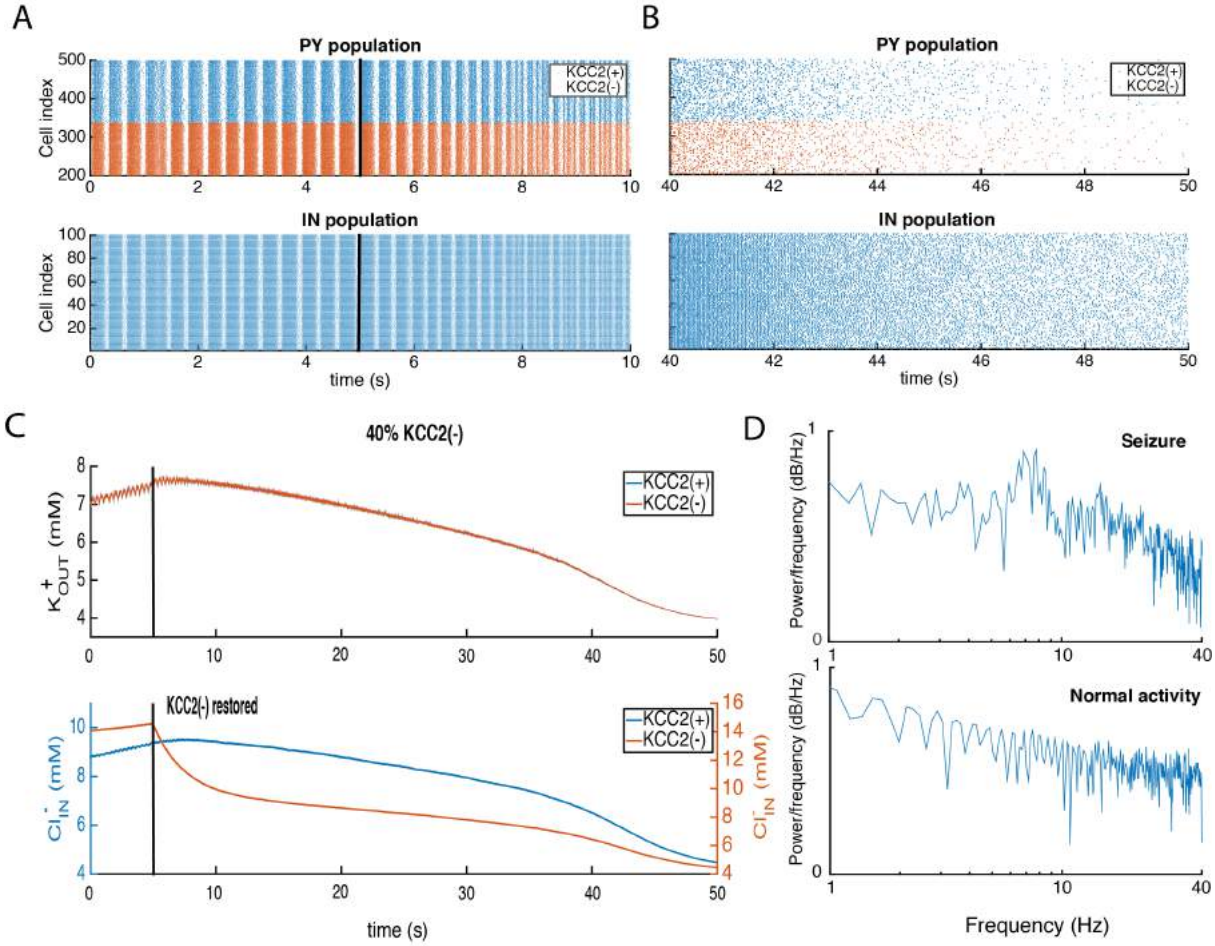

Figure II-7. Restoration of the KCC2(-) function in the network with realistic ion concentrations prevents seizure

A, B – raster plots of the network activity in the pyramidal cell (PY) and interneuron (IN) populations during seizure oscillations are shown on the left and those during the transition to the normal activity are shown on the right; the black line at 5 s corresponds to the moment of KCC2 restoration. C – changes in the extracellular potassium K^{+}_{OUT} and intracellular chloride Cl^{-}_{IN} concentrations after the restoration of the KCC2(-) cells; the black line indicates the moment of KCC2 restoration, as in panel A. D – power spectrum of the LFP generated by the network during epileptic oscillations and normal activity.

firing diminished the extracellular potassium concentrations, leading to the complete restoration of normal activity, Fig.II-7A, B. The biphasic decay of the extracellular potassium and intracellular chloride concentrations at approximately 40 s, Fig.II-7C, is explained by the fact that the synchronous bursting regime was inhibited at this time point, rapidly reestablishing the ion concentrations. At the end of this transition, the concentrations of the chloride and potassium ions became equilibrated in all neurons of the network and the activity switched to the stable asynchronous firing. We have found that restoration of KCC2 leads to the reversal of the activity from epileptic oscillations back to normal activity in networks with up to 100% of the pathological pyramidal cells (results not shown). Additionally, we simulated the restoration of the KCC2(-) cells in the network with the extracellular potassium in the bath and found similar results.

To compare the network state during epileptic oscillations following the recovery of the KCC2(-) cells, we plotted the corresponding power spectrums of the LFP generated by the network, Fig.II-7D. One can observe the characteristic peak on the LFP spectrum during seizure activity, which corresponds to the period of epileptic bursting, Fig.II-6A. After restoration of the KCC2 function in the pathological cells, the network switched to the asynchronous firing, which is characterized by a uniform LFP spectrum with the 1/f property (Bédard and Destexhe 2009).

II.2.5 Discussion

In the present work, we systematically studied the effect of KCC2 pathology found in the pyramidal cells of the human subiculum. We showed that the depolarizing GABA responses could be explained by the absence of the KCC2 cotransporter in the pathological pyramidal cells. Our model suggested that the KCC2(-) cells have an increased ability to participate in the self-sustained bursting activity caused by the increased extracellular potassium and intracellular chloride concentrations. Using a neural network model with realistic subiculum connectivity, we showed that addition of the KCC2(-) pyramidal cells to the network leads to the development of epileptic oscillations. An analysis of the intracellular and extracellular recordings from human subiculum epileptogenic slices showed that the power spectrum and the time course of the extracellular signal are reproduced by the proposed network model. An analysis of the pathological oscillations showed that a critical number of KCC2(-) cells is needed for seizure initiation. We found that the epileptic oscillations are robust and exhibit a wide range of synaptic conductances. We showed that pathological oscillations could be generated in the networks with fixed and endogenous potassium concentrations. We found that the restoration of KCC2(-) activity could reverse the epileptic oscillations in the network to the normal activity regime. These results show that the absence of KCC2 cotransporter in pyramidal cells could lead to seizures generation in the epileptic human subiculum.

Intracellular chloride homeostasis in pyramidal cells

The mechanisms of seizure initiation are one of the key questions in epilepsy research, for a review see (Zhang et al. 2011). Among other ion concentrations, the intracellular chloride homeostasis plays a particularly important role in synaptic transmission. Changes in the reversal potential substantially affect the efficiency of inhibition (Ben-Ari 2002). Studies on the developing brain showed that V_{GABA} in pyramidal cells is depolarizing due to the expression of the NKCC1 cotransporter. Later in development, NKCC1 becomes down-regulated, while KCC2 becomes up-regulated, leading to the inhibitory effect of GABA (Khalilov et al. 1999, Payne et al. 2003). Further studies showed that factors such as pH, and CO_2 among others could substantially change the value of V_{GABA} (Dulla et al. 2005) during the course of epileptic activity, including febrile seizures (Schuchmann et al. 2009, Tolner et al. 2011).

Recent studies suggested that local impermeant anions also play an important role in determining the baseline chloride concentrations (Glykys et al. 2014). This mechanism is complementary to the changes in the chloride concentration caused by GABA channel activation during synaptic stimulation (Fujiwara-Tsukamoto et al. 2007, Isomura et al. 2003). Taken together, these findings show that there are multiple factors that contribute to the chloride

concentrations in neurons and lead to the changes in the GABA reversal potential. Therefore, as shown in the present study, it is important to describe the mechanisms of chloride homeostasis in conjunction with the neural dynamics.

We showed that the depolarizing GABA responses of the pyramidal cells in epileptogenic human subiculum could be explained by the absence of the KCC2 cotransporter. We did not describe the hydrocarbonate changes in our model, and its concentration was assumed to be constant. This pathway is not the main point of our study, but it could be incorporated into the model including the dynamic HCO_3 concentrations, similar to (Doyon et al. 2011). Additionally, the NKCC1 cotransporter was not present in the model because the experimental tissue was derived from adult patients, potentially lacking the NKCC1 in pyramidal cells. In testing simulations, we explicitly added NKCC1 to our model and found that it led to higher intracellular chloride concentrations (data not shown). While the addition of the supplementary mechanisms to the model makes the chloride homeostasis more precise we found that the removal of the KCC2 alone is sufficient to explain the depolarizing GABA responses in human hippocampal tissue (Cohen et al. 2002).

The link between the extracellular potassium and intracellular chloride concentrations

The increased excitability resulting from the accumulation of extracellular potassium has been extensively studied in a large number of studies (Bazhenov et al. 2004, Fröhlich, Bazhenov and Sejnowski 2008, Ullah et al. 2009, Wei et al. 2014). Although the hypothesis that seizures are triggered by extracellular potassium concentration was suggested many years ago (Fertziger 1970), it is unclear whether the changes in the potassium concentrations are the reason for or a consequence of the epileptic oscillations.

Our work suggests that the increased extracellular potassium concentrations alone did not lead to seizure activity in the epileptogenic human subiculum. We showed that in the presence of high potassium in the bath solution, the epileptic oscillations could not be generated after the inhibitory neurotransmission is blocked by BIC. Instead of epileptic oscillations, the network generates periodic population bursts with a frequency that is significantly different from epileptic seizures, Fig.II-5C. This result suggests that the increased extracellular potassium concentration is not only principle factor contributing to seizure dynamics; however, intracellular chloride plays an important role as well.

The baseline intracellular chloride concentration significantly determines the efficiency of inhibition because it defines the value of the GABA reversal potential (Khalilov et al. 1999). Indeed the baseline chloride concentration is tightly linked to the extracellular potassium concentration via the KCC2 cotransporter, because it operates close to the thermodynamic equilibrium (Payne 1997). Thus, even a small increase in the extracellular potassium concentration leads to the

significant accumulation of chloride inside the neurons (Payne et al. 2003), thus reducing the efficiency of inhibition.

The role of the KCC2(-) cells

We found that the addition of the KCC2(-) cells to the subicular neural network with realistic connectivity leads to the development of oscillations that are similar to the seizure activity in human subicular slices. The addition of these cells leads to the substantial activation of the interneuron population, provoking an increase in the intracellular chloride concentrations in the pyramidal cells. As a result, it promotes an excitation-inhibition imbalance in the network, leading to generation of epileptic oscillations. These results are consistent with the finding of strong interneuron firing before seizure initiation (Gnatkovsky et al. 2008). The proposed mechanism of chloride accumulation in the pyramidal cells could also partially explain the failure of inhibition in the concept of inhibitory restraints before seizure initiation (Trevelyan et al. 2007, Schevon et al. 2012).

These findings predict that in realistic conditions where the ion concentrations are the result of network activity, the accumulation of both potassium and chloride could provoke seizure initiation in the local subicular network, Fig.II-6. Simultaneous measurements of the intracellular chloride and extracellular potassium concentrations are needed to support or falsify this hypothesis of seizure initiation. We suggest that new experiments on slices with well-controlled potassium concentrations combined with chloride imaging would help to support our predictions.

We found that the pathological KCC2(-) pyramidal cells possess higher chloride concentrations than the KCC2(+) cells, resulting in a higher resting potential and GABA reversal potential. This higher chloride concentration leads to the increased excitability of these cells. We hypothesize that the increased firing of these pathological cells would strengthen the synaptic connections between due to synaptic plasticity and lead to further epileptogenic activity in the KCC2(-) population. Further connectivity studies are needed to verify this prediction.

Additionally, we have found that restoring the KCC2 function of the pathological pyramidal cells leads to the restoration of the normal network activity, Fig.II-7. Indeed, we found that restoration of the KCC2 function in up to 100% of pathological cells in the network effectively blocks seizure activity. These results suggest that pharmacological strategies aimed at restoring or strengthening chloride homeostasis in pyramidal cells would be very efficient in preventing seizure activity.

Conclusions

Epilepsy is a complex disease of the brain that involves dynamic interactions of different components of the nervous system, from single molecules and neurons to the areas of the cortex and hemispheres. Due to the highly complex epileptic dynamics in the brain, it is necessary to incorporate experimental measurements into computational models to form rigorous and testable predictions (Lytton 2009, Ullah and Schiff 2009). Recent theoretical studies suggested that it would be hard to identify a single exceptional mechanism that leads to seizure; however, seizure dynamics involves multiple mechanisms (Jirsa et al. 2014, Proix et al. 2014, Naze et al. 2015). Nonetheless, we believe that studying the different pathways using theoretical models would help us to understand the general mechanisms underlying this complex disease.

In the present study, we have characterized one pathological pathway associated with chloride homeostasis in the human subiculum. Recent studies from epileptogenic peritumoral tissue (Pallud et al. 2014) suggested that KCC2 pathology is more general and is not restricted to the subiculum. Thus, studies regarding the role of chloride homeostasis deserve more attention in the context of pathological network dynamics combined with experimental studies. We believe that further investigation of the role of inhibition will lead to a deeper understanding of the epilepsy mechanisms, resulting in the successful discovery of new anti-epileptic treatments.

II.3 Detailed model description

Since Material and methods part is very small in the paper, we provide the full description of the model in the present section. We characterize single neuron model used for pyramidal cell and interneurons, subiculum connectivity structure, KCC2 model, extracellular potassium diffusion, formulate the LFP model and describe seizure detection algorithm. In the end of this section we provide the information about pharmacology of the ictal events in human subiculum slice recordings.

II.3.1 Seizure pharmacology

In order to clarify the role of synaptic mechanisms involved into seizure generation, we show the effects of various synaptic blockers for generation of the ictal discharges, Fig.II-8 (Huberfeld et al. 2011). Seizure activity was induced by application of 0.25 Mg^{2+} and 8 mM of K^{+} to the extracellular solution. After 30 minutes of extracellular solution application the recurrent ictal discharges became established, Fig.II-8A.

One can see that ictal discharges depend on the GABAergic neurotransmission since the pathological rhythm disappears after the blockade of inhibition by GABA-A, Fig.II-8B. This leads to generation of the population spikes similar to the Pre-Ictal Discharges (PID) happening before seizure initiation, Fig.II-8A (Huberfeld et al. 2011). Once established the PIDs did not depend on the NMDA and GABA neurotransmission, Fig.II-8C. But these discharges crucially depended on the recurrent AMPA synapses, Fig.II-8D, since they became completely blocked after the application of the NBQX, Fig.II-8D.

Thereby we conclude that generation of ictal discharges depend both on extracellular ion concentrations and synaptic neurotransmission via AMPA, GABA and NMDA synapses. If one of these components is missing, the ictal discharges could not be spontaneously generated in the slice.

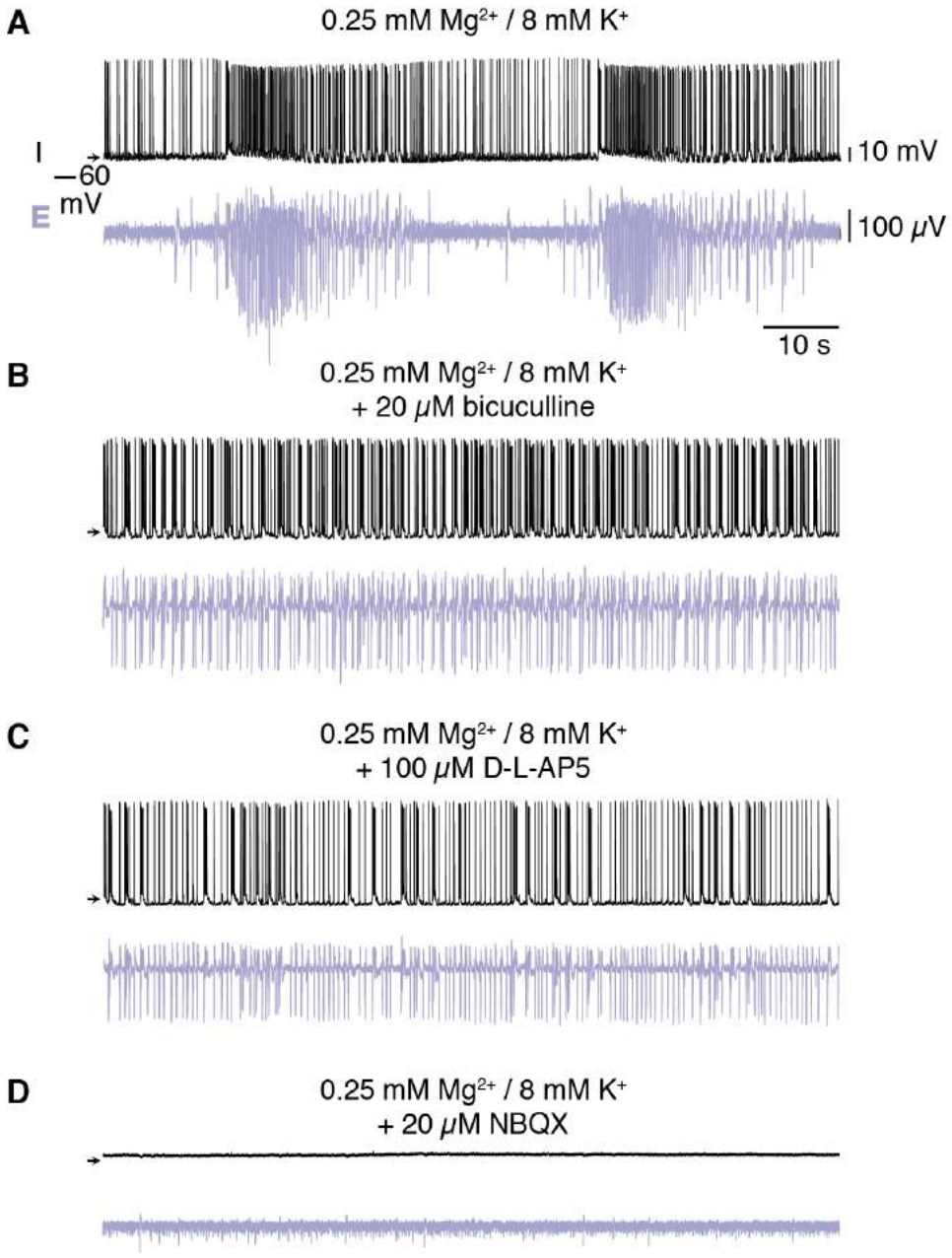

Figure II-8. Extracellular (E) and Intracellular (I) recordings from epileptogenic human subiculum slices

A – two ictal events with preceding PIDs induced by 0.25 Mg^{2+} and 8 mM of K^{+} in the extracellular solution. B – Blockade of GABA-A receptors by 20 μM of BIC suppressed the ictal events. C – blockade of NMDA receptors by 100 μM of D-L-AP5 suppressed the ictal events, but did not block the PIDs. D – blockade of AMPA receptors by 20 μM of NBQX suppressed both PID and Ictal discharges. Adapted from (Huberfeld et al. 2011).

II.3.2 Pyramidal cell and interneuron model

To model the behavior of the pyramidal cell and interneurons we use the models known from the literature (Mainen and Sejnowski 1996, Bazhenov et al. 2004, Fröhlich and Bazhenov 2006). For pyramidal cells we use the current set known for intrinsically bursting pyramidal cells of subiculum (Jung et al. 2001, Staff et al. 2000) and for the interneuron we use the model of fast spiking interneuron (Krishnan and Bazhenov 2011). The pyramidal and interneuron models differ by the amount of intrinsic currents and coupling conductances between soma and dendrite. The scheme of these models is present on Fig.II-9.

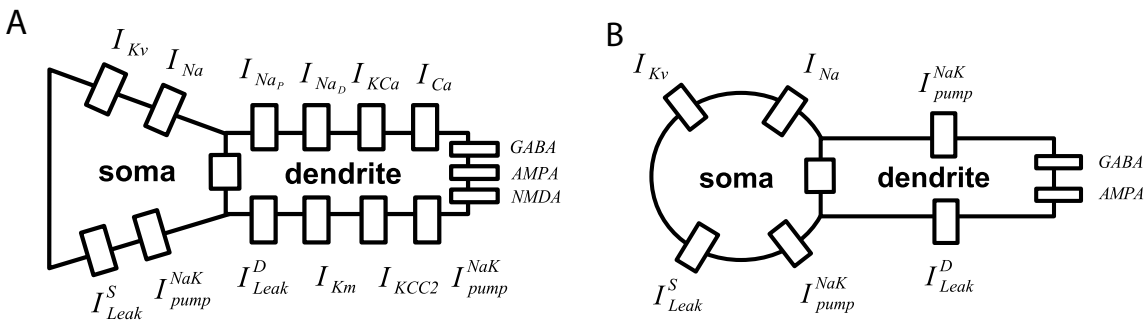

Figure II-9. Intrinsic currents in the single neuron models
A, B – the schemes of pyramidal cell and interneuron models with corresponding intrinsic currents, cotransporters, ion pumps and synapses.

Voltage on dendrite

$$C_m \frac{dV_D}{dt} = \sum_i I^i_{\text{int}} - g^D_C (V_D - V_S) + I^D_{Leak}$$

$$I^D_{Leak} = -G^L_{Cl}(V_D - V_{Cl}) - G^L_K (V_D - V_K) - G^L_{Na}(V_D - V_{Na})$$

$$\sum_i I^i_{\text{int}} = I_{Na_p} + I_{Na_D} + I_{KCa} + I_{Ca} + I^D_{Leak} + I_{Km} + I^{NaK}_{pump} + I_{syn}$$ for pyramidal cells

$$\sum_i I^i_{\text{int}} = I^D_{Leak} + I^{NaK}_{pump} + I_{syn}$$ for interneurons

Voltage on soma

$$g^S_C (V_D - V_S) = \sum_i I^i_{\text{int}} + I^S_{Leak}$$

$$I^S_{Leak} = -g^L_{Cl}(V_S - V_{Cl}) - g^L_K (V_S - V_K) - g^L_{Na}(V_S - V_{Na})$$

$\sum_i I^i_{\text{int}} = I_{Kv} + I_{Na} + I^S_{Leak} + I^{NaK}_{pump}$ for pyramidal cells and interneurons

Reversal potentials

$$V_K = \frac{RT}{F}\ln(\frac{K^+_{OUT}}{K^+_{IN}}) \quad V_{Na} = \frac{RT}{F}\ln(\frac{Na^+_{OUT}}{Na^+_{IN}}) \quad V_{Cl} = \frac{RT}{F}\ln(\frac{Cl^-_{IN}}{Cl^-_{OUT}}) \quad V_{GABA} = \frac{RT}{F}\ln(\frac{4Cl^-_{IN} + HCO3^-_{IN}}{4Cl^-_{OUT} + HCO3^-_{OUT}})$$

Na-K pump

$$A(K^+_{OUT}, Na^+_{IN}) = \frac{1}{(1+K^+_\alpha / K^+_{OUT})^2}\frac{1}{(1+Na^+_\alpha / Na^+_{IN})^3} \qquad I_{Kpump} = -2I\max A(K^+_{OUT}, Na^+_{IN})$$

$$I_{Napump} = 3I\max A(K^+_{OUT}, Na^+_{IN})$$

$$I^{NaK}_{pump} = I_{Kpump} + I_{Napump}$$

Somatic compartment

Delayed-rectifier K^+ current

$$I_{Kv} = G_{Kv} m_{iKv}(V_S - V_K)$$

$$dm_{iKv}/dt = -\frac{m_{iKv} - m^\infty_{iKv}}{\tau_{Kvm}}$$

$$a_{iKv} = 0.02\frac{V_S - 25}{1 - \exp(-(V_S - 25)/9)} \quad b_{iKv} = -0.002\frac{V_S - 25}{1 - \exp((V_S - 25)/9)}$$

$$\tau_{Kvm} = \frac{1}{((a_{iKv} + b_{iKv}))} \quad m^\infty_{Kv} = \frac{a_{iKv}}{(a_{iKv} + b_{iKv})}$$

Na^+ current

$$I_{Na} = G_{Na} m^3_{iNa} h_{iNa}(V_S - V_{Na})$$

$$dm_{iNa}/dt = -(m_{iNa} - m_\infty)/\tau_m$$

$$dh_{iNa}/dt = -(h_{iNa} - h_\infty)/\tau_h$$

$$am_{iNa} = 0.182\frac{V_S + 25}{1 - \exp(-(V_S + 25)/9)} \quad bm_{iNa} = 0.124\frac{V_S + 7}{1 - \exp(-(V_S + 25)/9)}$$

$$ah_{iNa} = 0.024\frac{V_S + 40}{1 - \exp(-(V_S + 40)/5)} \quad bh_{iNa} = 0.0091\frac{V_S - 65}{1 - \exp(-(-V_S - 65)/5)}$$

$$\tau_m = \frac{1}{am_{iNa} + bm_{iNa}} \quad \tau_h = \frac{1}{ah_{iNa} + bh_{iNa}} \quad m_\infty = \frac{am_{iNa}}{am_{iNa} + bm_{iNa}}$$

$$h_\infty = \frac{1}{1+\exp((V_S-55)/6.2)}$$

Dendrite compartment

Na^+ current

$$I_{NaD} = G_{NaD} m_{iNaD}^3 h_{iNaD}(V_D - V_{Na})$$

$$dm_{iNaD}/dt = -(m_{iNaD} - m_{iNaD}^\infty)/\tau_{mD}$$
$$dh_{iNaD}/dt = -(h_{iNaD} - h_{iNaD}^\infty)/\tau_{hD}$$

$$am_{iNa} = 0.182\frac{V_D+25}{1-\exp(-(V_D+25)/9)} \quad bm_{iNa} = 0.124\frac{V_S+25}{1-\exp(-(V_D+25)/9)}$$
$$ah_{iNa} = 0.024\frac{V_D+40}{1-\exp(-(V_D+40)/5)} \quad bh_{iNa} = 0.0091\frac{V_D-65}{1-\exp(-(-V_D-65)/5)}$$
$$\tau_{mD} = \frac{1}{2.9529(am_{iNaD}+bm_{iNaD})} \quad \tau_{mD} = \frac{1}{2.9529(ah_{iNaD}+bh_{iNaD})}$$
$$m_{iNaD}^\infty = \frac{am_{iNaD}}{am_{iNaD}+bm_{iNaD}} \quad h_{iNaD}^\infty = \frac{1}{1+\exp((V_D+55)/6.2)}$$
$$\tau_{mD} = \frac{1}{2.9529(am_{iNaD}+bm_{iNaD})}$$

Persistent Na^+ current

$$I_{NapD} = G_{NapD} m_{iNapD}(V_D - V_{Na})$$

$$dm_{iNapD}/dt = -(m_{iNapD} - m_{NapD}^{infity}(V_D))/0.1992$$
$$m_{NapD}^{infity}(V_D) = 0.02/(1+\exp(-(V_D+42)/5))$$

High-threshold Ca^{2+} current

$$I_{Ca} = G_{Ca} m_{Ca}^2 h_{Ca}(V_D - V_{Ca})$$

$$dm_{iHVA}/dt = -(m_{iHVA} - m_{Ca}^\infty)/\tau_{Ca}^m$$
$$dh_{iHVA}/dt = -(h_{iHVA} - h_{ca}^\infty)/\tau_{Ca}^h$$
$$\tau_{Ca}^m = 1/((am_{iHVA}(V_D) + bm_{iHVA}(V_D)))$$
$$\tau_{Ca}^m = am_{iHVA}(V_D)/(am_{iHVA}(VD) + bm_{iHVA}(V_D))$$
$$m_{Ca}^\infty = am_{iNaD}/(am_{iNaD} + bm_{iNaD})$$
$$\tau_{Ca}^h = 1/((ah_{iHVA}(V_D) + bh_{iHVA}(V_D)))$$

$h_{ca}^{\infty} = ah_{iHVA}(V_D)/(ah_{iHVA}(V_D) + bh_{iHVA}(V_D))$
$am_{iHVA}(V_D) = 0.055(-27 - V_D)/(\exp((-27 - V_D)/3.8) - 1)$
$bm_{iHVA}(V_D) = 0.94\exp((-75 - V_D)/17)$
$ah_{iHVA}(V_D) = 0.000457\exp((-13 - V_D)/50)$
$bh_{iHVA}(V_D) = 0.0065/(\exp((-V_D - 15)/28) + 1)$

Ca^{2+}-dependent K^+ current

$$I_{KCa} = G_{KCa} m_{iKCa}^2 (V_D - V_K)$$

$$dm_{iKca}/dt = (m_{iKCa} - m_{iKCa}^{\infty})/\tau_{Ca}$$
$$m_{iKCa}^{\infty} = (48/0.03(Ca_{IN}^{+})^2)/(48/0.03(Ca_{IN}^{+})^2 + 1)$$
$$\tau_{Ca} = (1/(0.03(48(Ca_{IN}^{+})^2/0.03 + 1)))/4.65$$

M-type K^+ current

$$I_{Km} = G_{Km} m_{Km} (V_D - V_K)$$

$$dm_{Km}/dt = (m_{Km} - m_{Km}^{\infty})/\tau_{Km}$$
$$m_{Km}^{\infty} = (a_{Km})/(a_{Km} + b_{Km})$$
$$\tau_{Km} = 1/(a_{Km} + b_{Km})/2.9529$$
$$a_{Km} = 0.001(V_D + 30)/(1 - \exp(-V_D + 30)/9))$$
$$b_{Km} = -0.001(V_D + 30)/(1 - \exp\{-V_D + 30)/9\})$$

Dynamic ion concentration of K_{OUT}^{+}, Cl_{IN}^{-} and Ca^{2+}

$$dK_{OUT}^{+}/dt = k_K/F/d(IK_{\Sigma} + I_{pump}^{NaK} - I_{KCC2}) + G$$
$$dCl_{IN}^{-}/dt = k_{Cl}/F(ICl_{\Sigma} - I_{KCC2})$$
$$dCa_{IN}^{+}/dt = (-5.1819e^{-5})/D_{Ca} I_{Ca} + (0.00024 - Ca_{IN}^{+})/\tau_{Ca}$$

$$ICl_{\Sigma} = g_{Cl}(V_D - V_{Cl}) + I_{GABA}$$
$$IK_{\Sigma} = g_K^L (V_S - V_K) + G_K^L (V_D - V_K) + I_{Kv}/200 + I_{KCa} + I_{Km}$$
$$G = k_{off}(B_{\max} - Bs) - \frac{k_{on}}{k1} Bs K_{OUT}^{+}$$
$$dBs/dt = k_{off}(B_{\max} - Bs) - k_{on} Bs K_{OUT}^{+}$$
$$k_{on} = \frac{k_{off}}{1 + \exp(-\{K_{OUT}^{+} - K_{Th}^{+}\}/1.08)}$$

Synaptic currents

$$I_{AMPA} = (V_D - V_{AMPA}) \sum_{i=1}^{C_{AMPA}} s^i_{AMPA} g^i_{AMPA} \qquad ds^j_{AMPA} / dt = -\frac{s^j_{AMPA}}{\tau_{AMPA}} + \sum_k \delta(t - t^k_j)$$

$$I_{GABA} = (V_D - V_{GABA}) \sum_{i=1}^{C_{GABA}} s^i_{GABA} g^i_{GABA} \qquad ds^j_{GABA} / dt = -\frac{s^j_{GABA}}{\tau_{GABA}} + \sum_k \delta(t - t^k_j)$$

$$I_{NMDA} = \frac{(V_D - V_{NMDA})}{(1 + Mg^{2+}_{OUT} \exp(-0.062 V_D) / 3.57)} \sum_{i=1}^{C_{NMDA}} s^i_{NMDA} g^i_{NMDA}$$

$$ds^j_{NMDA} / dt = -\frac{s^j_{NMDA}}{\tau^{decay}_{NMDA}} + \alpha x_j (1 - s^j_{NMDA})$$

$$dx_j / dt = -\frac{x_j}{\tau^{rise}_{NMDA}} + \sum_k \delta(t - t^k_j)$$

Synaptic noise

$\tau_{AMPA} \frac{dI_{AMPA}}{dt} = -I_{AMPA} + \sigma_{AMPA} \xi(t)$, where $\xi(t)$ is the white noise the mean 0 and variance 1.

Pyramidal cell parameters

$Mg^+_{OUT} = 0.25mM$, $Cl^-_{OUT} = 130mM$, $Mg^+_{OUT} = 0.25mM$, $HCO3^-_{IN} = 16mM$, $HCO3^-_{OUT} = 26mM$, $k_K = 10\ 1000cm^3$, $k_{Cl} = 100\ 1000cm^3$, $K_i = 150mM$, $d = 0.15m$, $Na^+_{OUT} = 130mM$, $Na^+_{IN} = 20mM$, $C_m = 0.75\mu F / cm^2$, $kT / F = 26.63mV$, $g^D_C = 0.60mS / cm^2$, $g^S_C = 100mS / cm^2$, $G_{Na} = 3450mS / cm^2$, $G_{Kv} = 200mS / cm^2$, $g^L_K = 0.042mS / cm^2$, $g^L_{Na} = 0.0198mS / cm^2$, $G_{NaD} = 1.1mS / cm^2$, $G_{NapD} = 3.5mS / cm^2$, $G_{HVA} = 0.0195mS / cm^2$, $G^L_K = 0.044mS / cm^2$, $G^L_{Cl} = 0.01mS / cm^2$, $G^L_{Na} = 0.02mS / cm^2$, $G_{NaD} = 1.1mS / cm^2$, $V_{Ca} = 140mV$, $\tau_{Ca} = 1000ms$, $D_{Ca} = 0.85cm^2 mM / \mu A$, $G_{KCa} = 2.5mS / cm^2$, $G_{Km} = 0.01mS / cm^2$, $K^+_\alpha = 3.5mM$, $Na^+_\alpha = 20mM$, $I^S_{\max} = 25\mu A / cm^2$, $I^D_{\max} = 25\mu A / cm^2$, $K^+_{Th} = 15mM$, $koff = 0.0008mM^{-1}ms^{-1}$, $k_{OFF} = 1mM^{-1}$, $B_{\max} = 500mM$, $k_1 = 1mM^{-1}$.

Interneuron parameters

$Cl^-_{OUT} = 130mM$, $Cl^-_{IN} = 3.70mM$, $K_i = 150mM$, $k_K = 10\ 1000cm^3$, $k_{Cl} = 100\ 1000cm^3$, $d = 0.15m$, $Na^+_{OUT} = 130mM$, $Na^+_{IN} = 20mM$, $C_m = 0.75\mu F / cm^2$, $kT / F = 26.63mV$,

$g_C^D = 2mS/cm^2$, $g_C^S = 100mS/cm^2$, $G_{Na} = 3450mS/cm^2$, $G_{Kv} = 200mS/cm^2$, $G_K^L = 0.035mS/cm^2$, $G_{Cl}^L = 0.01mS/cm^2$, $G_{Na}^L = 0.02mS/cm^2$, $g_{Na}^L = 0.0198mS/cm^2$, $g_K^L = 0.042mS/cm^2$, $K_\alpha^+ = 3.5mM$, $Na_\alpha^+ = 20mM$, $I_{\max}^S = 25\mu A/cm^2$.

Synaptic parameters

$V_{AMPA} = 0mV$, $V_{NMDA} = 0mV$ $\tau_{AMPA} = 5.4ms$, $\sigma_{AMPA}^{PY} = 0.5\mu A/cm^2$, $\sigma_{AMPA}^{IN} = 0.6\mu A/cm^2$.

II.3.3 Subiculum connectivity

We approximate the local connectivity structure based on work of (Peng et al. 2014). They performed the detailed path-clamp study on the mouse subiculum circuitry. The resulting scheme of connections is present on in Fig.II-10.

One can see that subiculum consists of two populations of pyramidal cells of regularly spiking and intrinsically bursting neurons. These pyramidal cell populations have different amount of connections with the interneurons, yet their recurrent connectivity is very similar. Surprisingly this study did not find any connections from bursting neurons to regularly spiking pyramidal cells.

We should admit the exact ratio of spiking-to-bursting pyramidal cells is a subject of controversy. The proportion of these cells in human subiculum tissue is close to 50/50 (Huberfeld et al. 2007), yet additional studies are needed to clearly determine this ratio. Also it is known that in conditions of the increased potassium regular spiking cells could be transformed into bursting cells (Fröhlich and Bazhenov 2006).

Taking into account these considerations we construct the local subiculum network that consist of regularly spiking pyramidal cells that could be turned into the bursting mode due to increased potassium concentrations. Thus in our network model we describe populations of PY and IN neurons with connection probabilities taken from Fig.II-10 for R and IN cells.

The resulting network structure for PY and IN population is summarized on Fig.II-11. For clarity we depict the representative network that consist of 80 pyramidal cells and 20 interneurons and show the connectivity matrix, Fig.II-11 B. In the simulations we describe PY and IN populations that consist of 841 and 225 neurons with the same connection probabilities.

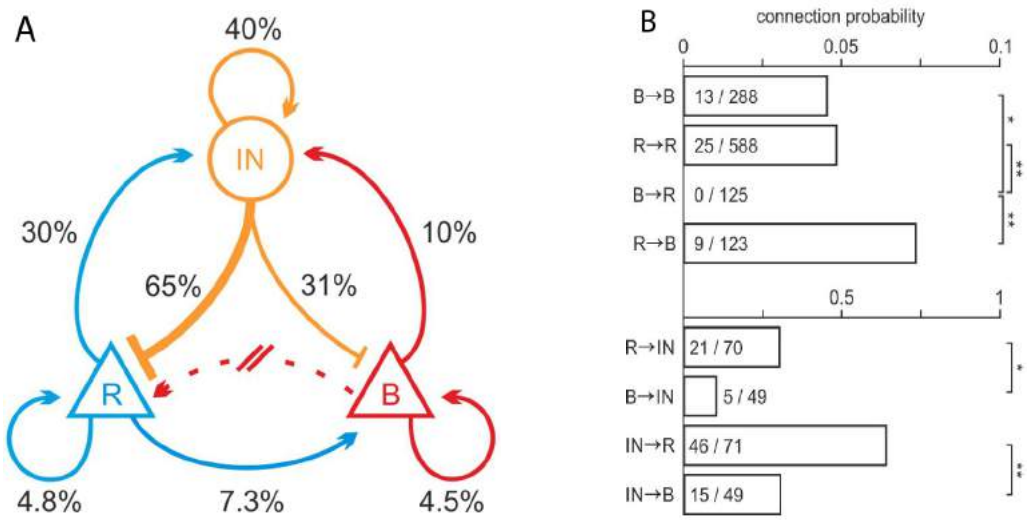

Figure II-10. Connectivity structure of mice subiculum
A – populations of regularly spiking (R), intrinsically bursting (B) pyramidal cells and interneurons (IN). Arrows and percent indicate the direction and probability of connections. B – the probability of connections calculated for different amount of recorded cells. Adapted from (Peng et al. 2014).

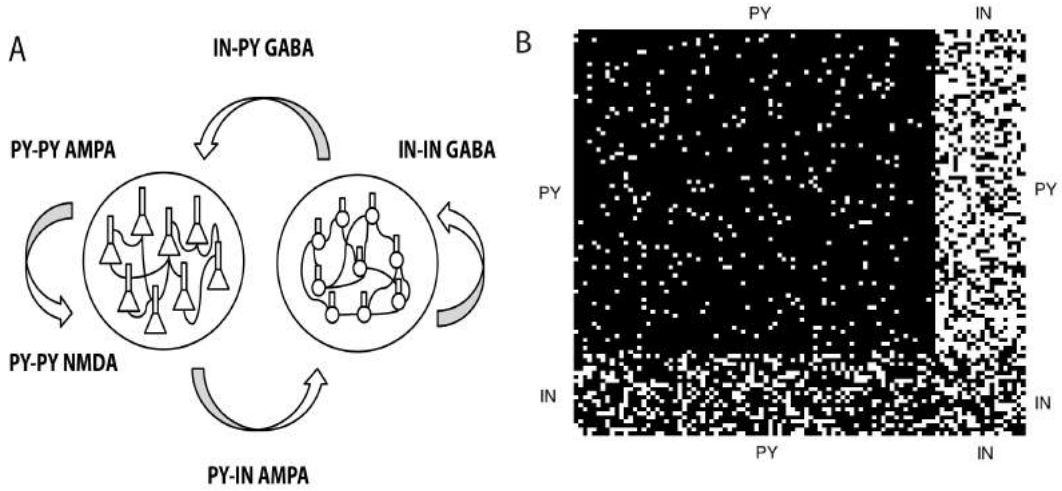

Figure II-11. Connectivity structure of the network model
A – connectivity structure of the neural network model consisting of pyramidal cells (PY) and interneurons (IN). B –connectivity matrix of the neural network of 80 PY and 20 IN with connection probabilities from Fig.II-10A (R and IN cells), white square – connection, black square – no connection.

According to this connectivity structure we assigned AMPA conductances for PY-PY and PY-IN connections, NMDA conductances for PY-PY connections and GABA conductances for IN-PY and IN-IN connections. The values for conductances are taken from a normal distribution with fixed mean and variance.

Synaptic conductances

PY-PY: $g_{AMPA} \sim N(1.5,0.15)\ nS/cm^2$, $g_{NMDA} \sim N(0.02,0.002)\ nS/cm^2$
PY-IN: $g_{AMPA} \sim N(1,0.1)\ nS/cm^2$
IN-PY: $g_{GABA} \sim N(0.7,0.07)\ nS/cm^2$
IN-IN: $g_{GABA} \sim N(0.5,0.05)\ nS/cm^2$

$N(\mu,\sigma)$ corresponds to the normal distribution with the mean μ and variance σ.

II.3.4 Kation chloride cotransporter model

Kation chloride cotransporters are the class of membrane proteins that use the potassium gradients to regulate the baseline chloride concentrations in various cells. In the nervous system these proteins play especially an important role since they maintain the baseline chloride concentration in neurons. They use potassium gradient created by sodium-potassium pump to transport ions to transport chloride ions. The cotransporters do not use energy to transport chloride ions because they always transfer ions with different charges so that the total charge does not change. It allows to perform the transport without energy loss. There are different types of cotransporters and exchanges and here we show their brief classification. The NKCC transfers Na^+, K^+ and $2Cl^-$ ions into the cells, anion exchangers transfers Cl^- and HCO_3^- in opposite directions; sodium-dependent anion exchangers transfer Na^+, HCO_3^- and H+ and Cl^- ions in opposite direction; and KCC transfer K^+ and Cl^- ions to the same direction (Payne et al. 2003).

Kation chloride cotransporter 2 (KCC2) is an important part of the chloride cotransporter family. It is widely expressed in the central nervous system, where it regulates the baseline chloride homeostasis in neurons. The cotransporter is crucial component for the normal brain function since KCC2 knockout mice die immediately after birth due to excitatory activity of GABA and glycine.

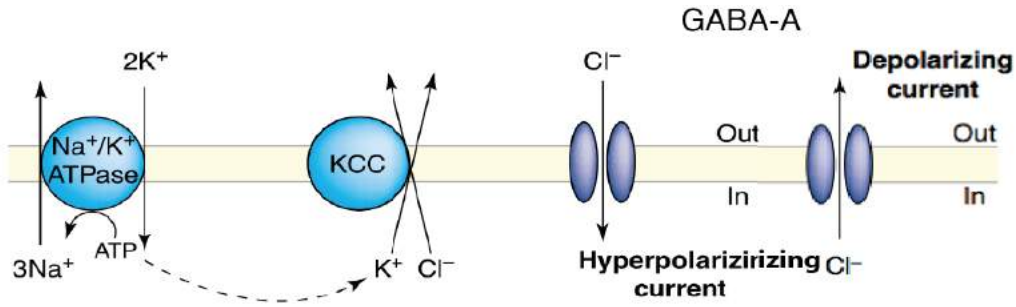

Figure II-12. The illustration of the KCC2 mechanism
Arrows indicate the direction of the ion transfer. Adapted from (Payne et al. 2003).

To illustrate the mechanism of KCC2 ion extrusion, we show it on the scheme, Fig.II-12. The baseline chloride concentration is the result of interaction of multiple factors such as inside and outside concentration of HCO_3^-, Cl^-, glycine, and K^+, dendrite size, diffusion as well as GABA-A activity, yet the KCC2 provides the most substantial contribution for reduction of the baseline chloride level (Doyon et al. 2011). In the present model the KCC2 action is described using the following model.

$$I_{KCC2} = \frac{I_{\max}(V_K - V_{Cl})}{(V_K - V_{Cl}) + V_{1/2}},$$

$$V_K = \frac{RT}{F}\log(\frac{K^+_{OUT}}{K^+_{IN}}),\ V_{Cl} = \frac{RT}{F}\log(\frac{Cl^-_{IN}}{Cl^-_{OUT}})$$

One could see that the current via KCC2 depends on the voltage difference between Nernst potential of V_{Cl} chloride and V_K potassium. Thereby depending on this difference the current via KCC2 could be inward or outward. In this way baseline chloride and potassium concentration could significantly change the rate of chloride and potassium extrusion into the extracellular space (Payne 1997).

KCC2 parameters: $I_{\max} = 2\mu A / cm^2$, $V_{1/2} = 40mV$.

II.3.5. Potassium diffusion model

In order to take into account the propagation of potassium in the extracellular space we consider the diffusion process between cells. In this network all pyramidal cells are connected with 4 neighbors. It allows potassium to propagate in the network between the neurons. For clarity we show the matrix only for 25-neuron network, yet in the simulations we used 841-neuron network. The pyramidal cell placement in the network space is present on Fig.II-13A.

The extracellular potassium concentration is described by the following reaction-diffusion equation for the neural network with continuous potassium concentration:

$$\frac{\partial K^+_{OUT}}{\partial t} = \frac{k_K}{Fd}(IK_\Sigma + I^{NaK}_{pump} - I_{KCC2}) + G + \varepsilon(\frac{\partial^2 K^+_{OUT}}{\partial x^2} + \frac{\partial^2 K^+_{OUT}}{\partial y^2}) \qquad (1)$$

Since the considered neural network of subiculum represents the local circuit, we have taken into account the periodic border conditions to compensate for K^+_{OUT} flow through the borders, Fig.II-13A.

$$\left.\frac{\partial K^+_{OUT}}{\partial x}\right|_I = -\left.\frac{\partial K^+_{OUT}}{\partial x}\right|_{III}, \quad \left.\frac{\partial K^+_{OUT}}{\partial y}\right|_{II} = -\left.\frac{\partial K^+_{OUT}}{\partial y}\right|_{IV} \qquad (2)$$

We interpret these conditions as putting the local neural network into a larger one, which is also engaged into epileptic oscillations and hence has similar potassium concentration.

We apply the following discretization to solve the ODE, equation (1). We assume that neurons are equally spaced on the X-Y grid (i and j indexes), Fig.II-13B. This leads to the following discrete approximation of the Laplace operator:

$$\frac{\partial^2 K^+_{OUT}}{\partial x^2} + \frac{\partial^2 K^+_{OUT}}{\partial y^2} = \frac{K^+_{OUT(i+1,j)} - 2K^+_{OUT(i,j)} + K^+_{OUT(i-1,j)}}{\Delta x^2} +$$
$$+ \frac{K^+_{OUT(i,j+1)} - 2K^+_{OUT(i,j)} + K^+_{OUT(i,j-1)}}{\Delta y^2}$$

since $\Delta y = \Delta x$ it becomes

$$\frac{\partial^2 K^+_{OUT}}{\partial x^2} + \frac{\partial^2 K^+_{OUT}}{\partial y^2} = \frac{K^+_{OUT(i+1,j)} + K^+_{OUT(i-1,j)} + K^+_{OUT(i,j+1)} + K^+_{OUT(i,j-1)} - 4K^+_{OUT(i,j)}}{\Delta x^2} \qquad (3)$$

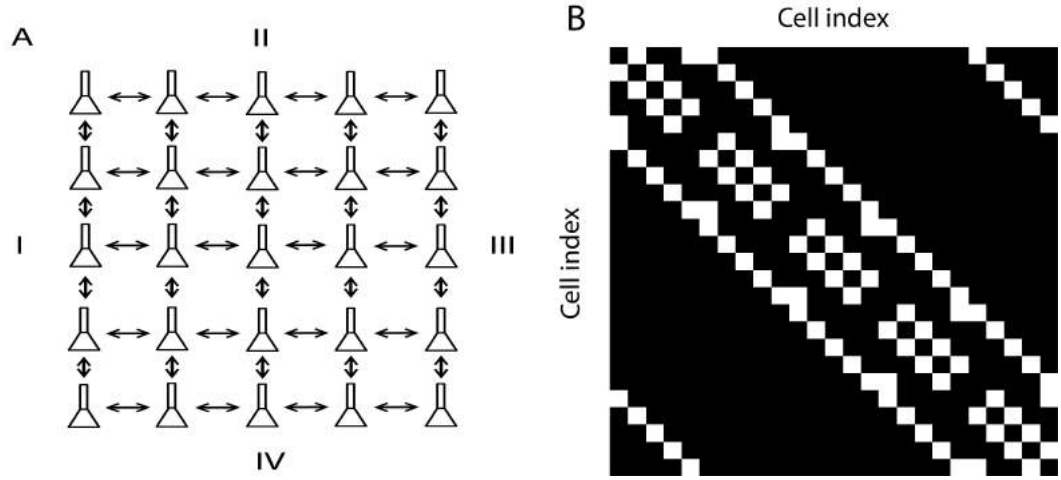

Figure II-13. Extracellular potassium diffusion in the neural network model
A – location of PY cells in the network and direction of the K^{+}_{OUT} diffusion. I, II, III and IV corresponds to the border neurons (periodic border conditions are not shown). B – adjacency matrix $\boldsymbol{D}$ of the PY cell location in the network in A, white square – connection (1), black square – no connection (0).

Thereby inserting equation (3) into (1) and using the border conditions, equation (2) we write down the discrete approximation for reaction-diffusion equation describing the extracellular potassium concentration:

$$\frac{dK^{+}_{OUT}}{dt} = \frac{k_K}{Fd}(IK_{\Sigma} + I^{NaK}_{pump} - I_{KCC2}) + G$$
$$+\frac{\varepsilon}{\Delta x^2}(K^{+}_{OUT(i+1,j)} + K^{+}_{OUT(i-1,j)} + K^{+}_{OUT(i,j+1)} + K^{+}_{OUT(i,j-1)} - 4K^{+}_{OUT(i,j)}) \quad (4)$$

Using adjacency matrix $\boldsymbol{D}$ for the neural network, Fig.II-13B, we rewrite this expression for the *i-th* neuron:

$$\frac{dK^{(i)}_{OUT}}{dt} = \frac{k_K}{Fd}(IK^{(i)}_{\Sigma} + I^{NaK(i)}_{pump} - I^{(i)}_{KCC2}) + G + \frac{\varepsilon}{\Delta x^2}(\sum_{k=1}^{N^2} D_{ik}K^{(k)}_{OUT} - 4K^{(i)}_{OUT}) \quad (5)$$

The last term corresponds to potassium diffusion between the pyramidal cells in the network, where ε corresponds to the value of the diffusion coefficient and D_{ik} is the element from the unitary adjacency matrix $\boldsymbol{D}$, Fig.II-13B, describing the *i-th* pyramidal cell location in the network space, Fig.II-13A.

To simulate the network with extracellular potassium we add the term corresponding to the diffusion from the bath solution equal for all neurons in the network:

$$\frac{dK^{(i)}_{OUT}}{dt} = \frac{k_K}{Fd}(IK^{(i)}_{\Sigma} + I^{NaK(i)}_{pump} - I^{(i)}_{KCC2}) + G + \frac{\varepsilon}{\Delta x^2}(\sum_{k=1}^{N^2} D_{ik}K^{(k)}_{OUT} - 4K^{(i)}_{OUT})$$

$$+\frac{\varepsilon_{bath}}{\Delta x_{slice}^2}(K_{bath} - K_{OUT}^{(i)}) \qquad (6)$$

It describes the diffusion of extracellular potassium from a large external reservoir to take into account the effect of high potassium concentration in the bath. ε_{bath} corresponds to the diffusion coefficient from the bath and x_{slice} is the depth of neurons in the slice.

Diffusion parameters: $\varepsilon = 4 \cdot 10^{-6} cm^2 / s$, $\varepsilon_{bath} = 4 \cdot 10^{-7} cm^2 / s$, $\Delta x = 50 \mu m$, $\Delta x_{slice} = 200 \mu m$.

II.3.6 Local field potential model

The derivation of the LFP model is taken from (Chizhov and Rodrigues 2014) and adapted to the neural network. In order to construct a model of the extracellular potential measured on layered neural structures, we make the following assumptions: 1- the neurons are homogeneously distributed on a two-dimensional grid; 2 - only one-type (pyramidal) cells influence the extracellular potential (Bédard et al. 2004); 3 - the complexities of neuronal dendritic trees can be neglected and single equivalent dendrites are aligned in vertical direction; 4 - the extracellular potential changes are negligible for transmembrane potential calculations. Note that in this derivation only synaptic activities are included, i.e. no active ionic currents are considered and compartments are passive.

Distributed neuron model

We model a neuron as a passive cylindrical dendrite with the soma at one extreme, i.e. as a boundary condition. Therefore the neuron is considered a passive cable aligned along the vertical coordinate z, with soma at $z=0$ and the end of the dendrite at $z=L$ (Fig.II-14A). Synaptic currents input into the soma, I_{syn}^{s}, and at the end of the dendrite, I_{syn}^{d}. The cable equation for the membrane potential $V(t,z)$ along the distributed model neuron is

$$\frac{1}{2\pi a}\frac{\partial}{\partial z}\left(\frac{1}{r_i}\frac{\partial V}{\partial z}\right)=j_m(z,t), \qquad (1)$$

where a is the radius of the dendrite, r_i is the specific intracellular resistivity. The transmembrane current $j_m(t,z)$ is a sum of a leakage and capacity terms, i.e.

$$j_m(z,t)=C\frac{\partial V}{\partial t}+g_L V, \qquad (2)$$

where g_L is the specific leak conductance, C is the specific capacitance. The voltage $V(z,t)$ is assumed to be measured from the resting level.

Under current clamp mode boundary conditions at the soma take the following form:

$$\left.\frac{1}{r_i}\frac{\partial V}{\partial z}\right|_{z=0}=\left(C\frac{dU}{dt}+g_L U\right)S^{soma}\equiv J_m^{s}(t), \qquad (3)$$

where we use the notation $U(t) \equiv V(t,0)$ for the measurable somatic voltage; J_m^s is the total current flowing through somatic membrane; S^{soma} is the somatic membrane area. At the end of the dendrite boundary conditions take the form:

$$\frac{1}{r_i}\frac{\partial V}{\partial z}\bigg|_{z=L} = I_{syn}^d. \qquad (4)$$

Extracellular field potential

Note from Equation (3) that the total transmembrane current J_m^s in one-compartment models consisting of only somas is always zero. Because J_m^s is the source that determines LFP, the one-compartment consideration leads to 0 as an estimate of LFP. In order to get the next level approximation, we derive the LFP equation resulting from the DN model. Following the work of (Nicholson and Llinas 1971) we consider a cylindrical layer of radius a_1 (Fig.II-14A), where neurons are homogeneously distributed with the density p per cortical area, their dendrites are aligned along the radial coordinate z from 0 to *L*. Our goal is to estimate the extracellular potential $\varphi(t,z)$ at the axis of symmetry.

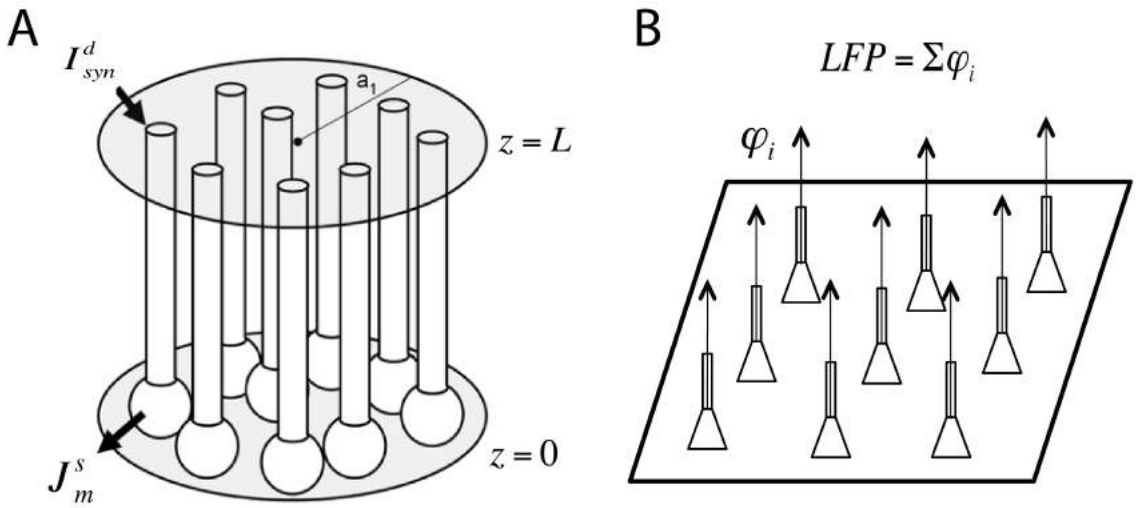

Figure II-14. Local field potential model
A – distributed neuron model where field potential is estimated on the central axis. B –field potential estimation from the neural network with neurons located on the grid.

Extracellular potential in a conductive medium is calculated as a superposition of current sources and described by the Poisson equation (Nicholson 1973):

$$\nabla \cdot (\sigma \nabla \varphi) = -J, \qquad (5)$$

where J is the average of the inward currents per unit volume; σ is the mean conductivity of extracellular medium, assumed to be a constant tensor. For a 1-d

source function $J(t,z)$ distributed in the cylinder, the solution of Equation (5) for the extracellular potential at $z=z_0$ is given by the convolution (Nicholson and Llinas 1971):

$$\varphi(t,z_0) = \int_0^L G(z_0,z)\,J(t,z)\,dz \qquad (6)$$

with the kernel that reflects the potential of a unit charge distributed on a disk with radius a_1:s

$$G(z_0,z) = \frac{1}{2\sigma}\left(\sqrt{(z_0-z)^2 + a_1^2} - |z_0 - z|\right) \qquad (7)$$

Assuming $a_1 >> L$, we get

$$G(z_0,z) \approx \frac{1}{2\sigma}\left(a_1 - |z_0 - z|\right) \qquad (7')$$

For the system of distributed parallel dendrites (i.e. DN model) with boundary sources at $z=0$ and $z=L$:

$$J(t,z) = 2\pi a p\, j_m(t,z) + p\, J_m^s(t)\,\delta(z-0) - p\, I_{syn}^d(t)\,\delta(z-L), \qquad (8)$$

After substitution (7') and (8) into (6), the potential φ becomes:

$$\varphi(t,z_0) = \frac{p}{2\sigma}\left(2\pi a \int_0^L j_m(t,z)\left(a_1 - |z_0 - z|\right)dz + J_m^s(t)(a_1 - z_0) - I_{syn}^d(t)\left(a_1 - |z_0 - L|\right)\right), \qquad (9)$$

Now we notice that the transmembrane current j_m may be calculated from (1). Thus substituting the first term in equation (1), in commas is rewritten and then integrated by parts with the boundary conditions defined in equations (3-4), as follows:

$$\begin{aligned}
2\pi a \int_0^L j_m(t,z)\left(a_1 - |z_0 - z|\right)dz &= \int_0^L \frac{1}{r_i}\frac{\partial^2 V}{\partial z^2}\left(a_1 - |z_0 - z|\right)dz \\
&= \frac{a_1 - |z_0 - z|}{r_i}\frac{\partial V}{\partial z}\bigg|_0^L - \frac{1}{r_i}\int_0^{\min(z_0,L)} \frac{\partial V}{\partial z}dz + \frac{1}{r_i}\int_{\min(z_0,L)}^L \frac{\partial V}{\partial z}dz \\
&= \left(a_1 - |z_0 - L|\right)I_{syn}^d(t) - \left(a_1 - z_0\right)J_m^s(t) - \frac{2V(t,\min(z_0,L)) - V(t,0) - V(t,L)}{r_i}
\end{aligned}$$

Inserting this expression into equation (9), $\varphi(t,z)$ is obtained as

$$\varphi(t,z_0) = \frac{p}{2\sigma r_i}\left(-2V(t,\min(z_0,L)) + V(t,0) + V(t,L)\right) \quad (10)$$

Considering the particular depths of somas (z_0=0) and above dendrites ($z_0 \geq L$), the somatic and dendritic extracellular potentials are

$$\phi(t,0) = -\phi(t,L) = \frac{p}{2\sigma r_i}(V(t,L) - V(t,0)) = \varphi_{DN} \quad (11)$$

Note that the extracellular potentials at the levels of somas and synapses are opposite in signs. As follows from equation (10), the distribution of φ_{DN} along *z*-axis is a linear combination of the signals.

In the discrete approximation the single neuron contribution to the LFP corresponds is approximated using phenomenological coefficient k.

$$\varphi = k[g_c^S(V_d - V_s)] \quad (12)$$

In case of neural network the total amount of LFP signal measured on the electrode is approximated by the linear sum of all dipoles φ generated by the network, Fig.II-14B:

$$LFP = \sum_{i=1}^{N} \varphi_i \quad (13)$$

This network LFP approximation is roughly consistent with the depth multi-electrode measurements (Sargsyan et al. 2001). It reveals the main intracellular term contributing to the LFP as a voltage difference between soma and dendrite, which is zero term in one-compartment models. This approximation is also consistent with the dipole LFP approximation from (Wendling et al. 2012, Buzsáki et al. 2012).

LFP parameter k is matched manually to approximate the amplitude of the experimental field potential. In all network simulations it is taken equal to $0.02 \mu A / mV$.

II.3.7 Seizure detection algorithm

In order to monitor the network state during simulations we developed simple algorithm for seizure detection. This algorithm scans the LFP spectrum with the time window of 5 second and estimates the amplitude of the major frequency on the power spectrum. If the amplitude of the major oscillation frequency is larger than threshold, the activity is classified as seizure. The values of threshold as well as time window are set manually to properly classify seizure activity based on visual introspection.

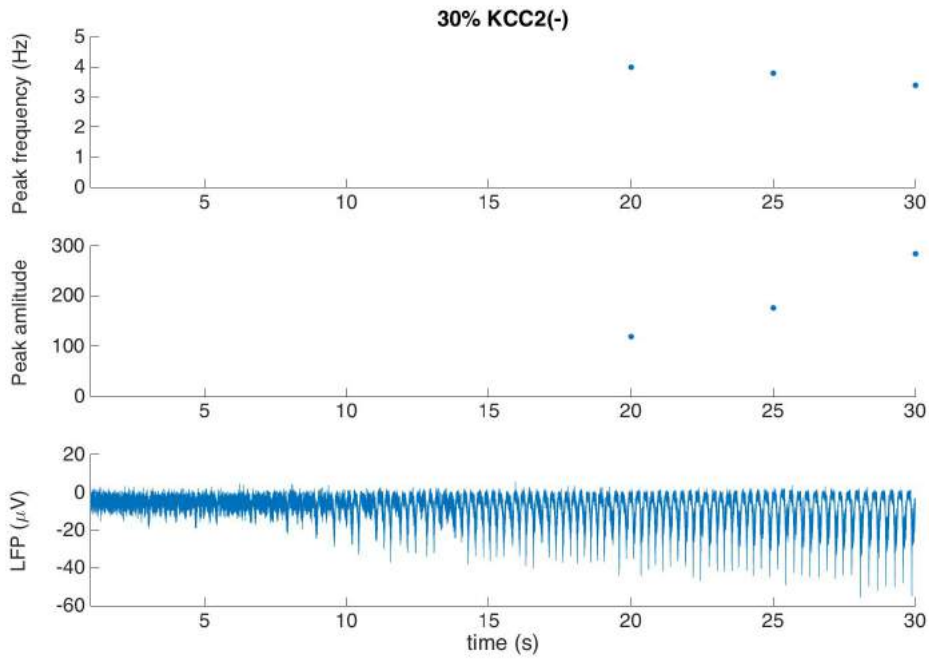

Figure II-15. Seizure detection algorithm
On the top and middle are present the frequency and value of maximal peak of oscillation frequency in the power spectrum (not shown) estimated with 5 second window. On the bottom is present the LFP generated by the network with extracellular potassium when seizure is initiated due to presence of 30% KCC2(-) cells.

To illustrate the results of the algorithm we apply it for the synthetic LFP generated by PY-IN network during seizure initiation, Fig.II-15. The blue dots on the top and middle traces show the moments when seizure was detected in the time series using 5 seconds window. The seizure threshold is set to 36. One could see that between 15 and 20 seconds the algorithm detects seizure activity. It shows that the peak amplitude is around 100 at 20 second, which means that seizure was initiated on the previous 5 seconds interval, i.e. between 15 and 20 seconds. One could see that there are also strong oscillations on the previous interval between 10 and 15 seconds, yet these oscillations do not have strong enough amplitude therefore they are not classified as seizure activity. We also

tested the algorithm to detect seizures in the experimental LFP recordings and found similar results, yet threshold and time window were tuned differently

II.4 Future directions

In this section we discuss the unsolved question in the present research and future directions for the next studies. In particular we discuss the following topics: KCC2 controversy, propagation of seizure activity, high frequency oscillations, mechanisms of seizure termination and links between biophysical and mean-field models.

KCC2 controversy

In the present model we investigated the consequences of KCC2 pathology in pyramidal cells of subiculum. It is known that the KCC2 might have both pro-epileptogenic and anti-epileptogenic action due to the extrusion of potassium ions into the extracellular space. Recent experimental work of Hamidi and Avoli (Hamidi and Avoli, 2015) showed that blockade of KCC2 reverses the activity from ictal to inter-ictal in the rat brain slices from piriform and entorhinal cortices. They proposed that down-regulation of KCC2 does not play the pro-epileptogenic role, yet it is a compensatory mechanism to prevent seizures. This interpretation contradicts the idea of pro-epileptic absence of KCC2 in the pyramidal cells found by Huberfeld and colleagues (Huberfeld et al. 2007, Huberfeld et al. 2011, Pallud et al. 2014).

The role of KCC2 for seizure generation is two-fold. At one side it regulates the baseline chloride concentration, that affects the efficiency of inhibition at the single cell level and on the other hand it contributes to the extracellular potassium concentration influencing the whole network. Both these mechanisms are important for maintaining the excitation-inhibition balance in the network, yet their role and significance might be different depending on the local circuit properties. One potential way to solve this controversy with the given model is to analyze the network behavior for different levels of KCC2 strength to find parameter regimes where KCC2 could be pro- or antiepileptic.

In our model of KCC2 we have taken into account the increase of extracellular potassium due to the KCC2 extrusion (Viitanen et al. 2010). Yet we have not found the significant increase of extracellular potassium due to KCC2 extrusion, consistently with (Doyon et al. 2011). The strength of KCC2 cotransporter in the model was motivated by measurements of GABA reversal potential in pyramidal cells (Fig.II-1). There are additional factors to be taken into account in a more detailed single neuron model such as surface of the pyramidal cell, amount of KCC2 expression in different parts of a neuron, location of GABA-A synapses and dendritic structure. We suggest that these specific details of neurons could play an important the role for determining the amount of extracellular potassium produced by KCC2. Therefore further experimental measurements of extracellular potassium combined with the detailed modeling are needed to properly explain consequences of KCC2 blockade.

Propagation of seizure activity

In our model of seizure initiation we restricted our analysis to the local random network without spatial connectivity. It was motivated by the fact that subiculum spatial connectivity is not known so well; yet the properties of a local circuitry are better estimated (Peng et al. 2014). As a drawback the proposed model does not allow to study the mechanisms of seizure propagation and spatiotemporal aspects of seizure dynamics.

Addition of the spatial extent to the model would help to test the hypothesis of extracellular potassium and intracellular chloride accumulation as factors contributing to seizure propagation. We speculate that intracellular chloride accumulation due to KCC2 pathology could be a candidate mechanism for failure of inhibitory restraints during seizure propagation in the cortex (Schevon et al. 2012, Trevelyan et al. 2007).

The spatiotemporal model could clarify the mechanisms inter-ictal and pre-ictal discharge propagation (Huberfeld et al. 2011). In particular could help to explain the delay between interneuron and pyramidal cell firing during the inter-ictal discharges (Cohen et al. 2002). In the recent computational works the mechanisms of seizure propagation have been studied in the topographically connected neural networks of leaky integrate-and-fire neurons (Hall and Kuhlmann 2013, Ursino and La Cara 2006). In these works the traveling and spiral waves were analyzed in response to the current stimulation. The authors speculated that these spatiotemporal activity patterns could play an important role for seizure propagation. We suggest that considering more biophysically realistic neurons with intrinsic bursting mechanisms would help to generate seizure-specific patterns of the neural activity allowing the detailed comparison with the LFP and Ca^{2+} imaging data.

High frequency oscillations

High frequency oscillations (HFO) or ripples are extracellularly recorded events occupying the frequency band of 8-200 Hz recorded extracellularly in normal hippocampus and parahippocampal structures. They are believed to reflect the inhibitory field potentials during the neural activity. These oscillations potentially represent the long-range synchronization of neuron clusters. HFO in the range of 250-600 Hz are considered to be pathological and are usually recorded in hippocampus of patients with temporal lobe epilepsy. Yet clear distinction between the normal and pathological activity could not be made based only on the frequency content of HFO, since the anatomical location also plays an important role (Engel et al. 2009).

The conclusion from unit and field potential recordings in rodents and humans is that fast ripples represent the neural activity during population spikes from clusters of abnormal synchronously bursting neurons in contrast to ripples representing field potentials of summated inhibitory post-synaptic potentials (Bragin et al. 2002). Despite the fact that HFO are definitely related to seizure dynamics and have an important prognostic value for seizure detection, their casual relation for seizure initiation is not direct (Quilichini et al. 2012).

In the proposed model we have not found HFO during transition to seizure activity. We hypothesize that it might be related to the fact that our model represents the local circuit, while spatially distinct neuron clusters are responsible for generation HFO (Bragin et al. 2002). We suggest that including the spatial structure into the network model would help to reproduce this activity.

Mechanisms of seizure termination

In this work we concentrated on the mechanisms of seizure initiation associated with chloride accumulation in the pyramidal cells. Yet our model could be extended to take into account the mechanisms of seizure termination. In theoretical studies has been proposed that dynamics of intracellular sodium Na^{+}_{IN} could play an important role for seizure termination (Krishnan and Bazhenov 2011, **CHAPTER I**). Recent imaging studies (Karus et al. 2015) found strong sodium accumulation in pyramidal cells during epileptoform activity suggesting the role of this ion for seizure termination. But additional research is needed to clarify the significance of this mechanism. Another pathways associated with seizure termination such as inactivation of Na^{+}-channels (Bazhenov et al. 2004), activation of Ca^{2+} and Na^{+} dependent potassium currents (Timofeev and Steriade 2004) or exhaustion of metabolic resources (Yamada et al. 2001, Kirchner et al. 2006) could also play an important role.

In some simulations we included the mechanism of intracellular sodium accumulation. We found periods of bursting and resting state activity in the pyramidal cells model with dynamic Na^{+}_{IN} and K^{+}_{OUT} concentrations similar to the results of (Barreto and Cressman 2011). Although in the network level we did not manage to find the regimes of network activity corresponding to recurrent seizures. We believe that additional parameter tuning could help to solve this problem in the next version of the model.

Biophysical and mean field models

Traditionally two approaches have been developed to describe neural activity. The mean field or neural mass models describe the behavior of large populations of neurons in terms of global variables and parameters such as population firing-rate, average synaptic gain etc. (Wilson and Cowan 1972,

Chizhov and Graham 2007) for a review see (Deco et al. 2008). This approach has the advantage that it uses smaller parameter set compared to the biophysical model. It allows to explicitly analyzing these models, which makes it easier to interpret. These mean field models have been successfully applied to study the neural activity during epilepsy (Wendling et al. 2002, Touboul et al. 2011, Bartolomei et al. 2014).

Despite advantages this approach such as mathematical simplicity and applicability to EEG and LFP signals, these models have serious drawbacks. The major problem is that they do not provide the detailed physiological interpretation of their parameters since they operate with the macroscopic variables. These macroscopic characteristics could be hardly translated into the level of neural networks and single neuron biophysics. It makes it hard to interpret the results of these models when searching for a particular pharmacological strategy against seizures.

On the other hand the biophysical single neuron and neural network models are specifically designed to study the mechanisms of pathology on the cellular level. However despite having the physiological interpretation, these models have very large parameter sets that does not allow using them to study the network behavior for all possible parameter combinations (Marder and Taylor, 2011).

To partially solve these questions (Naze et al. 2015) made an attempt to link the abstract mean-field model called epileptor (Jirsa et al. 2014) with the neural network approach. This problem has been partially solved for all-to-all connected network of Morris-Lecar and Hindmarch-Rose neurons, yet additional work is needed to move these models towards more biological realism.

We believe that mapping between neural mass and biophysical models would allow to restrict the parameter sets for biophysical models and to provide the physiological interpretation of the mean-field models. In particular we suggest that incorporating the slow processes of intracellular chloride accumulation into mean field description like epileptor would help to generalize the mechanisms of seizure initiation and propagation.

II.5 References

Barreto, E., & Cressman, J. R. (2011). Ion concentration dynamics as a mechanism for neuronal bursting. Journal of biological physics, 37(3), 361-373.

Bazhenov, M. et al. 2004. Potassium model for slow (2-3 Hz) in vivo neocortical paroxysmal oscillations. Journal of neurophysiology, 92(2), pp.1116–32.

Bazhenov, M., Timofeev, I., Steriade, M., & Sejnowski, T. J. (2004). Potassium model for slow (2-3 Hz) in vivo neocortical paroxysmal oscillations. Journal of neurophysiology, 92(2), 1116-1132.

Bédard, C., & Destexhe, A. (2009). Macroscopic models of local field potentials and the apparent 1/f noise in brain activity. Biophysical journal, 96(7), 2589-2603.

Bédard, C., Kröger, H. & Destexhe, A., 2004. Modeling extracellular field potentials and the frequency-filtering properties of extracellular space. Biophysical journal.

Beghi, E., Berg, A., Carpio, A., Forsgren, L., Hesdorffer, D. C., Hauser, W. A., ... & Tomson, T. (2005). Comment on epileptic seizures and epilepsy: definitions proposed by the International League Against Epilepsy (ILAE) and the International Bureau for Epilepsy (IBE). Epilepsia, 46(10), 1698-1699.

Ben-Ari, Y. (2002). Excitatory actions of GABA during development: the nature of the nurture. Nature Reviews Neuroscience, 3(9), 728-739.

Bragin, A., Mody, I., Wilson, C. L., & Engel, J. (2002). Local generation of fast ripples in epileptic brain. The Journal of neuroscience, 22(5), 2012-2021.

Brunel, N., & Wang, X. J. (2001). Effects of neuromodulation in a cortical network model of object working memory dominated by recurrent inhibition. Journal of computational neuroscience, 11(1), 63-85.

Buzsáki, G., Anastassiou, C. a & Koch, C., 2012. The origin of extracellular fields and currents--EEG, ECoG, LFP and spikes. Nature reviews. Neuroscience, 13(6), pp.407–20.

Buzsáki, G., Anastassiou, C. A., & Koch, C. (2012). The origin of extracellular fields and currents—EEG, ECoG, LFP and spikes. Nature reviews neuroscience, 13(6), 407-420.

Chizhov, A. V. (2002). Model of evoked activity of hippocampal neuron populations. Biophysics, 47(6), 1007-1015.

Chizhov, A. V., & Graham, L. J. (2007). Population model of hippocampal pyramidal neurons, linking a refractory density approach to conductance-based neurons. Physical Review E, 75(1), 011924.

Chizhov, A. V., Rodrigues S., Simple model relating extracellular potential to membrane currents of neuronal population, (2014) Proceedings of VIII Russian Neuroinformatics conference, 87-95.

Cohen, I., Navarro, V., Clemenceau, S., Baulac, M., & Miles, R. (2002). On the origin of interictal activity in human temporal lobe epilepsy in vitro. Science, 298(5597), 1418-1421.

Cressman Jr, J. R., Ullah, G., Ziburkus, J., Schiff, S. J., & Barreto, E. (2009). The influence of sodium and potassium dynamics on excitability, seizures, and the stability of persistent states: I. Single neuron dynamics. Journal of computational neuroscience, 26(2), 159-170.

de la Prida, L. M., Huberfeld, G., Cohen, I., & Miles, R. (2006). Threshold behavior in the initiation of hippocampal population bursts. Neuron, 49(1), 131-142.

Deco, G., Jirsa, V. K., Robinson, P. A., Breakspear, M., & Friston, K. (2008). The dynamic brain: from spiking neurons to neural masses and cortical fields. PLoS Comput. Biol, 4(8), e1000092.

Demont-Guignard, S., Benquet, P., Gerber, U., & Wendling, F. (2009). Analysis of intracerebral EEG recordings of epileptic spikes: insights from a neural network model. Biomedical Engineering, IEEE Transactions on, 56(12), 2782-2795.

Doyon, N. et al. 2011. Efficacy of synaptic inhibition depends on multiple, dynamically interacting mechanisms implicated in chloride homeostasis. PLoS computational biology, 7(9), p.e1002149.

Doyon, N., Prescott, S. A., Castonguay, A., Godin, A. G., Kröger, H., & De Koninck, Y. (2011). Efficacy of synaptic inhibition depends on multiple, dynamically interacting mechanisms implicated in chloride homeostasis. PLoS Comput. Biol, 7(9), e1002149.

Dulla, C. G., Dobelis, P., Pearson, T., Frenguelli, B. G., Staley, K. J., & Masino, S. A. (2005). Adenosine and ATP link P CO2 to cortical excitability via pH. Neuron, 48(6), 1011-1023.

Engel Jr, J., Bragin, A., Staba, R., & Mody, I. (2009). High-frequency oscillations: What is normal and what is not?. Epilepsia, 50(4), 598-604.

Fertziger, A. P., & Ranck, J. B. (1970). Potassium accumulation in interstitial space during epileptiform seizures. Experimental neurology, 26(3), 571-585.

Fisher, R. S., Pedley, T. A., & Prince, D. A. (1976). Kinetics of potassium movement in normal cortex. Brain research, 101(2), 223-237.

Florence, G., Dahlem, M. A., Almeida, A. C. G., Bassani, J. W., & Kurths, J. (2009). The role of extracellular potassium dynamics in the different stages of ictal bursting and spreading depression: a computational study. Journal of theoretical biology, 258(2), 219-228.

Fröhlich, F., & Bazhenov, M. (2006). Coexistence of tonic firing and bursting in cortical neurons. Physical Review E, 74(3), 031922.

Fröhlich, F., Bazhenov, M., & Sejnowski, T. J. (2008). Pathological effect of homeostatic synaptic scaling on network dynamics in diseases of the cortex. The Journal of Neuroscience, 28(7), 1709-1720.

Fröhlich, F., Bazhenov, M., Iragui-Madoz, V., & Sejnowski, T. J. (2008). Potassium dynamics in the epileptic cortex: new insights on an old topic. The Neuroscientist, 14(5), 422-433.

Fujiwara-Tsukamoto, Y., Isomura, Y., Imanishi, M., Ninomiya, T., Tsukada, M., Yanagawa, Y., ... & Takada, M. (2010). Prototypic seizure activity driven by mature hippocampal fast-spiking interneurons. The Journal of Neuroscience, 30(41), 13679-13689.

Fujiwara-Tsukamoto, Y., Isomura, Y., Imanishi, M., Fukai, T., & Takada, M. (2007). Distinct types of ionic modulation of GABA actions in pyramidal cells and interneurons during electrical

induction of hippocampal seizure-like network activity. European Journal of Neuroscience, 25(9), 2713-2725.

Glykys, J., Dzhala, V., Egawa, K., Balena, T., Saponjian, Y., Kuchibhotla, K. V., ... & Staley, K. J. (2014). Local impermeant anions establish the neuronal chloride concentration. Science, 343(6171), 670-675.

Gnatkovsky, V., Librizzi, L., Trombin, F., & de Curtis, M. (2008). Fast activity at seizure onset is mediated by inhibitory circuits in the entorhinal cortex in vitro. Annals of neurology, 64(6), 674-686.

Grafstein, B. (1956). Mechanism of spreading cortical depression. J Neurophysiol, 19(2), 154-171.

Hall, D., & Kuhlmann, L. (2013). Mechanisms of seizure propagation in 2-dimensional centre-surround recurrent networks. PloS one, 8(8), e71369.

Hamidi, S., & Avoli, M. (2015). KCC2 function modulates in vitro ictogenesis. Neurobiology of disease, 79, 51-58.

Hübel, N., & Dahlem, M. A. (2014). Dynamics from seconds to hours in Hodgkin-Huxley model with time-dependent ion concentrations and buffer reservoirs. PLoS computational biology, 10(12), e1003941.

Huberfeld, G. et al. 2007. Perturbed chloride homeostasis and GABAergic signaling in human temporal lobe epilepsy. The Journal of neuroscience : the official journal of the Society for Neuroscience, 27(37), pp.9866–73.

Huberfeld, G., De La Prida, L. M., Pallud, J., Cohen, I., Le Van Quyen, M., Adam, C., ... & Miles, R. (2011). Glutamatergic pre-ictal discharges emerge at the transition to seizure in human epilepsy. Nature neuroscience, 14(5), 627-634.

Huberfeld, G., Wittner, L., Clemenceau, S., Baulac, M., Kaila, K., Miles, R., & Rivera, C. (2007). Perturbed chloride homeostasis and GABAergic signaling in human temporal lobe epilepsy. The Journal of neuroscience, 27(37), 9866-9873.

Isomura, Y., Sugimoto, M., Fujiwara-Tsukamoto, Y., Yamamoto-Muraki, S., Yamada, J., & Fukuda, A. (2003). Synaptically activated Cl–accumulation responsible for depolarizing GABAergic responses in mature hippocampal neurons. Journal of Neurophysiology, 90(4), 2752-2756.

Jackson, J., Goutagny, R., & Williams, S. (2011). Fast and slow gamma rhythms are intrinsically and independently generated in the subiculum. The Journal of Neuroscience, 31(34), 12104-12117.

Jedlicka, P., Deller, T., Gutkin, B. S., & Backus, K. H. (2011). Activity-dependent intracellular chloride accumulation and diffusion controls GABAA receptor-mediated synaptic transmission. Hippocampus, 21(8), 885-898.

Jirsa, V. K., Stacey, W. C., Quilichini, P. P., Ivanov, A. I., & Bernard, C. (2014). On the nature of seizure dynamics. Brain, 137(8), 2210-2230.

Jung, H.Y., Staff, N.P. & Spruston, N., 2001. Action potential bursting in subicular pyramidal neurons is driven by a calcium tail current. The Journal of neuroscience : the official journal of the Society for Neuroscience, 21(10), pp.3312–3321.

Kager, H., Wadman, W. J., & Somjen, G. G. (2000). Simulated seizures and spreading depression in a neuron model incorporating interstitial space and ion concentrations. Journal of neurophysiology, 84(1), 495-512.

Kager, H., Wadman, W. J., & Somjen, G. G. (2007). Seizure-like afterdischarges simulated in a model neuron. Journal of computational neuroscience, 22(2), 105-128.

Karus, C., Mondragão, M. A., Ziemens, D., & Rose, C. R. (2015). Astrocytes restrict discharge duration and neuronal sodium loads during recurrent network activity. Glia, 63(6), 936-957.

Khalilov, I., Dzhala, V., Ben-Ari, Y., & Khazipov, R. (1999). Dual role of GABA in the neonatal rat hippocampus. Developmental neuroscience, 21(3-5), 310-319.

Kirchner, A., Velíšková, J., & Velíšek, L. (2006). Differential effects of low glucose concentrations on seizures and epileptiform activity in vivo and in vitro. European Journal of Neuroscience, 23(6), 1512-1522.

Kraio, R. P., & Nicholson, C. (1978). Extracellular ionic variations during spreading depression. Neuroscience, 3(11), 1045-1059.

Kraio, R. P., & Nicholson, C. (1978). Extracellular ionic variations during spreading depression. Neuroscience, 3(11), 1045-1059.

Krishnan, G. P., & Bazhenov, M. (2011). Ionic dynamics mediate spontaneous termination of seizures and postictal depression state. The Journal of Neuroscience, 31(24), 8870-8882.

Krishnan, G.P. & Bazhenov, M., 2011. Ionic dynamics mediate spontaneous termination of seizures and postictal depression state. The Journal of neuroscience : the official journal of the Society for Neuroscience, 31(24), pp.8870–82.

Llinas, R., & Nicholson, C. (1971). Electrophysiological properties of dendrites and somata in alligator Purkinje cells. Journal of Neurophysiology, 34(4), 532-551.

Lytton, W. W. (2008). Computer modelling of epilepsy. Nature Reviews Neuroscience, 9(8), 626-637.

Mainen, Z. F., & Sejnowski, T. J. (1996). Influence of dendritic structure on firing pattern in model neocortical neurons. Nature, 382(6589), 363-366.

Mainen, Z. F., & Sejnowski, T. J. (1996). Influence of dendritic structure on firing pattern in model neocortical neurons. Nature, 382(6589), 363-366.

Marder, E., & Taylor, A. L. (2011). Multiple models to capture the variability in biological neurons and networks. Nature neuroscience, 14(2), 133-138.

Naze, S., Bernard, C., & Jirsa, V. (2015). Computational Modeling of Seizure Dynamics Using Coupled Neuronal Networks: Factors Shaping Epileptiform Activity.

Nicholson, C. (1973). Theoretical analysis of field potentials in anisotropic ensembles of neuronal elements. IEEE Trans Biomed Eng, 20(4), 278-88.

Nicholson, C., & Llinas, R. (1971). Field potentials in the alligator cerebellum and theory of their relationship to Purkinje cell dendritic spikes. Journal of neurophysiology, 34(4), 509-531.

Pallud, J., Le Van Quyen, M., Bielle, F., Pellegrino, C., Varlet, P., Labussiere, M., ... & Huberfeld, G. (2014). Cortical GABAergic excitation contributes to epileptic activities around human glioma. Science translational medicine, 6(244), 244ra89-244ra89.

Payne, J. a et al. 2003. Cation-chloride cotransporters in neuronal communication, development and trauma. Trends in neurosciences, 26(4), pp.199–206.

Payne, J. a, 1997. Functional characterization of the neuronal-specific K-Cl cotransporter: implications for [K+]o regulation. The American journal of physiology, 273(5 Pt 1), pp.C1516–25.

Payne, J. A. (1997). Functional characterization of the neuronal-specific K-Cl cotransporter: implications for [K+] oregulation. American Journal of Physiology-Cell Physiology, 273(5), C1516-C1525.

Payne, J. A., Rivera, C., Voipio, J., & Kaila, K. (2003). Cation–chloride cotransporters in neuronal communication, development and trauma. Trends in neurosciences, 26(4), 199-206.

Peng, Y., Boehm, C., Maier, N., Schmitz, D., & Geiger, J. (2014, March). Functional subnetwork structure in the subiculum of mice. In ACTA PHYSIOLOGICA (Vol. 210, pp. 70-70). 111 RIVER ST, HOBOKEN 07030-5774, NJ USA: WILEY-BLACKWELL.

Proix, T., Bartolomei, F., Chauvel, P., Bernard, C., & Jirsa, V. K. (2014). Permittivity coupling across brain regions determines seizure recruitment in partial epilepsy. The Journal of Neuroscience, 34(45), 15009-15021.

Quilichini, P. P., Le Van Quyen, M., Ivanov, A., Turner, D. A., Carabalona, A., Gozlan, H., ... & Bernard, C. (2012). Hub GABA neurons mediate gamma-frequency oscillations at ictal-like event onset in the immature hippocampus.Neuron, 74(1), 57-64.

Renart, A., Moreno-Bote, R., Wang, X. J., & Parga, N. (2007). Mean-driven and fluctuation-driven persistent activity in recurrent networks. Neural computation, 19(1), 1-46.

Sargsyan, A. R., Papatheodoropoulos, C., & Kostopoulos, G. K. (2001). Modeling of evoked field potentials in hippocampal CA1 area describes their dependence on NMDA and GABA receptors. Journal of neuroscience methods, 104(2), 143-153.

Schevon, C. A., Weiss, S. A., McKhann Jr, G., Goodman, R. R., Yuste, R., Emerson, R. G., & Trevelyan, A. J. (2012). Evidence of an inhibitory restraint of seizure activity in humans. Nature communications, 3, 1060.

Schuchmann, S., Vanhatalo, S., & Kaila, K. (2009). Neurobiological and physiological mechanisms of fever-related epileptiform syndromes. Brain and development, 31(5), 378-382.

Staff, N. P., Jung, H. Y., Thiagarajan, T., Yao, M., & Spruston, N. (2000). Resting and active properties of pyramidal neurons in subiculum and CA1 of rat hippocampus. Journal of Neurophysiology, 84(5), 2398-2408.

Staff, N.P. et al. 2000. Resting and active properties of pyramidal neurons in subiculum and CA1 of rat hippocampus. Journal of neurophysiology, 84(5), pp.2398–2408.

Stanford, I. M., Traub, R. D., & Jefferys, J. G. (1998). Limbic gamma rhythms. II. Synaptic and intrinsic mechanisms underlying spike doublets in oscillating subicular neurons. Journal of neurophysiology, 80(1), 162-171.

Timofeev, I., & Steriade, M. (2004). Neocortical seizures: initiation, development and cessation. Neuroscience, 123(2), 299-336.

Tolner, E. A., Hochman, D. W., Hassinen, P., Otáhal, J., Gaily, E., Haglund, M. M., ... & Kaila, K. (2011). Five percent CO2 is a potent, fast-acting inhalation anticonvulsant. Epilepsia, 52(1), 104-114.

Touboul, J., Wendling, F., Chauvel, P., & Faugeras, O. (2011). Neural mass activity, bifurcations, and epilepsy. Neural computation, 23(12), 3232-3286.

Traub, R. D., Miles, R. I. C. H. A. R. D., & Wong, R. K. (1987). Models of synchronized hippocampal bursts in the presence of inhibition. I. Single population events. Journal of neurophysiology, 58(4), 739-751.

Trevelyan, A. J., Sussillo, D., & Yuste, R. (2007). Feedforward inhibition contributes to the control of epileptiform propagation speed. The Journal of neuroscience, 27(13), 3383-3387.
Ullah, G., & Schiff, S. J. (2009). Models of epilepsy. Scholarpedia, 4(7), 1409.

Ullah, G., Cressman Jr, J. R., Barreto, E., & Schiff, S. J. (2009). The influence of sodium and potassium dynamics on excitability, seizures, and the stability of persistent states: II. Network and glial dynamics. Journal of computational neuroscience, 26(2), 171-183.

Ursino, M., & La Cara, G. E. (2006). Travelling waves and EEG patterns during epileptic seizure: analysis with an integrate-and-fire neural network. Journal of theoretical biology, 242(1), 171-187.

Viitanen, T., Ruusuvuori, E., Kaila, K., & Voipio, J. (2010). The K+–Cl− cotransporter KCC2 promotes GABAergic excitation in the mature rat hippocampus. The Journal of physiology, 588(9), 1527-1540.

Volman, V., Ben-Jacob, E., & Levine, H. (2007). The astrocyte as a gatekeeper of synaptic information transfer. Neural computation, 19(2), 303-326.

Wei, Y., Ullah, G., & Schiff, S. J. (2014). Unification of neuronal spikes, seizures, and spreading depression. The Journal of Neuroscience, 34(35), 11733-11743.

Wendling, F., Bartolomei, F., Bellanger, J. J., & Chauvel, P. (2002). Epileptic fast activity can be explained by a model of impaired GABAergic dendritic inhibition.European Journal of Neuroscience, 15(9), 1499-1508.

Wendling, F., Bartolomei, F., Mina, F., Huneau, C., & Benquet, P. (2012). Interictal spikes, fast ripples and seizures in partial epilepsies–combining multi-level computational models with experimental data. European Journal of Neuroscience, 36(2), 2164-2177.

Whittington, M. A., Traub, R. D., Kopell, N., Ermentrout, B., & Buhl, E. H. (2000). Inhibition-based rhythms: experimental and mathematical observations on network dynamics. International journal of psychophysiology, 38(3), 315-336.

Wilson, H. R., & Cowan, J. D. (1972). Excitatory and inhibitory interactions in localized populations of model neurons. Biophysical journal, 12(1), 1.

Yamada, K., Ji, J. J., Yuan, H., Miki, T., Sato, S., Horimoto, N., ... & Inagaki, N. (2001). Protective role of ATP-sensitive potassium channels in hypoxia-induced generalized seizure. Science, 292(5521), 1543-1546.

Zhang, Z. J., Valiante, T. A., & Carlen, P. L. (2011). Transition to seizure: from “macro”-to “micro”-mysteries. Epilepsy research, 97(3), 290-299.

CHAPTER III
NOISE-INDUCED PHENOMENA IN SINGLE NEURONS

III.1 Introduction

This chapter is a review of the neural mechanisms associated with the stochastic processes present in the nervous system. Since this theme is a broad topic in neuroscience, we will concentrate on the role of noise in single neuron dynamics and computation. We will describe the classical models of neural noise sources, mechanisms of stochastic resonance, and a recently found phenomenon, the inverse stochastic resonance, which appears in models of single neurons and networks.

The brain is noisy due to various internal and external factors (Ermentrout et al. 2008). For example, if we measure the single cell activity in the MT area of the visual cortex in response to the same moving dot stimuli, we will see that the responses of cells are highly variable across the experimental trials (Shadlen and Newsome, 1998). Such variability is a common feature of cortical activity (Destexhe et al. 2003). This variability strictly contrasts with artificial systems like computers, where moving of a mouse would lead to the same cursor movement with almost 100% reliability. If computers were as reliable as neural systems, it would be impossible to use them for any computation. In contrast, the variability in the nervous system seems to be its immanent property (London et al. 2010).

Usually noise is considered to be an unwanted property that precludes the transmission of information. Neural systems should get rid of noise using multiple strategies, while recent research has established that noise could be also beneficial for detecting weak periodic signals via stochastic resonance effect (Wiesenfeld and Moss 1995). In essence stochastic resonance (SR) is the phenomenon by which the addition of noise allows the system to become entrained into periodic oscillations, which are not possible without such a stochastic input. This phenomenon is well known in a wide range of physical systems, while SR was first proposed to explain the Earth's ice ages (Benzi et al. 1982, Benzi et al. 1999). In these pioneer works they proposed the general mechanism for how weather perturbations could be amplified by periodic fluctuations of the environment and lead to ice age epochs. SR has also been found in neural systems such as the crayfish mechanoreceptor (Douglass et al. 1993) and in realistic models of neocortical pyramidal cells (Rudolph and Destexhe, 2001).

Another phenomenon related to SR that has been recently identified is the so-called inverse stochastic resonance (ISR). This phenomenon lies in the fact that addition of noise into the system prevents the generation of periodic oscillations, making it inverse to SR. While this phenomenon has been found so far in single neuron models (Gutkin and Tuckwell, 2009) and in small networks

(Tuckwell et al. 2009), the experimental evidence for this effect has not been presented yet.

III.2 Neural noise sources

The nervous system possesses many different forms of noise. At the single neuron level, it is usually the result of spontaneous mediator release, thermal noise, stochastic channel opening, and irregular synaptic activity (Softky and Koch 1993, Kandel et al. 2000). All these noise sources lead to high fluctuations in the membrane potentials of principal neurons. It has been shown that, in pyramidal cells of the visual cortex, up to 80% of noise fluctuations could be explained by the synaptic noise generated by excitatory and inhibitory conductances *in vivo* (Paré et al. 1998, Bower, 2013). How could neurons integrate the synaptic input in such noisy conditions is a problem that has been identified since early studies (Barrett and Crill 1974).

Several experimental preparations have shown that cortical neurons are always entrained into generation of irregular activity even without the presentation of any sensory stimulation (for a review, see El Boustani et al. 2007). This phenomenon could play an important role for information processing of natural stimuli in different sensory modalities. From an anatomical point of view, pyramidal cells receive thousands of synaptic inputs from other neurons, and these inputs lead to high fluctuations in the membrane potentials of neurons (Destexhe et al. 2003). Since neurons receive both excitation and inhibition from the network, the neural activity should be balanced at the single neuron level (Okun and Lampl, 2009). In the pioneer work of Vreeswijk and Sompolinsky (Vreeswijk and Sompolinsky 1998) it was showed theoretically that such a balance between excitation and inhibition could naturally emerge in large networks of excitatory and inhibitory neurons coupled by sparse synapses. This finding allowed to explain single neuron voltage fluctuations, asynchronous firing, and balanced input to neurons, Fig.III-1A, B. Notably, asynchronous activity in balanced networks does not require the addition of noise to generate the stochastic spike trains. The asynchronous state in these neural networks results from the nature of chaotic dynamics.

Later works have proposed that cortical pyramidal cells operate in a high-conductance regime, characterized by large excitatory and inhibitory conductances (Destexhe et al. 2003). They discovered that pyramidal cells in cat neocortex operate in inhibition-dominated regime in awake and sleeping states (Rudolph et al. 2007). In this regime, inhibitory conductances provide the largest contribution to membrane potential fluctuations, and spiking is possible only if inhibition is reduced, because that causes an increase of

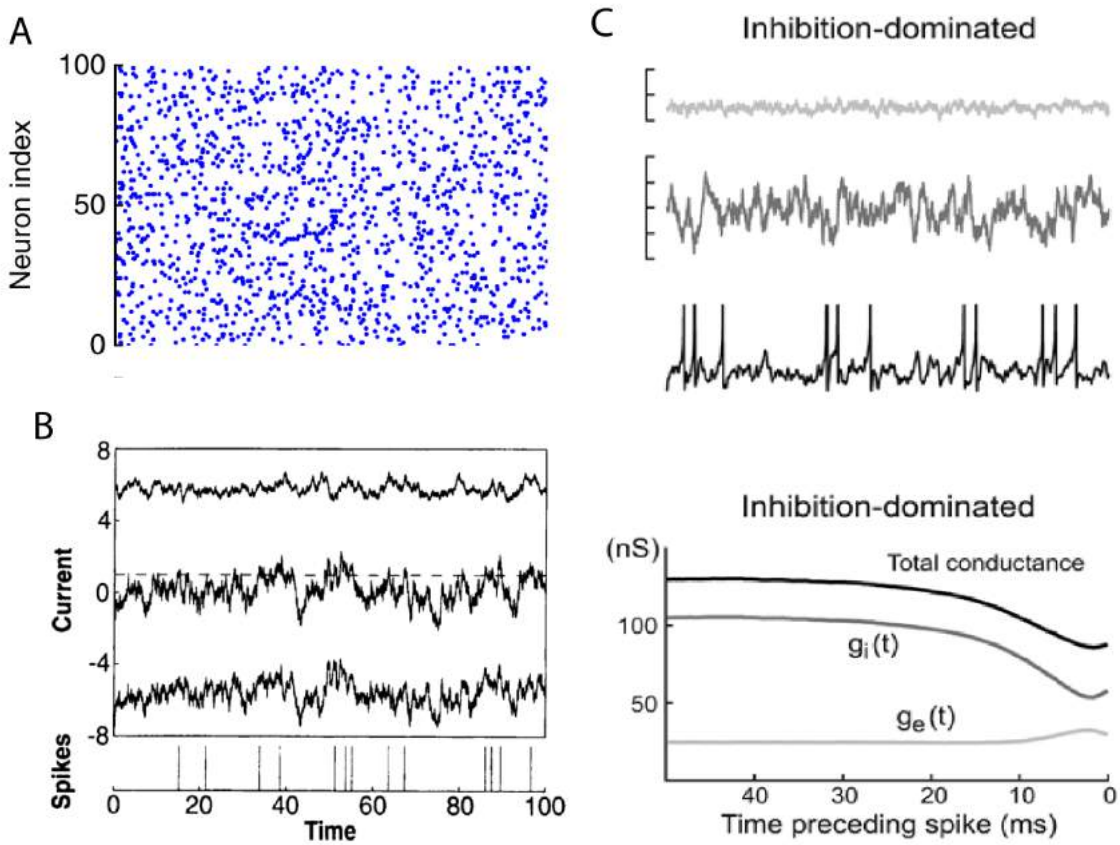

Figure III-1. Asynchronous and high conductance state in the neural network models
A – raster plot of a network of 100 representative neurons from 10000 neural network in the asynchronous state, adapted from (Ostojic, 2014). B – excitatory (positive) and inhibitory (negative) current and their sum (middle) received by the representative neuron from in the network in the balanced state. At the bottom the characteristic spike train is shown. Figure adapted from (van Vreeswijk and Sompolinsky, 1996). C – excitatory (top) and inhibitory (bottom) conductances received by the neuron in the 10000 neuron network with inhibition-dominated regime. Bottom – the corresponding increase of synaptic conductances and their sum during spike generation. Adapted from (El Boustani et al. 2007).

synaptic excitation, Fig.III-1 C. The authors found that this regime could be well reproduced in models of large networks generating self-sustained irregular states (El Boustani et al. 2007). These results suggested that most of the spikes in the neocortex are the result of recurrent network activity, and not directly evoked by external stimuli (Destexhe and Rudolph-Lilith 2012).

Balanced networks (Vreeswijk and Sompolinsky 1998) and networks operating at a high-conductance state (El Boustani et al. 2007) showed that synaptic noise in single neurons is not a side effect of neural dynamics, but an emerging (network) phenomenon in the nervous system. Since most of the membrane potential fluctuations are the result of noisy input from the network, they can be reasonably approximated by a stochastic process (Bower 2013). Stochastic inputs into the neuron could be beneficial for single neuron computation. It has been shown that synaptic noise could lead to increased responsiveness to the subthreshold inputs (Hô and Destexhe 2000), make the synapses location-independent (Rudolph and Destexhe 2003), increase temporal processing for coincidence detection (Softky and Koch 1993, Destexhe et al. 2003), modulate single neuron intrinsic properties (Wolfart et al. 2005), and improve the reliability of spike trains (Mainen and Sejnowski 1995). Various consequences of synaptic noise are well summarized in (Destexhe and Rudolph-Lilith 2012, Bower, 2013). In the next sections we will specifically concentrate on the effect that SR and ISR has on single neurons.

III.3 Stochastic resonance

The term SR was initially introduced in the context of statistical physics (Benzi et al. 1982) , but it quickly received a lot of interest in biological fields. Classical SR is observed when noise is added to the system allowing the input signal to be detected in the output by looking at the signal-no-noise (SNR) ratio.

In single neurons, SR has been studied in different animals and various parts of the nervous system. SR been found in multimodal neurons of the shark sensory system (Braun et al. 1994) and it has been shown to facilitate the processing of information about temperature and electrical fields. SR has also been found in the auditory system of crickets and shown to allow auditory neurons selective to frequencies centered at 23Hz to efficiently process information about possible predators, Fig.III-2A. In an experiment by Levin and Miller (1996) the addition of white noise to a periodic stimulus lead to the SNR peak measured on the power spectrum, Fig.III-2B.

Cortical neurons are definitely different from neurons in sensory systems (Douglass et al. 1993, Braun et al. 1994, Levin and Miller, 1996). In cortical cells, “noise” received by neurons is not external, but generated by the network itself. Due to the complex synaptic organization of the mammalian neocortex, it is not feasible yet to directly measure SR in single neurons during *in vivo* cortical

processing. For this reason, a realistic model of neocortical pyramidal cell and synaptic input has been proposed to explain SR (Rudolph and Destexhe 2001). The neuron in this model receives synaptic input from thousands of realistic conductance-based synapses on the dendritic tree and soma and the periodic synaptic input, Fig.III-2C. These synapses are activated by the Poisson statistics, which gives rise to noisy synaptic input. Depending on the amount of synaptic noise, the periodic input is efficiently amplified, such that the number of emitted spikes during the up-phase of the oscillation increases with respect to the noise-free case (Fig.III-2 D).

One could see that SR phenomenon is present in neurons, yet whether it has the functional role should depend on the particular system. Choosing the proper SNR metric is indeed crucial, since it implies a particular computation performed by neurons that is not always precisely defined in neural systems (McDonnell and Ward 2011). The notion of SNR came from artificial systems and it is not clear how well it could be applied for biological computations. Usually the power spectrum of the output signal is used to locate the resonance, and then the SNR is computed for different noise variances. Noise can be considered harmful for particular computations but beneficial for others, therefore the definition of noise and signal in single neurons should be carefully chosen.

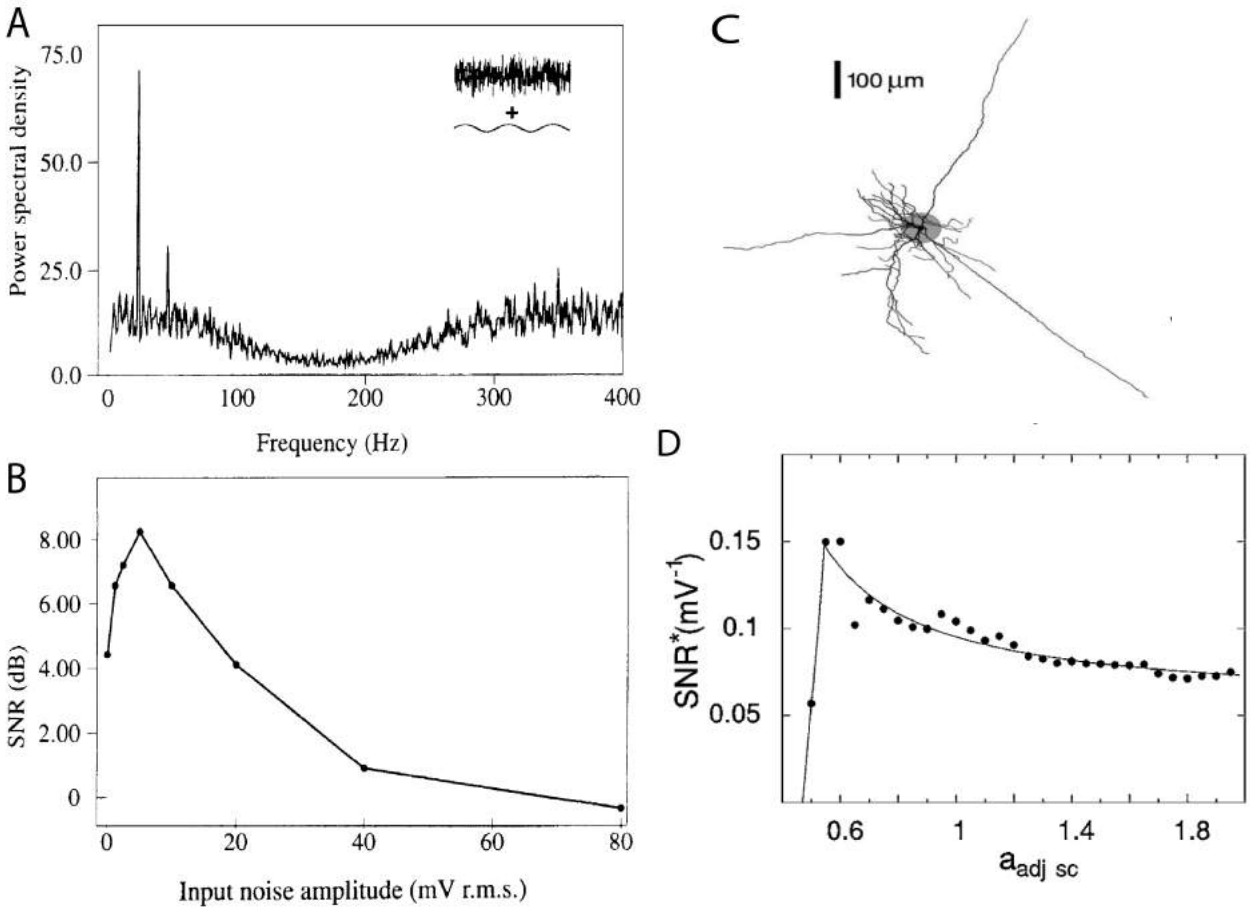

Figure III-2. Stochastic resonance of single neurons
A – power spectrum calculated for a spike train of a neuron in the cricket auditory system in response to stimulation of a 23 Hz sine wave signal with superimposed white noise stimuli (inset). B – signal-to-noise ratio (SNR) calculated as a peak on the power spectrum from A for different noise variances. Panels A and B are adapted from (Levin and Miller 1996). C – single neuron model of the pyramidal cell from cat visual cortex V1 (Rudolph and Destexhe 2001). Neuron receives 3376 GABA synapses on the whole dendritic tree and 16563 AMPA synapses located on the dendritic tree except at the somatic proximal region to mimic realistic cortical connectivity, shaded area. D – signal-to-noise ratio (SNR) calculated as the number of additional spikes generated by the neuron when stimulated in response to cosine stimuli and synaptic conductance noise. Panels C and D are adapted from (Rudolph and Destexhe 2001).

III.4 Inverse stochastic resonance

In the work of (Tuckwell and Gutkin 2008) it was shown that white noise of a particular variance could efficiently terminate firing in a simple network consisting of two quadratic integrate-and-fire neurons, Fig.III-3A. The reason for this phenomenon is that the phase space of the coupled system has a resting state attractor, even in the presence of input currents. Once the system trajectory moves into this attractor, Fig.III-3B, spiking activity stops and the network remains silent indefinitely. This effect constitutes the inhibition of neuronal spiking by noisy input. Interestingly the phenomenon in this two-neuron network was observed for both type I and type II neurons (Izhikevich 2007).

Later network models of working memory consisting of quadratic integrate-and-fire neurons showed that noise inhibition could help terminating pathologic memories due to ISR (Dipoppa and Gutkin 2013). Similar effects have been discovered in the classical Hodgkin-Huxley (HH) model (Gutkin and Tuckwell, 2009, Uzuntarla et al. 2012). Gutkin and Tuckwell have found that when the neuron receives white noise stimuli, the model becomes efficiently inhibited for a particular noise variance, when the mean is near the subthreshould regime, Fig.III-3C. To quantify noise inhibition, they proposed to measure the number of spikes generated by the model in response to the current noise stimulation, Fig.III-3D. This curve has a characteristic dip, when noise variance is optimal for inhibition. It was proposed to call this effect the inverse stochastic resonance (ISR), since the input-output characteristic of the system, i.e., the number of spikes emitted as a function of the noise variance is reduced. It is inverse to the classic SR, in which the input-output characteristic is enhanced for a particular noise variance. In subsequent works, ISR was found to be sensitive to correlations in the noise input when modeled by an Ornstein-Uhlenbeck process (Guo 2011). Guo has found that increasing the correlation time constant alters the location of the minimum of the characteristic ISR curve by moving it towards larger noise variances, Fig.III-3D.

We should say that, in all aforementioned works, the ISR has been found in computational models of single neurons and networks, while there was no direct measurements of the ISR has been present in real neurons. On the other hand ISR requires specific parameter tuning for the noise variance and input mean. Despite the fact that it has been observed in the classical HH model, its relevance in real neurons is not clear, since the ISR requires specific input characteristics, while it has been observed that real single neurons do not seem to require detailed parameter tuning (Prinz et al. 2004, Marder and Taylor 2011). Thus, experimental evidence should be presented to confirm the existence of ISR and its relevance for neural computations. On the other hand the general mechanisms of ISR such as existence of two solutions

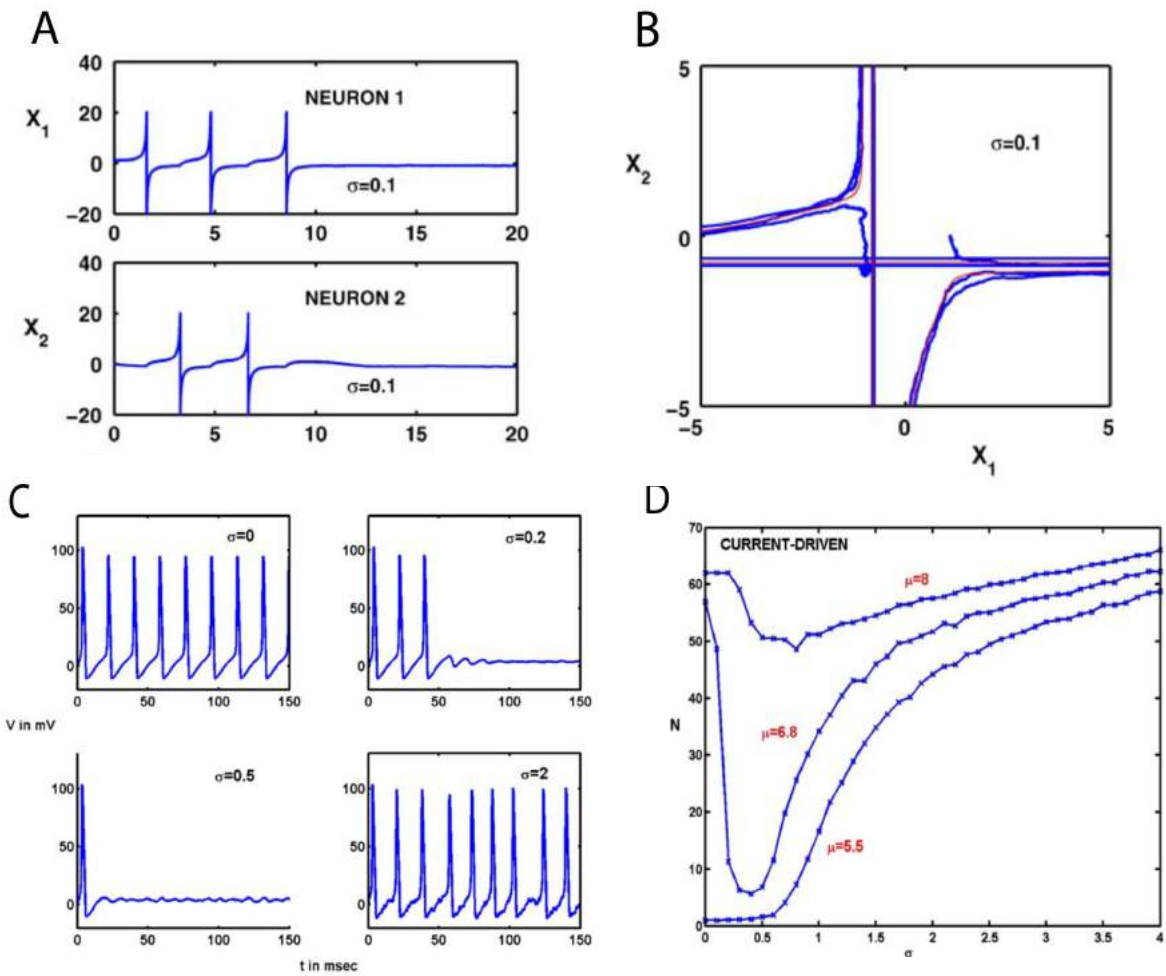

Figure III-3. Inverse stochastic resonance in single neuron and network models
A – time series of quadratic integrate-and-fire neurons in the network when both of them receive noise with the variance σ. B – trajectory of neurons in the phase space, central point corresponds to the resting state. Panels A and B are adapted from (Gutkin et al. 2008). C – Voltage trajectories of Hodgkin-Huxley (HH) model when stimulated by current noise with the mean $\mu = 6.8pA$ and different variances, $\sigma = 0.5pA$ corresponds to the noise variance optimal for inhibition. D – number of spikes N generated in the HH model during 1000 ms when it receives the white noise with the mean μ and noise variance σ. Panels C and D are adapted from (Gutkin and Tuckwell 2009).

for one parameter set, i.e. bistability suggest that it could be also found in other systems having similar properties.

III.5 Conclusions

In this brief review we covered the role of noise in single neuron and network models. Neural network models (van Vreeswijk and Sompolinsky 1996) and (El Boustani et al. 2007) provide the insights into how the synaptic noise received by neurons could be generated in the central nervous system. This noise could enhance the input-output properties of information transmission of single neurons via SR effect (Rudolph and Destexhe 2001). In the sensory nervous systems, SR could also play the role for detecting and amplifying the biologically relevant signals (Wiesenfeld and Moss 1995). Related to the SR phenomenon, ISR has been recently identified only in the models of single neurons (Gutkin and Tuckwell, 2009, Tuckwell and Jost 2010) and neural networks (Gutkin et al. 2008, Dipoppa and Gutkin 2013). In spite of its potential functional role, ISR has not been properly studied yet.

Identifying the constructive role of noise does not provide an answer for the question of why neural systems could take advantage of it (McDonnell and Ward 2011). One could use the evolutionary argument that noise is an unavoidable property of the environment, as well as an inherent ingredient of organisms, due to the various biophysical and biochemical constraints governing at the single cell and system levels (Tsimring 2014). We could therefore speculate that evolutionary pressure gave advantage to neural systems that could benefit from noise for useful computations, for example, favoring those single neurons properties that lead to better predator detection in the environment (Levin and Miller 1996).

In the next section we shall study the role of synaptic noise in cerebellar Purkinje cells. We will show that ISR takes place in the cerebellum and allows cerebellar neurons to optimally transmit information about stimuli.

III.6 References

Barrett, J. N., & Crill, W. E. (1974). Specific membrane properties of cat motoneurones. The Journal of physiology, 239(2), 301-324.

Benzi, R., Parisi, G., Sutera, A., & Vulpiani, A. (1982). Stochastic resonance in climatic change. Tellus, 34(1), 10-16.

Benzi, R., Sutera, a & Vulpiani, a, 1999. The mechanism of stochastic resonance. Journal of Physics A: Mathematical and General, 14(11), pp.L453–L457.

Bower, J. M. (2013). 20 years of computational neuroscience. Verlag: Springer.

Braun, H. a et al. 1994. Oscillation and noise determine signal transduction in shark multimodal sensory cells. Nature, 367(6460), pp.270–273.

Destexhe, A., & Rudolph-Lilith, M. (2012). Neuronal noise (Vol. 8). Springer Science & Business Media.

Destexhe, A., Rudolph, M. & Paré, D., 2003. The high-conductance state of neocortical neurons in vivo. Nature reviews. Neuroscience, 4(9), pp.739–51.

Dipoppa, M., & Gutkin, B. S. (2013). Flexible frequency control of cortical oscillations enables computations required for working memory. Proceedings of the National Academy of Sciences, 110(31), 12828-12833.

Douglass, J.K. et al. 1993. Noise enhancement of information transfer in crayfish mechanoreceptors by stochastic resonance. Nature, 365(6444), pp.337–340.

El Boustani, S. et al. 2007. Activated cortical states: Experiments, analyses and models. Journal of Physiology Paris, 101(1-3), pp.99–109.

Ermentrout, G.B., Galán, R.F. & Urban, N.N., 2008. Reliability, synchrony and noise. Trends in neurosciences, 31(8), pp.428–34.

Guo, D., 2011. Inhibition of rhythmic spiking by colored noise in neural systems. Cognitive neurodynamics, 5(3), pp.293–300.

Gutkin, B.S. & Tuckwell, H., 2009. The inhibition and modulation of rhythmic spiking by noise in the Hodgkin-Huxley neuron. , p.31907.

Hô, N. & Destexhe, a, 2000. Synaptic background activity enhances the responsiveness of neocortical pyramidal neurons. Journal of neurophysiology, 84(3), pp.1488–1496.

Izhikevich, E. M. (2007). Dynamical systems in neuroscience. MIT press.

Kandel, E. R., Schwartz, J. H., & Jessell, T. M. (Eds.). (2000). Principles of neural science (Vol. 4, pp. 1227-1246). New York: McGraw-Hill.

Levin, J.E. & Miller, J.P., 1996. Broadband neural encoding in the cricket cercal sensory system enhanced by stochastic resonance. Nature, 380(6570), pp.165–168.

London, M. et al. 2010. Sensitivity to perturbations in vivo implies high noise and suggests rate coding in cortex. Nature, 466(7302), pp.123–7.

Mainen, Z.F. & Sejnowski, T.J., 1995. Reliability of spike timing in neocortical neurons. Science (New York, N.Y.), 268(5216), pp.1503–1506.

Marder, E. & Taylor, A.L., 2011. Multiple models to capture the variability in biological neurons and networks. Nature neuroscience, 14(2), pp.133–138.

McDonnell, M.D. & Ward, L.M., 2011. The benefits of noise in neural systems: bridging theory and experiment. Nature reviews. Neuroscience, 12(7), pp.415–426.

Okun, M., & Lampl, I. (2009). Balance of excitation and inhibition. Scholarpedia,4(8), 7467.

Ostojic, S., 2014. Two types of asynchronous activity in networks of excitatory and inhibitory spiking neurons. Nature neuroscience, 17(4), pp.594–600.

Paré, D., Lang, E.J. & Destexhe, a, 1998. Inhibitory control of somatodendritic interactions underlying action potentials in neocortical pyramidal neurons in vivo: an intracellular and computational study. Neuroscience, 84(2), pp.377–402.

Prinz, A. a, Bucher, D. & Marder, E., 2004. Similar network activity from disparate circuit parameters. Nature neuroscience, 7(12), pp.1345–1352.

Rudolph, M. & Destexhe, a, 2001. Do neocortical pyramidal neurons display stochastic resonance? Journal of computational neuroscience, 11(1), pp.19–42.

Rudolph, M. & Destexhe, a, 2003. Characterization of subthreshold voltage fluctuations in neuronal membranes. Neural computation, 15(11), pp.2577–618.

Rudolph, M. et al. 2007. Inhibition determines membrane potential dynamics and controls action potential generation in awake and sleeping cat cortex. The Journal of neuroscience : the official journal of the Society for Neuroscience, 27(20), pp.5280–5290.

Shadlen, M.N. & Newsome, W.T., 1998. The variable discharge of cortical neurons: implications for connectivity, computation, and information coding. The Journal of neuroscience : the official journal of the Society for Neuroscience, 18(10), pp.3870–96.

Softky, W.R. & Koch, C., 1993. The highly irregular firing of cortical cells is inconsistent with temporal integration of random EPSPs. The Journal of neuroscience : the official journal of the Society for Neuroscience, 13(1), pp.334–350.

Tsimring, L. S. (2014). Noise in biology. Reports on Progress in Physics, 77(2), 026601.

Tuckwell, Æ.H.C., 2008. Random perturbations of spiking activity in a pair of coupled neurons. , pp.135–139.

Tuckwell, H.C. & Jost, J., 2010. Weak noise in neurons may powerfully inhibit the generation of repetitive spiking but not its propagation. PLoS computational biology, 6(5), p.e1000794.

Tuckwell, H.C., Jost, J. & Gutkin, B.S., 2009. Inhibition and modulation of rhythmic neuronal spiking by noise. , pp.1–8.

Uzuntarla, M., Cressman, J. R., Ozer, M., & Barreto, E. (2012). Inverse stochastic resonance induced by ion channel noise. BMC Neuroscience, 13(Suppl 1), P181.

Van Vreeswijk, C. & Sompolinsky, H., 1996. Chaos in neuronal networks with balanced excitatory and inhibitory activity. Science (New York, N.Y.), 274(5293), pp.1724–1726.

Vreeswijk, C. V., & Sompolinsky, H. (1998). Chaotic balanced state in a model of cortical circuits. Neural computation, 10(6), 1321-1371.

Wiesenfeld, K. & Moss, F., 1995. Stochastic Resonance and the Benefits of Noise. Nature, 373.

Wolfart, J. et al. 2005. Synaptic background activity controls spike transfer from thalamus to cortex. Nature neuroscience, 8(12), pp.1760–1767.

CHAPTER IV
INVERSE STOCHASTIC RESONANCE

IV.1 Introduction

This chapter mostly consists of a paper submitted to the PLOS Computational Biology. In the **IV.3 Detailed model description** we provide additional information about the model and algorithms being used in this study. In **IV.4 Future directions** section we discuss the unsolved problems raised in this research and potential ways to deal with them. The manuscript is written together with Sarah Rieubland and Arnd Roth, while Boris Gutkin and Michael Häuser added substantial corrections.

The overall aim of this work is to provide the theoretical explanation for effect of current noise inhibition, so-called inverse stochastic resonance (ISR) found in the Purkinje cells. It has been initially discovered in a small network of two quadratic integrate-and-fire neurons (Tuckwell 2008) and then in a classical Hodgkin-Huxley model (Gutkin et al. 2009). The name of this effect is derived from the classical stochastic resonance (SR) known in the nonlinear dynamics for a long time (Rouvas-Nicolis et al. 2007). In case of SR the input-output characteristic of the system shows the peak for particular noise variance, while in case of ISR there is dip of output firing-rate, therefore it is called inverse. The ISR has been studied theoretically, in (Gutkin et al. 2008, Tuckwell et al. 2009, Tuckwell and Jost 2010) yet it has not been shown that it is present in the nervous system and what functional role it could play.

According to the previous theoretical works it was predicted that the ISR should be present in dynamical systems with a subcritical Andronov-Hopf bifurcation that allows the bistability between resting and periodic spiking solutions. Initially the ISR has been found in 4-dimensional Hodgkin-Huxley system. Since it is not trivial to visualize the dynamics of more than two variables, we decided to use minimal system to describe the ISR. This motivated us to use the adaptive exponential integrate-and-fire model from (Brette and Gerstner 2005). It is two-dimensional that allows to apply the phase-plane analysis and posses the nonlinearity needed to describe the bifurcation between resting state and spiking (Touboul and Brette 2008). Apart from the theoretical tractability the parameters of this model could be extracted from the electrophysiological recordings (Badel et al. 2008). These two arguments motivated us to use this model to describe the ISR in the Purkinje cells.

IV.2 Article 2
Inverse stochastic resonance in cerebellar Purkinje cells

Anatoly Buchin[1,2 ¶ *], Sarah Rieubland[3¶], Michael Häusser[3], Boris Gutkin[1,4&] Arnd Roth[3&]

[1] Group for Neural Theory, Laboratoire des Neurosciences Cognitives, École Normale Supérieure, Paris, France
[2] Institute of Physics, Nanotechnology and Telecommunications, Peter the Great St. Petersburg Polytechnic University, Saint Petersburg, Russia
[3] Wolfson Institute for Biomedical Research, University College London, United Kingdom
[4] Center for Cognition and Decision Making, Department of Psychology, NRU Higher School of Economics, Moscow, Russia

¶ These authors contributed equally to this work
& These authors also contributed equally to this work

IV.2.1 Abstract

Purkinje neurons play an important role in cerebellar computation since their axons are the only projection from the cerebellar cortex to deeper cerebellar structures. They have complex internal dynamics, which allow them to fire spontaneously, display bistability and also to be involved in network phenomena such as high frequency oscillations and travelling waves. Purkinje cells exhibit type II excitability, which can be revealed by a discontinuity in their f-I curves. We show that this excitability mechanism allows Purkinje cells to be efficiently inhibited by noise of particular variance, a phenomenon known as inverse stochastic resonance (ISR). While ISR has been described in theoretical models of single neurons, here we provide the first experimental evidence for this effect. We find that an adaptive exponential integrate-and-fire model fitted to the basic Purkinje cell characteristics using a modified dynamic IV method displays ISR and bistability between the resting state and a repetitive activity limit cycle. ISR allows the Purkinje cell to operate in different functional regimes: the all-or-none toggle or the linear filter mode, depending on the variance of the synaptic input. We propose that synaptic noise allows Purkinje cells to quickly switch between these functional regimes. Using mutual information analysis, we demonstrate that ISR can lead to an optimal information transfer between the input and output spike train of the Purkinje cell. These results provide the first experimental evidence for ISR and suggest a functional role for ISR in cerebellar information processing.

IV.2.2 Author Summary

How individual neurons generate output spikes in response to the various combinations of inputs they receive is a central issue in contemporary neuroscience. Due to their large dendritic tree and complex intrinsic properties, cerebellar Purkinje cells are an important model system to study this input-output transformation. Here we examine how noise can change the parameters of this transformation. In experiments we found that spike generation in Purkinje cells can be efficiently inhibited by noise of a particular amplitude. This effect is called inverse stochastic resonance (ISR) and has previously been described only in theoretical models of single neurons. We explain the mechanism underlying ISR using a simple model fitted to match the properties of individual Purkinje cells, which were characterized experimentally. We found that ISR is present in cerebellar Purkinje cells when the mean input current is near threshold for spike generation. ISR can be explained by the co-existence of resting and spiking solutions of the simple model. Changing the input noise variance provides a flexible mechanism to change the lifetime of the resting and spiking states, suggesting a mechanism for a tunable filter with long time constants implemented by a Purkinje cell population in the cerebellum. Finally, ISR leads to optimal information transfer from the input to the output of a Purkinje cell.

IV.2.3 Introduction

Understanding the way neurons integrate synaptic inputs and provide appropriate outputs are crucial steps in the process of understanding neural circuits and relating their function to the function of specific brain areas. The cerebellar circuit is believed to be involved in ongoing motor control and motor learning, and an increasing amount of evidence suggests that it is the primary location of motor memories (Attwell et al. 2001). Purkinje neurons play a central role in the cerebellum, as they gather thousands of excitatory and inhibitory synaptic inputs from the molecular layer and provide the sole output of the cerebellar cortex. Describing and modeling the spiking response of Purkinje cells to synaptic inputs is therefore central to understanding cerebellar information processing.

Purkinje cells are spontaneously active even in the absence of synaptic input (Häusser and Clark 1997). It has been proposed that this notable intrinsic property is tightly linked to their type II excitability (Williams et al. 2002, Fernandez et al. 2007), which is manifested by the non-zero minimum firing frequency in response to tonic current injection, and the characteristic discontinuity in the frequency-current relationship. This property is thought to be due to voltage-gated ion channels, such as resurgent sodium currents (Khaliq et al. 2003) or hyperpolarization-activated currents (I_h) (Williams et al. 2002), which are active at rest. Such intrinsic mechanisms also underlie the ability of Purkinje cells to switch between spontaneous firing (up states) and quiet periods (down

states). These have been observed *in vitro* (Llinas and Sugimori 1980, Williams et al. 2002) and *in vivo* in anaesthetized (Loewenstein et al. 2005) and awake animals (Yartsev et al. 2009). The transition between these two states can be controlled by climbing fiber synaptic input (Loewenstein et al. 2005, Yartsev et al. 2009) or by molecular layer interneuron input (Oldfield et al. 2010). However, the presence of these up and down states in awake animals has been controversial (see Discussion).

While the existence of up and down states is a consequence of the intrinsic biophysics underlying the type II excitability of Purkinje cells (Loewenstein *et al.* 2005, Fernandez et al. 2007), we can nevertheless expect synaptic input, specifically random noise-like synaptic inputs, to play an important role in patterning such firing behavior. An interesting dynamical phenomenon, inverse stochastic resonance (ISR), has been described recently in persistently periodically firing model neurons: variance-dependent inhibition of spiking in response to noise stimulation, including purely excitatory noise (Tuckwell et al. 2009). The unique defining characteristic of ISR is that inhibition of spiking shows a nonlinear tuning with respect to input noise statistics, notably the variance. This phenomenon was first identified in computational models of bistable recurrent neural circuits, where the bistability was between a persistent spiking and quiescent states (Gutkin et al. 2009), Gutkin and Tuckwell 2009) and later shown in a single bistable neuron model (Gutkin et al. 2008). The key to ISR is the bistability between a steady state ("rest") and a periodic activity state ("spiking"), a characteristic of systems with sub-ctritical Andronov-Hopf bifurcations. Interestingly, ISR appears to be robust to changes in noise color (Guo 2011) and has also been demonstrated in spatially extended models of action potential propagation (Tuckwell and Jost 2010). Further analysis showed that ISR should be a generic phenomenon in dynamical systems with steady-state/limit cycle multi-stability, yet so far no direct experimental measurement of ISR has been reported (but see (Paydarfar et al. 2006) for hints of ISR in squid axons). Here we provide, to the best of our knowledge, the first experimental characterization of ISR in neuronal responses.

In this study we demonstrate ISR experimentally in Purkinje neurons and study its implications for cerebellar information processing. We find that Purkinje cells recorded in cerebellar slices show clear evidence for ISR. Their firing is reduced or can even be stopped in response to noisy current injection, with a nonlinear dependence of the firing rate on noise variance, which is characteristic for ISR. We further demonstrate that an empirically-based adaptive exponential integrate-and-fire model, quantitatively parameterized to fit Purkinje cell data using a modified dynamic IV method, reproduces both the bistability and ISR behavior of Purkinje cells. Finally, we show that the optimal noise variance for ISR also yields a local maximum in mutual information between the input and output spike train. Under these conditions, ISR leads to optimal inhibition of self-sustained spiking and thus provides the highest information transmission capacity for transient synaptic stimuli.

IV.2.4 Materials and Methods

Slice preparation and patch-clamp recording: 250-300 μm thick parasagittal slices of cerebellar cortex were made from 18-24 day old Sprague Dawley rats by standard techniques (Davie et al. 2006). Briefly, rats were anaesthetized with isofluorane for several minutes and decapitated in accordance with Home Office regulations. Slices were cut using a vibrating slicer (Leica VT1200S), after z-axis vibration was minimized to $< 0.1\,\mu m$. The slices were incubated in carbogen-saturated ACSF at 34°C for 30 min and then at room temperature for at least 30 min before use within four hours. Standard ACSF contained (in mM) 125 NaCl, 2.5 KCl, 2 $CaCl_2$, 1 $MgCl_2$, 25 $NaHC0_3$, 1.25 NaH_2PO_4 and 25 D-glucose (final osmolarity $310\,mmol/kg$) and bubbled with carbogen (95% oxygen, 5% carbon dioxide), giving a pH of 7.4. Slices were placed in a standard ACSF-perfused bath at 32-34 °C and visualized with an upright microscope (Zeiss Axioskop) using infrared-differential interference contrast optics, optimized as described previously (Davie et al. 2006). Whole-cell current-clamp recording were made from the soma using Axoclamp 2A, 2B or Multiclamp 700B amplifiers. Glass pipettes (4-7 MΩ) were filled with intracellular solution containing (in mM): 130 K-methanesulfate, 10 HEPES, 7 KCl, 0.05 EGTA, 2 Na_2ATP, 2 MgATP and 0.5 Na_2GTP, titrated with KOH to pH 7.2. Compensation for the access resistance of the pipette and for the capacitance of the pipette were performed and monitored throughout the recording. Recordings were abandoned when the resistance exceeded $40\,M\Omega$. The recorded potential and current were filtered at 3 or $10\,kHz$ and digitized at $50\,kHz$. Single patch-clamp recordings were performed using the electrode for both injection of current and recording of the voltage, for the ISR and hysteresis experiments. For the dynamic IV method and fitting parameters to the model, simultaneous double patch-clamp recordings were made at the soma, using one electrode to inject the current and one to record the voltage. The current and voltage were recorded by the amplifier and acquired by using Axograph (www.axograph.com/). The traces were then imported into Igor Pro for analysis.

Bistability and ISR analysis: To test for inverse stochastic resonance (ISR), current injection protocols were composed of series of $0.5 - 1\,s$ periods of noise followed by $0.5 - 1\,s$ period without noise. The injected noise waveforms were generated by an Ornstein-Uhlenbeck process:

$$\tau \frac{dx}{dt} = \mu - x + \sqrt{2\sigma^2\tau}N(0,1) \qquad (1)$$

where μ is the mean, σ the variance, and $N(0,1)$ a Gaussian white noise process with zero mean and variance equal to 1. For these protocols, the time constant was $\tau = 2$ ms, the noise amplitude σ varied in the range of $0 - 500\,pA$, with a step size of $\Delta\sigma = 20, 50$ or $100\,pA$. The mean changed with the holding current $I_{in} = -500 - 0\,pA$, and was adapted for each cell to explore particularly the region of bistability. The resulting firing frequency f during the noise injection

period and the mean noise amplitude σ were used to generate the ISR curve. All the curves measured with a holding current in the bistability range or higher (with non-zero firing rate at zero noise amplitude $f(\sigma = 0) \neq 0)$) were averaged and smoothed with a Gaussian filter with a width similar to the step size in noise amplitude (10 or 20 pA). The optimal noise amplitude for reduction in firing σ_{opt} was obtained for each cell as the minimum of the ISR curve, and the step noise amplitude of the stimulation provided the measurement error.

As the bistability of Purkinje cells is history dependent, it was necessary to measure the ISR curves in comparable conditions (silent or firing). We injected a noise waveform with linearly increasing and decreasing amplitudes ($0.5\, nA/s$, Fig.IV-8E). We analyzed the firing frequency in intervals of $200\, ms$, and separated intervals where the cell was firing in the previous intervals, and intervals where the cell was previously silent. For each category, we obtained the ISR curves by performing a running average (bin size = $20\, p$A, Fig.IV-8F).

To characterize the bistability of Purkinje cells, slow ramps of current were injected ($0.9\, nA/s$), ascending for $1\, s$ and descending for $1\, s$, and repeated 10 times. The cell was first hyperpolarized to -$65\, mV$ to stop firing. For each spike, the instantaneous frequency and the instantaneous injected current was calculated. The range of bistability was quantified as the difference between the frequency of the first spike (during the ascending ramp of current, $f_{up,}$) and the last spike (during the descending ramp f_{down}) $\Delta f = f_{up} - f_{down}$, and as the difference of injected current for the first and last spike $\Delta I = I_{up} - I_{down}$.

The dynamic IV method: The dynamic IV method developed by (Badel et al. 2008) is based on a simple representation of neuronal biophysics, where subthreshold injected current (I_{in}) is split into ionic transmembrane current (I_m) and capacitive current (I_C). In addition, the neuron receives noisy current input (I_{noise}) from background synaptic activity and other sources of high frequency noise. This can be rearranged to find the ionic current flowing through the neuronal membrane. Thus, by injecting a rapidly fluctuating current I_{in} to a neuron, the relationship between ionic current and voltage, during physiological spike generation, can be found.

$$I_m(V,t) = I_{in}(t) - C\frac{dV}{dt} + I_{noise} \qquad (2)$$

The injected noise current was the sum of two waveforms generated by Ornstein-Uhlenbeck processes (equation 1), with time constants $\tau_{fast} = 3\, ms$, $\tau_{slow} = 10\, ms$ (mimicking excitatory and inhibitory synaptic currents (Badel et al. 2008)). Two different amplitudes of noise were used, $\sigma = 153\, pA$ or $\sigma = 235\, pA$, and the mean was adapted according to the injected holding current. Individual protocols were composed of $500\, ms$ without noise followed by $20\, s$ of the noise waveform. The membrane potential V was recorded in response to the noisy current injection, and the ionic transmembrane current I_m was calculated by

subtracting the capacitive current I_C from the injected current I_{in} (equation 2). The after-hyperpolarization and the initial repolarization phase of each action potential ($10\,ms$ after the peak) were excluded from the analysis. As the distribution of the data points is approximately Gaussian for a given voltage, the dynamic IV curve can be defined as the average of I_m versus V (Fig.IV-3C):

$$I_{dyn}(V) = mean[I_m(V,t)] \qquad (3)$$

The capacitance (used to evaluate the capacitive current) was estimated by minimizing the variance of I_m within individual voltage bins. Equation (2) can be transformed by inserting the estimated capacitance C_e:

$$\frac{I_{in}}{C_e} - \frac{dV}{dt} = \frac{I_m}{C} + \left(\frac{1}{C_e} - \frac{1}{C}\right) I_{in} - \frac{I_{noise}}{C} \qquad (4)$$

The variance of this function is:

$$var[\frac{I_{in}}{C_e} - \frac{dV}{dt}]_V = var[\frac{I_m}{C}]_V + (\frac{1}{C_e} - \frac{1}{C})^2 var[I_{in}]_V + var[\frac{I_{noise}}{C}]_V \qquad (5)$$

When (1/Ce-1/C) becomes zero, i.e. the estimated capacitance is correct, this variance is minimized.

The dynamic IV curve can be transformed into an integrate-and-fire (IF) type neuronal model, with voltage dynamics of the type shown in equation (6), where $F(V)$ is a nonlinear function of voltage:

$$\frac{dV}{dt} = F(V) + \frac{I(t)}{C} \qquad (6)$$

$F(V)$ is related to the dynamic IV curve by equation (7):

$$F(V) = -\frac{I_{dyn}(V)}{C} \qquad (7)$$

The experimentally derived $-I_{dyn}(V)/C$ curve can be fitted with a function $F(V)$ describing an exponential integrate-and-fire (EIF) model (Fourcaud-Trocme et al. 2003), containing a linear part and an exponential rise to the action potential (Fig.IV-3D):

$$F(V) = \frac{1}{\tau_m}(E_L - V + \Delta_T \exp(\frac{V - V^T}{\Delta_T})) \qquad (8)$$

The parameters are membrane time constant τ_m, resting potential E_L, threshold potential V^T, and spike slope factor Δ_T.

aEIF model: The exponential integrate-and-fire model with adaptation (Badel et al. 2008) is defined by:

$$C\frac{dV}{dt} = -g_L(V - E_L) + g_L\,\Delta_T e^{\frac{V-V^T}{\Delta_T}} - w + I_{in}(t) \qquad (9)$$

$$\tau_w\frac{dw}{dt} = a(V - E_L) - w \qquad (10)$$

$If\ V > V_{spike}$ then $V \rightarrow V_r$ and $w \rightarrow w_r$

where C is the capacitance, E_L is the leak reversal potential, g_L is the leak conductance, V^T is the threshold potential, Δ_T is the spike slope factor, V_r is the membrane potential reset after a spike, w is the adaptation current, a is the level of subthreshold adaptation, τ_w is the adaptation time constant and b is the adaptation current reset after a spike, V_{spike} is the conditional threshold for spike generation ($V_{spike} = 0$).

Simulations: All simulations were done in Matlab R2014b using the forward Euler method with an integration step of $0.1\ ms$. We confirmed that this integration step produces stable numerical results. The bifurcation and phase-plane analyses were carried out in XPPAUT 7.0.

Parameter fitting for the aEIF model: Fitting electrophysiology data of Purkinje cells to an aEIF model was achieved using a combination of the dynamic IV method and the procedure used for fitting an aEIF model to synthetic data described in (Brette and Gerstner 2010).

Passive parameters

A good estimate of the membrane time constant τ_m of the Purkinje cell is obtained by fitting the late phase of the voltage response to a short current pulse ($0.5\ ms$, $1\ nA$) (Roth and Häusser 2001), Fig.IV-9. As the aEIF remains a single compartment model, we use the approximation of the capacitance obtained using the dynamic IV method (although not optimal, as the somato-dendritic coupling of Purkinje cells is high). The reversal potential E_L is also best estimated using the dynamic IV method, as the cell is spontaneously active. We estimate the value for the leak conductance at the soma and proximal dendrite using the membrane time constant and the capacitance according to $g_L = {}^{C}/_{\tau_m}$.

Subthreshold adaptation

The subthreshold adaptation parameter a was determined as follows: when the potential V is fixed, the adaptation current w is close to $a(V - E_L)$. Therefore the linear part of the dynamic IV curve (apart from the exponential term) is:

$$I_{dyn} = (g_L + a)(V - E_L) \quad (11)$$

We obtain the parameter a by subtracting the leak conductance g_L from the slope fitted to the linear part of the dynamic IV curve.

Spike-triggered adaptation

To determine the contribution of spike-triggered adaptation, we use the voltage response to noise injection in a similar way as for constructing the dynamic IV curve. Far away from threshold, the adaptation current is:

$$w = -I_{in} - C\frac{dV}{dt} - g_L(V - E_L) \quad (12)$$

This estimate is composed of the spike-triggered adaptation w_{spike} and the subthreshold adaptation $a(V - E_L)$. We can express w_{spike} as:

$$w_{spike} = -I_{in} - C\frac{dV}{dt} - (g_L + a)(V - E_L) \quad (13)$$

We plotted the estimated w_{spike} against time since the last action potential (Fig.IV-3E). The distribution of the data points is approximately Gaussian for a given time. Therefore we defined the time course of the spike-triggered adaptation after a spike as the average of w_{spike} versus time. The curve can be fitted by a single exponential yielding an estimate of the time constant τ_w and the value of the spike-triggered adaptation reset b, with $w_{spike}(t = 0) = b$ (Fig.IV-3F).

The parameters of the aEIF model were set to the values determined by fitting data from a representative Purkinje cell. A variation of the parameters within the range occurring in the Purkinje cell population was performed to determine their influence on the ISR range. We note that all occurring parameter combinations were restricted to $\frac{a}{g_L} > \frac{\tau_m}{\tau_w}$, corresponding to type II excitability (Fig.IV-4D). The representative parameters were:

$C = 268\,pF$, $E_L = -51.31\,mV$, $V^T = -53.23\,mV$, $\Delta_T = 0.85\,mV$, $g_L = 8.47\,nS$, $a = 37.79\,nS$, $b = 441.12\,pA$, $\tau_w = 20.76\,ms$.

Noise stimulus was modeled as $I(t) = I_{mean} + I_{noise}(t)$, where I_{mean} is constant and $I_{noise}(t)$ is current noise with zero mean generated using an Ornstein-Uhlenbeck process with amplitude σ and time constant $\tau_c = 2\ \mathrm{ms}$.

Noise stimulus with an additional timed excitatory synaptic input was modeled as $\mathrm{I(t)} = \mathrm{I_{mean}} + \mathrm{I_{noise}(t)} + \mathrm{I_{syn}(t)}$, where $\mathrm{I_{syn}(t)}$ is the biexponential

excitatory synaptic input, described as the solution of the equation:

$$\tau_1\tau_2\frac{d^2}{dt^2}I_{syn} + (\tau_1 + \tau_2)\frac{d}{dt}I_{syn} + I_{syn} = Am(1 - I_{in})\delta\,(t - t_{st})/K\left(\tau_{1,}\tau_2\right)$$

where t_{st} is the stimulation time, Am is the amplitude of the stimulus, and

$$K\left(\tau_{1,}\tau_2\right) = \frac{1}{\tau_2 - \tau_1}\left[\left(\frac{\tau_2}{\tau_1}\right)^{\frac{\tau_1}{\tau_1 - \tau_2}} - \left(\frac{\tau_2}{\tau_1}\right)^{\frac{\tau_2}{\tau_1 - \tau_2}}\right] \qquad (14)$$

with rise time constant $\tau_1 = 1.5\ ms$ and decay time constant $\tau_2 = 10\ ms$.

ISR Range

To estimate the ISR range in the parameter space, we rescaled the aEIF model in the following way (Touboul and Brette, 2008):

$$\frac{d\overline{V}}{d\overline{t}} = -\overline{V} + e^{\overline{V}} - \overline{w} + \overline{I} \qquad (15)$$

$$T\frac{d\overline{w}}{d\overline{t}} = -A\overline{V} - \overline{w} \qquad (16)$$

where $T = \tau_w/\tau_m$, $A = a/g_L$, $\overline{I} = \frac{I}{g_L\Delta_T} + \left(1 + \frac{a}{g_L}\right)\frac{(E_L - V^T)}{\Delta_T}$, $\overline{t} = \frac{t}{\tau_m}$, $\overline{b} = \frac{b}{g_L\Delta_T}$, $\overline{V_{rest}} = \frac{V_{reset} - V^T}{\Delta_T}$, $\overline{V} = \frac{V - V^T}{\Delta_T}$, $\overline{w} = \frac{w + a(E_L - V^T)}{g_L\Delta_T}$

The bistability range in the model is defined similarly as for the recorded Purkinje cells, by the following expression: $\Delta I = I_{up} - I_{down}$, where I_{up} corresponds to the minimal current needed to elicit a spike when the model starts from the rest state and I_{down} is the maximal current at which the spiking stops given that the model starts in the periodic spiking state, Fig.IV-4D. The value of I_{up} is referred to as the rheobase current, and for the aEIF model possessing type II excitability it has the following analytical expression (Touboul and Brette 2008):

$$I_{up} = (g_L + a)\left[V^T - E_L - \Delta_T + \Delta_T log\left(1 + \frac{\tau_m}{\tau_w}\right)\right] + \Delta_T g_L\left(\frac{a}{g_L} - \frac{\tau_m}{\tau_w}\right) \qquad (17)$$

Probability of Spiking

The probability of spiking is proportional to the fraction of time the trajectory spends in the region of V-w phase space leading to a spike. We measured the amount of time t_{rest} the aEIF model has spent in the basin of attraction of a stable fixed point. Then the probability of being in the rest state is calculated as $P_r = \frac{t_{rest}}{t}$, where t is the total integration time. There are only two states in the phase space of aEIF model: spiking and rest. Therefore the probability of spiking is calculated as $P_{sp} = 1 - P_r$.

For simulations with Ornstein-Uhlenbeck noise, the probabilities and averaged firing rates were calculated after 20 repetitions with duration of $30\,s$ each. We tested longer simulations and found that $30\,s$ ensures an accurate and stable estimate. For simulations with excitatory biexponential input (equation 14), the probabilities P_{sp} were calculated in bins of $20\,ms$ in 1000 sweeps with a duration of $6\,s$ each.

Mutual information rate

To calculate the mutual information rate (MI) between the input and output spike trains we used the context tree weighting algorithm as described in (London et al. 2002). We simulated the aEIF model, extracted the input and output spike times, and then used the algorithm with bin size b = 25 ms and depth parameter D = 40 bins, corresponding to a time window of 1 s. The total duration of a sweep was 1,000 s. The algorithm was used 10 times for each data point to provide a reliable estimate of mutual information.

IV.2.5 Results

IV.2.5.1 Purkinje cells exhibit inverse stochastic resonance (ISR)

To test whether Purkinje cells (PCs) exhibit inverse stochastic resonance, we made patch-clamp recordings from PCs in rat cerebellar slices. We injected noisy current waveforms and observed the resulting firing behavior (Fig.IV-1A). The noise protocol consisted of a series of ten $1\ s$ noise periods alternating with $1\ s$ rest periods. The noise waveform was generated by an Ornstein-Uhlenbeck process with time constant t = 2 ms and increasing amplitude σ to represent the synaptic currents received by the cell (see Methods). We observed that the firing frequency of PCs is initially reduced in response to increasing noise amplitude. This counter-intuitive effect is characteristic of ISR, where the relationship between firing rate and noise amplitude has a minimum, or "tuning" (here at amplitude $\sigma = 100pA$; Fig.IV-1B). All Purkinje cells tested exhibited ISR, and the optimal noise level for firing rate inhibition for the population was $\sigma_{opt} = 152 \pm 64\ pA$ (n = 19, Fig.IV-1C). However, ISR is variable across cells, and some cells can be fully silenced in response to optimal noise amplitude injection (Fig.IV-SIC). In that case, the cell is generally silenced even during periods with no noise injection, if they follow periods with optimal amplitude noise. This shows that the firing rate in one interval is not only determined by the noise amplitude and mean (holding current), but also by the cell's activity in the previous interval.

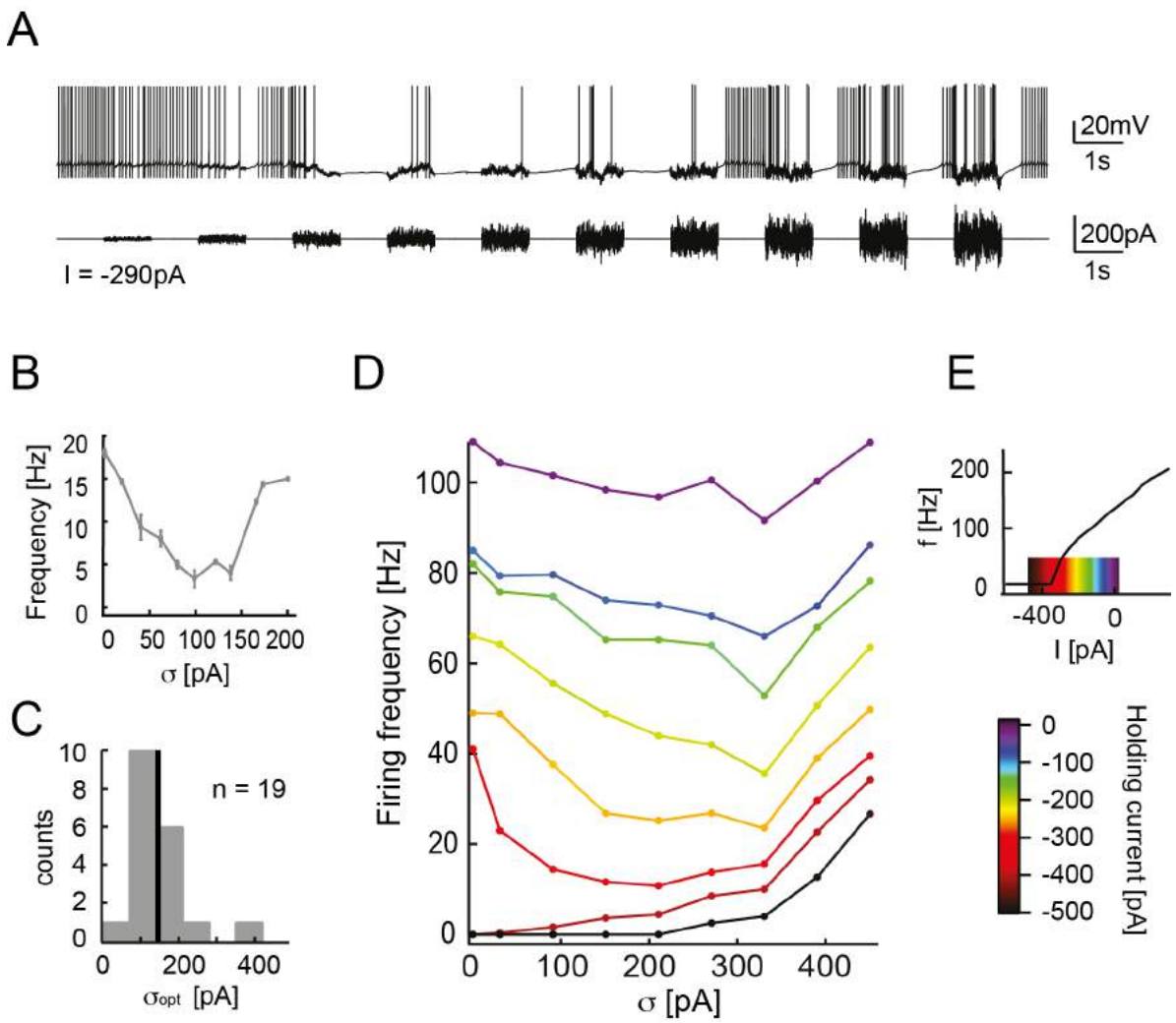

Figure IV-1. Cerebellar Purkinje cell show inverse stochastic resonance (ISR)
A. Whole-cell patch-clamp recording from a Purkinje cell in a cerebellar slice, showing current injection of $1\ s$ noise waveform periods with increasing amplitude, and recorded membrane potential V_m. Holding current is $I = -290pA$. The firing rate of the Purkinje cell (PC) is reduced for intermediary noise amplitude. B. Firing frequency during $1\ s$ noise injection vs. noise amplitude σ corresponding to the trace in A. Error bars are standard deviation. The firing rate is minimum for σ=100pA. C. The ISR is observed in all Purkinje cells tested. Summary of optimal noise amplitude σ= 152.60 ± 64.42 pA (n=19). D. ISR curve of a different PC, generated with a current injection protocol of continuously changing noise amplitude and for a series of holding current, exploring the full range of the f-I curve (E). The firing rate is most reduced when the cell is hyperpolarized to the edge of the f-I curve step. The optimal noise amplitude for inhibition of firing is σ=200pA. E. Frequency vs. current generated with steps current injection of $1\ s$. The color code corresponds to the region explored for the ISR curve in D.

ISR appears to mediate transitions between a firing state and a silent state. To account for the resulting history dependence, we injected a noise waveform with continuously changing noise amplitude (Methods, Fig.IV-SIE), and generated ISR curves using only intervals in which the cell is initially in the firing state (Fig.IV-1D, SIF). We observed that the optimal noise amplitude σ consistently reduces the firing rate across a range of mean holding currents. However, the reduction is most pronounced when the cell is hyperpolarized relative to its resting membrane potential (holding current $I_{in} = -290\,pA$ for traces in Fig.IV-1A, B). When the cell is hyperpolarized sufficiently to prevent firing, the noise injection then acts in the expected way

and the firing rate only increases (Fig.IV-1D, $I_{in} = -400\,pA$). In this case, the noise amplitude needs to be large enough to bring the cell to threshold. We observe that there is an optimal holding current for which the cell's firing rate is reduced the most ($I_{in} = -350\,pA$, red), as there is an optimal noise level σ_{opt}. This phenomenon is qualitatively similar to the previously reported ISR in the Hodgkin-Huxley neuron model (Gutkin and Tuckwell 2009). As Purkinje cells have type II excitability, we observe in particular that the optimal holding current corresponds to the region of the "discontinuity" in the f-I curve (red in Fig.IV-1E). It appears therefore that the ISR phenomenon is linked to the bistability of Purkinje cells.

IV.2.5.2 ISR parameters are related to Purkinje cell bistability

We examined the link between the Purkinje cell intrinsic property of bistability and the modulation of firing by noise. Type II excitability is traditionally characterized by a step or discontinuity in the f-I curve (Fig.IV-1E), as opposed to the continuous f-I curve of type I excitability (Touboul and Brette 2008). However, we observed that different Purkinje cells can show a wide range of type II behavior. The firing rate hysteresis in response to slow ramps of current allows a more precise characterization of this property than f-I curves (Williams et al. 2002). Cells were held at $-65\,mV$ to prevent spontaneous firing and an ascending and descending ($0.9nA/s$) ramp of current was injected (Fig.IV-2A). The first spike occurs at a different instantaneous frequency and current than the last spike (Fig.IV-2B). This hysteresis illustrates that the cell is in a different condition during the ascending and descending phases of the ramp.

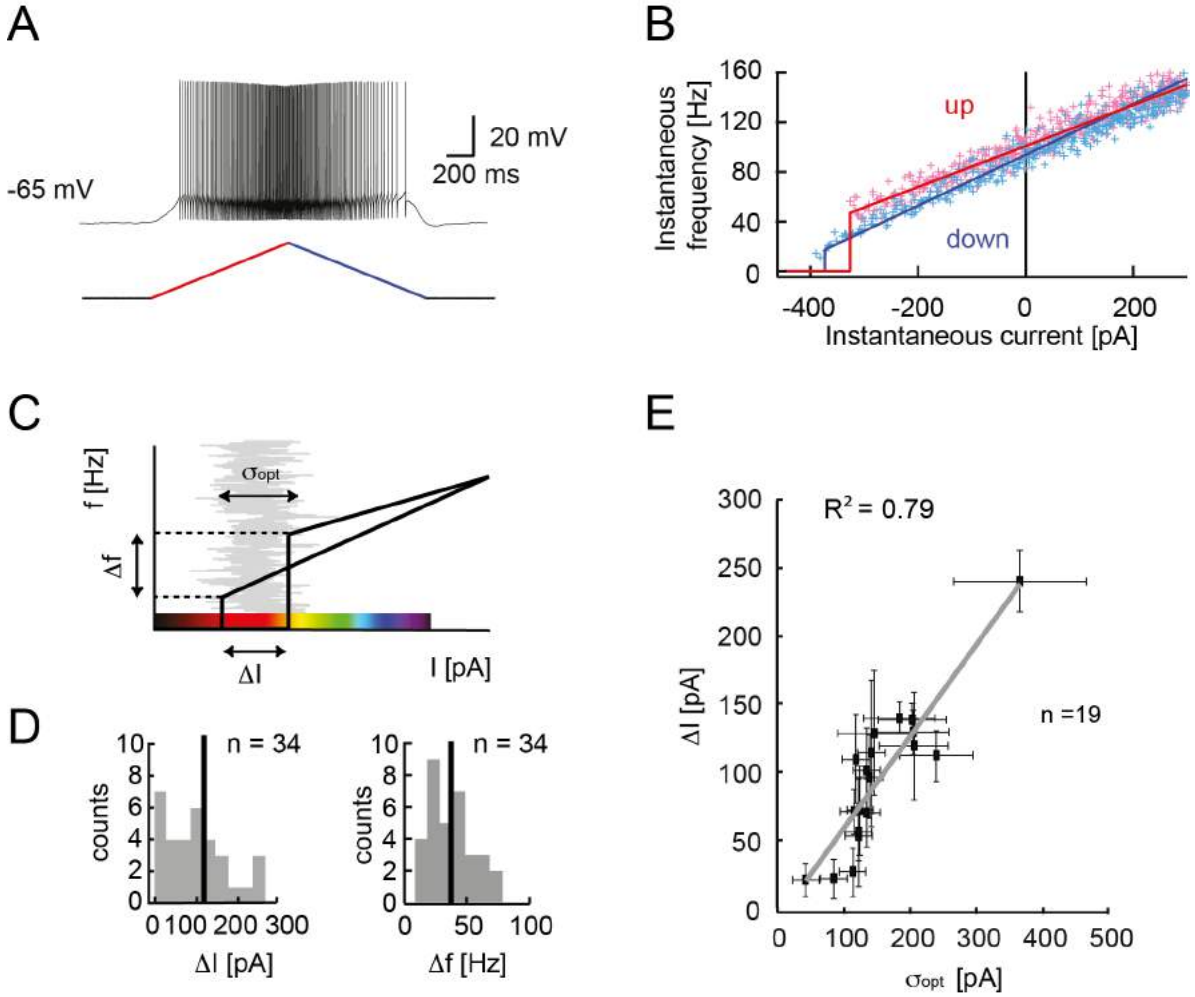

Figure IV-2. Experimental characterization of Purkinje cell bistability
A. Whole-cell patch-clamp recording from a Purkinje cell, showing a representative hysteresis measurement with slow current ramp injection ($0.9\,nA/s$) ascending (red) and descending (blue), and the resulting PC membrane potential firing. B. Instantaneous firing frequency and current for each spike. Linear fit of the ascending ramp (red) and the descending ramp (blue) are averages of 10 . trials C. Characterization of the hysteresis using the difference in frequency between first and last spike Δf and difference in current ΔI and population data. The color code illustrates the region explored for the ISR curve. Red corresponds to both the hysteresis and the optimal ISR (Fig1 C, D). D. Correlation between the width of the hysteresis range ΔI and the optimal noise level for ISR σ_{opt}. Error bars are standard deviation, $R^2 = 0.79$ n= 19.

We quantified the difference between the instantaneous frequency of the first spike (ascending) and the last spike (descending) (Δf) and the difference of injected current for first and last spike (ΔI; Fig.IV-2C). Across a population of Purkinje cells, we observed a wide range of hysteresis parameters $\Delta f = 38.17 \pm 19.12\,\mathrm{Hz}$, $\Delta I = 110.28 \pm 84.57\,\mathrm{pA}$ (mean ± S.D., n=34). Hysteresis as characterized by these parameters offers a quantification of the degree of bistability of individual Purkinje cells. Using the same color code for the hysteresis plot (Fig.IV-2C) and the ISR curve (Fig.IV-1D), we highlight the suspected link between the two phenomena. The inhibition of firing in response to noisy input is indeed more pronounced when the cell is hyperpolarized to the hysteresis region where both spiking and rest states can exist. To illustrate this relationship empirically, we compared the hysteresis parameters with the parameters of ISR. We found a correlation between the width of the hysteresis range ΔI and the optimal noise amplitude (R^2 = 0.79; n = 19 cells) (Fig.IV-2D). This suggests that the noise amplitude required for ISR is on the order of the difference in the holding currents at which the cell makes transitions from the firing to the silent state and vice versa.

IV.2.5.3 An adaptive exponential integrate-and-fire (aEIF) model describes Purkinje cell firing

We employed a reduced model approach to understand the relationship between the intrinsic property of bistability and ISR. Our choice of a minimal spiking neuron model, which can describe the bistability of Purkinje cells was motivated by several requirements. The model should have sufficiently rich dynamics to account for the bimodal behavior of Purkinje neurons, and be of sufficiently low dimensionality to allow analytical insights. The adaptive exponential integrate-and-fire model (aEIF) was chosen since it can reproduce a range of different firing regimes including type II excitability (Touboul and Brette 2008) and we can quantitatively fit the parameters of the model to electrophysiological data from individual PCs. The aEIF also allows a detailed examination of the links between hysteresis, bistability and ISR. In order to quantitative fit the model to the experimental data, we used the dynamic IV method (Badel et al. 2008) for the parameters of the basic aEIF model together with a modified version of this method for the adaptation parameters (see Methods for details). Briefly, the dynamic IV method relies on accessing passive and active membrane mechanisms during physiological spike generation. It provides a simple representation of the ionic transmembrane current I_m as a function of the injected current I_{in} and membrane potential V by subtracting the capacitive current from I_{in}.

$$I_m(V,t) = I_{in}(t) - C\frac{dV}{dt} + I_{noise} \qquad (19)$$

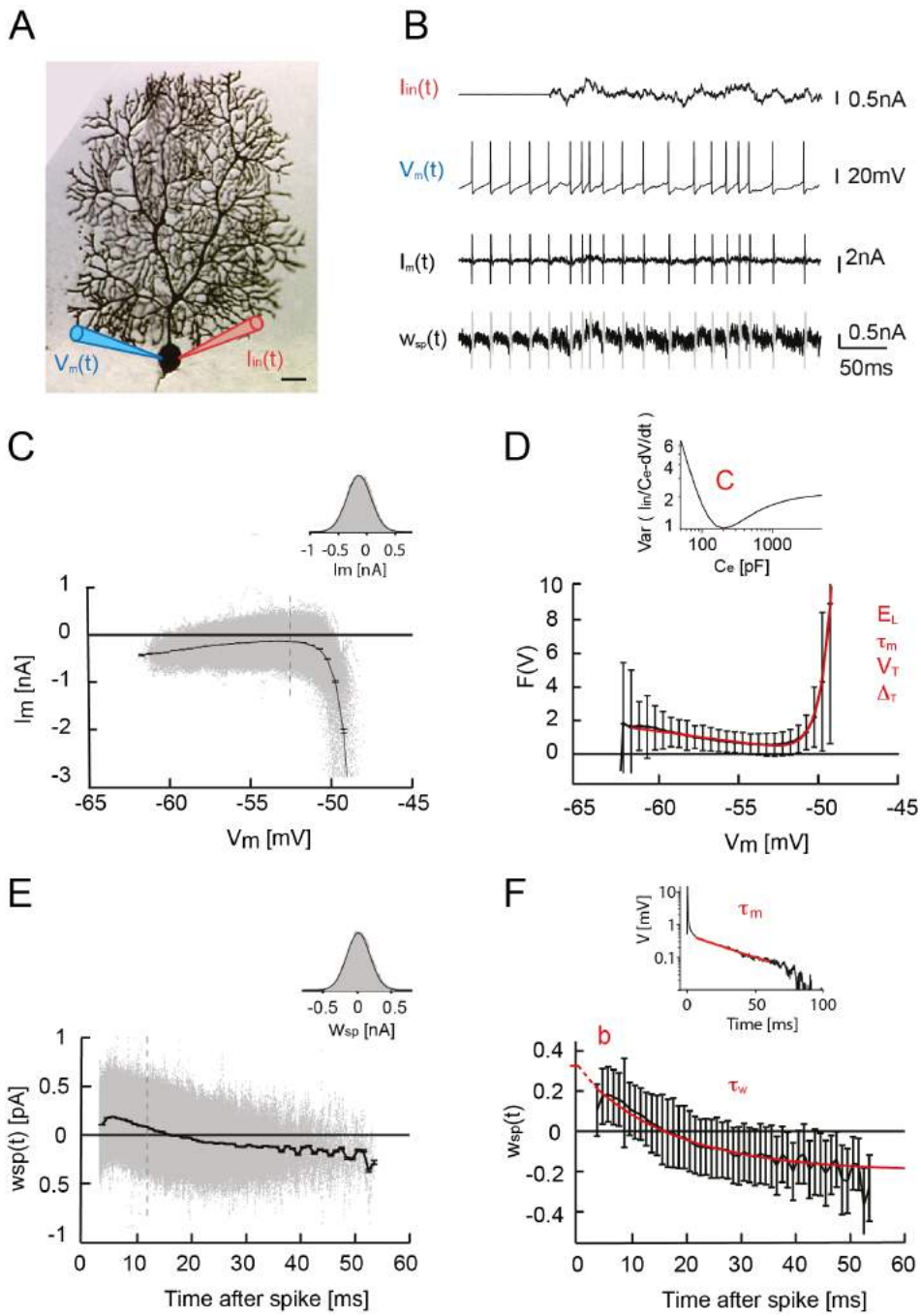

Figure IV-3. aEIF model fitting procedure to Purkinje cell experimental data
A. Double somatic whole-cell patch-clamp recording from a representative Purkinje cell: one electrode for current injection and one for voltage recording (scale bar: 100 μm). B. Traces of injected noise current $I_{in}(t)$, recorded membrane potential $V_m(t)$, in spontaneously active PC, calculated membrane current $I_m(t)$, and calculated spike-dependent adaptation current $w_{sp}(t)$. C. I_m vs. V_m and dynamic IV curve as the average over V_m. Error bars are SEM. Inset the distribution of points at V_m = -52mV is Gaussian. D. Fitting the dynamic IV curve $F(V) = -I_{dyn}/C$ with the EIF model function. Parameters are; resting potential E_m membrane time constant τ_m, threshold potential V_T, and spike slope factor Δ_T. Error bars are SD. Inset. Capacitance determination by minimizing the variance of I_m. E. Spike triggered adaptation $w_{sp}(t)$ plotted versus time after the last spike. Error bars are SEM. Inset the distribution of points at t=12ms is Gaussian. F. The spike-triggered adaptation is fitted to a single exponential, with time constant τ_w and w_{sp} (t=0) = b. Error bars are SD.

In order to mimic excitatory and inhibitory synaptic currents, the injected current was a sum of two Ornstein-Uhlenbeck processes with time constants $\tau_{fast} = 3\,ms$, $\tau_{slow} = 10\,ms$ (Badel et al. 2008). Measuring the membrane potential using an electrode while simultaneously injecting current can be inaccurate because of the voltage drop across the electrode. Therefore, to measure the true membrane potential V, we performed double somatic patch-clamp recordings from PCs in slices (Fig.IV-3A). The ionic current through the membrane I_m was calculated using equation (2) and plotted against the voltage (Fig.IV-3B, C). The distribution of the I_m data points is Gaussian for a given voltage (Fig.IV-3C, inset), the dynamic IV curve is therefore defined as the average of I_m versus V (Fig.IV-3D). The capacitance can be estimated by minimizing the variance of I_m within individual voltage bins (Fig.IV-3D, inset) (see Materials and Methods). The dynamic IV curve can be readily transformed into an integrate-and-fire (IF) type neuronal model, where $F(V)$ is a nonlinear function of voltage.

$$F(V) = \frac{1}{\tau_m}(E_L - V + \Delta_T \exp\left(\frac{V - V^T}{\Delta_T}\right) \qquad (20)$$

The experimentally derived $F(V) = -I_{dyn}(V)/C$ curve can therefore be fitted with a function $F(V)$ describing an exponential integrate-and-fire (EIF) model (Fourcaud-Trocme et al. 2003), with parameters membrane time constant τ_m, resting potential E_L, threshold potential V^T, and spike slope factor Δ_T. Average values for our PCs were: $C = 195.4 \pm 53.3\,pF$, $E_L = -51.9 \pm 1.9\,mV$, $V^T = -54.1 \pm 2.3\,mV$, $\Delta_T = 1.0 \pm 0.2\,mV$, $\tau_m = 4.4 \pm 1.2\,ms$ (n = 7 cells).

It is interesting to note the difference between the dynamic IV of PCs and those previously reported for pyramidal cells (Badel et al. 2008). The spontaneous, self-sustained, activity of PCs means that the IV dynamic curve sits above zero, and V_m never effectively reaches the resting potential E_L. The aEIF model with these parameters is spontaneously active but it is not able to show type II excitability. To account for this essential property, we chose to extend the model with voltage-dependent adaptation. The method we used to fit the adaptation is inspired by the procedure used for fitting an aEIF model to synthetic data as described in (Brette and Gerstner 2010). Since the PC is spontaneously active, the classical dynamic IV method yielded a good approximation of the capacitance and reversal potential E_L. (for more details see Supplementary materials). However, the time constant determined by the dynamic IV method in Purkinje cells reflects the only fast time constant of a soma while the total membrane time constant, needed for the aEIF, depends on the large proximal dendrite as well. To compensate for this issue we estimate the full membrane time constant τ_m of Purkinje cell by fitting the voltage response to a short current pulse (0.5 ms, 1 nA), Fig.IV-9A (Roth and Häusser 2001). From this, we can estimate the value for the leak conductance g_L at the soma and proximal dendrite, using the membrane time constant and the capacitance $g_L = C/\tau_m$. We determine the subthreshold adaptation parameter a using the

same approximation as in (Brette and Gerstner 2010, Materials and Methods): by subtracting the leak conductance g_L from the slope fitted on the linear part of the dynamic IV curve.

The voltage-dependent adaptation strength is the key parameter for type II excitability. To define it, we followed a method similar to the dynamic IV. To access the contribution of spike-triggered adaptation, we rearranged equation (13) using the approximation (see Materials and Methods):

$$w_{spike} = -I_{in} - C\frac{dV}{dt} - (g_L + a)(V - E_L) \qquad (21)$$

As w_{spike} is triggered at each spike, we plotted the estimated w_{spike} against the time since the last action potential (Fig.IV-3E). The distribution of the data points is Gaussian for a given time (Fig.IV-3E, inset). Therefore we defined the time course of the spike-triggered adaptation after a spike as the average of w_{spike} versus time. The curve can be fitted by a single exponential that yields an estimate of the time constant τ_w. The adaptation parameters fitted to data from PCs were $a = 36.1 \pm 6.3\, nS$, $b = 408.0 \pm 128.0\, pA$, $\tau_w = 14.8 \pm 6.3\, ms$ (n = 7). The threshold parameters Δ_T and V^T are not influenced by adaptation, and were therefore used as fitted with the dynamic IV method.

IV.2.5.4 The aEIF model reproduces Purkinje cell bistability and ISR

We used the empirically fitted adaptive exponential integrate-and-fire model (aEIF) to describe simple spike firing of a Purkinje cell in response to noise steps of increasing amplitude (see Fig.IV-4A). The parameters of the model are quantitatively fitted for each cell using the modified dynamic I-V method as described above. All simulations were done for a set of the parameters representing one typical Purkinje cell, cell 1, Fig.IV-1A, B.

The response of the model to current ramps showed clear hysteresis of the firing rate as a function of the current (Fig.IV-4C). The mechanism for this hysteresis is fairly straightforward: the threshold for spike generation in the aEIF (and by extension in the PC) depends on the adaptation variable (Touboul and Brette 2008). Since adaptation increases with each successive spike, the current threshold also increases: it has a higher value when the last spike in the train is produced as compared to the first spike. This explains the different thresholds for the symmetric upstroke and downstroke of the current injection ramp.

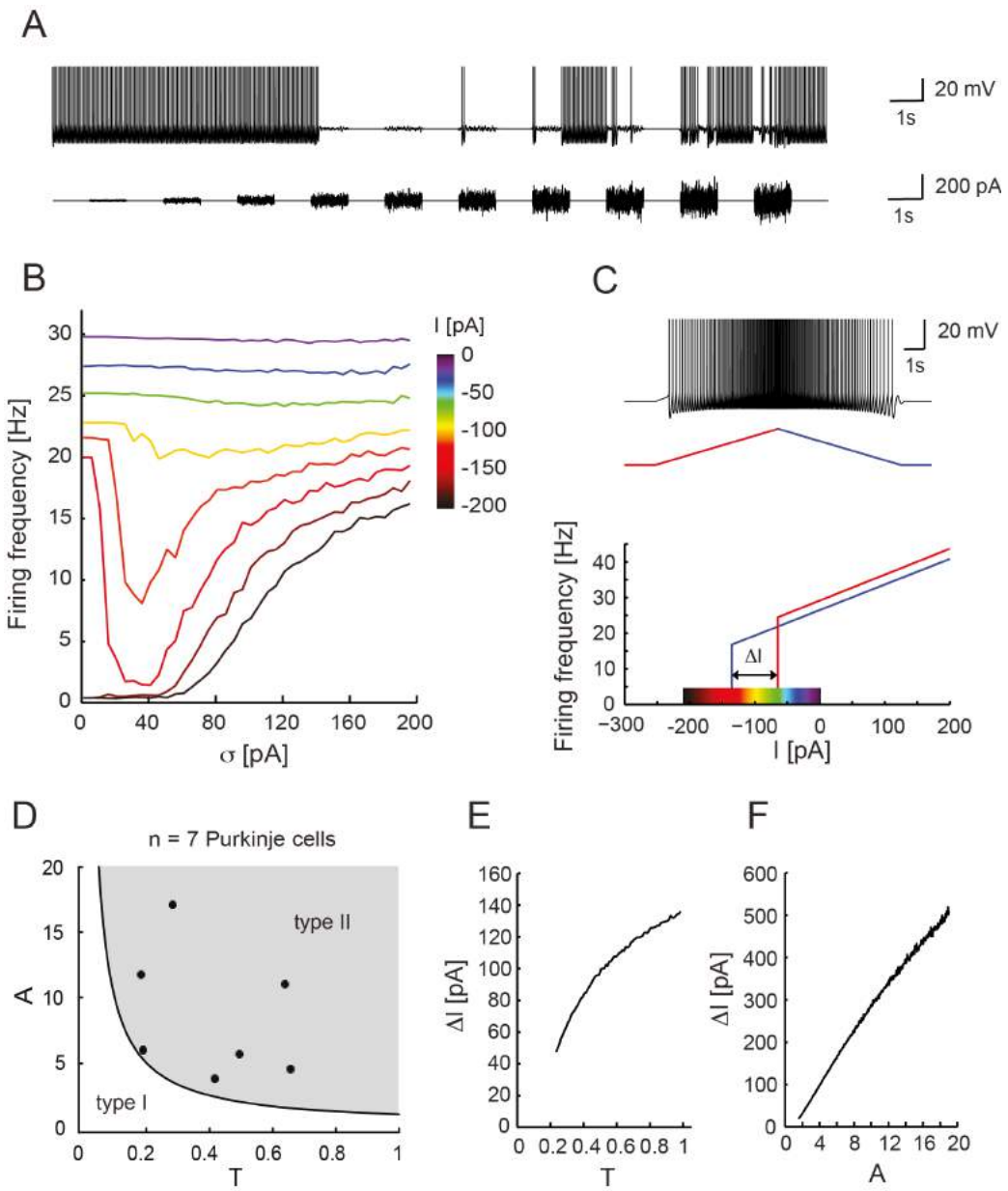

Figure IV-4. Hysteresis and ISR of the aEIF model
A Voltage response of the aEIF model to Ornstein-Uhlenbeck current noise injection with increasing amplitude. B. Mean firing-rate of the aEIF model in response to current noise stimulation with amplitude σ and mean I (color code). C. Hysteresis of the aEIF model. Top. Voltage response to ascending (red) and descending (blue) ramp of current. Bottom. Instantaneous firing-rate vs instantaneous injected current. Color code is the same as in B. D. Parameter space of the rescaled aEIF model, white region - type I excitability, gray region – type II excitability. The 7 fitted cells are in type II region. E, F. Dependence of the hysteresis size ΔI on the parameters $T = \tau_w/\tau_m$ (E) and $A = a/g_L$ (F).

Next we examined the firing rate responses of the model to current noise generated as in the experiment (Fig.IV-4B). The mean of the input was chosen to be within the hysteresis range to reproduce the experimental conditions. When the mean input current was close to $-150\,pA$ the model demonstrated strong inhibition of firing by the injected noise. While extremely weak noise did not have much effect on spiking, noise with an optimal variance around $30\,pA$ (that is still relatively small) efficiently switched the system from spiking to the rest state. Once an up-to-down transition occurred, the amount of current needed to elicit new spikes increased. This was due to the asymmetrical shape of the basin of attraction for the stable fixed point (see Section 5 below). Therefore, at the optimal noise variance the model preferentially remained in the resting state for an extended period of time. Interestingly, the variance of the noise optimal for spike-inhibition was unable to switch the model back from the rest state to the spiking state, hence we observe virtually no spontaneous down-to-up transitions. Noise with a sufficiently large variance was able to switch the system between spiking and rest. This variance-dependent inhibition by noise current led to dependence between the mean firing rate and noise variance that had a clear minimum (Fig.IV-4B).

When the mean input current was outside the hysteresis region, this effect markedly decreased, or no ISR was observed. In the range above the hysteresis region (input current mean approx. $-100pA$), this happened because the model was monostable, continuously spiking and the input noise resulted in a weak modulation of the firing pattern. When the input was below the hysteresis range, near $-200pA$, the aEIF model preferentially stayed in the rest state at low noise values and spiked only if the input noise had a large enough variance (i.e. the spikes were directly evoked by the noise excursions above spike threshold).

To estimate the strength of ISR as a function of the model parameters and clarify the most important parameter combinations we rescaled the model (see Materials and Methods). This allowed us to significantly reduce the number of parameters. We estimated the bistability region of the rescaled aEIF model in terms of the hysteresis range $\Delta I = I_{up} + I_{down}$, i.e. the difference between threshold currents in the up-and-down ramp. The larger this difference, the stronger was the bistability and the more ISR would be present (meaning that the minimum of the firing rate vs. noise amplitude curve was deeper). According to our analysis the key parameters of the model are the voltage-dependent adaptation and the adaptation time constant. We found an approximately linear relationship with the range of bistability for the adaptation time constant T (Fig.IV-4E) as well as for the adaptation parameter A (Fig.IV-4F). This implied that the

larger and the slower the adaptation, is the more prominent the difference between I_{up} and I_{down}, and accordingly the larger the ISR range and the stronger the bistability. In conclusion, ISR is present for a wide parameter range as long as the model exhibits type II behavior.

Although the aEIF model can exhibit either type I or type II excitability depending on the parameter values (*A* and *T*) (Touboul and Brette 2008), our experimental results from 7 Purkinje cells showed that all measured neurons possess type II excitability in the model parameter space (Fig.IV-4D). However, the size of the hysteresis region and the amplitude of the minimal firing frequency varied from cell to cell.

IV.2.5.5 Bifurcation analysis of the aEIF model

To understand the behavior of the model related to ISR, we examined the phase space of the model. The phase space of the model when the input mean is in the hysteresis (equivalently: bistability) regime consists of two areas: the basin of attraction of a stable fixed point and the spike generation area (Fig.IV-5A). The drop-like set marked by the solid black line corresponds to the basin of attraction of a stable fixed point, the rest state. When a trajectory initiates in this region the system moves to the stable fixed point, e.g. the blue trajectory. Outside of this region all trajectories are spiking, for example the red trajectory. After each spike the system is immediately reset to V_{reset}, so that the attraction basin is not crossed (dashed line). This implies that when the voltage of the model is transiently perturbed outside the droplet region, the model will continue spiking. This kind of behavior constitutes the bistability in the model, i.e. the coexistence of a spiking (limit-cycle) and a resting-state attractor for the same parameter set.

To obtain a more general picture of the mechanism underlying bistability we performed a bifurcation analysis of the model. Fig.IV-5B shows the bifurcation diagram of the aEIF model (in the V-I plane) in the subthreshold regime (i.e. the bifurcation of the steady states). There are two fixed points corresponding to stable and unstable equilibria or fixed points in Fig.IV-5B. When the input current I gradually increases, the rest fixed point loses stability via an Andronov-Hopf bifurcation (HB), which accounts for type II excitability. Due to the intersection of the nullclines there are two unstable equilibria after

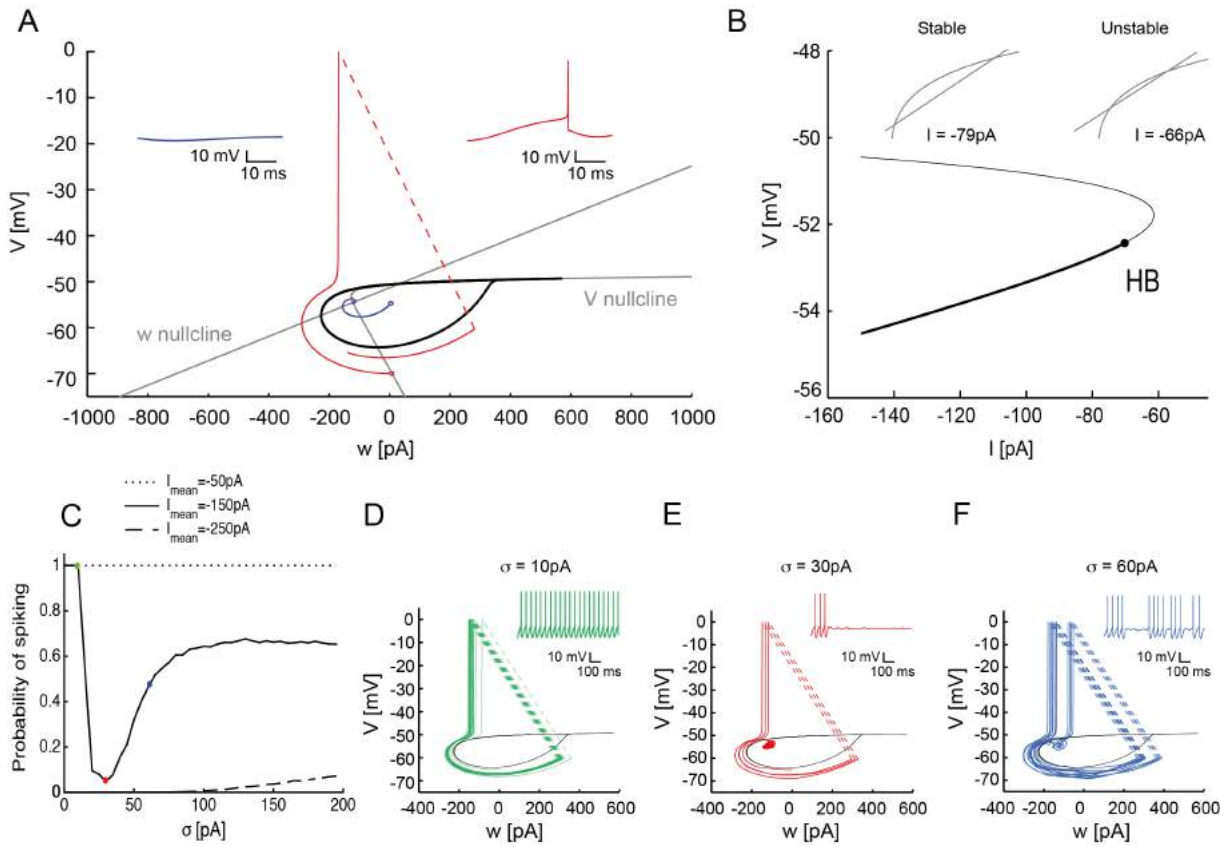

Figure IV-5. Bifurcation diagram and phase plane of the aEIF model
A. Phase-plane of the model. Gray lines are the null-clines of the model. Drop-like set (black) corresponds to the basin of attraction of a stable fixed point. Red and blue trajectories correspond to rest and spiking respectively (inset). B. Bifurcation diagram of the aEIF model. Solid and thin lines represent stable and unstable fixed points for different values of I. Inset shows the intersection of the null-clines before and after HB point. Point corresponds to Andronov-Hopf Bifurcation (HB). C. Probability of spiking during the stimulation by noise with various means (compare with Fig4B). D, E, F. Phase plane of the model with the corresponding trajectories and voltage traces (inset) when stimulated by Ornstein-Uhlenbeck noise for $1000\ ms$ with the mean $I = -150\ pA$ and amplitudes $\sigma = 10\ pA, 30\ pA$ and $60\ pA$.

the HB point which merge and disappear at higher values of input current I (see insets). At higher input currents, there are no fixed points and there is only a spiking regime in the model. We can see that in the input ranges where ISR is present, the model has a stable equilibrium (a focus) and an unstable fixed point: this is a clear signature of the bistability as the upper unstable point corresponds to the voltage projection of the separatrix (see above) between the rest and the periodic processions toward the spiking threshold and the voltage reset.

To study the probability of transition to spiking we performed multiple numerical simulations when the model was stimulated by current noise with various means and amplitudes (variances). The resulting probability is shown in Fig.IV-5C. The comparison of this spiking probability and the mean firing rate (Fig.IV-4B) shows that these dependences have essentially the same shape. The similarity indicates that the mean firing-rate represents the balance of the probabilities of down-to-up and up-to-down state transitions. When the mean current is within the bistability range, there is strong inhibition of spiking near $30\,pA$ noise variance (red dot). For noise near 10 pA variance (green dot) the model preferentially stays in the spiking basin of attraction. However, when the noise amplitude becomes large (60pA; red dot) we observe random noise-driven crossings of the separatrix and transitions between spiking and rest. For still larger values of noise variance there is an increase in spiking probability, as it would be expected from a noise-driven threshold system. When the mean input current is beyond or below the bistability region $I = [-100pA, -200pA]$, there is no significant inhibition of spiking (and so no ISR; Fig.IV-5C, dashed and dotted lines). Fig.IV-5D–F show the trajectories in phase space for mean current within the bistability range and three different values of noise variance. In all cases initial conditions were initialized in the spiking region and then the model was stimulated with noise input with various amplitudes. This illustrates directly the phenomenon of ISR tuning as summarized in Fig.IV-5C.

IV.2.5.6 Functional role of ISR

Bistability can significantly influence the output spike pattern and the response of a PC to external input. As discussed in the previous section, bistability and ISR can be explained using an aEIF model, implying that only the spike generating mechanism and a slow voltage-dependent adaptation are necessary for the phenomenon. In this section we investigate the role of bistability for processing of a transient external input when different levels of synaptic noise are present. Our goal is to examine if there is a link between ISR

and the ability of the PC to respond to aspects of the incoming transient input (i.e. the signal).

To study the role of ISR for the input-output relationship of PCs, the model was held in the bistability range by adjusting the mean input current, and received two additional inputs: ongoing synaptic current noise and a brief excitatory current pulse (the signal) at a pre-set time (see Materials and Methods). To examine the input-output function of the model, we computed peristimulus time histograms (PSTHs, Fig.IV-6). Since we were interested in understanding the role played by the ISR in the stimulus-induced transitions from the quiescent to the spiking state, initially the model was set in the rest state in all simulations.

In the case of low noise amplitude (Fig.IV-6A), the model remained in the rest state before the arrival of the excitatory signal input, and hence the spiking probability was zero before the signal input; the basin of attraction of the rest fixed point is larger than the fluctuations induced by the noise. In this case the short synaptic excitatory input lad to a clear sharp transition to the spiking state (Fig.IV-6A). Once initiated, this spiking was not effectively inhibited by low-amplitude synaptic noise. Therefore the model remained tonically spiking after the application of the excitatory stimulus. In this situation the model acted as a latch, where the persistent spiking indicated that a stimulus has

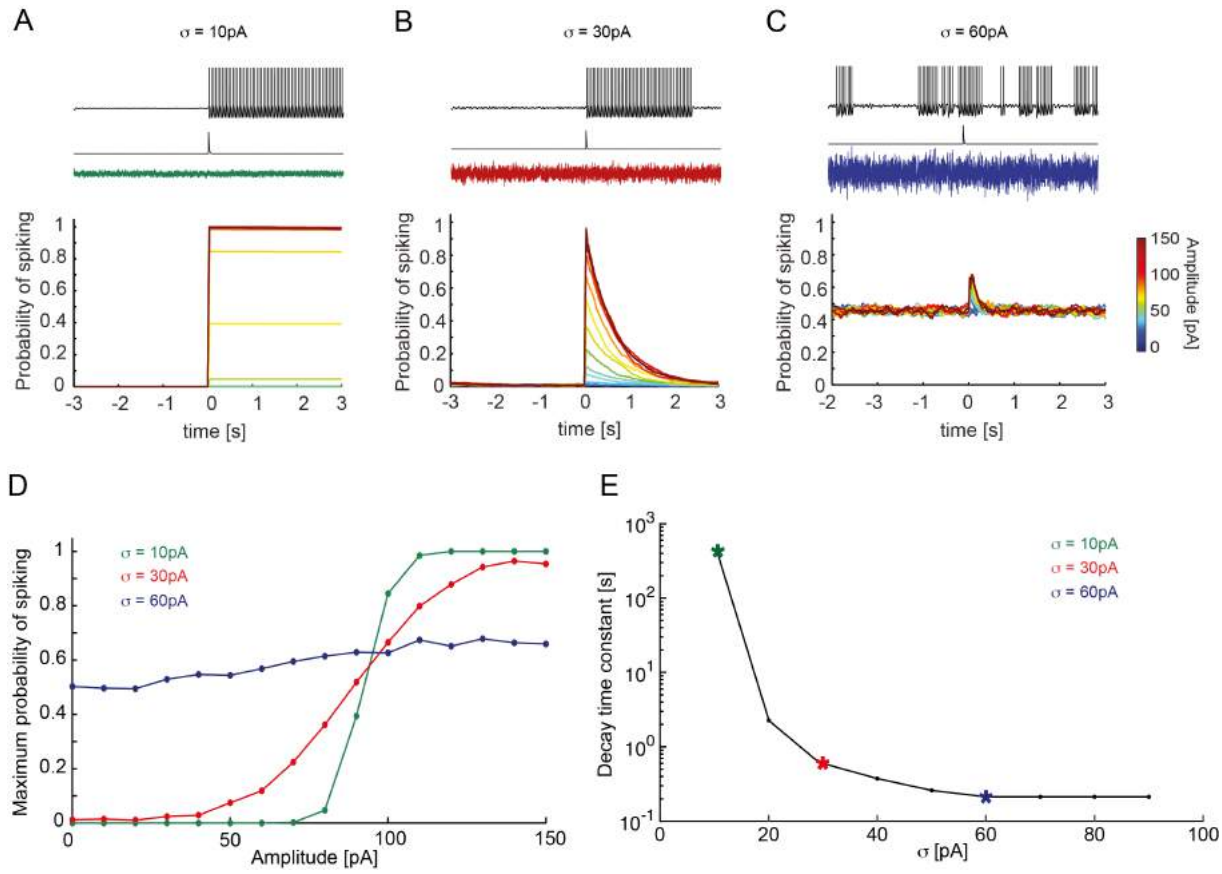

Figure IV-6. ISR transforms brief inputs into long-term firing states depending on background noise

A, B, C. Characteristic voltage traces of the aEIF model in response to a single synaptic excitatory input in the presence of different levels of background noise with amplitude $\sigma = 10\,pA, 30\,pA$ and $60\,pA$. Bottom. Corresponding probability of spiking for a range of input amplitudes (color code). D. Maximal probability of state transition vs. synaptic input amplitude for 3 background noise amplitudes, E. Decay time constant for the duration of the spiking state induced by the synaptic input of $100\,pA$. Remark: two points corresponding to $\sigma = 0\,pA, 100\,pA$ are not on E plot because for $\sigma = 0\,pA$ the duration of stimulus-induced spiking state is infinite, while for $\sigma = 100\,pA$ the duration of this state could not be distinguished from the firing baseline.

occurred at some point in the past. Had the model started in the spiking regime, the transient excitatory stimulus could switch it from spiking to rest (simulations not shown).

When the noise amplitude was optimal for inhibition (Fig.IV-6B), the model remained mostly in the rest state before application of the excitatory stimulus due to the ISR. Therefore the probability of spiking before the arrival of the signal input was small. When the transient stimulus was applied it led to an increase of spiking probability and a finite number of periodic spikes were triggered. After the end of the transient stimulus, the spiking probability gradually decreased to zero due to noise-induced inhibition indicative of ISR. Hence at optimal ISR noise amplitude, the model produced a transient spiking response to the transient stimulus, yet with a duration of the response that was significantly longer than the stimulus itself. Moreover, the probability of the response was related to the stimulus amplitude. Hence, the timing of the input and its amplitude could be decoded from the PC spiking activity.

In the case of high noise amplitude the model randomly switched between spiking and rest (Fig.IV-6C). This led to constant baseline probability of ~0.5 for spiking even in the absence of the stimulus. Once a stimulus was applied, it increased the probability of spiking compared to the baseline. The spiking probability decayed back to the baseline more rapidly than in the case of optimal noise amplitude for inhibition. Note that while there were spikes that were directly triggered by the transient stimulus, these spikes are hardly distinguishable from random spiking caused by the large amplitude noise. In this case the model acted neither as a latch nor is it able to signal the transient stimulus amplitude with any fidelity.

We summarize the noise-dependent effect on the response to the transient signal by plotting the peak probability of spiking as a function of the signal input amplitude, a signature of the input-output relation of the model (Fig.IV-6D). At low noise amplitude the input-output relation is close to all-or-none, but with noise amplitude in the optimal ISR range, the response becomes more proportional to the input amplitude (a flatter sigmoid). Above the ISR range, the input-output relation is almost flat (little information in the output about the input). For the optimal noise amplitude (red curve Fig.IV-6D) we see a sigmoid response behavior depending on the input amplitude. Below ~$50\ pA$ the model does not respond to the excitatory input by spiking because the input is not strong enough to bring the model out of the rest state. The peak probability saturates after ~$125\ pA$ amplitude. This means that beyond this value the model

becomes insensitive to the amplitude of the input and will respond with the same amount of spiking even for larger amplitudes of the excitatory input.

Next we study the duration of a spiking state caused by signal input stimuli. Fig.IV-6E shows the decay time constant of the spiking probability triggered by the transient input signal (Fig.IV-6A-C). For low values of synaptic noise, $\sigma = 10\,pA$ the model spikes for long periods of up to >1000 seconds. As noise amplitude increases, it significantly shortens the duration of the spiking induced by the stimulus. The reason for this effect is the following. As the noise variance approaches the ISR region (30 pA variance; green asterisk Fig.IV-6E), the lifetime of the spiking state decreases, because the noise turns off the stimulus-evoked persistent firing after which the model stays quiet. When noise increases beyond ISR-optimal variance, the model starts generating spikes that are not evoked by the stimulus (Fig.IV-6E, blue asterisk). This leads to lower values of the decay time constant as the model is switched ever more quickly between spiking and silent states by the noise.

We suggest that this may be a viable mechanism by which synaptic noise may control the duration of spiking responses induced by the external stimulus. In the low noise regime, spiking induced by the external stimulus would lead to long-lived spiking states, while in the presence of progressively stronger synaptic noise, the duration of the spiking state would become progressively shorter. In general, the probability of spiking in a PC population receiving the same single stimulus decays exponentially, but with different time constants set by the noise amplitude. Thus, in the optimal ISR noise regime the cell acts as a quasi-linear filter of the input, while in the low noise regime it acts as a memory device. Changing noise variance rapidly switches the cell from one mode to the other. Thus, the amplitude of the synaptic noise provided by ongoing parallel fiber input could provide rapid mechanism to set the duration of a spiking state caused by external signal stimuli such as a synchronous volley of parallel fiber input.

IV.2.5.7 ISR optimizes information transfer

We showed in the previous sections that ISR significantly modulates the persistent and stimulus-evoked firing in the experiment and the quantitative model of a PC. Here we examine how ISR affects the transfer of information across a PC for a series of input signals similar those shown in Fig.IV-6. To do

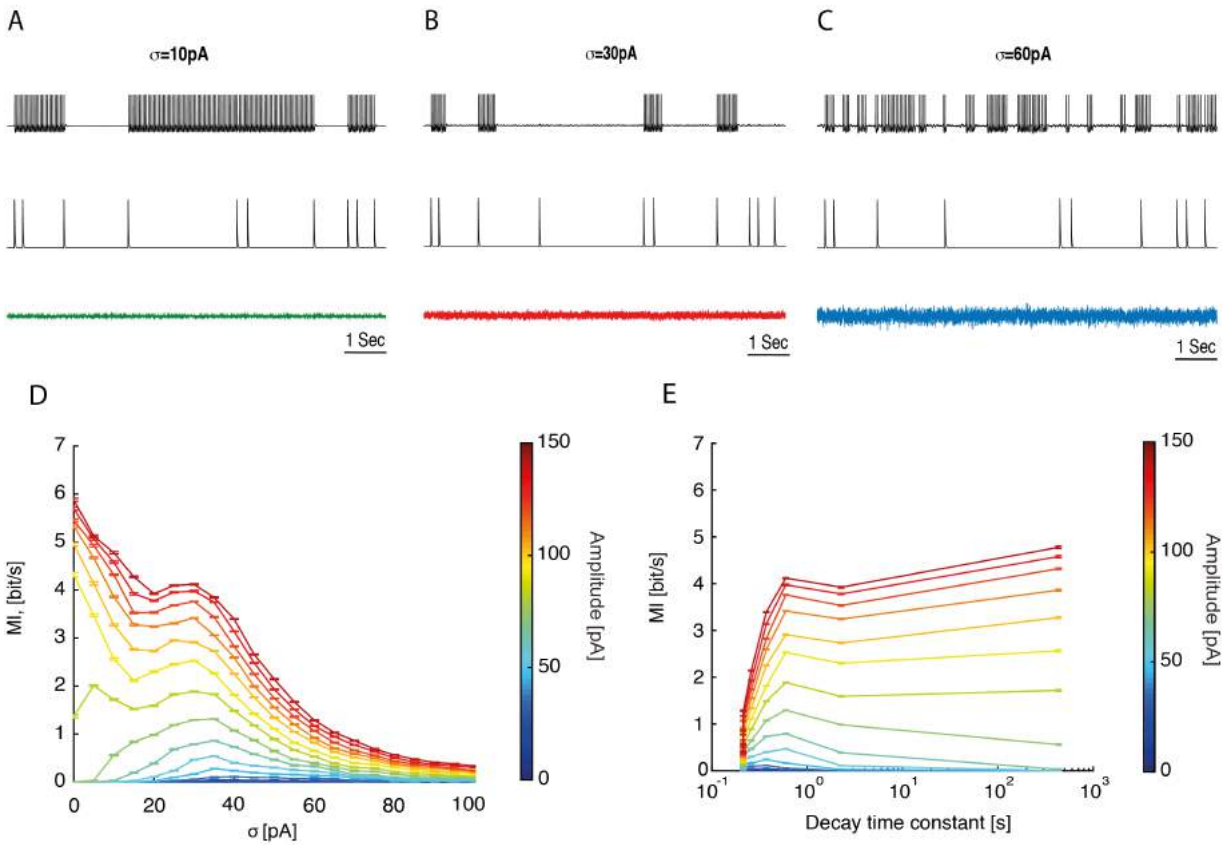

Figure IV-7. ISR leads to local optimum of mutual information between the input and output spike-train.

A, B, C. Voltage traces of the aEIF model in response to series of synaptic excitatory inputs, in addition to background stimulation noise with amplitude $\sigma = 10\,pA, 30\,pA$ and $60\,pA$, input amplitude Am=100pA. Top. Corresponding voltage trace. Bottom. Input to the model. D. Mutual Information of the input and output spike train of the aEIF model. MI is computed for the full value of mutual information; MI_{DU} for DOWN-UP transitions, MI_{UD} for UP-DOWN transitions. E. MI as a function of the decay time constant (duration of a spiking), Fig.IV-6E. Remark for E: two points corresponding to $\sigma = 0\,pA, 100\,pA$ are not on E plot similar to Fig.IV-6E. For $\sigma = 0\,pA$ the duration of stimulus-induced spiking state is infinite, while for $\sigma = 100\,pA$ the duration of this state could not be distinguished from the firing baseline.

so we take advantage of our quantitatively based aEIF model. The input for these numerical experiments consisted of synaptic noise with a parametrically adjusted amplitude and a Poisson signal spike train of 1Hz mean rate. This stimulus frequency is chosen for its relevance to the behavioral timescale (Yartsev et al. 2009). Depending on the synaptic noise amplitude, the state of the PC model can switch between periodic spiking (up state) and rest (down state) in response the incoming inputs (Fig.IV-7A-C).

In the case of low variance noise, with the cell starting in the down state, the synchronous synaptic input can trigger an up state, which persists until the next one (Fig.IV-7A). Given that the cell is in the up state, this next input then provokes the transition to the down state. This up-down transition will depend on the proper timing (or the relative phase of the spiking trajectory of the model) of an input: most efficient were
inputs that were time at a phase when the trajectory is close to the basin of attraction of a stable fixed point (Fig.IV-5A). The down-up transitions did not depend on the specific timing of the input because the trajectory stayed in the resting state basin of attraction and did not have any definable phase in its noise driven fluctuations. Thus, a series of signal inputs caused continuous switching of the system back and forth between up and down states (Fig.IV-7A).

When the noise variance was optimal for ISR (Fig.IV-7B), the cell demonstrated a characteristic type of behavior. Due to the noise-induced inhibition of sustained firing, the model was in the resting state most of the time. Even when the initial conditions were chosen in the up state, the model quickly switched to the down state (Fig.IV-6B). Once the external input was present, it brought the cell to spiking and the model stayed in the up state for ~1 sec (decay time constant, Fig.IV-6E) followed by a transition to the down state because of the ISR effect. Thus, ISR ensured a resting baseline with minimal spurious spiking before the subsequent external inputs, making the firing output sparse and causing the onset of spiking to be related to the onset of the signal stimuli.

In case of strong synaptic noise, the cell is switching between up and down states even in the absence of external stimuli (Fig.IV-7C). In this case an external stimulus leads to an increased probability of spiking compared to the baseline (Fig.IV-6C). However, these additional spikes are rare compared to random firing caused by noise (Fig.IV-7C). To study the efficiency of information transfer of the PC model we measured the mutual information rate between the input and output spike train for different levels of synaptic noise variance and input amplitudes. Fig.IV-7D shows the mutual information rate for different input

amplitudes ranging from subthreshold (0 - 90 pA) to suprathreshold (100 – 150 pA) as a function of noise amplitude. A peak in MI appears around $\sigma = 30\,pA$ for a range of input amplitudes. This corresponds to the ISR noise variance optimal for inhibition. For the subthreshold input amplitudes this peak is global, while for the suprathreshold amplitudes it becomes local.

The presence of the MI peak for subthreshold input is the consequence of the classical stochastic resonance (SR) effect that has been extensively studied (McDonnell and Ward 2011). The contribution of ISR to this effect is the following. When the noise amplitude is optimal for inhibition, it provides a stable down state for a cell in the absence of an input. In this case the incoming input is amplified by noise due to the SR effect and will trigger spiking, i.e. produce an up state. Then due to the influence of ISR this stimulus-induced spiking will terminate before the next input. This leads to a strong temporal association between the input and output spike trains. Each input spike will correspond to a ~1 second (decay time constant, Fig.IV-6E) spike train in the output with a high probability. After each input spike the cell will return to the down state due to ISR. This leads to the mutual information peak near the noise amplitude optimal for the ISR.

In the case of suprathreshold input, the MI was maximal for zero noise variance because a strong input could reliably trigger up and down transitions. In this case the noise plays mostly a disruptive role because it adds additional spurious output spikes unassociated with the input stimuli. However, in the presence of ISR the number of these spikes is smaller since synaptic noise prepares the baseline, setting the spontaneous spiking activity close to zero, thereby making the input and output spike train temporally associated. Therefore we observe a local peak of MI associated with ISR even for the suprathreshold input amplitudes.

To study the relationship between the duration of a spiking state and mutual information we combine the time constant estimation (Fig.IV-6E) with our mutual information measure (Fig.IV-7D). As shown in Fig.IV-7E, a peak near 1 second spiking duration is present for all input amplitudes, which is the consequence of ISR. Similar to Fig.IV-7D, this MI peak is global for the subthreshold input and becomes local for suprathreshold input. For subthreshold input, this means that the synaptic noise amplitude optimal for ISR corresponds to the optimal duration of the spiking state for information transfer measured by the output spikes, and for both types of input, long durations of the spiking state can coexist with high rates of information transfer.

IV.2.6 Discussion

We have characterized the effects of noise on the dynamical response regimes of cerebellar Purkinje neurons. We showed experimentally that simple spike firing in Purkinje cells can be efficiently inhibited by noisy input current if its variance is within a specific range, a phenomenon called inverse stochastic resonance (ISR). We then used an adaptive exponential integrate-and-fire (aEIF) model to quantitatively fit experimental data on subthreshold and spiking behavior of individual Purkinje cells using a modified dynamic IV method. For each cell, the resulting aEIF models exhibited parameter combinations generating bistable behavior. We found a good qualitative match between ISR measured experimentally in our Purkinje cells and in the aEIF model in terms of the hysteresis of the relation between firing rate and current, and the shape of the ISR curve. Analysis of the model revealed that ISR can be explained by the coexistence of a spiking and a resting state attractor. Using numerical simulations we showed that synaptic noise allows the Purkinje cell to switch between spiking up and silent down states, with their durations determined by the variance of the synaptic noise input. Our simulations further showed that ISR allows the PC to respond to transient inputs like a tunable filter, whose time constant can be set by the noise variance in a wide range, from a memory-toggle mode to a rapid filter mode. Finally, we show that a noise variance, which is optimal for ISR, leads to a local maximum of mutual information rate between the input and output spike train. These findings show that ISR is present in Purkinje cells and suggest possible roles for ISR in information processing in the cerebellar cortex.

Purkinje cells display ISR

Traditionally, noise has been seen as enhancing neural responses by increasing the probability of crossing the spiking threshold, and increasing the reliability of the spike train (Mainen and Sejnowski 1995). Furthermore, a nonlinear relationship was found between various measures of signal transmission (usually for a subthreshold stimulus) and the noise amplitude, a phenomenon known as stochastic resonance (SR). Much work on SR has identified the various stimulus and neuronal conditions for its existence, and potential functional roles (for a review see (McDonnell and Ward 2011).

A related, yet distinct phenomenon, where noise selectively decreases the probability of spiking, or converts persistent spiking activity into a short-lived

transient followed by long-term quiescence has only recently been identified. This effect has become known as inverse stochastic resonance (Gutkin et al. 2009). Initially described in bistable networks of spiking neurons (Gutkin et al. 2008), this phenomenon has subsequently been observed and analyzed in single neuron models, including in spatially extended ones (Tuckwell and Jost 2010). At optimal noise amplitude, the duration of the transient intrinsic activity is minimized as the noise effectively quenches the neuronal response. Modeling work suggested that bistability is a necessary condition, while simulations of compartmental models proposed that ISR results from noise injection at the site of spike generation. Further work showed that colored noise is more efficient at producing ISR when compared to white noise (Guo 2011), thereby hinting that synaptic noise may be particularly efficient at producing ISR in bistable neuronal systems. To our knowledge, the functional significance of ISR has not yet been analyzed, with the exception of (Dipoppa and Gutkin 2013) where ISR was suggested to play a role in limiting the duration of pathological working memories. Experimentally, signatures of noise-induced quenching of periodic activity were observed in the classical squid axon preparation (Paydarfar et al. 2006), where noise injection effectively stopped repetitive spiking, yet no tuning properties of the noise amplitude were noted.

In this study we present several lines of experimental evidence for ISR in cerebellar Purkinje cells. We found that simple spike firing in these neurons can be efficiently inhibited by current noise injections to the soma when the mean of the input current is in the subthreshold range (Fig.IV-1D, E). To quantify this effect we measured the average firing frequency as a function of the input noise variance. We found the characteristic minima of the firing rate for particular noise amplitudes, which are optimal for ISR in different neurons (Fig.IV-1B, C). Notably we observed that all Purkinje cells we studied displayed ISR (Fig.IV-1C).

To identify the range of the mean input current for which ISR can be observed, we applied a symmetric current ramp protocol (Fig.IV-2A, B). We found that the area of hysteresis between the ascending and descending instantaneous f-I curves indicates the range of mean currents at which ISR is present (Fig.IV-1D). This hysteresis, which can be defined as the difference in currents (ΔI) between the first and last spike in response to the symmetric ramp, measures the degree of bistability of a particular cell. We found a strongly positive correlation between the degree of bistability of an individual Purkinje cell and the noise amplitude, which is optimal for ISR in this cell. This argues for a strong link between ISR and the bistable behavior of Purkinje cells.

This hysteresis is also the reason why the occupancy of up and down states during noisy current injection is history-dependent (Fig.IV-1A). Thus, simple noise injection protocols such as the one in Fig.IV-1A cannot cleanly separate the steady-state ISR effect and the memory effect. We therefore switched to a noise injection protocol in which noise variance continuously changes (Suppl. SI). The results obtained by brief constant-variance noise injections (Fig.IV-1A) and the continuous noise protocol show a similar dependence of ISR on noise variance (Fig.IV-8B, D, F).

The visibility of Purkinje cell bistability in firing patterns of Purkinje cells recorded *in vivo* varies depending on experimental conditions, animal species and different regions of the cerebellum (Schonewille et al. 2006, Zhou et al. 2015). There is evidence for up and down states in ketamine-anesthetized rats (Rokni et al. 2009) and in awake behaving cats (Yartsev et al. 2009). The presence of patterns and pauses in Purkinje cell simple spike activity *in vivo* could be interpreted to result in part from their bistable behavior (Regan et al. 2007). On the other hand, recordings from Purkinje cells in the lateral and intermediate regions of the cerebellum concerned with arm movements do not show obvious up and down states (Norris et al. 2004, Roitman et al. 2009).

One possible solution of this controversy is that different degrees of visibility of Purkinje cell bistability can be explained by different neuromodulatory states in the cerebellum (Rokni et al. 2009). For example (Williams et al. 2002) have shown that serotonin can transform a tonically spiking Purkinje cell into one, which displays bistability. There is evidence that other biophysical mechanisms could regulate Purkinje cell bistability: for example, Bergmann glia could change the extracellular K^+ concentration by Ca^{2+}-dependent K^+ uptake (Wang et al. 2012) thus modulating the Purkinje cell excitability. Another possible explanation is that the properties of Purkinje cells could be different in various cerebellar zones (Urbano et al. 2006, Zhou et al. 2015). Also, our data demonstrates that Purkinje cells can exhibit various amounts of bistability (Fig.IV-2C and Fig.IV-4D), which may represent diversity both within and across different zones of the cerebellum.

As we show in this study, changing the mean and the standard deviation of the synaptic input current is a very fast way to move Purkinje cells in and out of the range of bistability. Thus, even if bistability is not always engaged and overtly visible *in vivo* (Schonewille et al. 2006), it is nevertheless likely that the underlying mechanisms are continuously present, and can influence Purkinje cell firing and network function in the cerebellum (Loewenstein et al. 2005).

ISR in the Purkinje cell model

Several detailed Purkinje cell models capturing the membrane properties as well as an anatomical structure of these neurons have been published, e.g. (Leigh et al. 1993, Roth and Häusser 2001). Usually such models have numerous state variables describing the membrane potential and voltage-gated conductances in multiple compartments. The advantage of their biological realism is balanced by the large number of variables and parameters they contain. This high dimensionality does not allow a straightforward application of dynamical system theory to gain insight into the mechanisms of excitability, which makes the interpretation of these models at times difficult.

For this reason we decided to use a reduced minimal model, the adaptive integrate and fire (aEIF) model, to study ISR and bistability. The advantage of this model is that it is well studied in terms of dynamical system analysis (Touboul and Brette 2008) and further relates to the normal form reductions of higher-dimensional models (including those with multiple compartments), making it in a sense a canonical model of spike generation. This allows us to use the dynamical system approach to analyze the model behavior. Despite the relative simplicity of the aEIF model, the estimation of the model parameters from experimental data is still a challenging task. Recently, the dynamic IV method (Badel et al. 2008) has been described to identify the parameters of aEIF models from intracellular recordings. Although it has not been used for spontaneously firing neurons, such as Purkinje cells, we show that it can be successfully applied to these neurons after necessary modifications of the dynamic IV method (see Materials and Methods).

We found that an aEIF model with the parameters provided by a modified dynamic IV method allows us to qualitatively reproduce ISR and the hysteresis of the firing rate of the Purkinje cell. Remaining quantitative differences are likely to be due to the dynamic IV procedure, which does not allow us to estimate parameters related to the dendrite. This might be negligible for neurons with a relatively small dendritic tree (Badel et al. 2008), but for Purkinje cells it represents a problem. To compensate for this issue we have included a passive dendrite in the aEIF model and estimated the dendrite parameters (Supp. II). We have found that ISR effect is still present in the model with a passive dendrite, but the shape of the ISR curve becomes wider, which makes the model more consistent with the experimental data. We argue that using a two-compartment

aEIF model would allow a quantitative match of the experimental ISR curve, but in a two-compartment aEIF model it is more difficult to precisely estimate the necessary parameters from somatic intracellular recordings.

The aEIF model has a very rich repertoire of dynamical states and can be tuned to reproduce the spiking behavior of many different neurons (Badel et al. 2008). The relevant property for bistability and ISR is type II excitability, due to the presence of a Andronov-Hopf bifurcation. This bifurcation is responsible for the transition from the rest state to the spiking state and backwards. Crucially, it allows the model to have a spiking and a resting state attractor for the same parameter set. We show that the bimodal behavior of Purkinje cells as well as ISR can be explained by this bistability of the aEIF model solutions. When the initial conditions are set inside the rest state attractor, the model will come to the resting state, while in all other cases the model will continuously generate spikes (Fig.IV-5A). The key parameter for bistability in the model is the mean of the input current. If it is in the bistable region of the f-I curve, then the model displays bistability most clearly in the presence of noise (Fig.IV-4C).

When the model is in this regime, synaptic noise of particular amplitude is able to move the system preferentially to the basin of attraction of the rest state. This happens because the shape of the basin of attraction provides non-symmetric probabilities for up-to-down and down-to-up transitions. In the case of ISR, the probability of down-to-up transitions becomes very low, reducing the occupancy of the spiking state. This leads to a “latch” effect – once the system moves to the basin of attraction of the rest state, it cannot go back because the noise amplitude is not strong enough. Essentially this mechanism constitutes the main explanation for the ISR effect. Thus, ISR is possible only if the model is bistable. Rescaling of the model revealed the key parameter combinations responsible for bistability and ISR, such as adaptation and its timescale (Fig.IV-4D, E, F).

Functional consequences of ISR

The function of cerebellar Purkinje cells is often considered in the context of adaptive filter models of the cerebellum (Dean and Porrill 2011, Dean et al. 2010). A key property in this framework is the linearity of the input-output relation of Purkinje cells. Our data shows that above the minimum firing frequency, the relationship between the input current and the output firing rate is highly linear (Fig.IV-2B). This is in line with previous findings (Walter and Khodakhah 2006), as well as with the linear phase response curve behavior of Purkinje cells (Phoka

et al. 2010, Couto et al. 2015). On the other hand, the step-linear shape of the f-I curve, which is a hallmark of the type II excitability of Purkinje cells, and the binary nature of the bistable behavior underlying ISR appear to contradict the idea that Purkinje cells perform linear transformations of their inputs. Since we show that Purkinje cells can operate in both regimes depending on the input current (Fig.IV-2B), and the bistable behavior is stochastic, we suggest that this apparent contradiction can be resolved at the level of populations of Purkinje cells. We show that the size of the region of bistability varies in different Purkinje cells, as does the absolute position of the steps in the f-I curve. It is also likely that different Purkinje cells in a population receive background synaptic input with different mean and variance, for example due to variability in the local structure of the feedforward inhibition circuit represented by molecular layer interneurons. This diversity in the intrinsic properties and the synaptic input in a population of Purkinje cells could result in an approximately linear input-output relation at the population level.

In addition to this approximate linearity, behaviorally relevant adaptive filters need to implement time constants, which are much longer than the typical membrane constants of single Purkinje cells or other cerebellar neurons. The up and down states with their potentially long lifetimes could provide the necessary mechanism for filters with long time constants. Furthermore, our model suggests that the lifetime (in a single Purkinje cell) or the filter time constant (in a population of Purkinje cells) can be regulated by changing the variance of the input noise (Fig.IV-6E). An alternative interpretation of the potentially long lifetimes of up and down states is that they could implement a form of short-term memory. This is in line with a recent study (Clopath et al. 2012) which showed that bistability of Purkinje cells can increase their pattern storage capacity. Tunable Purkinje cell bistability could also be involved in generating the conditioned responses observed in (Johansson et al. 2014).

We propose the following mechanism of up and down state transitions in ISR. When synaptic noise is optimal for inhibition (Fig.IV-6B), the Purkinje cell preferentially stays in the resting state in the absence of specific signal stimuli. Once the neuron receives a strong external signal input, it brings the cell to the spiking state. The duration of this induced spiking can last up to several seconds, which is much longer than the membrane time constant of the Purkinje cell (Fig.IV-6B). Eventually, the cell stops firing due to ISR and thus prepares for the next signal input. Thereby, when the noise variance is optimal for ISR, the Purkinje cell acts as a filter with a long time constant because a brief external input can trigger a long-lasting up state. In this case, input noise optimal for ISR plays two roles. First, it prepares the baseline for the next input due to the inhibition of spiking. Second, it sets the mean lifetime of the up state, and therefore the time constant of the filter.

For noise amplitudes below the ISR peak, the lifetimes of the up and down states increase further, leading to a different mode of operation of the Purkinje

cell. In this mode, most transitions from up to down and from down to up are triggered by external signal inputs (Fig.IV-6A). In this regime, the Purkinje cell acts like a toggle switch (Loewenstein et al. 2005). Thus, the amount of synaptic noise provided by parallel fiber input can tune Purkinje cell responses in a wide range between a toggle and a linear filter mode. This mode switch could occur at a very fast time scale, since the noise level in the parallel fiber population can change quickly. However, once the synaptic noise variance becomes too large (Fig.IV-6C and Fig.IV-7C), most transitions between spiking and rest are triggered by the noise, and the Purkinje cell cannot reliably perform either of the two modes of operation.

To quantify how different input noise levels affect the information transmission capacity of the Purkinje cell, and to examine the potential role of ISR in information processing in the cerebellum, we estimated the mutual information between a signal input spike train and the output spike train of the Purkinje cell model at different levels of noise variance. We found that for the noise amplitude optimal for ISR, the mutual information rate has a local optimum, indicating that synaptic noise of particular amplitude can significantly enhance the transmission of information across the Purkinje cell to downstream neurons. In summary, ISR could provide a mechanism for setting both the time constants of temporal filters implemented by the firing of a Purkinje cell population, and the maximum rate of information that Purkinje cells can pass on to downstream targets.

IV.2.7 Supplementary information

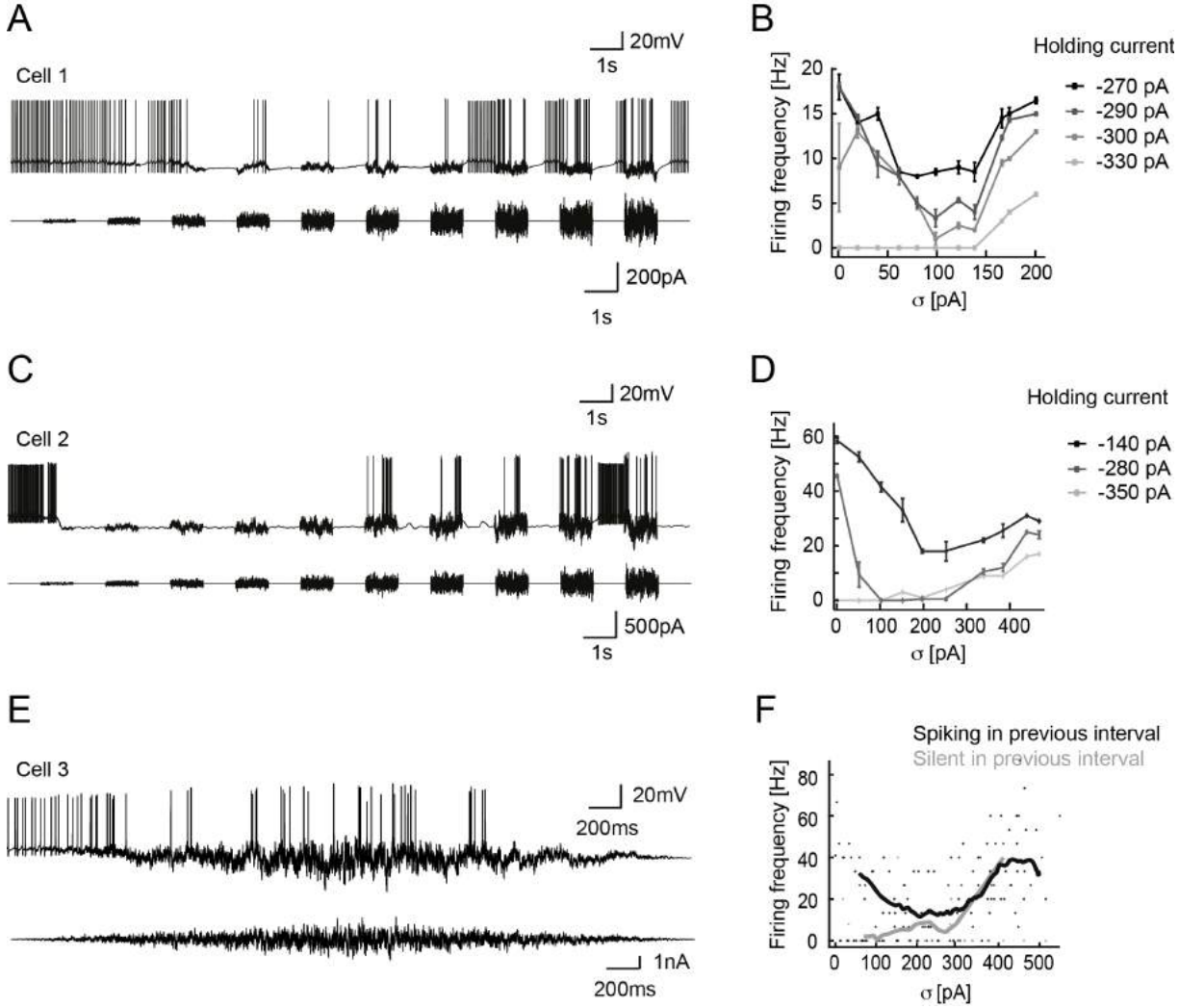

Figure IV-8. History dependence of the ISR curve
A. Current injection of $1\,s$ noise waveform periods for Cell 1, as in Fig.IV-1B. B. Firing frequency vs noise amplitude σ for five different holding current I_{in}. C. Current injection of $1\,s$ noise waveform periods for a different cell (Cell 2) with a more pronounced bistability. The firing frequency during each noise period is influenced by the state of the cell (firing or silent). D. The firing frequency vs noise amplitude σ for three different holding currents I_{in} illustrates the history dependence of the ISR curves. E. Current injection of noise waveform with linearly increasing and decreasing amplitude for Cell 3. Periods of 200 ms duration were separated according to the state (firing or silent) of the previous interval. F. Firing frequency vs. noise amplitude σ for the two categories. Continuous curves are running averages.

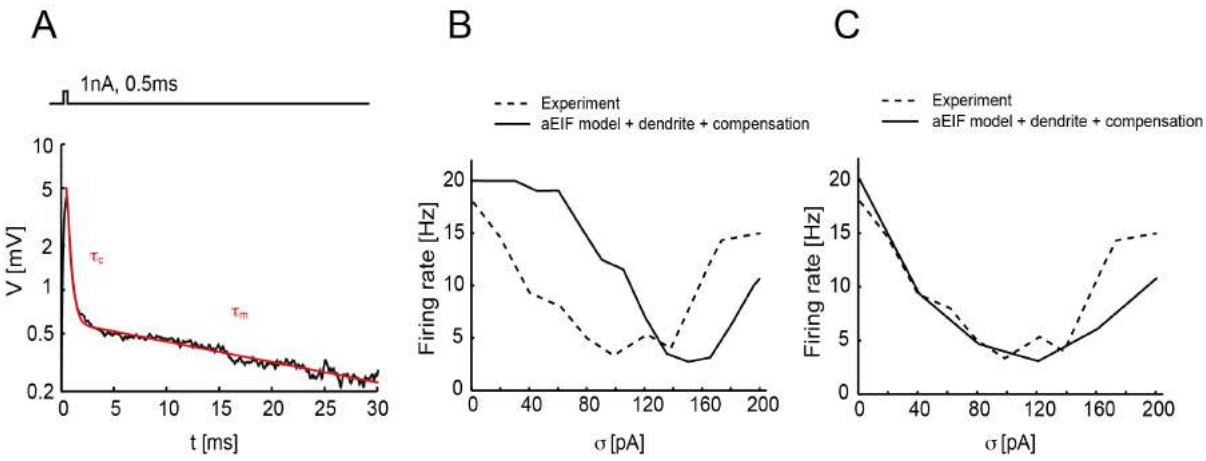

Figure IV-9. ISR and dendrite filtering

A. Experimental determination of dendritic filtering properties. Voltage response of a Purkinje cell (black) to a short current pulse ($0.5\ ms$, $1\ nA$), fitted with a biexponential function with time constants τ_m and τ_c (red). B. Mean firing rate in the experiment and the aEIF model in response to current noise stimulation, using the estimated dendrite filter parameters, $g_C = 10.2nS$. C. Mean firing rate of the aEIF model with optimized $g_C = 7.5nS$ to quantitatively match the experimental ISR.

The effect of dendrites on ISR in Purkinje cells

For all simulations in the main text we use the single-compartment aEIF model. Using the dynamic IV method (see Materials and Methods), we estimated the parameters of the aEIF model for different Purkinje cells. However, fitting of the parameters of an aEIF model based on data obtained with somatic recordings describes mostly the somatic properties of a neuron. This leads to the discrepancy between the optimal noise levels for the single-compartment model and actual data (compare Fig.IV-1B and Fig.IV-4B; model based on recordings from the same cell). This discrepancy is expected because the single-compartment aEIF model does not include the dendrite compartment. Since they have an important role in in the biophysics of Purkinje cells, here we determine the implications of including the dendrites in a reduced model and evaluate the role of dendrites for the ISR phenomenon.

While it is a single-compartment model, we want to take advantage of the aEIF model to allow phase-plane analysis, rather than fitting a two-compartment model or using the biophysically detailed approach, which could not be studied analytically. To compensate for the absence of a dendrite in the aEIF model, we add a passive dendrite compartment to it. Then we estimate the parameters of the dendrite using the impulse response of a Purkinje cell, use these parameters in the aEIF model, and show that ISR is still present.

Two-compartment model

To evaluate the role of dendrites in the aEIF model, we first consider a two-compartment model in the passive regime. It makes it analytically easier to start with this passive case that corresponds to the subthreshould behavior of the membrane potential. Then we will use this estimation in the following subsection.

Here are the two equations describing the current balance in the somatic and dendritic compartment of the model:

$$C_m \frac{dV_D}{dt} = -g_l(V_D - E_m) - \frac{g_c}{(1-p)}(V_D - V_S)$$
$$C_m \frac{dV_S}{dt} = -g_l(V_S - E_m) - \frac{g_c}{p}(V_S - V_D) + I_{in}(t) \qquad \text{(S1)}$$

where V_S corresponds to the somatic voltage and V_D is the voltage of the

dendritic compartment, and where C_m is the membrane capacitance. The parameter $p = \frac{S_1}{S_1 + S_2}$ represents the somatic surface area S_1 as a fraction of the total surface area of the soma and dendrites, $S_1 + S_2$, g_C is the coupling conductance between the compartments and g_l is the leak conductance. Since (S1) is a system of linear differential equations, it can be solved analytically by subtraction of the second equation from the first, followed by integrating the system:

$$\frac{d(V_S - V_D)}{dt} = -\frac{1}{C_m}\left(g_l + \frac{g_c}{p} + \frac{g_c}{1-p}\right)(V_S - V_D) + \frac{I(t)}{C_m}$$

$$V_S - V_D = \frac{1}{C_m} e^{-\frac{t}{\tau_c}} \int_0^t I_{in}(s) e^{\frac{s}{\tau_c}} ds \qquad \text{(S2)}$$

where $\tau_c = \frac{C_m}{g_l - g_C / p(p-1)}$ and $g_l = \frac{C_m}{\tau_S}$. This describes the voltage difference between the somatic and dendritic compartments in the subthreshold regime.

The following dendrite estimation is strictly valid only in the subthreshold regime. When the voltage goes beyond the threshold it becomes incorrect. But given that most of the time the membrane potential is subthreshold (Fig.IV-5), and the action potential upstroke is very fast because of the exponential term, we assume here that this approximation is sufficient to capture the main effect of a passive dendrite.

Estimation of dendrite parameters

To estimate the parameters of the Purkinje cell dendrite, we approximate the cell as a two-compartment model as described in the previous section. Then we aim to determine the kernel response to an infinitely short current injection as in (Clopath et al. 2007). Experimentally, we inject a brief current pulse (duration dur = 0.5 ms and amplitude 1 nA) into the soma and measure the somatic voltage response, which is then fitted by the kernel response $K(t)$ (Fig.IV-9A). This kernel can be derived analytically from (S1) in the following form (for details see (Gerstner and Kistler 2002)):

$$K(t)=\frac{I}{C_m}e^{-t\left(\frac{1}{\tau_s}+\frac{1}{\tau_c}\right)}\left(e^{\frac{t}{\tau_s}}\left(e^{\frac{dur}{\tau_c}}-1\right)(p-1)\tau_c+e^{\frac{t}{\tau_c}}\left(e^{\frac{dur}{\tau_s}}-1\right)p\tau_s\right) \quad \text{(S3)}$$

where τ_S is the membrane time constant, τ_c is the coupling time constant, C_m is the somatic capacitance, dur is the duration of the pulse, and p is the relative somatic surface area.

We fit the experimentally measured voltage response with this biexponential kernel with (C_m, p, τ_S, τ_c) as free parameters. Since the Purkinje cell has a large dendritic tree, the single pulse response consists of two phases: fast equilibration of membrane potential between the somatic and dendritic compartment via the coupling conductance, and slow discharging of the membrane potential in the entire neuron towards the resting potential via the leak conductance. The coupling conductance between two compartments is then defined as $g_C = C_m p(1-p)(\frac{1}{\tau_C}-\frac{1}{\tau_S})$.

Table of parameters.

C_m	τ_S	τ_C	p	*dur*	*I*
66.97pF	*32.91ms*	*0.70ms*	*0.07*	*0.5ms*	*1nA*

The effect of dendrites on ISR

As mentioned above, the aEIF model contains only one single compartment. In this section we use the passive dendrite model derived in the previous section and include it into the aEIF model. To achieve this, we add the dendritic term that represents the passive filtering property of the dendritic compartment, as described in (S1-S2):

$$C\frac{dV}{dt}=-g_L(V-E_L)+g_L\Delta_T e^{\frac{V-V^T}{\Delta_T}}-w+I(t)-\frac{g_C}{pC_m}e^{-\frac{t}{\tau_C}}\int_0^t I(\tau)e^{\frac{\tau}{\tau_C}}d\tau \quad \text{(S4)}$$

$$\tau_w\frac{dw}{dt}=a(V-E_L)-w \quad \text{(S5)}$$

As it is not possible to experimentally determine all the parameters of the spiking aEIF model and the dendritic parameters of a Purkinje cell at the same time, we follow an *ad hoc* strategy: we use both the parameters of the simple aEIF model fitted to data from a Purkinje cell (see Materials and Methods) and the dendritic parameters determined for the same cell, as described above.

The addition of an effective dendrite compartment brings an additional current to the aEIF model as $I(t)$ is replaced by

$$I(t) - \frac{g_C}{pC} e^{-\frac{t}{\tau_C}} \int_0^t I(\tau) e^{\frac{\tau}{\tau_C}} d\tau \qquad \text{(S6)}$$

The additional current represented by the integral term significantly changes the total input to the cell. It provides a current sink, which is dependent on the input. This significantly reduces the total amount of input current. It becomes necessary to compensate for this current sink to keep the model within the same ISR range as the aEIF model without a dendrite.

Dendrite compensation

We are motivated by the fact that in the experiment it is relatively easy to change the mean of the input current $I(t)$ compared to changing other parameters. Therefore we develop a compensation model that keeps the aEIF model tuning in the same bistability range as if the dendrite was not present.

First let us consider the external input to the aEIF model (S4) that can be decomposed into two components:

$$I(t) = I_{mean} + \sigma\eta(t) \qquad \text{(S7)}$$

where I_{mean} corresponds to the constant current while $\sigma\eta(t)$ is the noise part, with Ornstein-Uhlenbeck noise $\eta(t)$. We use the following analytical expression to keep the model within the same mean of an input current tuned for ISR:

$$I_{comp} = \frac{I_{mean}}{1 - g_C / pG} \qquad \text{(S8)}$$

where $G = g_l + \frac{g_C}{p(1-p)}$ is the total conductance. Thus, the compensated input to the aEIF model will be

$$I(t) = I_{comp} + \sigma\eta(t) \qquad \text{(S9)}$$

After this compensation, the aEIF model with a dendrite is again able to display ISR because the bistability range of input current is preserved (Fig.IV-9B). Addition of a dendrite with compensation indeed changes the shape of the ISR curve. These changes are expected from the compensation model we use. The mean of a compensated input (S6) is tuned in the bistability regime. But the variance of the noise component stays the same. This leads to changes in variance tuning because the total input to the model including noise will be filtered by the dendrite. It results in a smaller effective noise variance because of the attenuation by the dendrite, and shifts the ISR region to the right since the effective noise amplitude will be lower (Fig.IV-9B).

Unfortunately, fitting an aEIF model using the dynamic IV procedure is not perfect because it takes into account not only the somatic properties of a cell, but partially also the dendrite (Badel et al. 2008). To separately estimate the dendrite parameters of the Purkinje cell we use the impulse response of the cell (Fig.IV-9A). Then we use the aEIF model with mean current compensation and dendrite parameters estimated from the experiment. As a consequence, the dendrite effect is taken into account twice – using the dynamic IV fitting and the impulse response of the cell. This leads to the quantitative mismatch between the experimentally measured ISR and model ISR (Fig.IV-9B). Since the dendrite is overestimated in the model, we reduce the coupling conductance g_C from 10.2 nS to 7.5 nS (Fig.IV-9C). This allows a more precise quantitative match between the experimental and model ISR.

In the previous sections we have shown that ISR is still present in the aEIF model even if the effects of a dendrite are included. But the mean input current has to be rescaled according to the dendrite parameters. Indeed, addition of the dendrite changes the tuning for the ISR, shifting the optimal noise amplitude to values more similar to those observed experimentally. It is likely that fitting the parameters of a two-compartment or multicompartmental model to the data would probably lead to an even better quantitative match between the experiment and the model. But unfortunately it would not be amenable to phase plane analysis.

IV.3 Detailed model description

In this section we provide the additional information about the computational models used in this project. In particular we describe the bifurcation structure and the phase plane analysis of the aEIF model, mutual information algorithm used in information analysis and an estimation of the synaptic input to the Purkinje cell.

IV.3.1 Adaptive exponential integrate-and-fire model

The biophysics of neurons is well understood in terms of channels, currents, conductances and membrane properties. Since the discovery of (Hodgkin and Huxley 1952) a lot of important mechanisms modulating single neuron behavior were to the singe neuron description (Koch and Segev 1998). Despite the fact that these mechanisms are well understood in terms of neuron biophysics, studying all of them at once even in the mathematical models is a challenging task. The drawback of the detailed biophysical models is that they have very large parameter and variable sets, which does not allow to completely study their behavior for all possible parameter combinations (Marder and Taylor 2011).

To partially solve this problem several authors have introduced the minimal approach towards single neuron computation (Izhikevich 2003, Brette and Gerstner 2005). They proposed minimal two-dimensional models to describe the single neuron behavior. Despite their simplicity minimal models are able to capture multiple dynamic behaviors of single neurons, such as regular spiking, spike-frequency adaptation and bursting. Comparisons with the Hodgkin-Huxley models and single neuron recordings showed that these models are capable to properly match up to 98% of spike times in response to the *in vivo*-like current noise stimuli (Brette and Gerstner 2010).

Generally speaking all these two-dimensional models are the class of models described by the following equation $dV/dt = F(v) - w + I$, where F is a smooth convex function with negative derivative at $-\infty$ and infinite at $+\infty$ (Touboul 2008). In this section we describe the bifurcation properties of the aEIF model belonging to this class and used in our study.

Most of the results in this section are taken from (Touboul and Brette 2008). We decided to add it to this chapter to make the model description presented in the paper more consistent. We describe only the subthreshould behavior of the aEIF model. The information about firing behavior of the model could be found in the following works (Gerstner and Brette 2009, Brette and Gerstner 2010).

aEIF model equations and rescaling

The original aEIF model is described using two variables describing the membrane potential V and adaptation current w. The dynamics of the system is governed by equations (1-2):

$$C\frac{dV}{dt} = -g_L(V - E_L) + g_L\Delta_T \exp(\frac{V - V^T}{\Delta_T}) - w + I \qquad (1)$$

$$\tau_w \frac{dw}{dt} = a(V - E_L) - w \qquad (2)$$

if $V \geq Tr$ then $V = V_{reset}$ and $w = w + b$ (3)

Once the membrane potential V is close to V^T enough it starts to grow rapidly due to the exponential term. This divergence models the initial phase of spike. Once the membrane potential reaches the upper threshold Tr, V is reset, while the adaptation variable w is increased in according to the equation (3).

The physiological interpretation of this model is the following V describes the membrane potential difference between the inside and outside of the neuron membrane. The current passing through the membrane consist of capacitance, ionic and injected current to the cell. w describes the adaptation currents present in the neuron. This current increases with each spike providing the negative current to the voltage equation (1). Thus this current provides a negative feedback, which results with a decrease of a spiking frequency adapting the neuron spiking towards the input.

The exponent in equation (1) describes an action of a sodium channel by neglecting sodium inactivation and assuming infinitely fast activation. Since the activation function is described using Boltzmann functions (Izhikevich 2007), the approximated current is exponential near spike initiation therefore it is approximated using the exponent with Δ_T slope factor. The second variable, equation (2) could model the spike-triggered adaptation for $a > 0$ or dendritic compartment for $a < 0$. The coupling variable a could result from the linearization of potassium ion channel or from the axial conductance in case of dendritic compartment.

Model parameters and dimensionality

C	g_L	E_L	Δ_T	V^T	τ_w	a	V_{reset}	b	I
pF	nS	mV	mV	mV	ms	nS	mV	pA	pA

The aEIF model with 9 parameters could be rescaled to 5 parameter combinations describing the essential properties of the model (Touboul and Brette, 2008). Equations (4-6) describe the dynamics of the rescaled model.

$$\frac{d\overline{V}}{dt} = -\overline{V} + e^{\overline{V}} - \overline{w} + \overline{I} \qquad (4)$$

$$\bar{\tau}\frac{d\bar{w}}{dt} = \bar{a}\bar{V} - \bar{w} \qquad (5)$$

if $\bar{V} \geq \overline{Tr}$ -> $\bar{V} = \overline{V_{reset}}$ and $\bar{w} = \bar{w} + \bar{b}$ (6)

In these equations membrane potential and adaptation variables should be rescaled in the following way:

$$\bar{V} = \frac{V - V^T}{\Delta_T} \qquad (7)$$

$$\bar{w} = \frac{w + a(E_L - V^T)}{g_L \Delta_T} \qquad (8)$$

The dynamics of the model then depends on the following parameter combinations.

Parameter combinations

$\bar{\tau}_w$	$\bar{a}$	$\bar{I}$	$\bar{b}$	$\bar{V}_{reset}$	$\bar{t}$
$\frac{g_L \tau_w}{C}$	$\frac{a}{g_L}$	$\frac{I}{g_L \Delta_T} + (1 + \frac{a}{g_L})\frac{E_L - V^T}{\Delta_T}$	$\frac{b}{g_L \Delta_T}$	$\frac{V_{reset} - V^T}{\Delta_T}$	$\frac{t}{\tau_m}$

In the following sections we will use the rescaled version of the aEIF model, equations (4-6) to show the excitability properties of this system.

Null-clines and excitability types

The dynamics of the model in the phase space (V, w) is defined by the number and type of the fixed points, which could be found as intersections of two null-clines, equations (1-2).

$$w = -g_L(V - E_L) + g_L \Delta_T \exp(\frac{V - V^T}{\Delta_T}) + I \qquad (9) \qquad \text{V-nullcline}$$

$$w = a(V - E_L) \qquad (10) \qquad \text{w-nullcline}$$

The first equation (9) is a convex function because of an exponential term, while the second equation (10) is just a linear function. The mutual positions of the nullclines is controlled by the amount of the injected current I, which is the parameter determining the null-cline intersection. When I is negative, the nullclines intersection gives the two fixed points. When I is increasing the system looses its stability via one of the following mechanisms

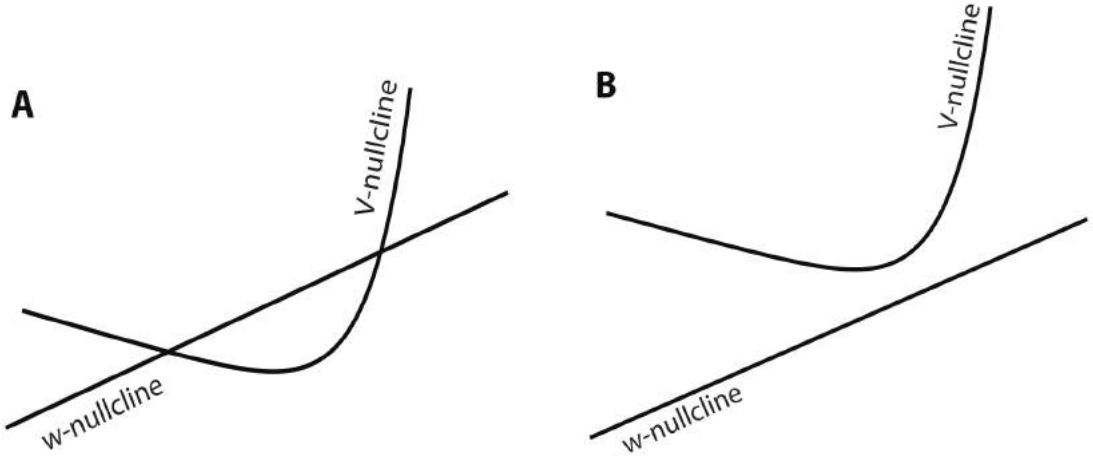

Figure IV-10. Nullclines and phase portrait of the aEIF model
A, B - the nullcline position in case of intersection and without it, correspondingly. Horizontal and vertical axes correspond to V and w. Adapted from (Touboul and Brette, 2008).

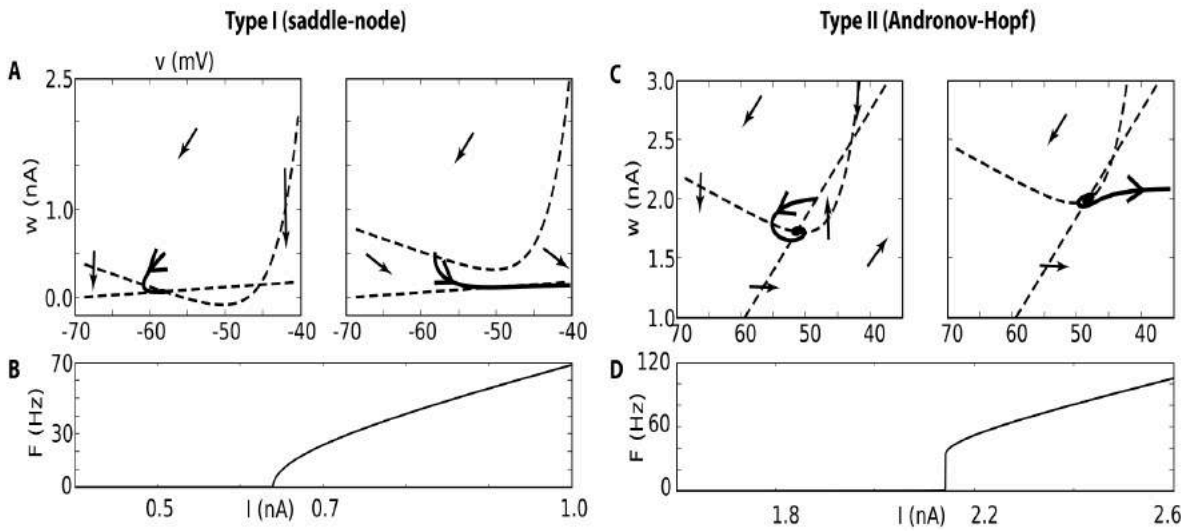

Figure IV-11. Excitability of the aEIF model
A, B – phase portrait and F-I curve of the system with type I excitability ($\frac{a}{g_L} < \frac{\tau_w}{\tau_m}$). C, D – the same for type II excitability ($\frac{a}{g_L} > \frac{\tau_w}{\tau_m}$). Arrows indicate the direction of the vector field. Adapted from (Touboul and Brette 2008).

depending on the model parameters.

If $\frac{a}{g_L} < \frac{\tau_w}{\tau_m}$ the aEIF model undergoes a saddle-node bifurcation (SN), i.e. stable and unstable points merge and disappear, Fig.IV-12A. This mechanism of loosing stability determines the type I excitability of the model meaning that the current-frequency, i.e. F-I curve, is continuous, Fig.IV-12B. It happens because the vector field is arbitrarily small near the bifurcation point, so the trajectory could
When the input current I increases the V-nullcline goes up and fixed points goes from 2 to zero. Thereby the trajectories move from rest to spiking. The excitability properties of the model depend on the mechanism of this transition as well as the bifurcation structure of the model.

When $\frac{a}{g_L} > \frac{\tau_w}{\tau_m}$ the system undergoes the Andronov-Hopf bifurcation (HB) before the SN bifurcation. It means that the stable point becomes unstable before merging with the saddle point, Fig.IV-12C. This property of loosing stability is responsible for type II excitability of the model, meaning that the F-I curve is discontinuous, Fig.IV-12D. It means that there is a sharp input threshold after which the firin-rate suddenly jumps from zero.

In the limit case when $\frac{a}{g_L} = \frac{\tau_w}{\tau_m}$ there is a Bogdanov-Takens bifurcation. It has co-dimension two meaning that to achieve this point two parameters should be changed simultaneously $\bar{a}$ and $\bar{I}$. At the bifurcation point the family of unstable periodic orbits generated around the HB collides with the SN fixed point and disappears via saddle-homoclinic bifurcation. This bifurcation is very specific for the parameter choices therefore we do not show its phase portrait.

Rheobase current

Rheobase current is defined as a minimum current injected to the neuron, which results in successful spike generation. It is the first point when the stable fixed point becomes unstable, which depends on the excitability type of the model.

For type I excitability it is calculated at the point of SN bifurcation, when the nullclines have one intersection point:

$$I_{rh}^{I} = (g_L + a)[V^T - E_L - \Delta_T + \Delta_T \log(1 + \frac{a}{g_L})]$$

For type II excitability it corresponds to HB point:

$$I_{rh}^{II} = (g_L + a)[V^T - E_L - \Delta_T + \Delta_T \log(1 + \frac{\tau_m}{\tau_w})] + \Delta_T g_L (\frac{a}{g_L} + \frac{\tau_m}{\tau_w})$$

SN bifurcation also occurs in type II excitability. It happens when the input current I same rheobase current for type I excitability.

Model threshold

Usually threshold for action potential generation is described as a voltage-threshold, although this threshold is not a particular model parameter. Single parameter for the threshold is possible only the linear integrate-and-fire model where it could be easily calculated analytically. In the nonlinear neural models such as aEIF the threshold corresponds to the separatrix in the phase space separating resting and spiking solutions. Therefore the area in the phase space where the trajectory crosses the separatrix corresponds to the threshold.

Nevertheless it is possible to determine the voltage threshold for a stationary voltage as a maximum voltage reached when $I < I_{rh}^{I,II}$. Due to nonlinearity this voltage threshold depends on the excitability type. It is defined as follows:

type I

$$V^{THR} = V^T + \Delta_T \log(1 + 1/g_L)$$

type II

$$V^{THR} = V^T + \Delta_T \log(1 + \tau_m / \tau_w)$$

Subthreshould oscillations

Since the aEIF model is dissipative system with a strong leak current all the subthreshould oscillations are damped and self-sustained oscillations are not possible in this model (Touboul 2008). Depending on parameter combinations a / g_L and τ_m / τ_w , the aEIF model could have type I or II excitability, Fig.IV-12A.

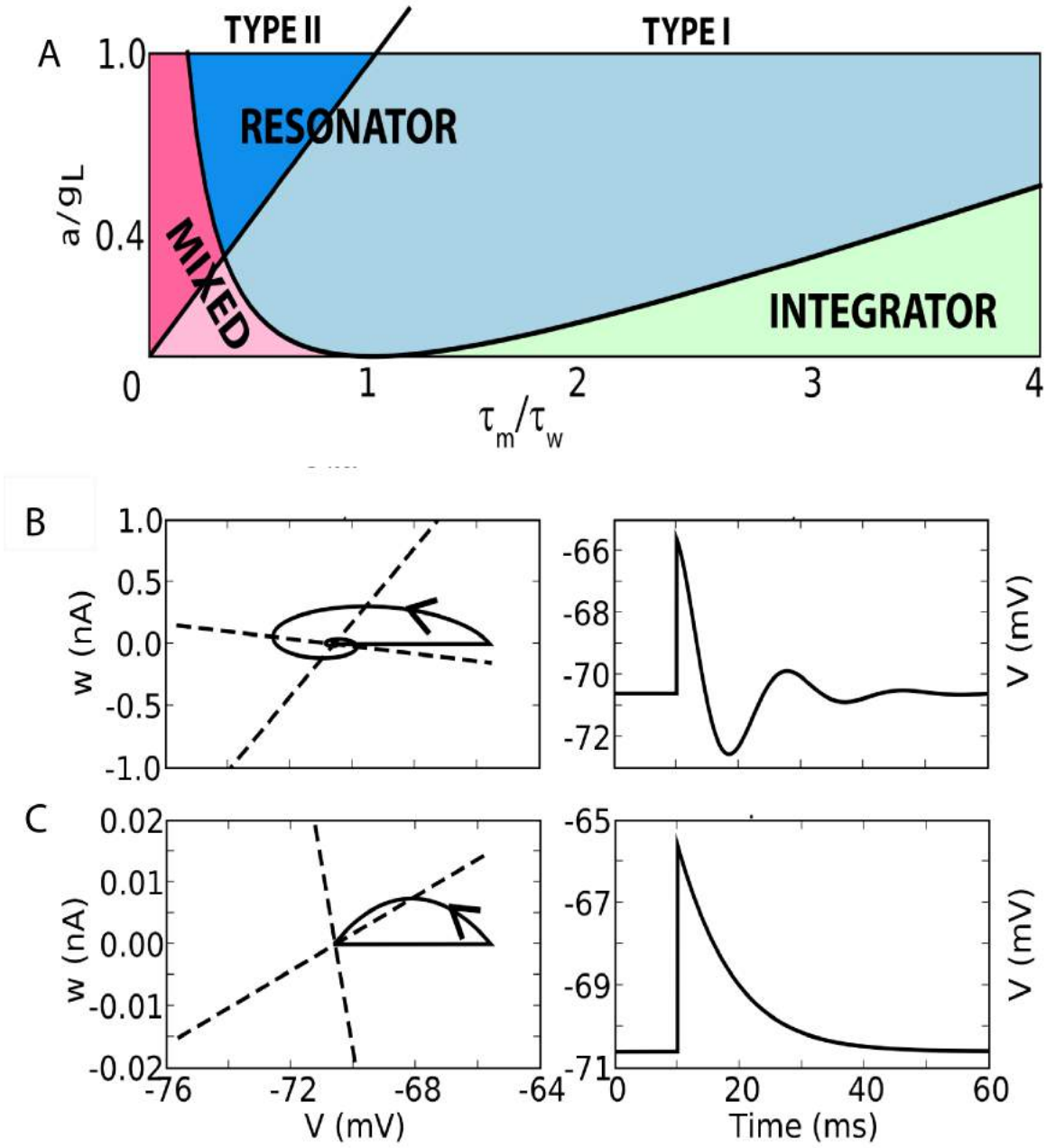

Figure IV-12. Subthreshould oscillation regimes of the aEIF model
A – parameter space of the model, blue – resonator, green – integrator, red – mixed mode. B, C – oscillations for type II and I excitability, trajectory in the phase space on the left, voltage V trajectory as a function of time. Adapted from (Touboul and Brette 2008).

The dynamics of the system near the threshold is determined by the eigenvalues. When the eigenvalues are complex, there are subthreshould oscillations near the resting state. In this regime the model oscillates when it is perturbed around the rest, Fig.IV-12B. The behavior of the model in this regime is called *resonator* since it demonstrates the resonance for the oscillatory input. When the eigenvalues are real and negative, local perturbations from the resting state will decay exponentially without oscillations, Fig.IV-12B. In this regime the model behavior is called *integrator* because there is no resonant input frequency and therefore it could only integrate the input. For the particular choice of model parameters there is also a *mixed* regime, Fig.IV-12A. In this regime the aEIF model behaves like an integrator or resonator depending on the amplitude of the input (Touboul and Brette 2008).

IV.3.2 Mutual information estimation algorithm

In this section we provide a short description of a Mutual Information (MI) algorithm used from the work of (London et al. 2002). Full description is present in the supplementary of the corresponding paper. Here we describe only the general framework of this method.

A first step to estimate the mutual information is to digitalize a spike train, Fig.IV-13A with the bin size Δt starting from the same time point. Then the MI algorithm operates with the digitalized spike trains. We applied it for the spike trains generated by the aEIF model for various noise variances and input amplitudes. The characteristic spike train of the aEIF model is present on Fig.IV-13B.

MI is estimated using the standard formula applied for single neuron input IN_n and output OUT_n spike trains of the length n:

$$MI(IN_n, OUT_n) = \overline{H}(OUT_n) - \overline{H}(OUT_n | IN_n)$$

where $\overline{H}(OUT_n)$ and $\overline{H}(OUT_n | IN_n)$ corresponds to the estimated entropy of OUT_n and IN_n spike trains. To illustrate this point we consider the spike train as $H(OUT_n | IN_n) = (x_1, x_2, ..., x_n)$, where $x_i \in \{0,1\}$ corresponds to the *i-th* bin. The corresponding string describes one realization of the stochastic process $x_i = \{x_i\}_{i=1}^{n}$. Then for an infinitely long spike train we could write the following expression using MacMillan-Brieman theorem:

$$-\frac{1}{n}\log_2 p(x_1, x_2, ..., x_n) \xrightarrow[n \to \infty]{} H$$

It means that Shennon information entropy approaches the entropy rate H of **X**, where $p(x_1, x_2, ..., x_n)$ is the probability to obtain the string $(x_1, x_2, ..., x_n)$ as a realization of **X**. Since $p(x_1, x_2, ..., x_n)$ is not known from one sequence we use an estimator $\overline{p}(x_1, x_2, ..., x_n)$:

$$\overline{H}_n = -\frac{1}{n}\log_2 \overline{p}(x_1, x_2, ..., x_n)$$

Given that the probability $\overline{p}(x_1, x_2, ..., x_n)$ is not known, there is need to use an algorithm to estimate all possible Markov processes with the length of D bins. The context-tree weighting algorithm proposed by (Willems et al. 1995) provides such estimation. This algorithm creates the binary tree based on the digitalized spike train and estimates the entropy of the source that is most likely to generate

the sequence $(x_1, x_2, ..., x_n)$. The same method is applied for estimation of the conditional entropy. Then the difference between the maximal entropy estimation for the output and input entropy corresponds to the mutual information between the spike trains. Since the algorithm does not always provide exactly the same estimate for different runs, the results should be averaged.

The general problem of the entropy estimators is under-sampling. If the spike-train is very long, the difference between the various entropy sources becomes negligible. While in the experimental conditions as well as in time-constrained simulations the sample size is always fixed. Therefore there is a need to use maximally efficient algorithms to estimate entropy from the available sequences. The context-dependent tree algorithm and corresponding mutual information estimate provides an efficient way to measure information content for the digitalized neurophysiological signal like spike-trains.

Parameters of MI algorithm: $b = 25ms$ - bin size, $D = 1000ms$ or 40 bins – length of the suffix-tree, $T = 1000s$ - length of the input and output spike train, $N = 10$ - the number of algorithm runs for MI average.

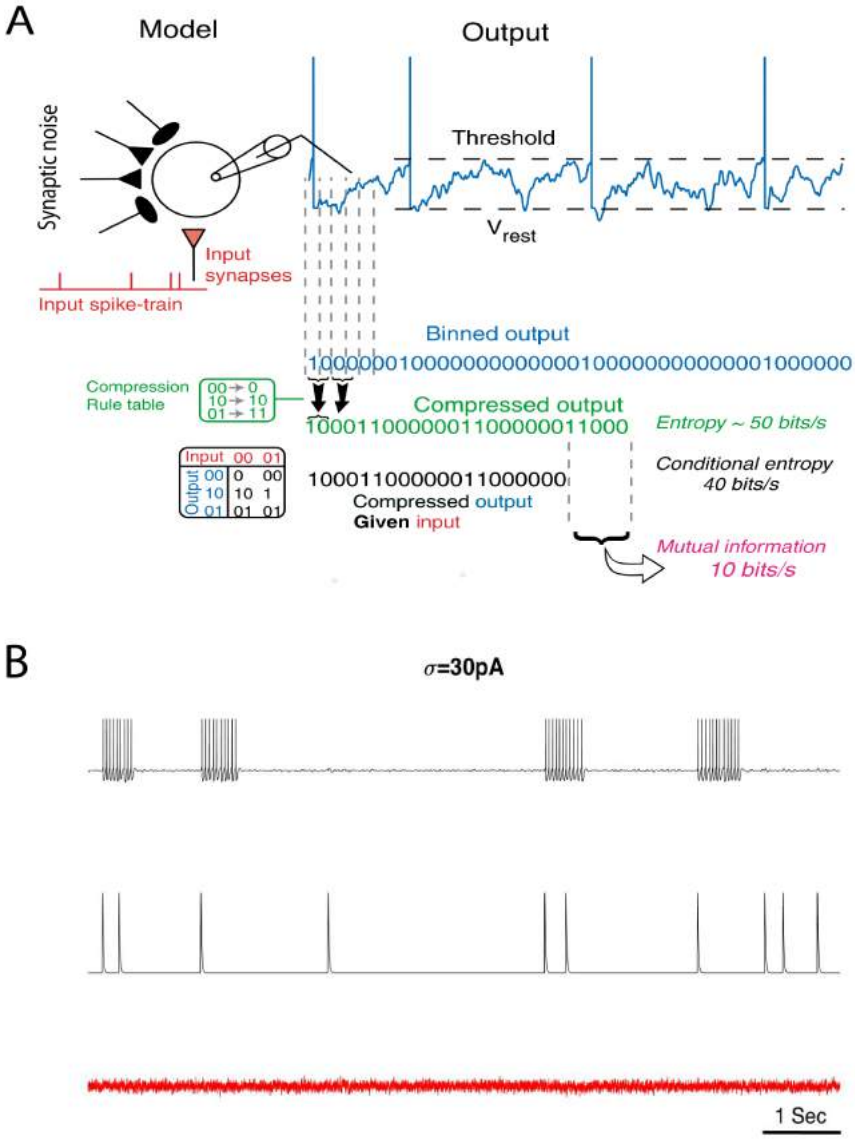

Figure IV-13. Mutual information measure in a single neuron model
A – neuron model with the input and output spike train. Adapted from (London et al. 2002). On the left is present the model receiving the background synaptic input and input spike-train. Input and output spike trains are digitalized. Compressed output corresponds to the full entropy calculated according to the compression rule table, green digits. Conditional entropy is calculated based on the input-output table, black digits. The difference between the full and conditional entropy corresponds to the mutual information. B –characteristic spike train of the aEIF model in response to the input stimuli and synaptic noise during 10 seconds. Upper trace – voltage trajectory of the model, middle trace – input spike train (Poisson process, 1 Hz), bottom trace – synaptic noise at the ISR amplitude, $\sigma = 30\,pA$.

IV.3.3 Synaptic noise estimation for Purkinje cell

Since we do not have explicit data about the Parallel Fiber (PF) input to the Purkinje cell, we use the theoretical considerations to calculate the synaptic noise produced by PF synapses. We take the following assumptions: 1) firing on PF synapses is uncorrelated therefore could be well approximated using the independent Poisson process; 2) the synaptic strength is normally distributed in the synaptic population; 3) all PF synapses have same similar kinetics 4) all synapses have the same release probability. Using these assumptions we describe the following characteristic monosynaptic EPSP using the biexponential function:

$$EPSP = A[\exp(-\frac{t-t_{pre}}{\tau_r}) + \exp(-\frac{t-t_{pre}}{\tau_d})]$$

where t_{st} - is the timing of the presynaptic spike, $A = 0.13pA$ - is the maximal EPSC amplitude, $\tau_r = 0.2ms$, $\tau_D = 2ms$ - are the corresponding rise and decay time constants. These parameters are chosen to match the EPSC waveform produced by the activation of a single granule cell (Isope and Barbour. 2002). The characteristic EPSC calculated with these parameters is present on Fig.IV-14A.

Assuming that parallel fibers fire independently and share substantially the same properties we derive the following expression for the EPSPs sum generated by the parallel fiber synapses:

$$EPSPs = \sum_{i=1}^{M} EPSP_i$$

$$M = N\ F\ P_r\ R\ T$$

where $N = 150\ 000$ is the average number of parallel fiber synapses on Purkinje cell (Wilms and Häusser 2015), $F = 0.01$ is the fraction of spontaneously active synapses (Wilms et al. 2006), $P_r = 0.44$ is the single synapse release probability (Valera et al. 2012), $R = 1Hz$ is the average synapse rate (Wilms et al. 2006) and $T = 1s$ is the period of simulation.

The resulting sum of EPSCs is present on Fig.IV-14B. One can see that resulting synaptic input resembles the colored noise. The mean μ of the signal is equal to 15.78 pA and variance σ to 91.74 pA. The current noise variance optimal for inhibition in the ISR experiments varied between 20 to 400 pA for different cells, Fig.IV-1C. One can see that the amount of analytically calculated current noise fits well within the range of noise variance optimal for ISR. These

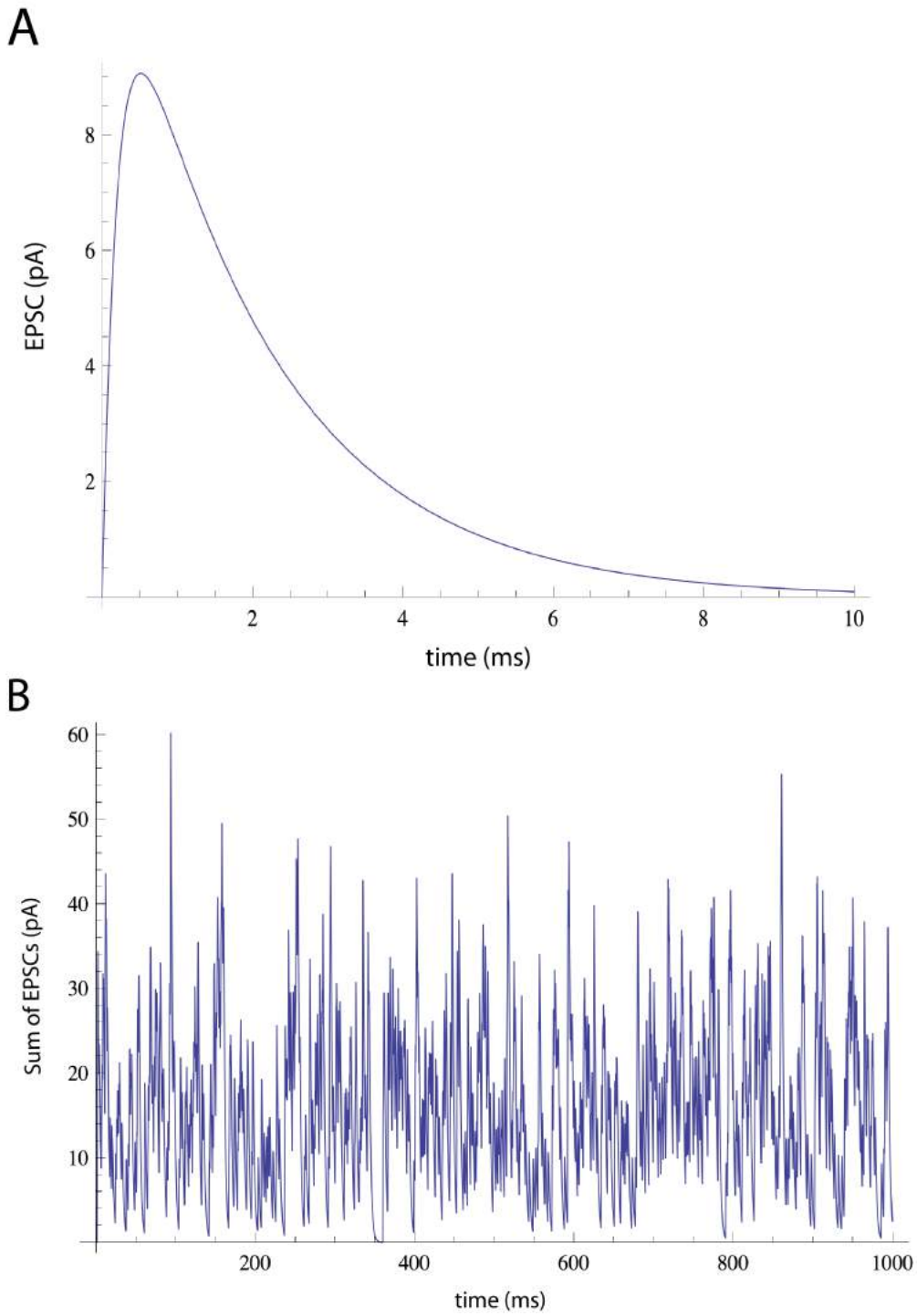

Figure IV-14. Calculation of parallel fiber input to the Purkinje cell
A – EPSC single EPSC formed by a single parallel fiber synapse. B – sum of EPSCs provided by the parallel fiber synapses.

theoretical considerations show that it is generally possible to observe the ISR for the physiological range of parallel fiber activity.

IV.4 Future directions

In this section we discuss the unsolved questions raised in this research and potential ways to solve these problems. We discuss the following topics: fitting of the two-compartment model to Pukinje cells, the model of realistic synaptic noise and the links between biophysical and phenomenological models.

Fitting of two-compartment model to Purkinje cells

Initially the procedure of dynamic I-V has been developed for the pyramidal cells (Badel et al. 2008) possessing relatively small dendritic tree compared to the Purkinje cells. The role of dendrites in these neurons could be partially taken into account by single compartment aEIF model in the form of adaptation. While for large neurons it represents the problem since the neuron dendritic tree could not be well approximated only by adaptation properties. To take into account the complete influence of dendrites one could use the two-compartment aEIF model (Clopath et al. 2007). When the two-compartment aEIF model is used together with dynamic I-V the influence of the dendritic tree is taken into account twice, first in the form of adaptation and second in form of dendrite compartment. We found that application of such model leads to the overestimation of the dendritic tree, Fig.IV-9. The consequence of this dendrite overrepresentation in the model is that the ISR curve could not be perfectly matched with the experimental data. Yet we showed that manual compensation for the soma-dendrite coupling within the reasonable range of dendric conductance could compensate for this effect. Therefore we conclude that to properly describe the Purkinje cell behavior using aEIF model it is necessary to perform additional modifications for the dynamic I-V method. This would allow to use the dynamic I-V method to describe the behavior of large neurons such as Purkinje cells.

Model of realistic synaptic noise

In this work we provided estimation of the synaptic input received by the Purkinje cell via parallel fibers input (IV.3.3 Synaptic noise estimation for Purkinje cell). We followed multiple assumptions about the synaptic input such as independence, equal summation of EPSPs and the similar kinetics. Using these approximations allowed us to consider the input to the Purkinje cell in the form of synaptic noise, which could be approximated using Ornstein-Uhlenbeck process.

In this description we intentionally excluded a lot of complexity of the realistic synaptic input received by the Purkinje cell. In particular we did not include the spatial location of the synapses. While it is known that it could play the substantial role for synaptic integration (Remme et al. 2009, Bollman et al. 2009). We suggest that that the next logical step is to consider the Purkinje cell model with the detailed dendritic tree with spatially distributed synapses where

synapse location is taken from available Ca^{2+} imaging data (Wilms and Häusser 2015). This would allow to find the regimes of synaptic activity where noise approximation of the synaptic input (Renart et al. 2007, Gerstner and Kistler 2002) correctly describes the input to the Purkinje cell.

Biophysical and phenomenological models

In our framework we restricted description of the Purkinje cell dynamics using the phenomenological aEIF model. We are aware that realistic dynamics of the Purkinje cell could not be completely described using this approach. For example the depolarizing plateau characteristic for bistability could not be explained using simple aEIF model since there is no dynamic mechanism for it. If this dynamics need to be taken into account, it is possible to use models with more complex nonlinearity to explain this particular property (Loewenstein et al. 2005).

On the other hand it has been proposed that neural circuits could generate very similar behavior for a broad range of biophysical parameters in single neurons and small networks (Prinz et al. 2004, Marder and Taylor 2011). While application of the minimal models allows getting insights into the low-dimensional dynamical system responsible for complex single neuron behavior (Izhikevich 2007). The major drawback of this approach is that it could not provide explicit predictions in terms single neuron biophysics. To our knowledge there is no widely accepted method to link parameters of the phenomenological and biophysical single neuron models, except the dynamic I-V (Badel et al. 2008). We propose that combination of these models could help to solve these problems. In such top-down approach the minimal model should be used to tune parameters of the biophysical one to match the dynamic behavior. This would allow to restrict the biophysical parameters of the realistic models and find regions in the parameter space corresponding to the desired dynamic behavior. Finding this match could help to provide explicit predictions in terms of single neuron biophysics that could be then tested experimentally. For example this approach could be used in the present aEIF model in conjunction with the detailed Purkinje cell model from (Häusser and Roth 2001) to identify biophysical constrains for ISR and bistability. We believe that developing this hybrid approach could provide better links between the phenomenological and biophysical models.

IV.5 References

Attwell, P. J., Rahman, S., & Yeo, C. H. (2001). Acquisition of eyeblink conditioning is critically dependent on normal function in cerebellar cortical lobule HVI. The Journal of Neuroscience, 21(15), 5715-5722.

Badel, L., Lefort, S., Brette, R., Petersen, C. C., Gerstner, W., & Richardson, M. J. (2008). Dynamic IV curves are reliable predictors of naturalistic pyramidal-neuron voltage traces. Journal of Neurophysiology, 99(2), 656-666.

Badel, L., Lefort, S., Brette, R., Petersen, C. C., Gerstner, W., & Richardson, M. J. (2008). Dynamic IV curves are reliable predictors of naturalistic pyramidal-neuron voltage traces. Journal of Neurophysiology, 99(2), 656-666.

Brette, R., & Gerstner, W. (2005). Adaptive exponential integrate-and-fire model as an effective description of neuronal activity. Journal of neurophysiology, 94(5), 3637-3642.

Clopath, C., Jolivet, R., Rauch, A., Lüscher, H. R., & Gerstner, W. (2007). Predicting neuronal activity with simple models of the threshold type: Adaptive exponential integrate-and-fire model with two compartments. Neurocomputing, 70(10), 1668-1673.

Clopath, C., Nadal, J. P., & Brunel, N. (2012). Storage of correlated patterns in standard and bistable Purkinje cell models.

Couto, J., Linaro, D., De Schutter, E., & Giugliano, M. (2015). On the Firing Rate Dependency of the Phase Response Curve of Rat Purkinje Neurons. PLoS Comput Biol, 11(3), e1004112.

Davie, J. T., Kole, M. H., Letzkus, J. J., Rancz, E. A., Spruston, N., Stuart, G. J., & Häusser, M. (2006). Dendritic patch-clamp recording. Nature protocols, 1(3), 1235-1247.

Davie, Jenny T., Beverley A. Clark, and Michael Häusser. "The origin of the complex spike in cerebellar Purkinje cells." The Journal of Neuroscience 28, no. 30 (2008): 7599-7609.

Dean, P., & Porrill, J. (2011). Evaluating the adaptive□filter model of the cerebellum. The Journal of physiology, 589(14), 3459-3470.

Dean, P., Porrill, J., Ekerot, C. F., & Jörntell, H. (2010). The cerebellar microcircuit as an adaptive filter: experimental and computational evidence. Nature Reviews Neuroscience, 11(1), 30-43.

Dipoppa, M., & Gutkin, B. S. (2013). Correlations in background activity control persistent state stability and allow execution of working memory tasks. Frontiers in computational neuroscience, 7.

Fernandez, F. R., Engbers, J. D., & Turner, R. W. (2007). Firing dynamics of cerebellar purkinje cells. Journal of neurophysiology, 98(1), 278-294.

Fourcaud-Trocmé, N., Hansel, D., Van Vreeswijk, C., & Brunel, N. (2003). How spike generation mechanisms determine the neuronal response to fluctuating inputs. The Journal of neuroscience, 23(37), 11628-11640.

Gerstner, W., & Kistler, W. M. (2002). Spiking neuron models: Single neurons, populations, plasticity. Cambridge university press.

Guo, D. (2011). Inhibition of rhythmic spiking by colored noise in neural systems. Cognitive neurodynamics, 5(3), 293-300.

Gutkin, B. S., Jost, J., & Tuckwell, H. C. (2008). Transient termination of spiking by noise in coupled neurons. EPL (Europhysics Letters), 81(2), 20005.

Gutkin, B. S., Jost, J., & Tuckwell, H. C. (2009). Inhibition of rhythmic neural spiking by noise: the occurrence of a minimum in activity with increasing noise. Naturwissenschaften, 96(9), 1091-1097.

Gutkin, B., Jost, J., & Tuckwell, H. C. (2008). Random perturbations of spiking activity in a pair of coupled neurons. Theory in Biosciences, 127(2), 135-139.

Häusser, M., & Clark, B. A. (1997). Tonic synaptic inhibition modulates neuronal output pattern and spatiotemporal synaptic integration. Neuron, 19(3), 665-678.

Johansson, F., Jirenhed, D. A., Rasmussen, A., Zucca, R., & Hesslow, G. (2014). Memory trace and timing mechanism localized to cerebellar Purkinje cells.Proceedings of the National Academy of Sciences, 111(41), 14930-14934.

Khaliq, Z. M., Gouwens, N. W., & Raman, I. M. (2003). The contribution of resurgent sodium current to high-frequency firing in Purkinje neurons: an experimental and modeling study. The Journal of neuroscience, 23(12), 4899-4912.

Leigh, J., De Schutter, E., Lee, M., Bower, J., & DeFanti, T. (1993). Realistic modeling of brain structures with remote interaction between simulations of an inferior olivary neuron and a cerebellar Purkinje cell. In In Proceedings of the Society for Computing Simulation, High Performance Computing.

Llinas, R., & Sugimori, M. (1980). Electrophysiological properties of in vitro Purkinje cell somata in mammalian cerebellar slices. The Journal of Physiology, 305(1), 171-195.

Loewenstein, Y., Mahon, S., Chadderton, P., Kitamura, K., Sompolinsky, H., Yarom, Y., & Häusser, M. (2005). Bistability of cerebellar Purkinje cells modulated by sensory stimulation. Nature neuroscience, 8(2), 202-211.

London, M., Schreibman, A., Häusser, M., Larkum, M. E., & Segev, I. (2002). The information efficacy of a synapse. Nature neuroscience, 5(4), 332-340.

Mainen, Z. F., & Sejnowski, T. J. (1995). Reliability of spike timing in neocortical neurons. Science, 268(5216), 1503-1506.

Norris, S. A., Greger, B., Hathaway, E. N., & Thach, W. T. (2004). Purkinje cell spike firing in the posterolateral cerebellum: correlation with visual stimulus, oculomotor response, and error feedback. Journal of neurophysiology, 92(3), 1867-1879.

Oldfield, C. S., Marty, A., & Stell, B. M. (2010). Interneurons of the cerebellar cortex toggle Purkinje cells between up and down states. Proceedings of the National Academy of Sciences, 107(29), 13153-13158.

Paydafar, D., Forger, D. B., & Clay, J. R. (2006). Noisy inputs and the induction of on–off switching behavior in a neuronal pacemaker. Journal of neurophysiology, 96(6), 3338-3348.

Phoka, E., Cuntz, H., Roth, A., & Häusser, M. (2010). A new approach for determining phase

response curves reveals that Purkinje cells can act as perfect integrators. PLoS Comput Biol, 6(4), e1000768-e1000768.

Raman, I. M., & Bean, B. P. (1997). Resurgent sodium current and action potential formation in dissociated cerebellar Purkinje neurons. The Journal of neuroscience, 17(12), 4517-4526.

Roitman, A. V., Pasalar, S., & Ebner, T. J. (2009). Single trial coupling of Purkinje cell activity to speed and error signals during circular manual tracking. Experimental brain research, 192(2), 241-251.

Rokni, D., & Yarom, Y. (2009). State-dependence of climbing fiber–driven calcium transients in Purkinje cells. Neuroscience, 162(3), 694-701.

Roth, A., & Häusser, M. (2001). Compartmental models of rat cerebellar Purkinje cells based on simultaneous somatic and dendritic patch□clamp recordings. The Journal of Physiology, 535(2), 445-472.

Rouvas-Nicolis, C., & Nicolis, G. (2007). Stochastic resonance. Scholarpedia, 2(11), 1474.

Schonewille, M., Khosrovani, S., Winkelman, B. H., Hoebeek, F. E., De Jeu, M. T., Larsen, I. M., ... & De Zeeuw, C. I. (2006). Purkinje cells in awake behaving animals operate at the upstate membrane potential. Nature neuroscience, 9(4), 459-461.

Shin, S. L., Rotter, S., Aertsen, A., & De Schutter, E. (2007). Stochastic description of complex and simple spike firing in cerebellar Purkinje cells. European Journal of Neuroscience, 25(3), 785-794.

Touboul, J., & Brette, R. (2008). Dynamics and bifurcations of the adaptive exponential integrate-and-fire model. Biological cybernetics, 99(4-5), 319-334.

Tuckwell, H. C., & Jost, J. (2010). Weak noise in neurons may powerfully inhibit the generation of repetitive spiking but not its propagation.

Tuckwell, H. C., Jost, J., & Gutkin, B. S. (2009). Inhibition and modulation of rhythmic neuronal spiking by noise. Physical Review E, 80(3), 031907.

Urbano, F. J., Simpson, J. I., & Llinás, R. R. (2006). Somatomotor and oculomotor inferior olivary neurons have distinct electrophysiological phenotypes. Proceedings of the National Academy of Sciences, 103(44), 16550-16555.

Walter, J. T., Alvina, K., Womack, M. D., Chevez, C., & Khodakhah, K. (2006). Decreases in the precision of Purkinje cell pacemaking cause cerebellar dysfunction and ataxia. Nature neuroscience, 9(3), 389-397.

Wang, F., Xu, Q., Wang, W., Takano, T., & Nedergaard, M. (2012). Bergmann glia modulate cerebellar Purkinje cell bistability via Ca2+-dependent K+ uptake. Proceedings of the National Academy of Sciences, 109(20), 7911-7916.

Williams, S. R., Christensen, S. R., Stuart, G. J., & Häusser, M. (2002). Membrane potential bistability is controlled by the hyperpolarization□activated current IH in rat cerebellar Purkinje neurons in vitro. The Journal of physiology, 539(2), 469-483.

Willems, F. M., Shtarkov, Y. M., & Tjalkens, T. J. (1995). The context-tree weighting method: basic properties. Information Theory, IEEE Transactions on, 41(3), 653-664.

Yartsev, M. M., Givon-Mayo, R., Maller, M., & Donchin, O. (2009). Pausing Purkinje cells in the cerebellum of the awake cat. Frontiers in systems neuroscience, 3.

Zhou, H., Voges, K., Lin, Z., Ju, C., & Schonewille, M. (2015). Differential Purkinje cell simple spike activity and pausing behavior related to cerebellar modules.Journal of neurophysiology, 113(7), 2524-2536.

GENERAL CONCLUSIONS

Historically much of research in computational neuroscience concerned the dynamics of single neurons and networks using simplified models of neurons such as leaky integrate-and-fire, e. g. (Brunel, 2000, Brunel et al. 2001, Brunel and Rossum, 2007) or even more abstract threshold neurons (Hopfield, 1982, Dayan and Abbott, 2001). Despite the advantages of these models such as simplicity and theoretical tractability, this minimalistic approach does not take into account several important features of the neuronal membrane, such as threshold variability (y Arcas et al, 2003, Platkiewicz and Brette 2011, Chizhov et al. 2014) and adaptive properties (Maravall et al. 2007, Gutkin and Zeldenrust 2014).

On the other hand a significant body of research has been devoted to the development of a very detailed models of single neurons and networks, e.g. (Traub et al, 1991, Markram 2006). The advantage of the biological plausibility of these models is compensated by the high degree of complexity. Large numbers of variables and parameter sets do not allow application of theoretical tools such as phase plane analysis and bifurcation theory to get the insights into the detailed mechanisms of neural excitability on a single cell and neural network level.

Besides that it has been proposed that despite large number of parameters in the biological neural models their dynamics takes place only a limited region of the parameter space (Prinz et al. 2004, Marder and Taylor 2011). It other words general properties of model solutions are very robust to parameter changes, showing that there is a map towards low-dimensional models preserving the general properties of the detailed ones (Izhikevich 2003, Fairhall and Sompolinsky 2014). Therefore we conclude that in neural modeling it is necessary to keep the balance between the biological plausibility to provide testable experimental predictions and model simplicity to allow gaining the insights into the generic mechanisms of excitability.

In the first part of this thesis we showed that combination of single neuron bursting properties due to internal Ca^{2+} dynamics and network recurrent excitation plays an important role for generation of epileptic oscillations. When excitation-inhibition balance is impaired due to intracellular chloride accumulation the recurrent excitation and pyramidal cell bursting currents provoke generation of hyper-synchronous epileptic bursts (**CHAPTER II**) similar to other epilepsy models (Bazhenov et al. 2004, Krishnan and Bazhenov, 2011). Unlike the known models we emphasize the role of coupled dynamics of extracellular potassium and intracellular chloride in seizure initiation. Thus we conclude that single neuron sub-threshold nonlinearity provided by slow Ca^{2+}-dependent potassium currents are important for seizure generation in temporal lobe epilepsy.

In the second part of this thesis we showed that adaptation properties of Purkinje cells allow these neurons to display the inverse stochastic resonance,

bistability and firing-rate hysteresis (**CHAPTER IV**). Without correct description of adaptation and action potential nonlinearity of the neuronal membrane it is impossible to explain these effects found experimentally. An ability of the brain to adapt its activity to changes in the environment is a generic property of the nervous system (Fairhall et al. 2001). On the single cell level such adaptation is usually the result of multiple slow potassium currents (Benda and Herz 2003, Izhikevich 2007, Buchin and Chizhov, 2010).

On the other hand the significance of subthreshold single neuron nonlinear properties is still an open question in computational neuroscience. Classical models of cortical dynamics such as balanced networks (van Vreeswijk and Sompolinsky, 1996) and network models of high-conductance state (Boustani et al. 2007) do not explicitly take them into account (**CHAPTER III**) and implicitly argue that such properties may not be of importance. While even if certain properties of cortical dynamics could be explained without membrane nonlinearities, there are regimes of input integration requiring the complex threshold, which could not be fully explained by fixed threshold integrate-and-fire model (y Arcas et al. 2003).

Another relatively unexplored topic in computational models of neural systems is related to ion concentration changes in the brain. In the majority of biophysical models these concentrations are assumed to be constant due to various homeostatic mechanisms. These assumptions seems to be reasonable for the normal brain function, yet in the case of epilepsy and spreading depression the ion concentrations become an important factor determining the neural excitability (Fröhlich et al. 2008, Bazhenov et al. 2004). Despite the fact that potassium concentration changes are known to be associated with spreading depression and seizures for a long time (Grafstein, 1956, Sypert and Ward, 1974), only recently computational models started taking these pathways into account (**CHAPTER I**). In our model of seizure initiation we propose that increased activation GABAergic synapses leads to intracellular chloride accumulation thereby provoking seizure onset in a realistic neural network model (**CHAPTER II**). Moreover recent works (Jedlička and Backus, 2006, Raimondo et al. 2012) suggested that intracellular chloride could also serve as a mechanism of short-time inhibitory plasticity, so-called “ionic plasticity” even during physiological regimes of interneuron activity. Thus we suggest that incorporation of ion concentration changes into biophysical models of single cells and networks deserves more attention in case of normal and pathological brain dynamics.

In conclusion, in this thesis we have developed two projects. In the first one we proposed a novel mechanism of intracellular chloride accumulation in pyramidal cells of human subiculum related to temporal lobe epilepsy. This model predicts that accumulation of intracellular chloride could provoke seizure initiation in temporal lobe epilepsy. We showed that restoration of the KCC2 cotransporter blocks the seizure activity in the realistic neural network of subiculum, suggesting that restoration of chloride homeostasis could be an

efficient strategy against seizure initiation. In the second project we showed that cerebellar Purkinje cells could be efficiently inhibited by noise, a phenomenon known as inverse stochastic resonance. This noise inhibition is explained by coexistence of spiking and resting state solution near Andronov-Hopf bifurcation. We found that inverse stochastic resonance allows a neuron to optimally transmit information about the input stimuli leading to the peak of mutual information between the input and output spike train. We conclude that the results of this thesis show the importance of single neuron subthreshold nonlinearity and adaptation properties in case of normal and pathological brain dynamics.

The work on this thesis generated many ideas about future research directions. We propose that development of spatially structured networks possessing chloride accumulation mechanism would help to explain the mechanisms of inhibitory restrains proposed in (Trevelyan et al. 2007, Schevon et al. 2012) controlling seizure propagation in the cortex (**CHAPTER II, II.4 Future directions**). Development of the cerebellum network model possessing the inverse stochastic resonance would help to justify the adaptive filter model of cerebellum (Dean and Porrill 2011) requiring adjustable properties potentially implemented by the spiking state of a Purkinje cell population. Also the recordings of the Purkinje cell synaptic input *in vivo* similar to (Wilms and Häuser 2015) are needed to justify the presence and importance of inverse stochastic resonance in physiological conditions (**CHAPTER IV, IV.4 Future directions**).

References

Bazhenov, M., Timofeev, I., Steriade, M., & Sejnowski, T. J. (2004). Potassium model for slow (2-3 Hz) in vivo neocortical paroxysmal oscillations. Journal of neurophysiology, 92(2), 1116-1132.

Benda, J., & Herz, A. V. (2003). A universal model for spike-frequency adaptation. Neural computation, 15(11), 2523-2564.

Brunel, N. (2000). Dynamics of sparsely connected networks of excitatory and inhibitory spiking neurons. Journal of computational neuroscience, 8(3), 183-208.

Brunel, N., & Van Rossum, M. C. (2007). Lapicque's 1907 paper: from frogs to integrate-and-fire. Biological cybernetics, 97(5-6), 337-339.

Brunel, N., & Wang, X. J. (2001). Effects of neuromodulation in a cortical network model of object working memory dominated by recurrent inhibition. Journal of computational neuroscience, 11(1), 63-85.

Buchin, A. Y., & Chizhov, A. V. (2010). Firing-rate model of a population of adaptive neurons. Biophysics, 55(4), 592-599.

Chizhov, A. V., Smirnova, E. Y., Kim, K. K., & Zaitsev, A. V. (2014). A simple Markov model of sodium channels with a dynamic threshold. Journal of computational neuroscience, 37(1), 181-191.

Dean, P., & Porrill, J. (2011). Evaluating the adaptive filter model of the cerebellum. The Journal of physiology, 589(14), 3459-3470.

El Boustani, S., Pospischil, M., Rudolph-Lilith, M., & Destexhe, A. (2007). Activated cortical states: experiments, analyses and models. Journal of Physiology-Paris, 101(1), 99-109.

Fairhall, A. L., Lewen, G. D., Bialek, W., & van Steveninck, R. R. D. R. (2001). Efficiency and ambiguity in an adaptive neural code. Nature, 412(6849), 787-792.

Fairhall, A., & Sompolinsky, H. (2014). Editorial overview: Theoretical and computational neuroscience. Current opinion in neurobiology, (25), v-viii.

Fröhlich, F., Bazhenov, M., Iragui-Madoz, V., & Sejnowski, T. J. (2008). Potassium dynamics in the epileptic cortex: new insights on an old topic. The Neuroscientist, 14(5), 422-433.

Grafstein, B. (1956). Mechanism of spreading cortical depression. J Neurophysiol, 19(2), 154-171.

Gutkin, B., & Zeldenrust, F. (2014). Spike frequency adaptation. Scholarpedia, 9(2), 30643.
Hopfield, J. J. (1982). Neural networks and physical systems with emergent collective computational abilities. Proceedings of the national academy of sciences, 79(8), 2554-2558.

Izhikevich, E. M. (2003). Simple model of spiking neurons. IEEE Transactions on neural networks, 14(6), 1569-1572.

Jedlička, P., & Backus, K. H. (2006). Inhibitory transmission, activity-dependent ionic changes and neuronal network oscillations. Physiol. Res, 55, 139-149.

Krishnan, G. P., & Bazhenov, M. (2011). Ionic dynamics mediate spontaneous termination of seizures and postictal depression state. The Journal of Neuroscience, 31(24), 8870-8882.

Maravall, M., Petersen, R. S., Fairhall, A. L., Arabzadeh, E., & Diamond, M. E. (2007). Shifts in coding properties and maintenance of information transmission during adaptation in barrel cortex. PLoS Biol, 5(2), e19.
Marder, E., & Taylor, A. L. (2011). Multiple models to capture the variability in biological neurons and networks. Nature neuroscience, 14(2), 133-138.

Markram, H. (2006). The blue brain project. Nature Reviews Neuroscience, 7(2), 153-160.

Platkiewicz, J., & Brette, R. (2011). Impact of fast sodium channel inactivation on spike threshold dynamics and synaptic integration. PLoS Comput Biol, 7(5), e1001129-e1001129.

Prinz, A. A., Bucher, D., & Marder, E. (2004). Similar network activity from disparate circuit parameters. Nature neuroscience, 7(12), 1345-1352.

Raimondo, J. V., Markram, H., & Akerman, C. J. (2012). Short-term ionic plasticity at GABAergic synapses. Frontiers in synaptic neuroscience, 4.

Schevon, C. A., Weiss, S. A., McKhann Jr, G., Goodman, R. R., Yuste, R., Emerson, R. G., & Trevelyan, A. J. (2012). Evidence of an inhibitory restraint of seizure activity in humans. Nature communications, 3, 1060.

Sypert, G. W., & Ward, A. A. (1974). Changes in extracellular potassium activity during neocortical propagated seizures. Experimental neurology, 45(1), 19-41.

Traub, R. D., Wong, R. K., Miles, R., & Michelson, H. (1991). A model of a CA3 hippocampal pyramidal neuron incorporating voltage-clamp data on intrinsic conductances. Journal of Neurophysiology, 66(2), 635-650.

Trevelyan, A. J., Sussillo, D., & Yuste, R. (2007). Feedforward inhibition contributes to the control of epileptiform propagation speed. The Journal of neuroscience, 27(13), 3383-3387.

van Vreeswijk, C., & Sompolinsky, H. (1996). Chaos in neuronal networks with balanced excitatory and inhibitory activity. Science, 274(5293), 1724-1726.

Wilms, C. D., & Häusser, M. (2015). Reading out a spatiotemporal population code by imaging neighbouring parallel fibre axons in vivo. Nature communications, 6.

y Arcas, B. A., Fairhall, A. L., & Bialek, W. (2003). Computation in a single neuron: Hodgkin and Huxley revisited. Neural Computation, 15(8), 1715-1749.

ACKNOWLEDGEMENTS

Working on this thesis has been a great and exciting experience, which required hard work. I have been able to complete my research thanks to the support of many people. Here I want to thank all of them who helped me in this journey.

First of all I would like to thank my supervisor Boris Gutkin for his perfect supervision. Thanks to him I had an opportunity to choose the research subject by myself and find the answers to the questions I was mostly excited about. I want to acknowledge him for getting me to write the proposal by myself and allowing me to work in a most convenient way. Beyond science, I feel that I have learned a lot of general scientific skills by working with him and pedagogic skills when I was involved into teaching activities. Thanks to Boris I learned how to collaborate with many researchers in biology field and how to present my own ideas on the public meetings. The last, but not least I am extremely grateful to him for his help with grant writing. Without developing this skill this work would never have been started. I am also very grateful to my scientific co-supervisor Anton Chizhov for accepting to supervise this thesis. His original scientific ideas and gentle supervision helped my to develop my own scientific reasoning. Thanks to his co-supervision I have learned how to generalize the research results and think in a broad scientific context.

I am very grateful to all the members of the PhD committee for having accepted to read and criticize this thesis work. In particular I would like to thank Maxim Bazhenov and Volker Steuber for their patience and availability for scientific discussions. I also would like to thank my doctorate school Cerveau Cognition Comportement and former president François Couraud for accepting my PhD candidature for this thesis.

I want to acknowledge all the members of the Group for Neural Theory (GNT) and the Laboratoire des Neurosciences Cognitives (LNC) where I worked during my research. I would like to especially thank the head of our laboratory Etienne Koechlin for creating the atmosphere in our lab and Sharon Pepperkamp for the great work at Département des Etudes Cognitives (DEC). Thanks to these people I had the unique opportunity to enjoy and contribute to the great academic and social atmosphere in our department. The discussions with my colleagues were very stimulating and enriching experience. In particular I would like to express my gratitude to Dani Marti, Fleur Zeldenrust, Marie Rooy, David Schulz, Johann Lussange, Ralph Bourdoukan, Francesca Mastroguiseppe, Reinoud Maex, Flora Bouchacourt, Srjan Ostojic, Burak Yildiz, Erwan Ledoux, Sophie Deneve, Gabrielle Gutierrez and many other former and present members of the GNT. Also I would like to thank all the people I met during the conference meetings and scientific schools. In particular I would like to thank Beverley Clark, Jenny Davie, Catherine Schevon, Mickey London, Lea Goetz, Sebastian Naze, Timothee Proix, Daria Rylkova, Sergei Prokhorenko, Giri

Krishnan, Fabrice Wendling and Peter Jedlicka for inspiring discussions and reasonable criticism.

I want to especially acknowledge my collaborators. In particular I am very thankful to Richard Miles and Gilles Huberfeld who provided data and general research direction for the first project. I am extremely thankful to Sarah Rieubland, Arnd Roth for the experimental collaboration and guiding of the second project. I want to thank all the members of these groups for their social and scientific interactions. In particular I would like to thank Michael Häuser for the financial support during my visits to University College London.

During my PhD research and studies I lived an amazing period of my life thanks to the friends I met in Paris. Unfortunately this would be too long list, but I would like to thank Konstantin Brenner, Anna Zaytseva, Andrew Indukaev, Maria Khachaturyan, Pascal Plumet, Kristina Kovalskaya, Anton Zykov and many other friends. I want to especially acknowledge my family circle, my parents Elena Buchina and Yuri Buchin as well as my grand parents Margarita Bistrizkaya and Isay Kuzinets for their support.

I also want to acknowledge all funding agencies that have supported my research. In particular Labex grant that provided me the 3-year funding in 2012 – 2014 (ANR-10-LABX-0087 IEC and ANR-10-IDEX-0001-02 PSL) and Fondation du Recherche Médicale for one year grant in 2015 (FDT20140930942). Also I would like to acknowledge partial funding from Ecole Normal Supérieure and INSERM for my conference visits and defense expenses. Without this financial support this work would not be possible.